

Understanding the Solid Electrolyte Interphase Formed on Si Anodes in Lithium Ion Batteries



Yanting Jin

Department of Chemistry

University of Cambridge

This dissertation is submitted for the degree of

Doctor of Philosophy

To my mother Li-Ying and father Li-Ming.

Declaration

I hereby declare that except where specific reference is made to the work of others, the contents of this dissertation are original and have not been submitted in whole or in part for consideration for any other degree or qualification in this, or any other University. This dissertation is the result of my own work and includes nothing that is the outcome of work done in collaboration, except where specifically indicated in the text. This dissertation contains less than 60,000 words excluding the table of contents, figure captions, bibliography, acknowledgments and appendices.

Yanting Jin

September 2018

Acknowledgments

First and foremost, I would like to thank Prof. Clare P. Grey for giving me the opportunity to pursue my PhD degree. Her devotion and dedication to science is always an inspiration for me. I am grateful for her rigorous scientific training and the valuable experimental resources and research collaborations she provided.

At the start of my PhD, I received a lot of help from Drs. Ken Ogata, Benjamin Michaelis, Stefan Tappertzhofen and Prof. Stephen Hofmann from the department of engineering in Cambridge, regarding how to use chemical vapor deposition reactor to synthesize silicon nanowires. They spent a lot of time training me, sharing their expertise and helping me fixing the equipment. I am very thankful for their help.

For the NMR part, I am grateful for Dr. Gunwoo Kim as my first NMR mentor teaching me how to perform NMR experiment from scratch. Dr. Pieter M. M. Magusin, then, led me into more complicated solid-state NMR techniques and challenged me with more advanced topics. For the solution NMR part, Mr. Duncan J. Howe and Dr. Peter Grice provided me tremendous help for measuring all the liquid samples. The collaboration with Dr. Subhradip Paul in the DNP facilities in University of Nottingham was also very fruitful.

Many thanks go to Dr. Elizabeth Castillo-Martínez for her cheerful spirit and her day-to-day supervision. I would also like to thank Mr. Nis-Julian H. Kneusels for our colorations on additives, and Dr. Lauren E. Marbella for helping me preparing manuscripts. I have worked with Drs. David Jefferson, Jingyu Lu and Heather F. Greer on the TEM and would like to thank them for their patient help. Discussions with Prof. Luming Peng, Drs. Tao Liu, Wenbo Zhao, David M. Halat and Mr JeongJae Lee were also very fruitful, and I cannot solve the puzzles without their guidance.

I would also like to thank my funding body: Cambridge Trust and Chinese Scholarship Council for Ph.D. funding without which I wouldn't have been able to come to Cambridge, and Pembroke College for providing wonderful food and accommodations. Finally, I own my gratitude to my parents Liying Yuan and Liming Jin for their love and support at all time.

Abstract

The main aim of this thesis is to reveal the chemical structures of the solid-liquid interphase in lithium ion batteries by NMR spectroscopy in order to understand the working mechanism of electrolyte additives for achieving stable cycling performance.

In the first part, a combination of solution and solid-state NMR techniques, including dynamic nuclear polarization (DNP) are employed to monitor the formation of the solid electrolyte interphase (SEI) on next-generation, high-capacity Si anodes in conventional carbonate electrolytes with and without fluoroethylene carbonate (FEC) additives. A model system of silicon nanowire (SiNW) electrode is used to avoid interference from the polymeric binder. To facilitate characterization via one- and two-dimensional NMR, ^{13}C -enriched FEC was synthesized and used, ultimately allowing a detailed structural assignment of the organic SEI. FEC is found to first defluorinated to form soluble vinylene carbonate (VC) and vinoxyl species, which react to form both soluble and insoluble branched ethylene-oxide-based polymers.

In the second part, the same methodology is applied to study the decomposition products of pure FEC or VC electrolytes containing 1 M LiPF_6 . The pure FEC/VC system simplifies the electrolyte solvent formulation and avoids the interaction between different solvent molecules. Polymeric SEIs formed in pure FEC or VC electrolytes consist mainly of cross-linked PEO and aliphatic chain functionalities along with additional carbonate and carboxylate species. The presence of cross-linked PEO-type polymers in FEC and VC correlates with good capacity retention and high Coulombic efficiencies of the SiNWs anode. Using ^{29}Si DNP NMR, the interfacial region between SEI and the Si surface was probed for the first time with NMR spectroscopy. Organosiloxanes form upon cycling, confirming that some of the organic SEI is covalently bonded to the Si surface. It is suggested that both the polymeric structure of the SEI and the nature of its adhesion to the redox-active materials are important for electrochemical performance.

Finally, the soluble decomposition products of EC formed during electrochemical cycling have been thoroughly analyzed by solution NMR and mass spectrometry, in order to explain the

capacity-fading of Si anodes in a conventional EC-based electrolyte and address questions that arose when studying the additive-containing electrolytes. The detailed structures for the EC-degradation products are determined: a linear oligomer consist of ethylene oxide and carbonate units is observed as the major degradation product of EC.

List of Publications

Chapter 3 contains material from the publication:

Jin, Y.; Kneusels, N. H.; Magusin P. C. M. M.; Kim, G.; Castillo-Martinez, E.; Marbella, L. E.; Kerber, R. N.; Howe, D. J.; Paul, S.; Liu, T.; Grey, C. P. Identifying the Structural Basis for the Increased Stability of the Solid Electrolyte Interphase Formed on Silicon with the Additive Fluoroethylene Carbonate, *J. Am. Chem. Soc.* **2017**, 139, 14992 (DOI: 10.1021/jacs.7b06834)

Chapter 4 contains material from the publication:

Jin, Y.; Kneusels, N. H.; Marbella, L. E.; Castillo-Martinez, E.; Magusin P. C. M. M.; Weatherup R. S.; Jonsoon E.; Liu, T.; Paul, S.; Grey, C. P. Understanding Fluoroethylene Carbonate and Vinylene Carbonate Based Electrolytes for Si Anodes in Lithium Ion Batteries with NMR Spectroscopy, *J. Am. Chem. Soc.* **2018**, 140, 9854 (DOI: 10.1021/jacs.8b03408)

Contents

Contents	xii
List of Figures	xvi
List of Tables	xxi
List of Abbreviations	xxiii
Chapter 1 Introduction.....	1
1.1 Introduction to lithium ion batteries	1
1.2 Silicon anodes	6
1.2.1 Electrode structures.....	7
1.2.2 Polymeric binder	8
1.2.3 Electrolytes for Si anodes	9
1.3 Solid electrolyte interphase.....	9
1.3.1 Understanding SEI in baseline electrolyte.....	10
1.3.2 Understanding the role of additives	11
1.3.3 Ionic and electronic properties of SEI	13
1.3.4 Artificial interphase	15
1.4 Outline of the thesis	17
Chapter 2 Methodology.....	19
2.1 Chemical vapor deposition (CVD)	19
2.2 Electrochemistry	21
2.2.1 Galvanostatic voltage-capacity curve	21
2.2.2 Differential Capacity Analysis.....	22
2.3 Nuclear magnetic resonance (NMR)	23
2.3.1 NMR basics.....	23
2.3.2 Spin interactions.....	25
2.3.3 Chemical shift	25
2.3.4 Dipole-dipole coupling (through space)	26
2.3.5 J-coupling (through bond).....	27
2.4 NMR experiments.....	28
2.4.1 Spin operators	28
2.4.2 Spin echo.....	30
2.4.3 Two-dimensional NMR basics	32

2.4.4	Homonuclear correlation spectroscopy (COSY)	32
2.4.5	Heteronuclear correlation experiments	33
2.4.6	Diffusion ordered spectroscopy (DOSY).....	36
2.4.7	Solid-state NMR techniques	37
2.4.8	Dynamic nuclear polarization (DNP)	43
Chapter 3	Identifying key degradation products of fluoroethylene carbonate	47
3.1	Introduction.....	47
3.2	Experimental.....	48
3.2.1	Materials	48
3.2.2	Synthesis of $^{13}\text{C}_3$ -fluoroethylene carbonate	48
3.2.3	Synthesis of silicon nanowires.....	49
3.2.4	Electrolyte preparation and coin cell assembly	49
3.2.5	Solution NMR.....	50
3.2.6	Solid-state NMR	51
3.2.7	DNP NMR	52
3.3	Results.....	52
3.3.1	Electrochemistry	52
3.3.2	Soluble degradation products as measured by solution NMR.	54
3.3.3	Assignment of VC from analysis of the J-coupling.....	59
3.3.4	Assignment of branched oligomers and vinoxyl species.....	60
3.3.5	^{13}C ssNMR and DNP NMR detection of the SEI	61
3.4	Discussion.....	64
3.5	Conclusions.....	71
Chapter 4	Probing the interfacial structure between the SEI and the Si anode	73
4.1	Introduction.....	73
4.2	Experimental.....	74
4.3	Results.....	76
4.3.1	Electrochemistry	76
4.3.2	Organic SEI components revealed by ^1H and ^{13}C ssNMR	79
4.3.3	Molecular fragments in the organic SEI	83
4.3.4	Lithiated and fluorinated components in the SEI	86
4.3.5	The SiO_x -SEI interface	87
4.4	Discussion.....	91
4.5	Conclusions.....	97
Chapter 5	Electrochemical reduction products of ethylene carbonate	99
5.1	Introduction.....	99

5.2	Experimental.....	100
5.3	Results.....	102
5.3.1	Electrochemistry	102
5.3.2	^1H solution NMR of cycled electrolyte.....	103
5.3.3	Oligomers identified by ^1H - ^{13}C correlation NMR.....	104
5.3.4	^{13}C - ^{13}C correlation NMR	108
5.3.5	^1H and ^{13}C chemical shifts of oligomers.....	111
5.3.6	Confirmation of oligomers by mass spectrometry.....	112
5.4	Discussion.....	113
5.5	Conclusion	116
Chapter 6	Conclusions and Future Work	118
References	121
Appendix A	133
Appendix B	142
Appendix C	156
Appendix D	161

List of Figures

Figure 1.1 Schematics of basic components in a lithium ion battery cell and a mosaic model of the solid electrolyte interphase (SEI) adapted from ref. ⁵	2
Figure 1.2 Chemical structures of lithium salts and solvents in the electrolyte (a), and various additives (b) summarized from ref. ¹⁴	5
Figure 1.3 Electron energy diagram of a lithium ion battery cell (a) before and (b) after cycling. The Fermi energy levels of the anode and cathode are denoted as μ_A and μ_C , respectively. E_g represents the thermodynamic stability window of the electrolyte. OCV is the open circuit voltage.	6
Figure 1.4 Electrode structure and binder design for Si anodes. (a) Main failure modes for Si anodes. (b) General strategies for modifying active materials by using Si-C composite or SiO_x . (c) Various binder concepts for Si anodes. SEI, solid-electrolyte interphase. Figure adapted from ref. ^{16,17}	7
Figure 1.5 Degradation products in standard EC-based electrolyte and its influence on the composite electrode. (a-b) Major reduction products of EC. (c) Schematic showing microscale processes within the Si electrodes after cycling. A cross-section of the cycled composite electrode revealed by the FIB/SEM. Figure adapted from ref. ⁴⁴	10
Figure 1.6 Reduction products of FEC and VC proposed in the literature. (a) A Li ion conductive polyene-type cross-linked polymer derived from a four-electron reduction process of FEC proposed in ref ⁴⁸ based on observations from on-line electrochemical mass spectrometry. (b) A poly(VC) type polymer from the reduction of FEC and VC based on ssNMR data. ¹³ C chemical shifts are assigned on the structures and coloured in blue. Structure taken from ref. ⁴¹	11
Figure 1.7 Properties of SEI. (a) Schematic showing SEI should be Li ion conductive, but prevent solvent permeation or electron tunnelling to create new SEI. (b) Mechanism of Li ion transport in the SEI film. ⁵⁹ (c) Schematic of the Li ion transfer steps at the graphite/electrode interphase: the desolvation process is more energetically demanding than the diffusion of bare Li ions through the SEI. ⁴⁰	14
Figure 1.8 Examples for artificial SEI designs. Schematic of the general strategies for SEI studies (middle). (a) Coating Si nanoparticle with cyclic poly(acrylonitrile). ⁶¹ (b) Solid polymer electrolyte with high Li ion conductivity. ⁶² (c) A highly elastic binder for Si anode: the stress-strain curve of polyacrylic acid (PAA) and cross-linked polyrotaxane-PAA. ²⁹ (d) Artificial SEI with covalent bond to the Si particle. ⁶³	16
Figure 2.1 Schematic of the VLS growth mechanism for SiNWs (a), adapted from ref ⁷¹ . (b) A growth recipe used in this work. (c) Morphologies of SiNWs taken by SEM and TEM.	20
Figure 2.2 Chemical vapor deposition reactor for growth of SiNWs.	20
Figure 2.3 (a) Vector model representation of the bulk magnetization \mathbf{M} in an external B_0 field. Nuclear spins align (spin up) or against (spin down) the applied field, creating a Zeeman energy splitting. (b) Application of a 90° pulse along x-axis (viewed from the rotating frame, denoted	

as x^R). The rf pulse creates a static B_1 field along the x-axis and B_0 is reduced to ΔB . (c) Free precession of the magnetization within the xy-plane in the rotating frame.	24
Figure 2.4 Product operators for two spin system (left). Example of in-phase, anti-phase and multi-quantum operators (middle). Diagrams for determining the result of rotating in-phase operators about x, y or z axis under a 90° pulse (right, blue circles), and effect of the J-coupling on in-phase and anti-phase operators under free precession (right, red circles).	29
Figure 2.5 Analysis of single 90° pulse and spin echo pulse sequence on a two-spin system with J-coupling. The evolution of offset is ignored here, but the offset is recovered in the spin echo pulse sequence. The black rectangle denotes a 90° pulse and the white a 180° pulse; the same notation is used in the pulse sequences described below.	31
Figure 2.6 Basic pulse sequence for COSY with simplified product operator analysis given below the sequence.	33
Figure 2.7 Pulse sequences for (a) HSQC and (b) HMBC and the corresponding operator analyses. The coherence transfer step is highlighted in yellow and the multiple quantum generation step is highlighted in blue.	34
Figure 2.8 Principle of a DOSY experiment. (a) A basic DOSY pulse sequence based on the spin-echo. (b) Schematic of the spatial encoding and decoding along the z-axis due to the gradient pulses. (c) Data processing procedure to extract the diffusion coefficients for different chemical shifts and (d) a schematic the 2D DOSY spectrum showing the separation of a mixture with different diffusion coefficients.	36
Figure 2.9 Essential techniques in solid-state NMR. (a) Illustration of magic-angle spinning. The shielding tensor is represented here by an ellipsoid, and its z-axis in the principal axis frame is noted as Z^{PAF} . (b) Illustration of the basic principle underlying the Lee-Goldburg homonuclear decoupling sequence (the offset is chosen so that the effective field is tilted at the magic angle). (c) The cross-polarization pulse sequence, with a high power 1H decoupling sequence such as TPPM used for heteronuclear decoupling.	38
Figure 2.10 Pulse sequence corresponding to a homonuclear correlation experiment based upon dipolar coupling interactions. The C7 sequence is used to excite double quantum coherence under MAS. For the proton decoupling depicted in the upper section, dark grey denotes heteronuclear decoupling, while light grey denotes homonuclear decoupling. A schematic of the double quantum–single quantum correlation spectrum is illustrated on the right.	41
Figure 2.11 Pulse sequence corresponding to heteronuclear correlation experiments based upon dipolar coupling interactions.	42
Figure 2.12 Principles and applications of DNP NMR. (a) The polarization difference between electrons (green) and 1H (black) as a function of temperature at a field strength of 14 T. DNP transfer mechanisms: (b) the solid effect, induced by zero-quantum (middle) or double quantum (bottom) microwave irradiation; these transitions rely on hyperfine interactions (A_{hfi}) between the nucleus and the electron; (c) the cross effect, which involves two electrons and one nucleus, and its corresponding energy diagram when irradiating with microwaves at one frequency. The strong electron–dipolar coupling (d_{ee}) allows mixing of states 2, 3, 6 and 7 which are important for polarization transfer from electrons to nuclei. (d) Example of the use of DNP NMR to obtain surface information on a nanoporous silica-derived material. Figure adapted from ref ^{81,82} ...	43
Figure 2.13 Schematic of the DNP NMR experiments performed in this work.	45

Figure 3.1. Electrochemical performance of SiNWs half-cells cycled with LP30 electrolyte (1 M LiPF₆ in EC/DMC=50/50, v/v, black), and LP30 with 10 vol % FEC (LP30 + FEC, red) electrolytes at a rate of C/30 (120 mA g⁻¹) between 0.001–2 V at room temperature. (a) Galvanostatic charge-discharge profiles and the corresponding dQ/dV plots of SiNWs cycled in LP30 and LP30 + FEC in the 1st, 2nd, and 30th cycles, (b) the cycling stability and (c) the coulombic efficiency for LP30 (black squares) and LP30 + FEC (red dots). The open dots/squares denote the discharge/lithiation capacity and the filled denote the charge/delithiation capacity.53

Figure 3.2. ¹H solution NMR of (a) LP30 and (b) LP30 + FEC (c) LP30+¹³C₃ FEC (LP30 + 10 vol% ¹³C₃ FEC) before cycling (pristine), and after the 1st and 30th cycles. The y scale of the 5–10 ppm region is enlarged by 33 times compared to the 3–5 ppm region. ¹³C satellites are marked with an asterisk. All spectra were measured with a magnetic field strength of 9.4 T, except for the 30th cycle LP30+¹³C₃ FEC sample was measured at 11.7 T.55

Figure 3.3. 2D solution NMR spectra of the LP30 + ¹³C₃ FEC electrolyte after 30th cycles. (a) ¹H-¹³C HSQC with ¹³C decoupling, blue and red represent positive and negative peaks, respectively. (b) ¹³C-¹³C COSY spectra. The off-diagonal peaks are marked with dashed squares. Possible structures are given next to the corresponding peaks; species containing aldehyde terminal groups are shaded in blue and the cross-linking units are shaded in red. ..57

Figure 3.4. Multiplet pattern of cycled LP30 + ¹³C₃ FEC in region γ, (a) experimental pattern (the inset on the upper right-hand corner is the J-coupling constants of VC obtained from the ¹H NMR spectrum of VC as illustrated in Figure A.6); (b) simulated pattern of a four-spin system AA'XX' (cis-H-CR=CR-H) with the J-coupling constants used in the simulation listed on the upper right corner.59

Figure 3.5. ¹H-¹³C CP NMR spectra of SiNWs cycled in LP30 with 25 vol % ¹³C₃ EC (LP30 + ¹³C₃ EC). (a) and LP30 with 10 vol% ¹³C₃ FEC (LP30 + ¹³C₃ FEC) (b) electrolytes, for 30 cycles. The RT spectra were measured at room temperature by conventional ssNMR, while the 100 K spectra were measured using DNP NMR with the microwaves turned on. Ortho-dichlorobenzene (DCB) was used as a radical solvent in the DNP experiments and its isotropic resonances are labelled “DCB”; the spinning sidebands of all the resonances are marked with asterisks. Possible structures are given next to the various isotropic resonances where R represents CH/CH₂/CH₃ groups.62

Figure 3.6 2D ¹H-¹³C heteronuclear correlation (HETCOR) DNP-NMR of SiNWs cycled in LP30+¹³C₃ EC electrolyte (a) and LP30 + ¹³C₃ FEC electrolyte (b) for 30 cycles. Spinning sidebands arising from the DCB solvent are marked “ssb”; artefact peaks marked with # are due to spin locking along the effective field arising from the proton decoupling and they appear at the ¹H carrier frequency.¹⁰⁹ Full spectra and additional experimental details can be found in the Appendix A.63

Figure 4.1. Electrochemistry of SiNWs cycled in standard LP30, LP30 + 10 vol % FEC, and 1 M LiPF₆ in FEC or VC, electrolytes (colored in black, dark red, red and blue, respectively). The voltage profiles and the dQ/dV curves of the SiNWs at the 1st cycle (a-b) and the 50th cycle (c-d) for LP30, FEC and VC. Discharge/lithiation capacity versus cycle number (e) and the corresponding Coulombic efficiency (CE) during cycling (f) for all four electrolytes. The initial CE is shown in the insert in (f). Capacity loss (defined as the lithiation capacity minus the delithiation capacity) during each cycle (g) and accumulated capacity loss versus cycle number (h). The capacity loss of the 1st cycle is shown in the insert in (g). The legend in (g-h) is the

same as in (e). Cells were cycled at C/30 for the 1 st cycle, then at C/10 for later cycles between 0.001 V – 2 V.....	77
Figure 4.2. ¹ H MAS NMR spectra (a-c) and ¹ H- ¹³ C CP MAS NMR spectra (d-f) of SiNWs cycled in LP30, LP30 + 10 vol% FEC, pure FEC and VC electrolytes for the 1 st , 30 th and 50 th cycle. Spectra of SiNWs cycled in 95% natural abundance FEC+5 vol% ¹³ C ₃ FEC for 100 cycles are included in (b, e). All spectra were measured at room temperature using conventional ssNMR.	79
Figure 4.3. (a) ¹ H- ¹³ C CP DNP NMR (105 K) spectra of SiNW cycled in LP30 (black), FEC (red) and VC (blue) for 50 cycles, where the intense (truncated) peak at 74 ppm is due to the DNP solvent tetrachloroethane (TCE); * = spinning sidebands. (b) Conventional, room temperature ¹³ C CP NMR of SiNW cycled in FEC + 5% ¹³ C ₃ FEC for 100 cycles (i) measured by ¹ H- ¹³ C CP, (ii) measured by ¹³ C direct excitation (DE) with a recycle delay of 60 s to extract quantitative information.....	82
Figure 4.4. DNP enhanced 2D DQ – SQ ¹³ C – ¹³ C POST-C7 dipolar correlation spectrum of SiNW cycled in FEC+ 5% ¹³ C ₃ FEC for 100 cycles. 1D ¹ H- ¹³ C CP NMR and the total projection in the SQ dimension are overlaid on top. The corresponding molecular fragments are listed on the right panel. The branching fragments are colored in red; the fragments containing ethylene oxide carbons are colored in blue and the alkyl chains in black.	84
Figure 4.5. ⁷ Li and ¹⁹ F ssNMR spectra of SiNWs cycled 1M LiPF ₆ in pure FEC or VC electrolytes after 1 st , 30 th and 50 th cycles measured at MAS speed of 30 kHz. The grey line in (b) is ¹⁹ F NMR spectra of glass fiber separator after 50 cycles in FEC electrolytes measured at MAS of 25 kHz. Spinning sideband are marked with asterisks and dots.....	86
Figure 4.6 ²⁹ Si NMR spectra of cycled Si using different techniques. (a) ¹ H- ²⁹ Si CP DNP NMR of SiNWs after the first, 50 and 100 cycles; pristine silicon nanoparticles were measured by ¹ H- ²⁹ Si CP NMR without DNP and its spectrum is included for comparison. (b) ²⁹ Si DNP NMR using cross polarization (CP) and direct excitation (DE) on SiNWs cycled in LP30 for 50 cycles, with recycle delay of 3.5 s and 10 s, respectively. The CP spectrum mainly shows proton-containing surface species, whereas the DE spectrum (grey in b) mainly contains signals from the outer SiO _x shell on the SiNWs. (c) ¹ H- ²⁹ Si HETCOR of SiNWs cycled in FEC for 50 cycles with a 5 ms contact time and recycle delay of 3 s. (d) Cartoon showing possible Si surface structures and their corresponding chemical shifts; R denotes an alkyl group. The proposed structures are mainly based on the ¹ H- ²⁹ Si HETCOR result. ²⁹ Si shifts of SiO _x and Si species are summarized: crystalline silicon (c-Si) -81 ppm; amorphous silicon (a-Si) -40 to -70 ppm ¹³¹	88
Figure 5.1 Electrochemical performance of SiNWs cycled in LP30 (black) and LP30+ ¹³ C ₃ EC (blue) electrolytes. (a) Capacity retention, (b) Coulombic efficiency versus cycle number. (c) The voltage curves at the 2 nd , 30 th and 50 th cycle and (d) the their corresponding dQ/dV plot of cells cycled in LP30 electrolyte.	102
Figure 5.2 ¹ H solution NMR of the pristine and cycled electrolytes. The intensity is normalized by the most intense peak. The ¹³ C satellites are marked with asterisks.....	103
Figure 5.3 2D correlation NMR spectra of electrolytes after 30 cycles: LP30 sample in the upper panel and LP3+ ¹³ C ₃ EC sample in the lower panel. (a, d) ¹ H- ¹ H COSY, showing the proton-proton correlation; (b, e) ¹ H- ¹³ C HSQC showing the one bond proton-carbon correlation; (c, f) ¹ H- ¹³ C HMBC showing proton-carbon correlation through 2 to 4 bonds, one bond correlation artefact in HMBC is marked with "#".	104

Figure 5.4 ^1H solution NMR of cycled LP30 and LP30+ $^{13}\text{C}_3$ EC electrolytes. The black spectrum is the electrolyte measured immediately after cell disassembly, while the blue spectrum is acquired on the same sample but after water contamination. After moisture permeates into the NMR tube, the d_1 peak at 3.30 ppm corresponding to lithium methyl carbonate (LMC, LiOCOOCH_3) decreases with the concomitant emergence of new peaks labelled as a_3 and e that corresponds to methanol..... 107

Figure 5.5 ^1H DOSY of the LP30+ $^{13}\text{C}_3$ EC electrolyte after 30 cycles. The centre of the peak corresponds to the diffusion coefficient and the peak width is associated with fitting error. 108

Figure 5.6 Full ^{13}C - ^{13}C COSY spectrum of cycled LP30+ $^{13}\text{C}_3$ EC. The central diagonal peak of $^{13}\text{C}_3$ EC is removed for spectrum clarity. 109

Figure 5.7 ^{13}C - ^{13}C COSY spectra of cycled LP30+ $^{13}\text{C}_3$ EC electrolyte after 30 cycles (a-c). The 1D ^{13}C NMR spectrum and the extracted 1D slices from the COSY spectra (d). Proposed chemical structures derived from the correlation experiments (e)..... 110

Figure 5.8 ^{13}C and ^1H NMR shift predicted by ChemDraw Software for alkyl carbonate oligomers with different ending groups (hydroxide in black square, methoxide in red triangle, carbonate in blue dot) and different chain lengths (increasing ethylene oxide units from left to right). The atoms connected to the carbonate are labelled from 1 and onwards. The experimental ^{13}C and ^1H NMR shifts values are draw as solid lines with labels corresponding to the peaks observed in ^{13}C and ^1H NMR spectra. For oligomers containing methoxide ending group, the ^1H and ^{13}C NMR is also predicted for the methoxide, and they are labelled as the last number..... 111

Figure 5.9 ESI-HRMS spectrum of SiNWs cycled in LP30 electrolyte for 30 cycles. The cycled SiNWs were soaked in CH_3CN , then the solution is diluted before MS measurement..... 112

List of Tables

Table 2.1 Summary of the thermodynamics of the solid solution and two-phase reaction in a cell.....	22
Table 3.1 Electrolyte formulation with 1M LiPF ₆ in different solvent mixtures.....	49
Table 3.2 Summary of the assignments from HSQC, HMBC and ¹³ C COSY experiments for cycled LP30 + ¹³ C ₃ FEC electrolyte.	58
Table 4.1 Electrolyte formulations with 1 M LiPF ₆ in different solvent mixtures	74
Table 4.2 Summary of the DNP NMR samples.....	75
Table 4.3. Summary of the intensity and assignments of the peaks obtained by deconvolution of the ¹³ C direct excitation ssNMR spectrum of the ¹³ C ₃ FEC sample.....	83
Table 5.1 Assignments in 2D correlation NMR in Figure 5.3. Correlations value marked with * are not shown in the figure but are present in a lower contour level.	106
Table 5.2 Mass spectroscopy data and the proposed structures with their corresponding mass.	113

List of Abbreviations

COSY	Correlation spectroscopy
DFT	Density functional theory
DNP	Dynamic nuclear polarization
EC	Ethylene carbonate
FEC	Fluoroethylene carbonate
VC	Vinylene carbonate
HSQC	Heteronuclear single quantum correlation
HMBC	Heteronuclear multiple bond correlation
MAS	Magic-angle spinning
NMR	Nuclear magnetic resonance
SiNWs	Silicon nanowires
rf	Radio frequency
XRD	X-ray diffraction
ω_0	Larmor frequency

Chapter 1 Introduction

1.1 Introduction to lithium ion batteries

Lithium ion batteries (LIBs) have been widely applied in portable electronics and have drawn increasing attention for potential applications in electrical vehicles (EV) and distributed grid-storage.^{1,2} Vehicle electrification is now seen as a promising way to reduce the carbon emission and to improve the urban air quality. Countries including UK, France, Germany and China have announced plans to ban the sales of internal combustion engine vehicles by 2030 in order to meet the carbon reduction target. Though EVs are almost exclusively powered by LIBs, its market share is only 2 % and sales rely heavily on supporting government policy.³ For EVs to be more widely adopted, key properties of LIBs must be improved, including energy density, cycle life, cost, safety, fast-charging rate and grid compatibility.⁴

The current widely-used, commercial LIB chemistry is shown in Figure 1.1. The cell consists of a lithium transition metal oxide as the cathode, graphite as the anode and an organic liquid electrolyte. The state-of-the-art electrode materials and their future outlook are briefly summarized below.

Cathode materials

Most cathode materials are lithium transition metal oxides with a layered structure (LiMO_2 , $\text{M}=\text{Co}, \text{Ni}, \text{Mn}, \text{etc}$) that provides channels for Li ion diffusion. Pioneering works by Whittingham and Goodenough on ionic conductor and guest-host chemistry led to the widely applied cathode materials used at present. Among the layered oxides, LiCoO_2 was the first material to be successfully commercialized by Sony in 1991. Though LiCoO_2 offers a long

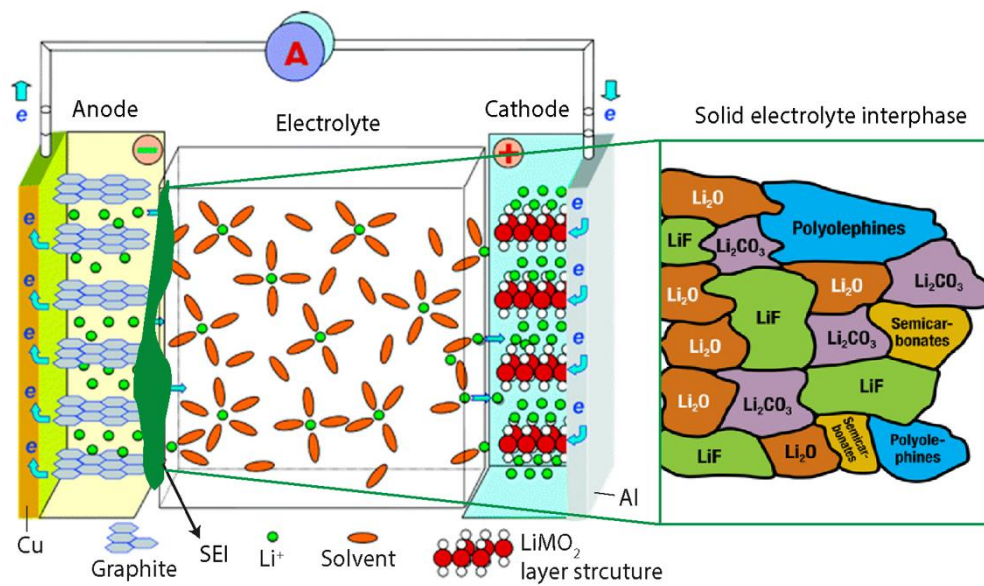


Figure 1.1 Schematics of basic components in a lithium ion battery cell and a mosaic model of the solid electrolyte interphase (SEI) adapted from ref.⁵

cycle life, only approximately 0.5 mol Li ion can be removed per unit cell because further delithiation destabilizes the layered structure, limiting the capacity of LiCoO₂ to 140 mAh/g.

To reduce the cost and increase the energy density further, the general strategy is to substitute cobalt with other transition metals. Nickel, manganese and cobalt (NMC) or nickel, cobalt and aluminium (NCA) type layered oxides are currently the two most widely used positive materials in EVs.⁵ In NMC, the Mn⁴⁺ is inactive in the structure, whereas the Co^{3+/4+} offers a one-electron redox process, and part of the nickel can offer two electron processes for the Ni^{2+/4+} couples. Hence, the higher the Ni content, the higher the capacity for different compositions of NMC cathodes. For example, the capacity of NMC-111 (LiNi_{1/3}Mn_{1/3}Co_{1/3}O₂) is ~160 mAh/g, whereas NMC-811 (LiNi_{0.8}Mn_{0.1}Co_{0.1}O₂) possess a theoretical capacity of 200 mAh/g. However, high Ni content cathodes exhibit significantly shorter cycle lives and lower thermal stabilities. Synthesizing NMC particles with Ni-rich cores and Mn-rich shells has been proposed as a feasible way to mitigate the capacity fading.⁶ Currently, intense research is being performed to improve the NMC-811 material. Another type of future cathode materials are the Li-rich oxides which incorporate lithium, nickel and manganese into the cobalt layer.⁸ The Li-rich NMC cathode offers significantly higher capacity (~300 mAh/g) as it is thought to exploit

the anion redox activity of oxygen, but it suffers from slow kinetics, rapid voltage fading and capacity fading that hinder its implementation in the near future.⁷

Anode materials

With respect to the anode chemistry, carbonaceous materials such as graphite are widely used in the anode.^{8–10} The operating voltage of graphite (50–200 mV vs. Li^+/Li) is similar to that of Li metal, which means that graphite can offer high voltage in a full cell. The commercialization of graphite anodes is closely related to the careful selection of electrolyte and additives as the operating voltage of the anode is below the stability window of the electrolyte solvents (<1.2 V vs. Li^+/Li). During cycling, a passivation layer called the solid electrolyte interphase (SEI) forms on the anode surface to prevent further electrolyte degradation as illustrated in Figure 1.1. In propylene carbonate (PC) based electrolyte, solvent co-intercalation with the Li ions occurs that exfoliates the graphite sheets. By replacing PC with ethylene carbonate (EC), the nature of the SEI layer is altered and EC enables reversible Li ion insertion/extraction into/from graphite layers. Another anode material is lithium titanate ($\text{Li}_4\text{Ti}_5\text{O}_{12}$, LTO), which is nominally SEI-free as its operating voltage is around 1.55 V vs. Li^+/Li and it is within the stability window of the solvents. LTO anodes provide fast charging capabilities at the expense of a reduced overall cell potential.¹¹

For next-generation anodes, Si-based materials and Li metal are expected to play an important role, because they both offer high capacities as well as low operating voltages. Unfortunately, the large volume variation of Si that occurs during lithiation/delithiation results in poor interfacial stability and unabated SEI growth. The major issues related to adopting Si anodes will be discussed in detail in the later sections. For Li metal, mossy and needle-like structures form (also known as Li dendrites) during Li deposition. These dendrites can penetrate the separator leading to cell short-circuiting, thermal runaway, and even explosion. During charge, non-uniform Li dissolution takes place on the dendritic Li and dead Li forms, which lowers the energy density of the cell as more Li metal is needed to compensate for the Li loss. Strategies to overcome these difficulties include surface coating, a judicious selection of electrolyte formulations, and finding a compatible solid electrolyte that exhibits sufficient ionic conductivity.

Electrolytes

Commercial LIBs typically contain organic liquid electrolytes based on lithium hexafluorophosphate (LiPF_6) dissolved in a mixture of linear and cyclic alkyl carbonate solvents. The bulky PF_6^- anion (Figure 1.2) is a soft Lewis acid that delocalises the negative charge and has low dissociation energy with Li cations so that its salt has high solubility as well as a high cation transference number (i.e. the portion of ionic conductivity arising from Li cations). Moreover, the PF_6^- anion passivates the aluminium current collector used on the cathode, thus enabling Al to operate at high voltage. Similar super acid anions including bis(trifluoromethanesulfonyl)imide (TFSI), and bis(oxalato)borate (BOB) are currently used as additives or replacement salts.⁸

The requirements for electrolyte solvents include high dielectric constant (to dissolve the Li salt) low viscosity and wide operating temperature. The state-of-the-art solvents are based on alkyl carbonates and normally a mixture is used to meet the criteria listed above. For example, the cyclic carbonates (e.g. EC), which are highly polar and rather viscous, are diluted with fluid linear carbonates such as dimethyl carbonate (DMC). To tailor the performance of LIBs, various additives are commonly added into the baseline electrolyte with concentration less than 5 wt%. Since the choice of solvents affects the solvation sheath of the Li ions, the properties of the SEI can be modified to achieve certain functions. While EC is indispensable for graphite anodes, additives such as fluoroethylene carbonate (FEC) and vinylene carbonate (VC) are particularly useful to extend the cycle life of alloy-type anodes. FEC and VC coordinate with Li ions and are preferentially reduced to form an effective SEI.

The main issue with liquid organic electrolytes is their poor intrinsic safety, especially at elevated temperatures. To replace the volatile and flammable liquid electrolyte, Li ion conductive solid electrolytes are attracting increasing attention. There are generally two types of solid electrolytes: polymer-based and inorganic-ceramic based. Poly(ethylene oxide) (PEO)-type solid polymer electrolytes have been used in batteries in an EV-sharing programme called Bluecar for urban transportation with limited drive-ranges.¹² However, the ionic conductivity and oxidation stability of PEO-based electrolytes still need to be improved. Promising inorganic solid electrolytes based on sulfides have been reported to have even higher ionic conductivity than liquid electrolytes,¹³ however, problems remain to be solved regarding

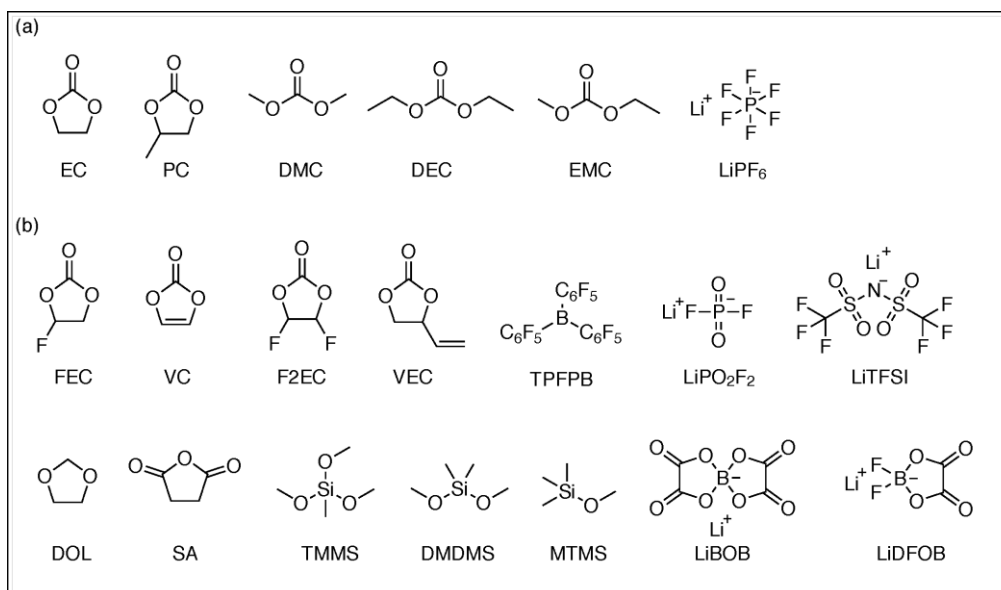


Figure 1.2 Chemical structures of lithium salts and solvents in the electrolyte (a), and various additives (b) summarized from ref. ¹⁴. Cyclic carbonate solvents: ethylene carbonate (EC) and propylene carbonate (PC); linear carbonates: dimethyl carbonate (DMC), diethyl carbonate (DEC) and the asymmetric ethyl methyl carbonate (EMC). Additives include carbonate based: fluoroethylene carbonate (FEC), vinylene carbonate (VC), difluoroethylene carbonate (F2EC)¹⁵ and vinylene ethylene carbonate (VEC)¹⁶. Ether-based solvent: 1,3-dioxolane (DOL); ester-based additive: succinic anhydride (SA)¹⁷; silane-based additives: monomethoxy trimethyl silane (MTMS), dimethoxy dimethyl silane (DMDMS) and trimethoxy methyl silane (TMMS).¹⁸ Boron-based anion receptor additive: tris(pentafluorophenyl)borane, (TPFPB)¹⁹, for stabilizing LiPF₆. And other Li salt additives: LiPO₂F₂, lithium bis(trifluoromethanesulfonyl)imide (LiTFSI), lithium bis(oxalato)borate (LiBOB) and lithium difluoro(oxalato)borate (LiDFOB).

conforming the solid active material to the solid electrolyte interphase and maintaining the interfacial reactions during cycling.

Solid electrolyte interphase

The principle of SEI formation is illustrated in Figure 1.3. The intrinsic thermodynamic stability window of the electrolyte is determined by the energy separation between the lowest occupied molecular orbital (LUMO) and highest occupied molecular orbital (HOMO) (denoted E_g in Figure 1.3) of the electrolyte. The open circuit voltage (OCV) of the cell is determined by the electrochemical potentials between the anode (μ_A) and the cathode (μ_C), which is

normally wider than E_g . During the first discharge process, electron flow in to the anode, pushing up the energy level of anode above the LUMO of the electrolyte to μ_A' (Figure 1.3b). Thus, the electrons from the anode tend to reduce the electrolyte unless a passivation layer (SEI) creates a barrier for electron transfer. Similarly, when electrons are pulled out of the cathode, the potential of the cathode decreases to an energy level of μ_C' below the HOMO that can oxidize the electrolyte. In this case, a cathode electrolyte interphase (CEI) forms to block electron transfer from the electrolyte to the cathode, thus preventing further oxidation of the electrolyte. The formation of SEI and CEI expands the stability window of the electrolyte, enabling the cell to operate in a kinetically stable environment.

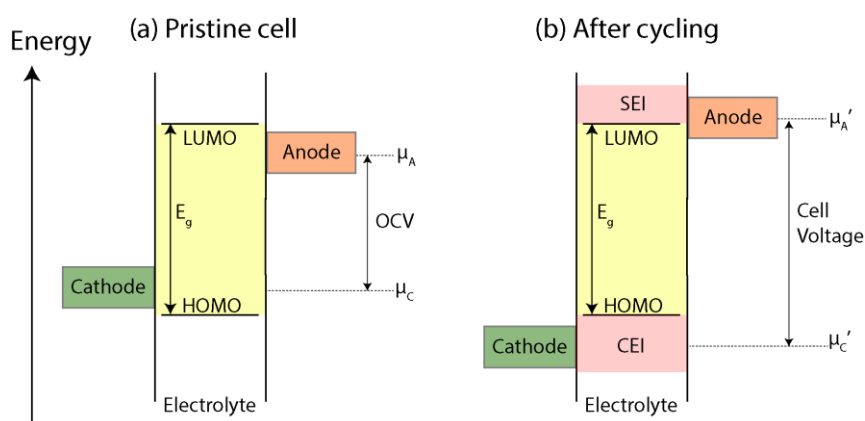


Figure 1.3 Electron energy diagram of a lithium ion battery cell (a) before and (b) after cycling. The Fermi energy levels of the anode and the cathode are denoted as μ_A and μ_C , respectively. E_g represents the thermodynamic stability window of the electrolyte. OCV is the open circuit voltage.

1.2 Silicon anodes

To increase the energy density further requires electrode materials with higher capacities and/or larger differences between the anode and the cathode electrochemical potentials. Silicon is one of the most promising anode materials because of its high capacity (3579 mAh/g for Si vs. 372 mAh/g for graphite) and its relatively low operating voltage (0.4 V vs. Li^+/Li). Other favourable features of Si include its earth-abundance, low environmental impact and the mature industrial infrastructure already available. Unfortunately, the lithiation of Si electrodes is accompanied by its large volume expansion ($\sim 300\%$, for the formation of $\text{Li}_{3.75}\text{Si}$),²⁰ which leads to pulverization for large Si particles (>150 nm) in the initial cycles. The large volume variation

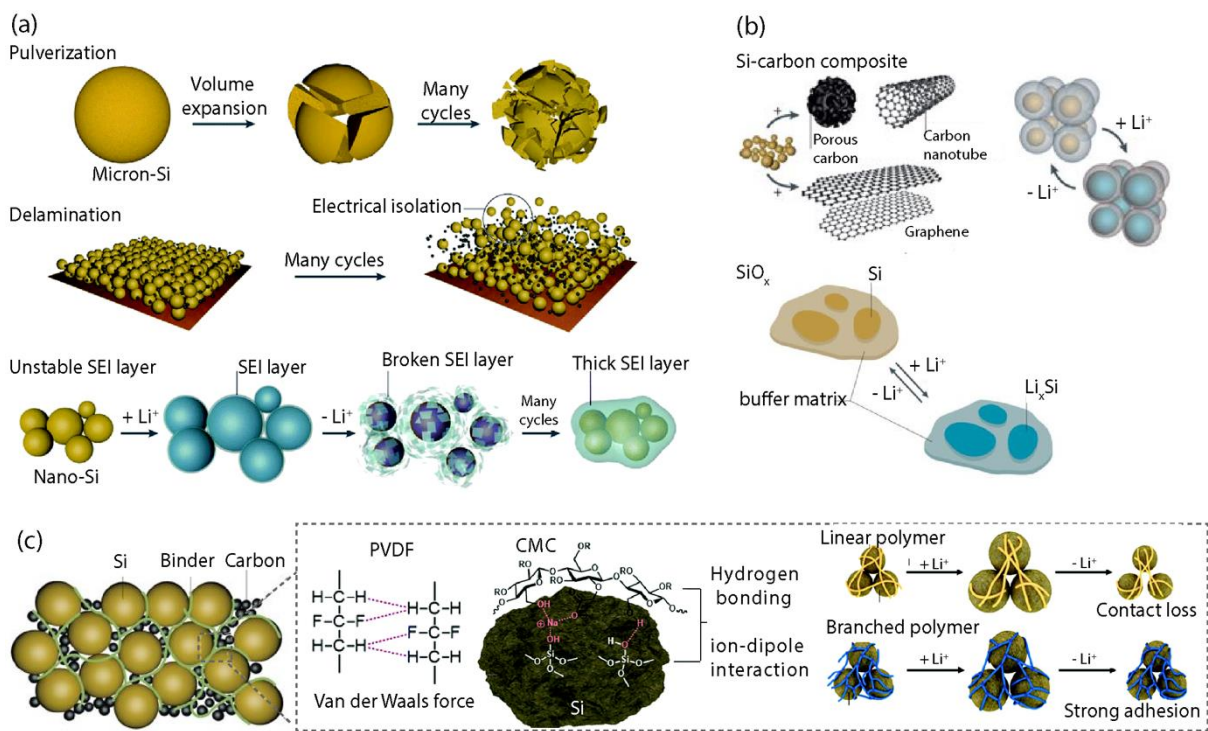


Figure 1.4 Electrode structure and binder design for Si anodes. (a) Main failure modes for Si anodes. (b) General strategies for modifying active materials by using Si-C composite or SiO_x. (c) Various binder concepts for Si anodes. SEI, solid-electrolyte interphase. Figure adapted from ref. ^{21,22}.

of the Si anode over long-term cycling results in delamination of the active material. Moreover, the continuous exposure of fresh Si surface during cycling causes uncontrolled SEI growth and poor cycling performance.⁵ These major degradation routes of the Si anode are summarized in Figure 1.4a. To date, various strategies have been employed to stabilize the Si anode that include 1) electrode structural engineering, 2) binder design and 3) a careful selection of compatible electrolyte formulations.

1.2.1 Electrode structures

A risk-reduction route to gradually improve the anode capacity is by using Si-C composite. Mixing Si with various carbon sources such as carbon nanotubes and/or graphene results in improved electronic conductivity of the Si electrode.^{23–27} Encapsulating Si within the carbon cage potentially avoids direct contact between the electrolyte and the Si surface (Figure 1.4b).²⁸ Though these hierarchal Si-C composites have been reported to significantly improve the cycle life of Si anodes, these delicate structures require lengthy synthesis steps and the Si-C

composite powder generally has poor tap density, rendering them unrealistic for industrial applications. Today, a low content of Si (< 5 %) is incorporated into the Si-C composite, thus it is necessary to reach low lithiation voltage to achieve the fully capacity of graphite (~0.05 V vs. Li⁺/Li). However, highly reactive lithium silicide (e.g. Li₁₅Si₄) forms in the low voltage region that exacerbates electrolyte reduction.

The first commercialized Si-based material was silicon monoxide (SiO). SiO is currently added into the carbon-based anode at 2-5 % and its low usage reflects the limitations on current Si technology. SiO has a better cycle life than pure Si, which has been attributed to the buffering layer formed during the initial cycle (Figure 1.4b). The buffer matrix prevents direct contact between the highly reactive lithium silicide and the electrolyte, thus minimizing further electrolyte reduction.²⁹ One drawback of SiO is its large irreversible capacity loss during the first cycle, necessitating a prelithiation step during fabrication to compensate for the capacity loss.

1.2.2 Polymeric binder

Practical electrodes are formed from a composite consisting of active material, conductive carbon, and polymeric binder as depicted in Figure 1.4c. The interactions between these components are critical for long-term cycling performance. Desired properties for the polymeric binder include 1) strong adhesion to the active material and the current collector, 2) low electrolyte uptake (to prevent solvent contact with the Si surface), and 3) high elasticity to accommodate the volume variations of Si during cycling.

Conventional binders, such as PVDF used in graphite anodes, are not suitable for Si anodes. PVDF has weak Van der Waals interactions with the Si surface, and it swells in carbonate electrolytes, leading to poor electrochemical performance.³⁰ Poly(carboxylic acid)-type polymer binders such as carboxyl methyl cellulose (CMC) and polyacrylic acid (PAA) have been reported to greatly enhance the cycle life of Si and other alloy-type anode materials.³¹ The carboxylic acid group potentially interacts with the hydroxyl groups on the Si surface in the form of hydrogen bonding or ion-dipole interactions, depending on the pH of the prepared electrode slurry.³² The pH also influences the conformation of the polymer. In neutral pH solvent, linear polymer is more stretched and is distributed more evenly within the composite

electrodes.³³ However, CMC and PAA are all linear polymers with poor mechanical properties. Recently, a cross-linked PAA polymer with high elasticity has been synthesized that shows promising results, allowing micron-sized Si to be cycled with stable capacities for 400 cycles.³⁴

1.2.3 Electrolytes for Si anodes

Apart from structural engineering and polymer binder design, one of the most cost-effective ways to improve the performance of the Si anode is to find a compatible electrolyte. For example, ether-based electrolytes such as 1,3-dioxolane (DOL) form a stable SEI on Si, however, the oxidation voltage of ether-based solvents is generally lower than alkyl carbonates resulting in severe oxidation when cycled at high voltage. Derivatives from alkyl carbonate-based solvent such as fluoroethylene carbonate (FEC) and vinylene carbonate (VC) are two of the most popular additives in LIBs. The electron-withdrawing group in FEC and the polymerizable double bond in VC make them more vulnerable to reduction. Their electrochemical reduction products and their reduction mechanism are the main focus of this thesis. Other additives for Si anodes are listed in Figure 1.2, which include siloxanes,¹⁸ lithium bis(oxalato)borate (LiBOB) and lithium difluoro(oxalato)borate (LiDFOB) salts.³⁵

1.3 Solid electrolyte interphase

Much effort has been dedicated to understanding the nature of the SEI that forms on Si anodes, with a variety of techniques employed including FTIR,^{36,37} XPS,³⁸⁻⁴⁰ TOF-SIMS,⁴¹ SEM, TEM,^{42,43} EIS,⁴⁴ Raman⁴⁵ and NMR spectroscopy.⁴⁶⁻⁴⁹ Previously detected SEI components in the EC/DMC system include a combination of inorganic and organic species, such as LiF, LiOH, Li₂CO₃, ROCO₂Li, ROLi and PEO-type oligomers or polymers. Of note, XPS measurements on the SEI using depth-profiling have shown that the SEI composition varies with the distance from the Si surface; the region near the electrode contains more inorganic Li salts, while the portion closest to the electrolyte at the surface has more organic species.³⁸ The composition of SEI is likely dynamic and air-sensitive: its thickness and spatial arrangement may vary depending on the electrolyte formulations as well as the cycling conditions (e.g. cutoff-voltages, cycle number, temperature, etc.).

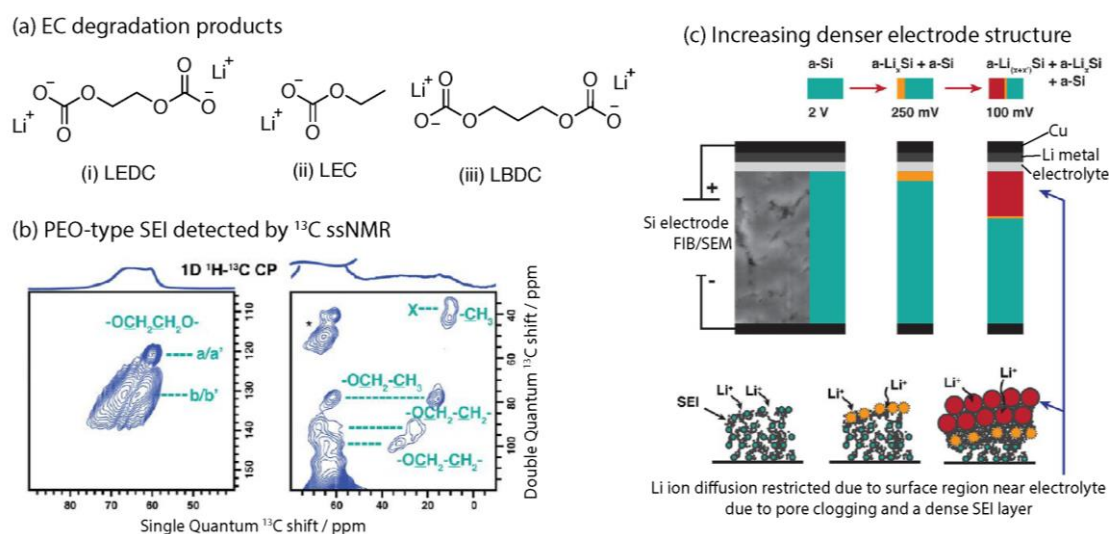


Figure 1.5 Degradation products in standard EC-based electrolyte and its influence on the composite electrode. (a-b) Major reduction products of EC. (c) Schematic showing microscale processes within the Si electrodes after cycling. A cross-section of the cycled composite electrode revealed by the FIB/SEM. Figure adapted from ref.⁴⁸

1.3.1 Understanding SEI in baseline electrolyte

Fundamental studies have been performed to understand the SEI composition formed on the Si composite electrode in standard EC-based electrolytes (Figure 1.5). It is widely agreed that lithium ethylene decarbonate (LEDC) is an important component of the organic SEI that forms from two-electron reduction of EC.^{50,51} Other organic species such as lithium ethylene carbonate (LEC) and lithium butylene dicarbonate (LBDC) have also been identified via detailed homonuclear ^{13}C and heteronuclear ^1H - ^{13}C NMR correlation experiments.⁴⁷ Apart from the short chain oligomers, the major insoluble organic SEIs from EC are reported to be PEO-type polymers.⁴⁸ Moreover, the SEI formation in the standard electrolyte correlates well with the increased tortuosity and pore clogging of the electrode as observed using focused ion beam and scanning electron microscopy, as illustrated in Figure 1.5c.⁴⁸ With a thickening SEI, capacity fading is primarily attributed to the slow Li ion kinetics, since the increased electrode tortuosity severely limits Li ion diffusion through the electrode and thus uniform lithiation.

1.3.2 Understanding the role of additives

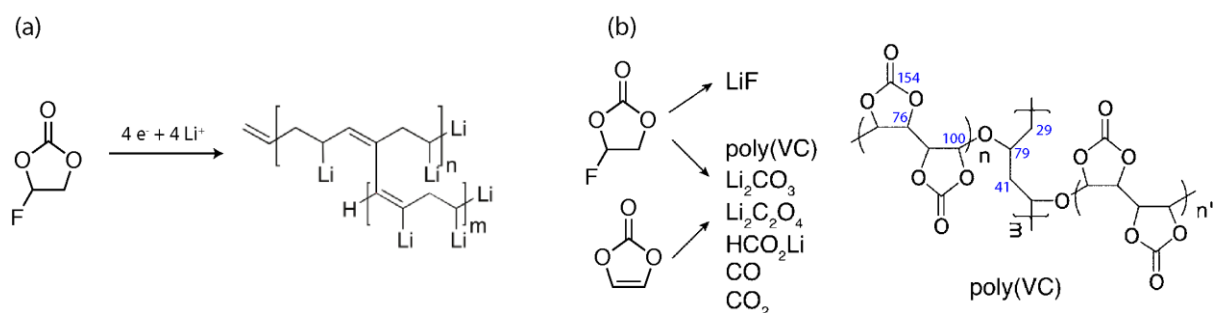


Figure 1.6 Reduction products of FEC and VC proposed in the literature. (a) A Li ion conductive polyene-type cross-linked polymer derived from a four-electron reduction process of FEC proposed in ref.⁵² based on the observations from on-line electrochemical mass spectrometry. (b) A poly(VC) type polymer from the reduction of FEC and VC based on ssNMR data. ^{13}C chemical shifts are assigned on the structures and coloured in blue. Structure taken from ref.⁴¹

Among the numerous possible electrolyte additives, FEC and VC are two of the most widely used and have been shown to improve the capacity retention of Si anodes and other types of electrode materials.^{9,53} However, the mechanisms by which these additives modify the nature of the SEI are not well understood due to the inherent difficulties associated with characterizing disordered interfacial structures. Characterization of the few nanometer-thick SEI layer is further convoluted by the fact that the material is usually air-sensitive and amorphous, the former presenting challenges in sample preparation and the latter with structural assignment with, for example, diffraction-based techniques. Despite these difficulties, electrolyte breakdown products in the presence of FEC have been characterized by a variety of spectroscopic and modelling approaches to provide insight into the chemical composition of the SEI on Si anodes.

Organic SEI from FEC/VC: poly(VC) or polyene?

The organic SEI derived from VC was characterized by Ota et al., who used solution NMR spectroscopy and gas chromatography to prove that poly(VC)-type species were formed on graphite cycled in pure VC electrolyte.⁴⁶ The formation of poly(VC) has been further confirmed by Ouatani et al., who directly synthesized poly(VC) via radical polymerization and compared the XPS valence spectra of synthetic poly(VC) with the SEI formed on graphite.⁵⁴

Moving from graphite to Si, the addition of VC also enhances the electrochemical performance for Si, and its beneficial effect is generally attributed to the polymeric species that are formed.⁵⁵ Though poly(VC) is often mentioned in the literature, there is no clear picture about its structural details nor an estimation of its molecular weight.

Fourier transform infrared (FTIR) spectroscopy suggested that FEC likely transforms to VC through HF elimination and subsequently polymerises to form poly(VC)-type species.³⁶ Strong evidence for the poly(VC) structure comes from a study reported by Michan et al., who used solid-state NMR (ssNMR) to analyse the precipitate formed by chemically reducing FEC with lithium naphthalenide.⁴⁹ A ¹³C NMR resonance at 100 ppm, which had not been previously observed in the decomposition products of EC, was assigned to an acetal carbon (a protonated carbon environment adjacent to two oxygen groups), and represents a potential cross-linking unit in poly(VC) as shown in Figure 1.6b. Of note, acetal carbons were observed in pioneering NMR studies of the SEI formed on graphite by Leifer et al.⁵⁶ However, some of the resonances in Michan et al.'s work⁴⁹ were partially obscured by the presence of excess lithium naphthalenide in the precipitate which complicated further analysis. Perhaps more importantly, the chemically induced FEC-polymer may differ from the organic SEI generated through electrochemical reduction, necessitating further studies on SEI decomposition products formed in battery materials over the course of cycling.

In contrast to poly(VC), polyene is proposed to form from the reduction of FEC mainly based on elemental analysis techniques and mass spectrometry.⁵⁷ Nakai et al. studied the reduction of FEC on Si by X-ray photoelectron spectroscopy (XPS) and time of flight–secondary ion mass spectrometry (ToF-SIMS) and found evidence for oxygen-deficient species such as polyene.⁴¹ The presence of low-oxygen content polyenes was further supported by energy-dispersive X-ray spectroscopy (EDS) and on-line electrochemical mass spectrometry (OEMS) performed during the reduction of FEC-based electrolyte on Si anodes.¹³ For example, Jung et al. studied the Si anode with 1 M LiPF₆ in EC: EMC (3:7 wt/wt) + 5 % wt FEC electrolyte by OEMS and observed the evolution of CO₂, H₂ and C₂H₄ gases during the electrochemical decomposition of FEC.⁵² The authors assumed that the origin of the H₂ gases comes from the reduction of FEC, and proposed a four-electron reduction mechanism for FEC leading to the formation of polyene as shown in Figure 1.6a. However, Metzger et al. from the same group

showed that the H₂ evolution stems solely from the reduction of the trace amount of water in the graphite/Li half-cell, since the detected amount of H₂ corresponds well to the typical H₂O contamination in carbonate electrolyte and H₂ does not increase during cycling once all H₂O is reduced.⁵⁸ The dispute in the organic SEI chemical structure requires more thorough studies in this area.

Interphase between SEI and Si: fluorosilicate or siloxanes?

During cycling, the Si surface can be modified by reacting with electrolyte. XPS work reported by Philippe et al. suggested that Si can be oxidized during cycling, forming lithium silicates and fluorosilicates in the presence of LiPF₆.¹⁶ Nakai et al. suggested that FEC can protect the Si surface against electrolyte oxidation, probably due to the formation of a passivation layer on Si surface.⁴¹ A recent detailed XPS study by Schroder concluded that the reduction of FEC leads to the formation of a kinetically stable SEI comprising predominately inorganic lithium fluoride and lithium oxide, which improves lithiation kinetics.⁴⁰

The nature of the interactions between the SEI species and the Si surface are critical for the stability of the SEI. However, the surface structures of cycled Si remain elusive due to the inherent difficulty in characterizing the buried interphase. Despite these difficulties, XPS studies have reported that, in the cycled Si electrode, the Si 2p peak corresponding to SiO₂ shifts to a lower binding energy, indicating that SiO₂ may be reduced due to alloying with Li or the formation of a Si-C species.⁶⁰⁻⁶² However, detailed information concerning the nature of the chemical species and structure of the cycled Si surface is still lacking.

1.3.3 Ionic and electronic properties of SEI

Apart from the chemical structures, little is known about the ionic and electronic properties of the interphase. It is well accepted that an ideal SEI should be Li ion conductive to facilitate the Li ion transport for high power applications. Other requirements of the SEI include that it is electronically insulating (i.e. prevents electron tunnelling) and exhibits low solvent permeation, so that fewer solvent molecules would be reduced as illustrated in Figure 1.7a.

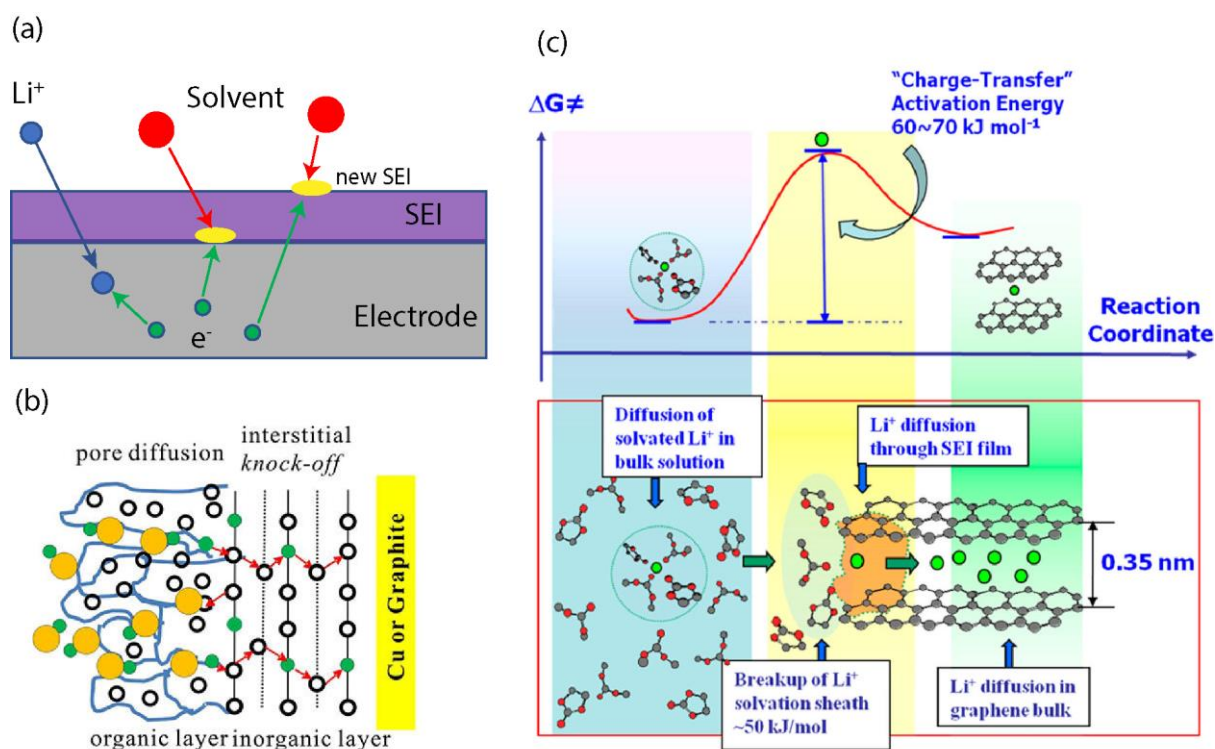


Figure 1.7 Properties of SEI. (a) Schematic showing SEI should be Li ion conductive, but prevent solvent permeation or electron tunnelling to create new SEI. (b) Mechanism of Li ion transport in the SEI film.⁶³ (c) Schematic of the Li ion transfer steps at the graphite/electrode interphase: the desolvation process is more energetically demanding than the diffusion of bare Li ions through the SEI.⁴⁴

Lu and Harris were the first to measure the Li ion self-diffusion process in the SEI by using ⁶Li and ⁷Li isotope labelling.⁶³ The SEI was first formed using ⁶LiCl salt and was subsequently soaked in bulk electrolyte containing natural abundant ⁷Li nuclei. The Li⁺ self-diffusion process is reflected by the ratio of ⁶Li/⁷Li measured by SIMS across the SEI (Figure 1.7b). A two-phase Li ion transport process is verified: Li⁺ ions first diffuse through the porous organic SEI layer, then migrate through the dense inorganic layer via interstitial defects.⁶³

In a working cell, the Li ion diffusion process at the electrolyte/electrode interphase is more complicated. The Li ions should first desolvate at the SEI-electrolyte interphase; the bare Li ions, then, diffuse through the SEI. For the graphite anode, it is difficult to distinguish between these two processes and the overall activation energy barrier (E_a) for them was found to be 50–100 kJ/mol by electrochemical impedance spectroscopy (EIS) as shown in Figure 1.7c.⁹ To elucidate which is the rate limiting step, Xu et al. used a nominally SEI-free LTO anode and

measured its E_a under the same condition as that for graphite and found it to be ~ 50 kJ/mol. The similar E_a values for a SEI-free LTO anode and a SEI-containing graphite anode suggests that it is the desolvation step, rather than the step of Li^+ diffusion through the SEI, that is more energetically demanding. Nevertheless, the authors also acknowledged that this conclusion applies to the graphite anode under ideal conditions, but it may change if a denser and more resistive SEI forms on alloy-type anodes. In general, the selection of solvent mixture alters the coordination shell of the Li ions, and it further influences the desolvation process, thereby affecting the rate performance of the battery.

To probe the role of electronic tunnelling through the SEI, an indirect approach has been employed where redox active ferrocene is injected into a cycled plastic bag cell.⁶⁴ After injection, ferrocene diffuses to the electrode surface to form ferrocenium if the SEI is not completely formed and electron tunnelling occurs. Alternatively, if the porosity of the SEI is large, ferrocenes easily diffuse to the electrode surface, close enough for electron-transfer to take place. By monitoring the evolution of the open circuit voltage and the cell impedance, important information can thus be obtained regarding the completeness of the SEI and the reduction kinetics within the SEI.

1.3.4 Artificial interphase

While sacrificial electrolyte additives such as FEC and VC can form a relatively stable SEI, unwanted side products such as CO_2 and H_2 gases evolve from the SEI-forming process, which are detrimental for commercial bag cells. As the additives are continuously decomposed, the depletion of the additives is reported to result in sudden cell failures.⁵² The consumption of additives would be more severe in commercial LIBs as much less electrolyte volume is used. Therefore, artificial SEIs have been designed with the aim of protecting Si anodes with fewer side-effects.

Pioneering work by Piper et al. reported a polymer-coating method that results in superior electrochemical performance for Si anodes.^{65,68,69} The Si nanoparticles were first mixed with polyacrylonitrile (PAN) solution to form conformal coatings. The slurry was then cast onto a Cu current collector and subjected to heat treatment to form the cyclic-PAN coating layer. The pyridine-type conjugated polymer offers both high Li ionic and electronic conductivities and it

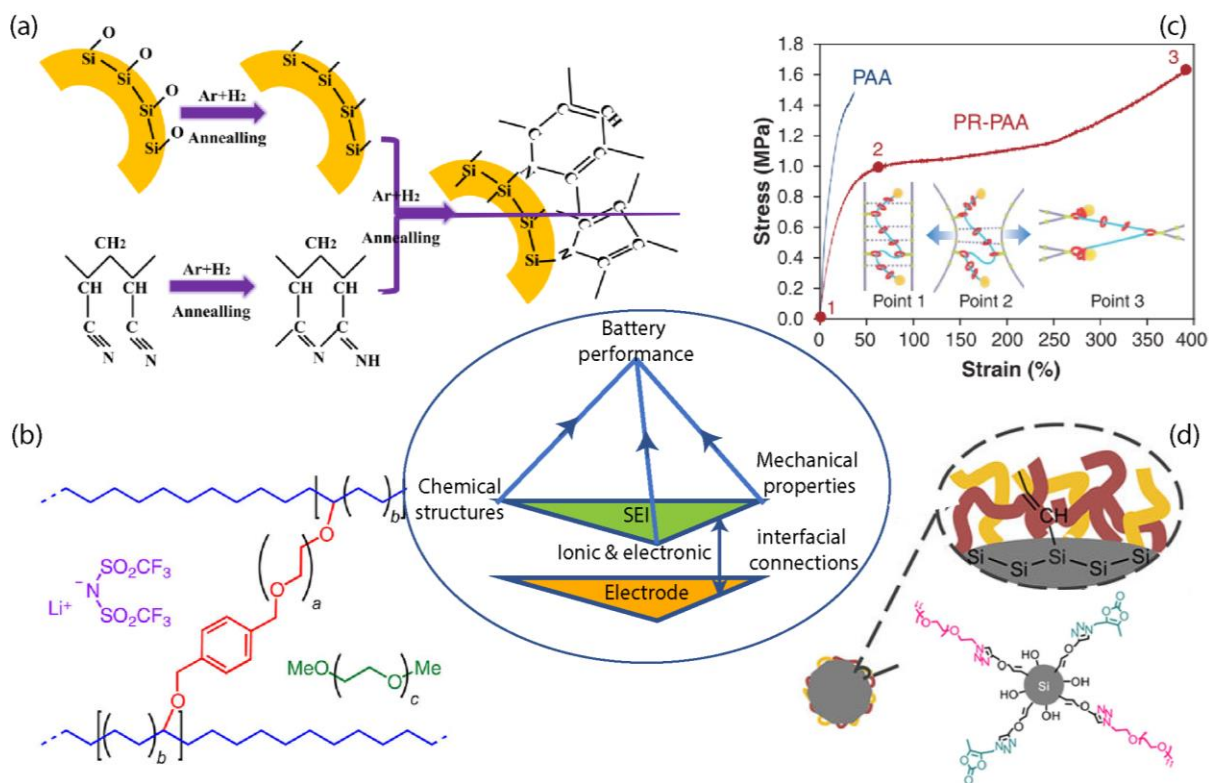


Figure 1.8 Examples for artificial SEI designs. Schematic of the general strategies for SEI studies (middle). (a) Coating Si nanoparticle with cyclic poly(acrylonitrile).⁶⁵ (b) Solid polymer electrolyte with high Li ion conductivity.⁶⁶ (c) A highly elastic binder for Si anode: the stress-strain curve of polyacrylic acid (PAA) and cross-linked polyrotaxane-PAA.³⁴ (d) Artificial SEI with covalent bond to the Si particle.⁶⁷

is used as the binder as well as the conductive matrix for the Si electrode. However, it is still unclear how the cyclic-PAN stabilizes the Si particles.

With respect to the Li ion conductivity, knowledge accumulated in the solid polymer electrolytes (SPE) area is relevant for designing an artificial SEI. A novel SPE consisting of cross-linked polyethylene-poly(ethylene oxide) was reported by Khurana et al.⁷⁰ Its structure is shown in Figure 1.8b with the PEO part providing Li ion conductivity and PE part offering mechanical stability. With optimized chain length and the weight percentage of plasticizer, the SPE exhibits high ionic conductivity ($>1.0 \times 10^{-4}$ S/cm) at room temperature. Moreover, though this SPE has a low modulus, it shows excellent resistance to Li dendrite growth, which

is unexpected based on the widespread belief that only mechanically strong SPE suppresses Li dendrite formation.

A mechanically flexible SEI is desirable for alloy-type anode materials so that large volume variations of the electrode can be accommodated. The highly elastic polymeric binder illustrated in Figure 1.8c is a recent breakthrough in this field. By incorporating polyrotaxanes in the conventional linear polyacrylic acid (PAA), the mechanical properties of the polymer are altered to be highly elastic. The sliding ring in the polyrotaxane acts like a pulley to lower the stress of an applied force. This polymer binder even enables stable cycling of micron-size Si without severe pulverization.³⁴

Apart from the desirable properties mentioned above, the interface between the SEI and the electrode is crucial for charge transfer. Gao et al. reported an artificial SEI consisting of PEO – VC type oligomers that are anchored on the SiNP via click chemistry.^{67,71} The authors emphasized that the covalent bonding between the SEI and Si nanoparticles helps to maintain stable electrochemical performance. Such interfacial engineering is also relevant for solid electrolytes, as most ionic or electronic resistance comes from the grain boundaries and the interfacial region in these materials.

1.4 Outline of the thesis

In this thesis, the main focus is to understand the chemical compositions of the SEI formed on the Si anode, and the working mechanisms of electrolyte additives: FEC and VC. Various NMR techniques have been employed to elucidate the structures of the SEI. The relevant methodologies are described in detail in Chapter 2.

In Chapter 3, the SEI components formed in a standard electrolyte with 10 vol % FEC were thoroughly analysed. Based on both the soluble and insoluble organic and inorganic species observed, a decomposition mechanism of FEC is proposed. With the presence of FEC, a cross-linked polymer forms and is identified as a key component for Si electrode stability.

To avoid interactions between different solvents, pure FEC and VC electrolytes with 1 M LiPF₆ salt were prepared. The SEI derived from these electrolytes were characterized in Chapter 4.

The cross-linked polymer has been verified using ^{13}C -homonuclear correlation spectroscopy and the percentages of each component revealed by quantitative NMR. Furthermore, the interfacial region between the SEI and Si as a function of cycling was first revealed by ^{29}Si DNP NMR and organosiloxanes were found to form on the Si surface.

In Chapter 5, the chemical structure of the electrochemical degradation products of EC are resolved by a comprehensive NMR study. Key oligomers are identified, and a failure mode when cycling Si in additive-free-EC based electrolyte is proposed. Finally, conclusion and future directions in artificial SEI and additive designs are presented in Chapter 6.

Chapter 2 Methodology

2.1 Chemical vapor deposition (CVD)

Nanowires used in this work are synthesized using a bottom-up method: chemical vapor deposition (CVD). In CVD growth, chemical vapor such as silane (SiH_4) is catalytically decomposed on metal nanoparticles to form liquid alloy droplets, which then precipitate along certain directions to form nanowires. The growth mechanism is known as the vapor-liquid-solid (VLS) mechanism and was proposed by Wagner in the 1960s⁷² based on two observations: (1) certain metal impurities are prerequisite for silicon nanowire (SiNW) growth and (2) small nanoparticles are located at the tip of the SiNW. A schematic of the VLS growth is shown in Figure 2.1a. The growth recipe used in this work is illustrated in Figure 2.1b. The sample should be heated up above the eutectic point for the Au–Si system ($364\text{ }^\circ\text{C}$), then the continuous feeding of Si source into Au–Si alloy leads to the supersaturation and SiNW growth.⁷³ A typical growth temperature is set to $500\text{--}570\text{ }^\circ\text{C}$ for a moderate growth rate as higher temperature induces severe side reactions between the SiNW and the substrate.

A homemade cold-wall CVD system used in this work is shown in Figure 2.2. Several parameters such as vacuum level and vapor flow rate are important for the growth. A high vacuum atmosphere ($\sim 10^{-8}$ mbar) is achieved by a turbomolecular pump. The flow of gases in the reactor is controlled by mass-flow controllers (MFC). Finally, the growth temperature, the most crucial parameter, is controlled by the DC current and is monitored by an infrared pyrometer based on black-body emissivity.

In general, CVD is a versatile tool to synthesize SiNWs with varied chemical structures and properties. For example, n-type SiNWs with increased electronic conductivity can be synthesized using a mixture of SiH_4 and PH_3 gases.⁷⁴ Heterostructures can also be synthesized

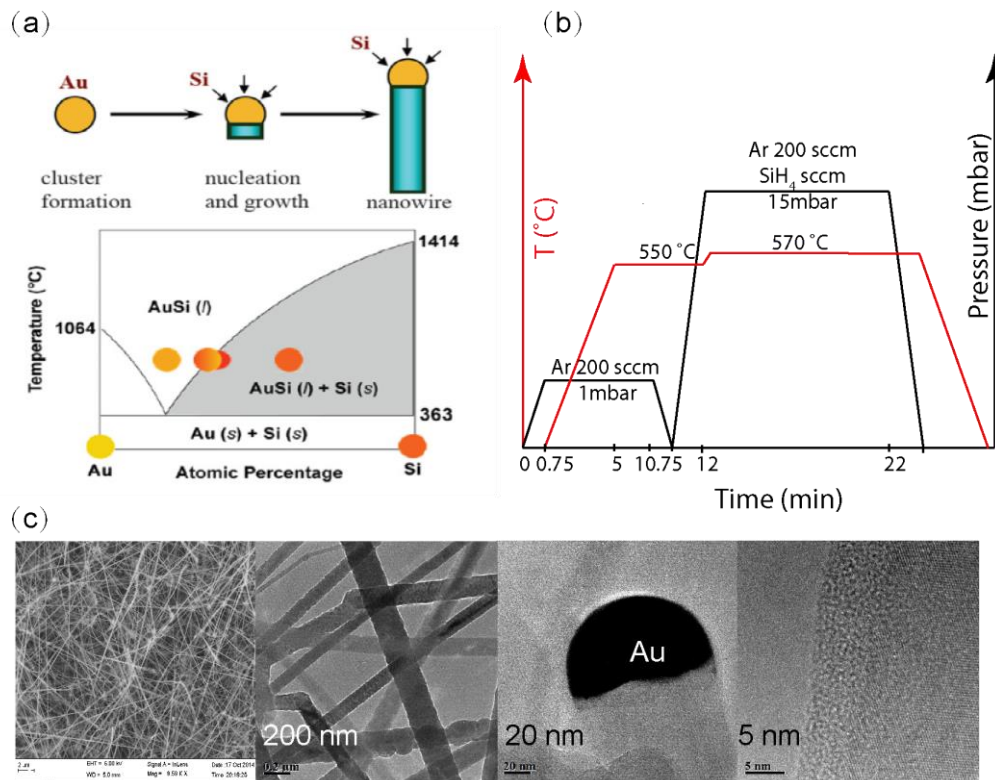


Figure 2.1 Schematic of the VLS growth mechanism for SiNWs (a), adapted from ref⁷⁵. (b) A growth recipe used in this work. (c) Morphologies of SiNWs taken by SEM and TEM.

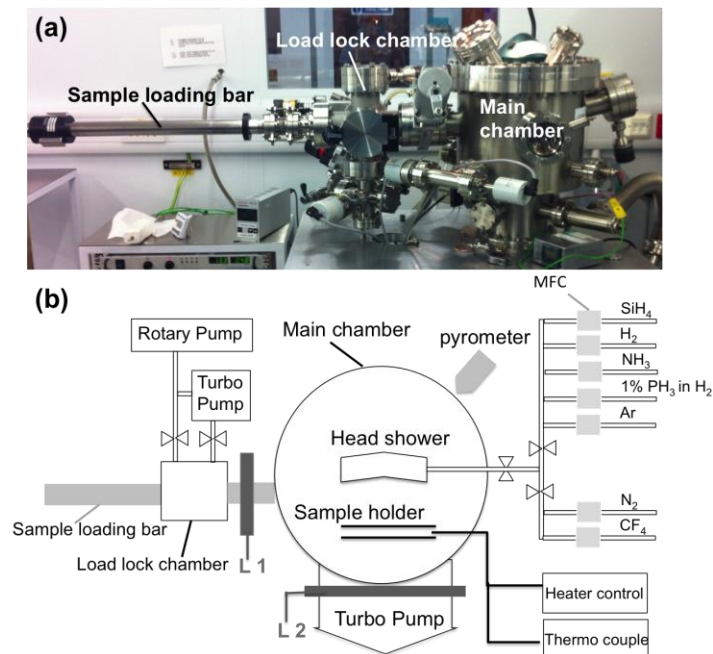


Figure 2.2 Chemical vapor deposition reactor for growth of SiNWs.

by increasing the growth temperature: SiH₄ decomposes at high temperature to form amorphous Si (a-Si) on the wall of crystalline SiNWs (c-Si). This side reaction has been utilized to form an a-Si/c-Si ‘core-shell’ structure, which has been reported to have improved electrochemical performance in lithium ion batteries.⁷⁶

2.2 Electrochemistry

For testing cycling performance, half-cells consisting of the material of interest (Si in this case) and Li metal are commonly employed. In the half-cells, a large amount of electrolyte and excess Li metal are used to ensure that the voltage change and the cycle life reflect the properties of the electrode materials. For a given material, two parameters are important: the theoretical specific capacity, noted as C_{th} (in mAh/g), and the average cycling voltage vs. Li⁺/Li, as the energy density of the cell is determined by the product of cell capacity and the voltage difference between cathode and anode: (Energy density) = (Cell Capacity) × (Voltage). C_{th} is a measure of the ability of a material to store Li ions per unit mass: $C_{th} = \frac{\Delta x \cdot F}{M} \times \frac{1000}{3600}$, where Δx is the number of Li ions (in moles) that react with one mole of electrode material, F is the Faraday constant, and M is the molecular weight of the active material.

Galvanostatic cycling (constant current with voltage cut-offs) is routinely used to test half-cells. The cycling rate is expressed using the C rate: C/n means a full (dis)charge of the cell to its theoretical capacity in n hours. By varying the cycling rate, kinetic information about electrochemical reactions can be obtained. Moreover, the voltage curves are useful for understanding the structural changes of the electrodes.

2.2.1 Galvanostatic voltage-capacity curve

As mentioned above, the voltage-capacity curve of the half-cell reflects the structural change and specific chemical reactions within the electrode material. A flat voltage plateau indicates a solid-solution reaction (i.e. single-phase reaction), whereas, a sloping voltage profile infers a two-phase reaction. The reason behind it is explained in the equations listed in Table 2.1. When the lithium ions are uniformly inserted or removed from the host without large structural

changes, a solid solution reaction takes place, where x in Li_xSi is a variable. Thus, the chemical potential of the phase varies continuously with lithium content and the voltage of the cell also changes as the reaction proceeds. Hence, the voltage-capacity curve for the solid-solution reaction is represented by a slope. If a two-phase reaction occurs, the chemical potentials of the products remain the same, as the Li compositions in these two phases are fixed. Therefore, a constant cell voltage or a plateau will be observed in the voltage-capacity curve.

Table 2.1 Summary of the thermodynamics of the solid solution and two-phase reaction in a cell.

solid-solution reaction (x varies)	two-phase reaction (x and y are fixed)
$x \text{Li}^+ + x e^- + \text{Si} \rightarrow \text{Li}_x\text{Si}$	$y \text{Li}^+ + y e^- + \text{Li}_x\text{Si} \rightarrow \text{Li}_{x+y}\text{Si}$
$\Delta G_r^\circ = \Delta G_f^\circ(\text{Li}_x\text{Si})$	$\Delta G_r^\circ = \Delta G_f^\circ(\text{Li}_{x+y}\text{Si}) - \Delta G_f^\circ(\text{Li}_x\text{Si})$
$E_{cell}^\circ = \frac{\Delta G_f^\circ(\text{Li}_x\text{Si})}{xF}$	$E_{cell}^\circ = \frac{\Delta G_r^\circ}{yF}$

2.2.2 Differential Capacity Analysis

To clearly identify the voltage plateaus, it is common to take the first differentiation of the voltage-capacity plot to generate the dQ/dV plot, where the peak height indicates the flatness of the plateau and the peak area is a measure of the plateau's capacity. A dQ/dV plot can also be used to ascertain some phase transformation. For example, Si can be fully lithiated to form $\text{c-Li}_{15}\text{Si}_4$. This highly reactive phase, $\text{c-Li}_{15}\text{Si}_4$, persists during the delithiation process and leads to a two-phase reaction, which is different from the delithiation of amorphous Li_xSi . Thus, a sharp peak ~ 450 mV in the dQ/dV plot (corresponding to a two-phase reaction) is a good indication that $\text{c-Li}_{15}\text{Si}_4$ forms on discharge. Understanding the phase transformation is useful to rationalize the capacity fading upon cycling.

2.3 Nuclear magnetic resonance (NMR)

In this work, NMR is heavily used to understand the molecular structure of amorphous species. Since its discovery by Rabi, Bloch, and Purcell in the 1940s, NMR has become an indispensable tool for chemists to reveal the chemical and structural information of solid and liquid phase samples. Solution NMR techniques are routinely used in organic chemistry and biochemistry to solve chemical structures as well as to understand the dynamics of small molecules. For insoluble materials, solid-state NMR (ssNMR) has an advantage in that it provides atomistic information about amorphous species, which cannot be easily obtained by diffraction-based techniques. Though ssNMR suffers from sensitivity issues when probing nuclei such as ^{13}C and ^{29}Si , recent progress in hyperpolarization techniques shows promising routes to overcome this; dynamic nuclear polarization (DNP)⁷⁷ is one of the most promising methods and has been successfully applied in materials systems including catalysts, perovskites and thin-film polymers.⁷⁸ A short introduction to the principles of NMR and DNP is given here, with the focus on the spin interactions and specific pulse sequences relevant to the work undertaken in this thesis; excellent reference books with further details about NMR can be found elsewhere.⁷⁹⁻⁸¹

2.3.1 NMR basics

Most nuclei possess an intrinsic spin, which is described by the nuclear spin quantum number (I) that takes integer or half-integer values. For a spin- I nucleus, there exist $2I+1$ spin states: $-I, -I+1, \dots, +I$. In the presence of an external magnetic field B_0 , the energy level of the spin states splits due to the Zeeman interaction between B_0 and the magnetic dipole moment. The splitting energy (ΔE) between consecutive spin states is given by:

$$\Delta E = \hbar|\omega_0| = -\hbar\gamma_I B_0 \quad (2.1)$$

where γ_I is the gyromagnetic ratio, \hbar is the reduced Planck's constant, and $\omega_0 = -\gamma_I B_0$ is the so-called Larmor frequency.

In the microscopic view, these polarized spins rotate around the magnetic field at the Larmor frequency (Figure 2.3a). For common nuclei subject to modern magnetic field strengths

($B_0 = 5\text{--}20\text{ T}$), ω_0 lies within the radio frequency region ($\sim 10^8\text{ Hz}$). For NMR-active nuclei in a macroscopic sample at thermal equilibrium, nuclear spins occupy energy levels according to the Boltzmann distribution. The equilibrium population difference gives rise to a bulk nuclear magnetization, which can be represented by a vector, \mathbf{M} , aligned with the z -axis.

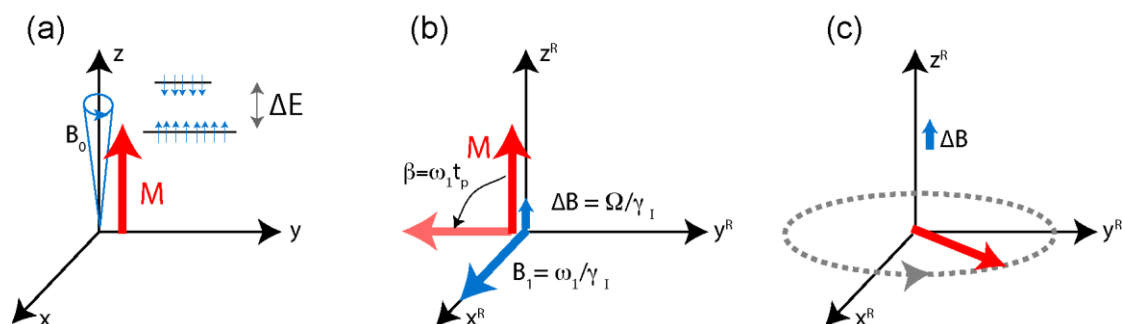


Figure 2.3 (a) Vector model representation of the bulk magnetization \mathbf{M} in an external B_0 field. Nuclear spins align (spin up) or against (spin down) the applied field, creating a Zeeman energy splitting. (b) Application of a 90° pulse along x -axis (viewed from the rotating frame, denoted as x^R). The rf pulse creates a static B_1 field along the x -axis and B_0 is reduced to ΔB . (c) Free precession of the magnetization within the xy -plane in the rotating frame.

In the simplest NMR experiment, a short radio frequency (rf) pulse is applied near the Larmor frequency and the rf power determines the nutation frequency of the spins around the applied rf axis (in the range of $\sim 10^4\text{ Hz}$). In the vector model under a rotating frame of reference (at the Larmor frequency), the rf pulse produces a static field B_1 that causes nutation of \mathbf{M} about B_1 at a frequency of $\omega_1 = -\gamma B_1$ for the duration of the pulse, t_p (Figure 2.3b). The rf pulse (denoted as β_ϕ) is characterized by its flip angle ($\beta = \omega_1 t_p$) and its phase (ϕ). The pulse angle is the nutation angle for \mathbf{M} , and the phase indicates the direction along which B_1 lies. After a 90_x° pulse, \mathbf{M} is nutated to the $-y$ axis in the transverse (xy) plane, and its precession about the z -axis is observed in the rotating frame determined by the reduced field (ΔB). Note that in a rotating frame, the B_0 field is reduced to $\Delta B = \frac{\Omega}{\gamma} = (\omega_{rf} - \omega_{rotating,frame})/\gamma$, where Ω is the difference (“offset”) between the Larmor frequency and the frequency of the chosen rotating frame (Figure 2.3c) which arises due to spin interactions that modify the Larmor frequency (described later). The precession of \mathbf{M} is recorded by a quadrature detector in the xy -plane. The recorded complex-valued data as a function of time is known as the free-induction decay (FID). The Fourier transform (FT) of the FID translates the time-domain information to a frequency-

domain signal. The experiment is then repeated multiple times to perform signal averaging so that a spectrum with improved signal-to-noise ratio can be obtained.

2.3.2 Spin interactions

Apart from the large Zeeman interaction ($\sim 10^7$ – 10^9 Hz), additional spin interactions lead to subtle shifts in the energy splitting of the spin states, which is the source of the local structural sensitivity of NMR. For paramagnetic materials, unpaired electron spins interact with nuclear spins (known as the hyperfine interaction, with a strength of 10^2 – 10^5 Hz), leading to large NMR shifts. For metals, Knight shifts (10^3 – 10^6 Hz) are induced by the coupling of nuclei with unpaired conduction electrons. Nuclei with $I \geq 1$ (such as ^7Li , ^{23}Na) have additional quadrupole coupling interactions (10^3 – 10^7 Hz), which arise from the coupling of the nuclear quadrupolar moment and the electric field gradient (EFG), if present, due to the asymmetry of the local charge distribution. For diamagnetic samples, three important spin interactions are present: (1) the chemical shift (10^2 – 10^5 Hz), which arises from electron shielding around the nucleus, (2) dipolar coupling (10^3 – 10^5 Hz) and (3) scalar coupling (1 – 10^3 Hz) between homo-/hetero-nuclei, which are mediated through space and through bond, respectively. In this work, the SEI mainly consists of diamagnetic species (with ^1H , ^{13}C , ^7Li and ^{19}F as the important NMR-active nuclei) and the three interactions mentioned above are explained in detail in the following sections.

2.3.3 Chemical shift

The chemical shift (CS) interaction is known to be the dominant shift mechanism in diamagnetic systems. Paired diamagnetic electrons around a nucleus are capable of generating a magnetic field, B' , which is proportional to B_0 but in the opposite direction, thus shielding the nucleus from the external magnetic field. While shielding occurs for a single nucleus, deshielding can happen within a molecule, where the B' fields generated by different nuclei undergo counter interactions with each other. Since the electron distribution around a nucleus is rarely a sphere, a shielding tensor is used to describe the shielding effect. The tensor contains both isotropic (*i.e.* orientation-independent for the molecule with respect to the external B_0 field) and anisotropic parts (*i.e.* orientation-dependent). In solution, the rapid tumbling motion

of the molecule averages the anisotropic component to zero on the NMR timescale; however, in solid-state NMR of powder samples, the chemical shift anisotropy (CSA) leads to a broad peak containing a distribution of chemical shifts. Though the resolution is reduced, the powder pattern line shape potentially provides important information about the local structure and symmetry around the nucleus.

Heavier atoms tend to have more low-lying energy states than lighter atoms, leading to a larger chemical shift range for heavy isotopes. For example, the common chemical shift range for ^1H is only 10 ppm, while for ^{13}C it is around 200 ppm. Moreover, the chemical shift of a given nucleus correlates with the electronegativity of the neighboring functional groups. Nuclei bonded to electron-withdrawing groups are less shielded and have a higher chemical shift. These empirical rules are often used for spectral assignments in this thesis.

2.3.4 Dipole-dipole coupling (through space)

Direct dipole-dipole (DD) coupling refers to the interaction between two nuclei through space without involving the electron clouds. The through-space interaction can be easily rationalized: a nuclear spin is intrinsically a magnet that generates a magnetic field surrounding itself; the second nuclear spin interacts with this magnetic field and this interaction depends on the distance between the two spins as well as their orientations in the magnetic field. The Hamiltonian for dipolar coupling between two spins \mathbf{I} and \mathbf{S} separated by a distance r_{IS} is expressed as:

$$\hat{\mathcal{H}}_{DD} = d_{IS} \left(\frac{\mathbf{I} \cdot \mathbf{S}}{r_{IS}^3} - 3 \frac{(\mathbf{I} \cdot \mathbf{r})(\mathbf{S} \cdot \mathbf{r})}{r_{IS}^5} \right) \quad (2.2)$$

where the vector \mathbf{r} is a line joining the nuclear magnetic dipoles moment \mathbf{I} and \mathbf{S} , and d_{IS} is the dipolar coupling constant that is given by:

$$d_{IS} = -\frac{1}{4\pi} \frac{\gamma_I \gamma_S \hbar}{r_{IS}^3} \quad (2.3)$$

The dipolar Hamiltonian can be expressed in spherical polar coordinates in the rotating frame, where we effectively observe the spins in an NMR experiment. During the frame

transformation, both time-dependent and time-independent terms are generated. A good approximation is obtained by preserving the time-independent terms to obtain the so-called first-order average Hamiltonian. In this simplified form, the homonuclear dipolar coupling is given by:

$$\hat{\mathcal{H}}_{DD}^{homo} = d_{IS}(3\cos^2\Theta_{IS} - 1) \left(I_z S_z - \frac{1}{2}(I_x S_x + I_y S_y) \right) \quad (2.4)$$

where Θ_{IS} is the angle between the vector \mathbf{r} that joins the spins \mathbf{I} and \mathbf{S} and the external B_0 field. Note that the hats above the operators I and S are omitted here to simplify the notation. For heteronuclear spin pairs, the magnetic field generated by one spin (I) is far off from the resonance frequency of other spins (S); therefore, some interactions can be omitted. The heteronuclear dipolar coupling Hamiltonian is truncated further and is given by:

$$\hat{\mathcal{H}}_{DD}^{hetero} = d_{IS}(3\cos^2\Theta_{IS} - 1)I_z S_z \quad (2.5)$$

In a liquid, the direct dipole-dipole coupling between nuclear spins averages to zero, however in a solid sample this interaction cannot be ignored. For high- γ nuclei that are close in space, such as ^1H and ^{19}F , the strong homonuclear dipolar interaction can significantly broaden the spectral lines. Magic-angle spinning and dipolar decoupling are essential techniques to minimize this interaction in high-resolution ssNMR spectra. For two dilute spin-half nuclei with heteronuclear dipolar coupling, the line-broadening effect is absent, but its powder NMR line shape has a horn-like pattern, also known as a Pake doublet, from which the heteronuclear dipolar constant can be derived and internuclear distances can be determined.

2.3.5 J-coupling (through bond)

Indirect dipole-dipole coupling, also known as J-coupling or scalar coupling, refers to the coupling between two nuclei that are mediated by their bonding electrons. Because of the Pauli exclusion principle, the two electron spins in a bonding orbital are paired with opposite values of the spin quantum number and exist in an equal mixture of two states: an ‘up-down’ state and a ‘down-up’ state. If a nuclear spin is now placed close to one electron with its magnetic moment pointing in the same directions as that of the electron, one electron spin state will be slightly favoured over the other state. Therefore, the electron spin distribution is slightly shifted

by the presence of the nuclear spin, with electrons close to the nucleus polarized in the same direction, while other electrons distant from the nucleus are polarized in the opposite way. The second nucleus that is bound to the first nucleus with shared electron pairs thus feels a non-zero magnetic field and this field can be reversed if the magnetic moment of the first nucleus changes. In this way, the two nuclei are indirectly coupled to each other via their interactions with the bonding electrons.

J-coupling patterns in ^1H NMR provide useful information about the spin system, whereas ^{13}C solution NMR is normally ^1H decoupled for simplicity in interpreting the spectra. Unlike solution NMR, J-coupling is rarely observed in solid-state NMR spectra as it is typically an order of magnitude smaller than other interactions. However, transfer of magnetization via this interaction can be used to probe chemical bond connectivity, as J-coupling acts exclusively through regions of shared electron density (e.g. covalent bonding and hydrogen bonding). The 2D correlation experiments in solution NMR which are used in this work are mainly based upon the J-coupling interaction.

2.4 NMR experiments

In this section the basic principles of 1D NMR and 2D homonuclear and heteronuclear correlations experiments are summarized. Two-spin systems with J-coupling are considered here. First, the basic product operators for two-spin systems are introduced, then these operators are used to rationalize the pulse sequences used for 1D and 2D NMR experiments. As will be seen later, spin states can be manipulated by rf pulses so that magnetizations can be transferred between coupled spins. By selectively observing the J-coupled systems in a molecule, it can be possible to assign the network of the molecule unambiguously.

2.4.1 Spin operators

For spin- $\frac{1}{2}$ nuclei, the x, y and z components of the magnetization are represented by the spin angular operators I_x , I_y and I_z , respectively. At equilibrium, the nuclei possess an I_z magnetization aligned with the B_0 field. For an uncoupled single spin, only transverse magnetization (I_x , I_y) is observable in an NMR experiment. For a two-spin system with

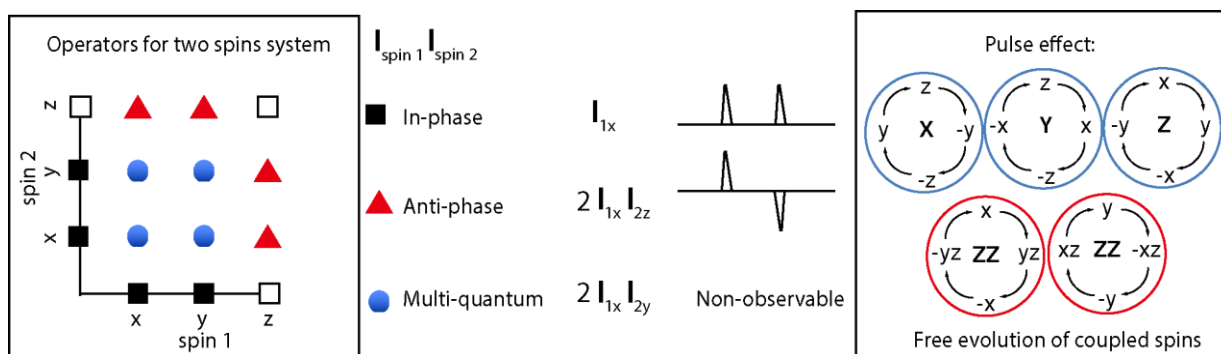


Figure 2.4 Product operators for two spin system (left). Example of in-phase, anti-phase and multi-quantum operators (middle). Diagrams for determining the result of rotating in-phase operators about x, y or z axis under a 90° pulse (right, blue circles), and effect of the J-coupling on in-phase and anti-phase operators under free precession (right, red circles).

J-coupling, there are 15 product operators as shown in Figure 2.4, left. Among them, only operators containing one transverse magnetization (also known as single quantum coherence) are observable, whereas multiple-quantum operators are not directly observable. For example, I_{1x} and $2I_{1x}I_{2z}$ both contain the transverse magnetisation on the first spin and they are thus observable. The difference between these two operators is that I_{1x} is an in-phase operator that leads to a doublet for the first spin with the same sign, whereas $2I_{1x}I_{2z}$ represents anti-phase magnetization that gives doublets containing opposite signs for the first spin (shown in Figure 2.4, middle).

An NMR experiment comprises rf pulses and the various delays between them. The effect of a rf pulse is to rotate the magnetization about x, y or z axis. The rotation direction induced by a 90° pulse is summarized in the blue circles in Figure 2.4, right. Since only hard pulses are considered here, we assume that the effect of nutation is nuclei-specific. In other words, heteronuclei will not be affected by an on-resonance rf pulse.

During the free precession period, spins rotate around the z-axis. For an uncoupled single spin, its Hamiltonian is given by $\hat{H}_{free} = \Omega I_z$, where Ω is the offset of the spin as illustrated in Figure 2.3c. For a J-coupled two spin system, the Hamiltonian under free evolution contains an extra J-coupling term and is written below:

$$\hat{H}_{free,two\ spins} = \Omega_1 I_{1z} + \Omega_2 I_{2z} + 2\pi J_{12} I_{1z} I_{2z} \quad (2.6)$$

where J_{12} is the scalar coupling constant between spins 1 and 2. Evolution under coupling renders the interconversion between the in-phase and anti-phase terms as illustrated in the red circles in Figure 2.4, right. For example, after evolving freely after time t , the in-phase magnetization I_x becomes $\cos(\pi J_{12}t)I_{1x} + \sin(\pi J_{12}t) 2I_{1y}I_{2z}$, which contains its original operator and the newly generated anti-phase term $2I_{1y}I_{2z}$. This calculation is also displayed in Figure 2.5 as step 2 to 3. By setting the evolution time to be $t = 1/(2J_{12})$, the in-phase term is converted to a pure anti-phase term (highlighted with a red triangle in Figure 2.5). Neglecting the evolution of offset magnetization, it is clear that anti-phase terms can be generated in a coupled spin system by a single pulse and a proper delay time.

2.4.2 Spin echo

One basic NMR pulse sequence is the spin echo, which comprises a 90° pulse and a 180° pulse separated by two equal free precession periods prior to the acquisition of the FID. In the vector model of this pulse sequence, the I_z magnetization is first rotated to the $-y$ axis after the 90°_x pulse, and dephasing then takes place during the free evolution period. The subsequent 180°_x pulse inverts the magnetization back towards the $+y$ axis. After the same evolution period, only the coherent magnetization, such as the offset magnetization, is refocused. Moreover, in the spin-echo pulse sequence, the FID can be acquired starting from the echo top, and so the resulting NMR spectrum has a flatter baseline and fewer artifacts than a single pulse experiment.

The above analysis performed in the vector model concludes that the spin echo sequence refocuses the offset magnetization, but this does not consider the effect of coupling between spins. Omitting the effect of offset, the product operator analysis of the pulse sequence for a coupled two-spin system is given in Figure 2.5. The analysis prior to the 180°_x pulse is identical to that of the single pulse experiment. The application of the 180°_x pulse does not affect the $\cos(\pi J_{12} \tau)I_{1x}$ term in step 3, therefore, only the anti-phase term $\sin(\pi J_{12} \tau)I_{1y} I_{2z}$ is considered in step 4. The 180°_x pulse inverts the signs of both spins 1 and 2 (e.g. from y to $-y$ for spin 1 and from z to $-z$ for spin 2, according to the pulse effect illustrated by the blue circles in Figure 2.4). Thus, the overall product operator remains unchanged. In other words, the spin-echo sequence is equivalent to a single pulse followed by a free evolution time of 2τ and another

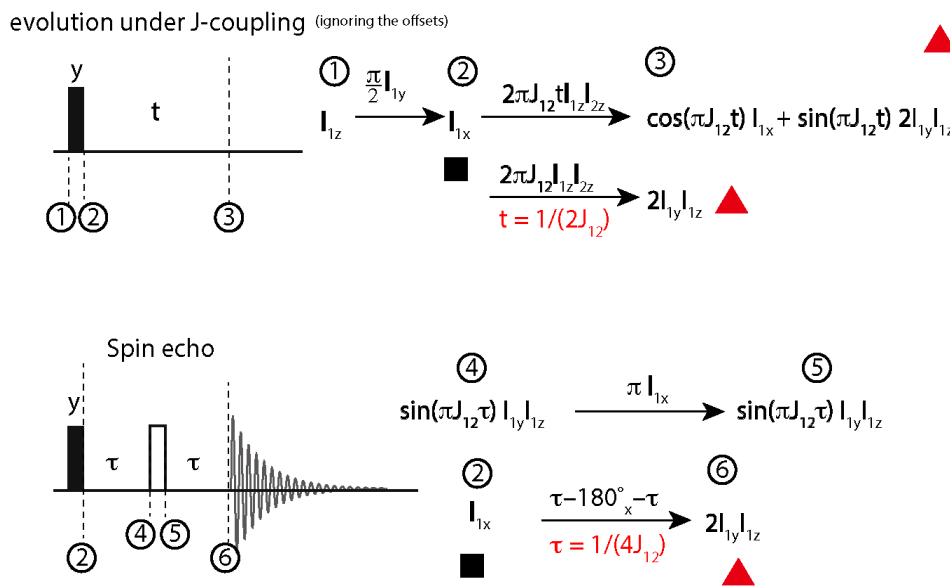


Figure 2.5 Analysis of single 90° pulse and spin echo pulse sequence on a two-spin system with J-coupling. The evolution of offset is ignored here, but the offset is recovered in the spin echo pulse sequence. The black rectangle denotes a 90° pulse and the white a 180° pulse; the same notation is used in the pulse sequences described below.

180° pulse. With $\tau = 1/(4J_{12})$, the same conversion from in-phase terms to anti-phase terms can be achieved.

Anti-phase states are crucial for coherence transfer and for generating multiple-quantum coherence. For example, by applying a 90° pulse along the y axis when the state of the spin system contains anti-phase magnetization $2I_{1x} I_{2z}$, coherence transfer between the two spins takes place.

$$2I_{1x}I_{2z} \xrightarrow{\frac{\pi}{2}I_{1y} + \frac{\pi}{2}I_{2y}} -2I_{1z}I_{2x} \text{ (coherence transfer)} \quad (2.7)$$

As shown in Equation ((2.7), the transverse magnetization, which is a coherence, is transferred from spin 1 to spin 2. This can be utilized in heteronuclear systems (e.g. ^1H and ^{13}C) in order to enhance the ^{13}C signal. The INEPT pulse sequence has been devised to induce such a coherence transfer. Apart from the coherence transfer, double-quantum coherence can be generated from the anti-phase term when the 90° pulse is applied along the x axis instead of the y axis. The transformation is given here:

$$I_{1x}I_{2z} \xrightarrow{\frac{\pi}{2}I_{1x} + \frac{\pi}{2}I_{2x}} -I_{1x}I_{2y} \text{ (Double quantum excitation)} \quad (2.8)$$

The double-quantum coherence is useful to filter uncoupled system and selectively probe dipolar coupled or J-coupled spins in 2D homonuclear or heteronuclear correlation experiments as discussed below.

2.4.3 Two-dimensional NMR basics

The introduction of two-dimensional NMR experiments enables us to unravel problems with increasing complexity. A general 2D NMR experiment can be summarized as follows: preparation \rightarrow evolution (t_1) \rightarrow mixing \rightarrow detection (t_2). In the preparation period, coherence is excited from the equilibrium state, then it evolves freely during t_1 . The evolution period is not a fixed time in a 2D experiment; rather it is incremented systematically in a series of separate experiments ($t_1 = \Delta_1, 2\Delta_1, 3\Delta_1 \dots$) until enough data points are generated for the so-called indirect dimension. Next comes the mixing period, during which the evolved magnetization is converted into observable signals and then recorded during the detection period, t_2 . A time domain matrix is generated from the 2D experiment, and performing a double Fourier transformation with respect to both t_2 and t_1 gives 2D NMR spectra that contain the correlation information.

2.4.4 Homonuclear correlation spectroscopy (COSY)

COSY is a homonuclear experiment used to identify J-coupled spins and is thus useful to determine the covalent bonding network in the molecule(s) of interest. A basic pulse sequence for COSY is shown in Figure 2.6. The analysis of this pulse sequence using product operators is given below the sequence. The first 90°_x pulse rotates both spins from I_z to the -y axis. During the free precession period (t_1), the magnetization evolves under the offset as well as the J-coupling between the two spins. The offset values are related to the chemical shifts of the nuclei. The corresponding product operator analysis shows that anti-phase terms are generated from the J-coupling (e.g. $\sin(\Omega_1 t_1) \sin(\pi J_{12} t_1) 2I_{1y}I_{2z}$). Moreover, after the evolution period, all of these terms acquire a t_1 frequency label with the offset from spin 1 (Ω_1).

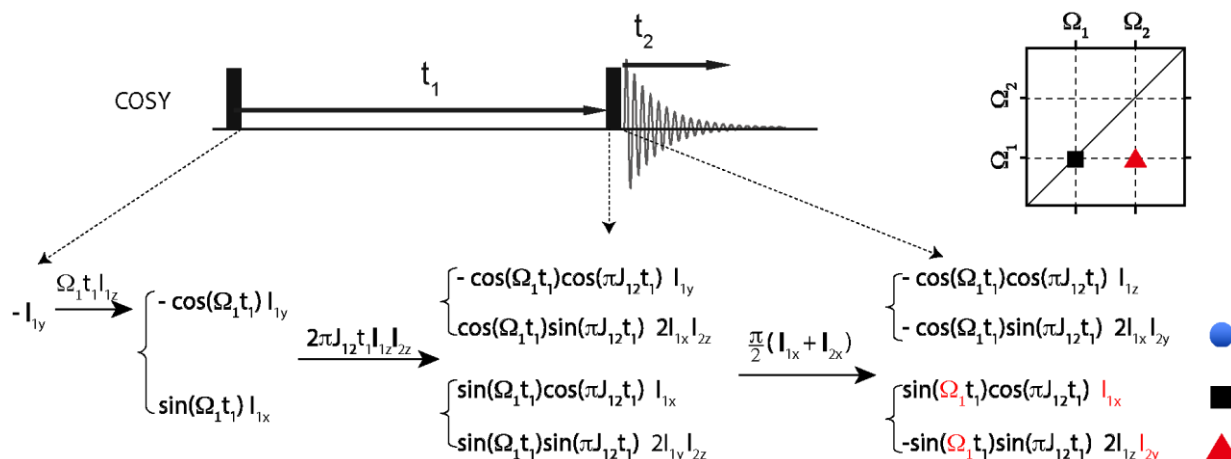


Figure 2.6 Basic pulse sequence for COSY with simplified product operator analysis given below the sequence.

The final 90°_x pulse acts on both spins and induces coherence transfer from $2I_{1y}I_{2z}$ to $2I_{1z}I_{2y}$. The last term $-\sin(\Omega_1 t_1) \cos(\pi J_{12} t_1) 2I_{1z}I_{2y}$, marked with a red triangle in Figure 2.6 is observable, and contains both transverse magnetization in spin 2 that can be observed in t_2 and an offset of spin 1 in the t_1 dimension; therefore, this term corresponds to a cross-peak in the 2D COSY spectrum. The third term, $\sin(\Omega_1 t_1) \cos(\pi J_{12} t_1) I_{1x}$, is an in-phase term and is observable as the offset of spin 1 in both the t_1 and t_2 dimensions, and thus appears as a diagonal peak in the COSY spectrum. In the analysis above, only J-coupled spins lead to the appearance of anti-phase terms and subsequently contribute to the appearance of cross-peaks in the COSY experiment. Therefore, COSY selectively probe the covalent bonding network.

In practice, double quantum filtered COSY (DQF COSY) is used to achieve proper phasing for both diagonal and cross-peaks. In this modification, by adding a third 90° pulse, the second, multiple quantum, term ($I_{1x}I_{2y}$) can be turned into an observable anti-phase magnetization ($I_{1x}I_{2z}$). Most COSY experiments in this work are performed using DQF COSY.

2.4.5 Heteronuclear correlation experiments

2D heteronuclear correlation spectra are particularly useful to identify basic units and molecular fragments in the system of interest. For the analysis of small organic molecules, ^1H – ^{13}C correlation experiments are essential to assign overlapping 1D proton peaks. Here, the two most commonly used pulse sequences, HSQC and HMBBC, and their working mechanisms are summarized.

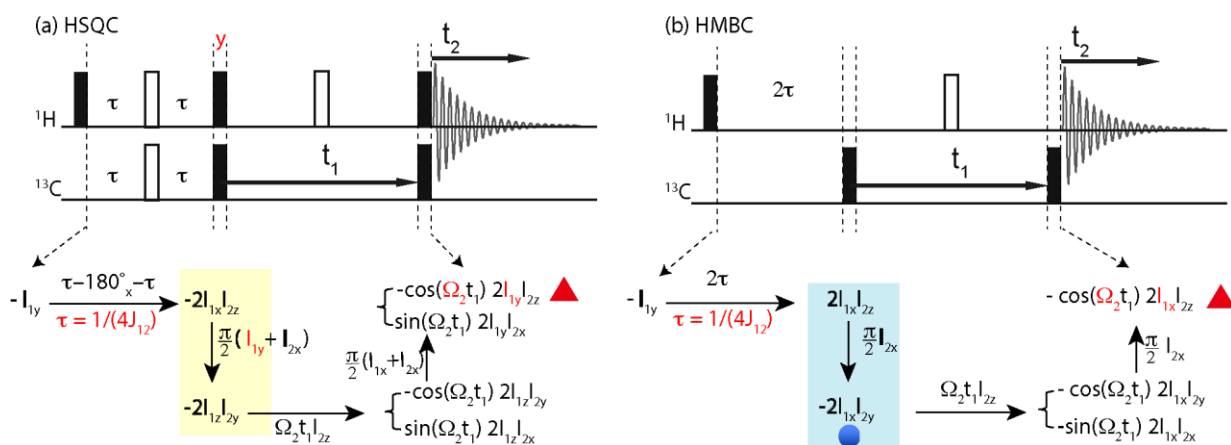


Figure 2.7 Pulse sequences for (a) HSQC and (b) HMBC and the corresponding operator analyses. The coherence transfer step is highlighted in yellow and the multiple quantum generation step is highlighted in blue.

2.4.5.1 Heteronuclear Single Quantum Correlation (HSQC)

HSQC is used to determine directly bonded heteronuclei, e.g. protons and carbons. A basic version of the HSQC pulse sequence is shown in Figure 2.7a. For the analysis here, spin 1 is ^1H and spin 2 is ^{13}C . The first period is a spin-echo which, with the choice of delay to be $\tau = \frac{1}{4J_{12}}$, results in a complete conversion from the in-phase to the anti-phase term for the coupled spins as seen in Section 2.4.2. For one-bond $^{13}\text{C}-^1\text{H}$ coupling, where $^1J_{\text{CH}} \approx 150$ Hz, the delay time is around $\tau \approx 1 - 2$ ms. Next, the second 90°_y pulse on spin 1 and the 90°_x pulse on spin 2 lead to a coherence transfer from $-2I_{1x}I_{2z}$ to $-2I_{1z}I_{2y}$, which then evolves under t_1 . Only the offset on spin 2 affects the evolution as the subsequent 180° pulse on spin 1 in the middle of the t_1 period refocuses both the offset of spin 1 and the coupling between spin 1 and 2. During the t_1 evolution period, the $-2I_{1z}I_{2y}$ term evolves to form $-\cos(\Omega_2 t_1) 2I_{1z}I_{2y} + \sin(\Omega_2 t_1) 2I_{1z}I_{2x}$ as shown in Figure 2.7a; both of the evolved terms acquire a frequency label according to the offset of spin 2. The final 90°_x pulse on both spins transfers the magnetization back to spin 1 (e.g. $-\cos(\Omega_2 t_1) 2I_{1z}I_{2y} \rightarrow -\cos(\Omega_2 t_1) 2I_{1y}I_{2z}$), while the remaining term is multiple-quantum and thus remains unobservable. The resulting spectrum, therefore, contains only a cross peak with the chemical shift of ^1H (Ω_1) in the direct dimension and the chemical shift of the respective J-coupled carbon (Ω_2) in the indirect dimension.

2.4.5.2 Heteronuclear Multiple-Bond Correlation (HMBC)

In the HMBC pulse sequence, a multiple-quantum coherence is excited, and correlation between heteronuclei (such as ^1H and ^{13}C) via 2-4 intervening chemical bonds can be determined. HMBC is particularly useful for assigning quaternary carbons, as such carbons do not appear in the HSQC spectrum.

The start of the HMBC pulse sequence is similar to HSQC, in that the ^1H magnetization is first rotated from I_{1z} to $-I_{1y}$, which is followed by a free precession period of 2τ . By setting $\tau = \frac{1}{4J_{12}}$, the in-phase term is completely converted to an anti-phase term ($-I_{1y} \rightarrow 2I_{1x}I_{2z}$). Next, a 90°_x pulse on ^{13}C gives rise to a double-quantum term ($2I_{1x}I_{2z} \rightarrow -2I_{1x}I_{2y}$). The step which generates double-quantum coherence is highlighted in blue in Figure 2.7b, and is different from HSQC, in which a coherence transfer is induced. The DQ coherence evolves in the t_1 period and acquires a frequency label containing the offset of spin 2. Lastly, the final 90°_x pulse converts the multiple-quantum term into an observable anti-phase magnetization.

Unlike HSQC, multiple-bond ^1H - ^{13}C J-couplings are much smaller and have a wider range than one-bond J-coupling constants ($^nJ_{\text{CH}}$, where $n = 2-4$, ranges from 3–10 Hz vs. $^1J_{\text{CH}} \approx 150$ Hz). Therefore, the delay time in HMBC experiments is much longer than that in HSQC (~20–80 ms vs. 1–2 ms) and it is difficult to choose a fixed delay time. One solution is to record several spectra with different delays. If this is very time consuming, one can instead set the delay according to the largest expected long-range coupling constants. Because this free precession delay is much longer in HMBC, spin-spin (T_2) relaxation of the transverse magnetization also leads to signal loss. Therefore, the anti-phase term generated at the end of the pulse sequence is directly observed instead of refocused using another spin-echo, which would lead to severer signal loss. Finally, ^1H decoupling is not applied during the acquisition as this would collapse the anti-phase peak to zero.

2.4.6 Diffusion ordered spectroscopy (DOSY)

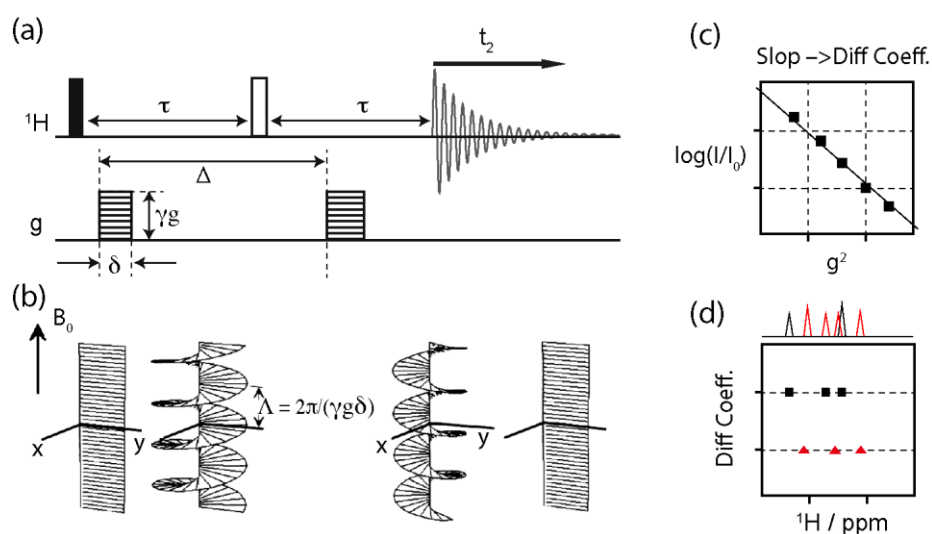


Figure 2.8 Principle of a DOSY experiment. (a) A basic DOSY pulse sequence based on the spin-echo. (b) Schematic of the spatial encoding and decoding along the z-axis due to the gradient pulses. (c) Data processing procedure to extract the diffusion coefficients for different chemical shifts and (d) a schematic the 2D DOSY spectrum showing the separation of a mixture with different diffusion coefficients.

DOSY is employed to separate a mixture of molecules in the solution-state based on their diffusivity differences. The DOSY pulse sequences are derived from spin-echo or stimulated echo under the effect of pulsed field gradient (PFG) and a basic version is shown in Figure 2.8a. The first 90° pulse rotate the magnetization to the y-axis, creating a magnetization ribbon in the yz-plane. Then a constant-gradient pulse twists the magnetization ribbon into a helix as shown in Figure 2.8b. The pitch of the helix is given by $\Lambda = 2\pi/q$, where $q = \delta\gamma g$ is the product of the duration (δ) and the amplitude (γg) of the gradient pulse. The gradient amplitude is determined by the gyromagnetic ratio of the observed nucleus (γ) and the gradient strength (g). The smaller the pitches, the higher the resolution for measuring the diffusion process.⁸²

After the first gradient pulse, the spatial positions of the spins are encoded. Then a diffusion time, Δ , follows to allow motions to occur. Finally, the second gradient pulse decodes the spatial information and brings the spins back into the yz-plane to form an echo if no diffusion or spin-spin lattice (T_2) relaxation takes place. In the presence of diffusion motion, the intensities of the echo decays as the strength of the gradient increases. A quantitative formula describing it is given below:

$$I = I_o \exp(-Dq^2(\Delta - \frac{\delta}{3})) \quad (2.9)$$

Where I is the observed intensity, I_o is the unattenuated signal intensity and D is the diffusion coefficient. With an optimized diffusion time and gradient pulse length, a pseudo 2D data is recorded by varying the gradient strength. Then the diffusion coefficient can be derived by fitting the exponential intensity decay versus the square of the gradient strength as shown in Figure 2.8c and the equation is given by:

$$\frac{\log(\frac{I}{I_o})}{\gamma^2 \delta^2 (\Delta - \frac{\delta}{3})} = -Dg^2 \quad (2.10)$$

Finally, a 2D DOSY spectrum is presented by plotting the chemical shifts in the F2 dimension and the diffusion coefficients in the F1 dimension (Figure 2.8d). The centre of a 2D cross peak in F1 dimension corresponds to the calculated diffusion constant, while the width of the peak correlates with the fitting error.

In a DOSY experiment, several factors are crucial for the successful separation of a mixture with overlapped signals. These include gradient linearity, temperature stability and a set of optimized parameters. Systematic errors arise when joule heating or transient eddy currents are induced by the PFG pulses. To compensate for these imperfections, advanced pulse sequences have been designed. The longitudinal eddy current delay sequence with bipolar gradient pulse pairs (“ledbpgp2s”) is employed in this thesis to separate the soluble degradation products in the cycled electrolyte.

2.4.7 Solid-state NMR techniques

Solid-state NMR (ssNMR) experiments are typically performed using powdered samples which contain randomly-distributed crystallites with all possible orientations with respect to the external B_0 field. In this situation, anisotropic spin interactions can lead to severely broadened spectra. Some essential techniques such as magic-angle spinning (MAS) and high-power decoupling are required to obtain high resolution ssNMR spectra.

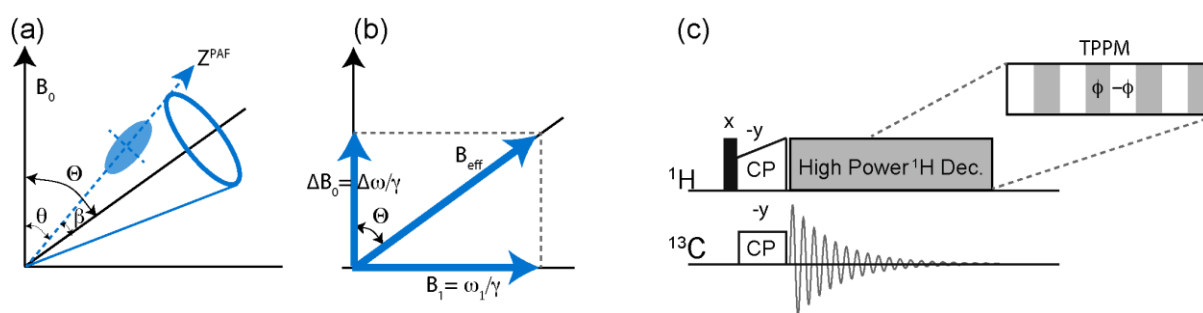


Figure 2.9 Essential techniques in solid-state NMR. (a) Illustration of magic-angle spinning. The shielding tensor is represented here by an ellipsoid, and its z-axis in the principal axis frame is noted as Z^{PAF} . (b) Illustration of the basic principle underlying the Lee-Goldburg homonuclear decoupling sequence (the offset is chosen so that the effective field is tilted at the magic angle). (c) The cross-polarization pulse sequence, with a high power ^1H decoupling sequence such as TPPM used for heteronuclear decoupling.

2.4.7.1 Magic-angle spinning

By spinning the sample physically at a specific angle (the “magic” angle) with respect to the external B_0 field, it is possible to average to zero the anisotropy associated with the chemical shift as well as hetero/homonuclear dipolar couplings. The anisotropic part of these spin interactions all contain an angle-dependent term $3 \cos^2 \theta - 1$, where θ is the angle between B_0 and the z-axis in the principal axis frame of the tensor describing the interaction (Z^{PAF}) as shown in Figure 2.9a. During the rotation of the sample, the θ value varies but the angle (β) between the Z^{PAF} and the spinning axis is fixed for each crystallite in a rigid solid sample. The average of the $3 \cos^2 \theta - 1$ term over the course of the rotation is given by: $\langle 3 \cos^2 \theta - 1 \rangle = \frac{1}{2} (3 \cos^2 \beta - 1) (3 \cos^2 \Theta - 1)$, where Θ is the angle between B_0 and the spinning axis. By fixing $\Theta = 54.74^\circ$ (the magic angle), this spatial term can be averaged to zero. The magic-angle spinning speed needs to be faster than the magnitude of the anisotropy in frequency units; otherwise spectral artifacts known as spinning sidebands radiate out from the central isotropic peak, separated by a multiple of the spinning speed, and lead to reduction in the signal intensity of the isotropic peak.

MAS experiments are often performed with rotor synchronization. During such an experiment, the length of the pulse sequence itself is a multiple of the rotor period – for example in a spin echo sequence choosing the interpulse delays so as to be equal to one (or more) rotor periods.

The FID is also recorded at certain multiples of the rotor period, so that the sample returns to its starting position during the acquisition. The Fourier transformation of the FID then yields a spectrum similar to that of the static (not spinning) sample but with reduced broadening from the dipolar or CSA interactions.

2.4.7.2 Homo/Heteronuclear decoupling

In cases where a fast MAS rate cannot be obtained, homonuclear decoupling can be achieved using a multiple pulse sequence. In particular, Lee-Goldburg (LG) decoupling is often used for ^1H homonuclear decoupling in the indirect dimension during a 2D experiment. In LG decoupling, the transmitter frequency of the rf pulse is deliberately chosen so that an offset is created in the rotating frame, and the effective field is tilted at the magic angle with respect to the B_0 field as illustrated in Figure 2.9b, so as to minimize the homonuclear coupling between protons.

In a heteronuclear system such as that containing ^{13}C and ^1H , MAS is largely ineffective in removing the heteronuclear dipolar coupling between ^{13}C and ^1H . The peak-broadening effect of heteronuclear coupling can be avoided by using high-power decoupling, where ^1H spins are irradiated on resonance while the ^{13}C FID is recorded. During high power decoupling, ^1H spins undergo repeated Zeeman transitions, with magnetization rapidly oscillating between positive and negative. Since the heteronuclear dipolar coupling strength depends on the net magnetization of ^1H along the z-axis as shown in Equation (2.5), the time-averaged dipolar coupling for ^1H - ^{13}C is zero under high-power decoupling conditions.

The dipolar coupling constant for directly bonded ^1H - ^{13}C spin pairs is about 22 kHz. The proton decoupling power needs to be set at least three times larger than the dipolar interaction strength, that is, >66 kHz, in order to fully remove the effects of heteronuclear dipolar coupling. A common decoupling pulse sequence is TPPM (two pulse phase modulation), as shown in Figure 2.9c. It consists of a repeated series of two pulses with flip angles slightly smaller than 180° and phases that differ by 10 – 70° . The optimal decoupling condition depends on the MAS rate and needs to be optimized. Another commonly used decoupling scheme is SPINAL64,⁸³ which is more efficient and more tolerant to experimental imperfections. Both TPPM and SPINAL64 are employed in this thesis.

2.4.7.3 Cross-polarization

Cross-polarization (CP) transfers the larger polarization of ^1H spins to nuclei such as ^{13}C or ^{29}Si in order to enhance the sensitivity of NMR experiments on low- γ and low natural-abundance spins. CP transfer is mediated by through-space dipolar interactions and the corresponding pulse sequence is shown in Figure 2.9c. First, a 90°_x pulse creates ^1H magnetization along the $-y$ axis, then a contact pulse is applied simultaneously to both ^1H and ^{13}C spins. In the double double-rotating frame, the contact pulse appears stationary along the $-y$ axis, and the resulting spin-lock field along the $-y$ axis maintains the spin polarization. The dipolar coupling between ^1H and ^{13}C depends on an operator containing $I_z S_z$ as shown in Equation (2.5), which acts only in a direction perpendicular to the spin-lock field. Thus, the dipolar operator cannot alter the net spin polarization along the spin-lock field, nor the net energy of the combined ^1H - ^{13}C spin system. Nevertheless, the dipolar interaction between the ^1H and ^{13}C spins can mediate energy exchange between the ^1H and ^{13}C spin baths. That is, the energy emitted from ^1H transitions is absorbed by the ^{13}C spins to build up a larger ^{13}C magnetization along the $-y$ axis. When the Hartmann-Hahn condition is met (i.e. when the ^{13}C contact pulse is the same amplitude as that for ^1H), the energy gaps of the rotating frame ^1H and ^{13}C spins are the same, thus the spin transition process results in no net energy change. Finally, the enhanced ^{13}C magnetization is recorded during high-power proton decoupling. The Hartmann-Hahn condition for CP transfer under MAS is different from that under static conditions, and is given by:

$$\omega_H = \omega_C + n\omega_r \quad (2.11)$$

where the nutation frequencies for ^1H and ^{13}C are ω_H and ω_C , respectively, ω_r is the rotation (MAS) frequency of the sample, and n is an integral number. A ramped contact pulse on ^1H is commonly used to cover a range of possible Hartmann-Hahn conditions for a non-uniform sample, which normally gives better signal enhancement. The CP pulse sequence is an essential component in generating enhanced transverse magnetization for low- γ nuclei and is the starting point for most of the correlation experiments in this thesis.

2.4.7.4 Homo/heteronuclear correlation experiments

Different from solution NMR, where J-couplings are exploited for correlation experiments, homo/heteronuclear correlation experiments in ssNMR mainly depend upon dipolar interactions. This is because typical dipolar coupling constants in solid sample are an order of magnitude larger than J-coupling constants, and the latter are usually too small to observe. However, the dipolar interaction is suppressed (averaged out) by fast MAS, leading to the acquisition of high-resolution ssNMR spectra. The dipolar interaction can be reintroduced under MAS using a multiple pulse sequence such as DRAMA or C7, so that spatial correlation information about the spin system can nonetheless be obtained.⁸⁴

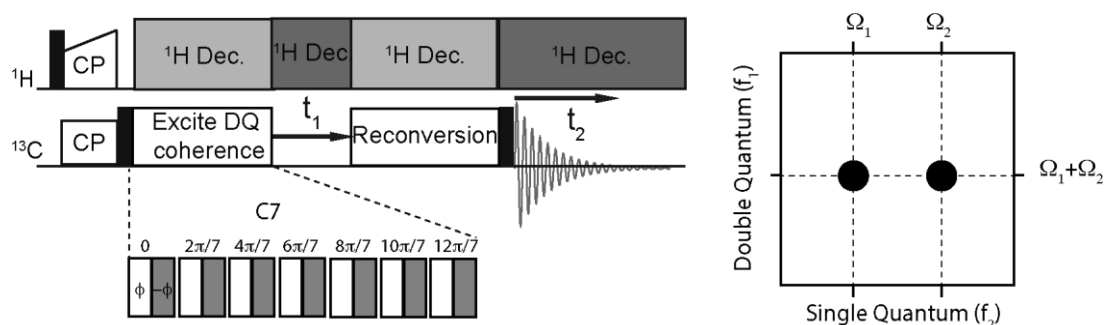


Figure 2.10 Pulse sequence corresponding to a homonuclear correlation experiment based upon dipolar coupling interactions. The C7 sequence is used to excite double quantum coherence under MAS. For the proton decoupling depicted in the upper section, dark grey denotes heteronuclear decoupling, while light grey denotes homonuclear decoupling. A schematic of the double quantum–single quantum correlation spectrum is illustrated on the right.

The C7 sequence, which is used to generate a double quantum (DQ) coherence between the dipolar-coupled spin pairs, consists of $7 \times (2\pi_\phi \ 2\pi_{-\phi})$ pulses with an adjusted rf amplitude so that the duration of the composite pulses is a multiple of the rotor period. The phase of the 2π pulse, ϕ , increases by $\frac{2\pi}{7}$ during each step. The underlying principle of the C7 pulse sequence in generating DQ coherence is beyond the scope of the current explanation and can be found in Ref. ⁷⁹. The generated DQ coherence is then used for a homonuclear correlation experiment.

A typical pulse sequence for homonuclear correlation using multiple-quantum coherence is shown in Figure 2.10. The first CP step creates ^{13}C transverse magnetization in the xy-plane,

which is then returned to the z-axis by the following 90° pulse. Using this enhanced longitudinal magnetization on ^{13}C , DQ coherence is generated with the aid of a recoupling pulse sequence such as C7. The DQ coherence then evolves during t_1 before being transferred back to the z-axis (and converted to zero quantum coherence, ZQ) by a reconversion pulse. The final 90° pulse converts this ZQ coherence to transverse magnetization which is observed in the t_2 period. A Fourier transform of the 2D data results in a DQ spectrum in the indirect dimension (f_1), and a SQ spectrum in the direct dimension (f_2). This so-called DQ–SQ correlation spectrum acquired using C7 pulse sequence can be used to identify networks of dipolar-coupled spins.

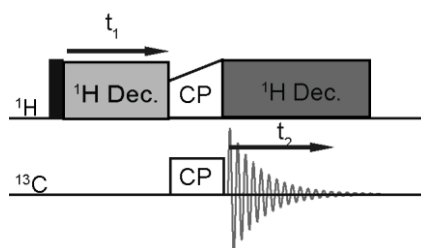


Figure 2.11 Pulse sequence corresponding to heteronuclear correlation experiments based upon dipolar coupling interactions.

Similar to the homonuclear correlation experiments just described, 2D heteronuclear correlation spectroscopy (HETCOR) can be used to confirm spectral assignment by, for example, correlating the chemical shifts of protons with another nucleus (e.g. ^{13}C) via their dipolar coupling interactions. The HETCOR pulse sequence is shown in Figure 2.11. The sequence starts with a 90° proton pulse to create transverse magnetization, which then evolves during t_1 (with simultaneous application of a homonuclear proton decoupling pulse such as LG); this magnetization is subsequently transferred to ^{13}C via a CP step. The resulting ^{13}C magnetization is then detected under conditions of high-power proton decoupling (e.g. SPINAL64). Since CP is mediated via dipolar coupling, CP transfer is only possible for spins with close spatial proximity (around a few Å). A short CP contact time should be chosen in order to selectively probe ^{13}C nuclei that are spatially close to the ^1H spins.

2.4.8 Dynamic nuclear polarization (DNP)

Though ssNMR provides atomic information about bulk materials, sensitivity becomes the limiting factor when ssNMR is applied to study surface structures. One solution to that problem is the use of hyperpolarization methods. Dynamic nuclear polarization (DNP) is one of the most promising methods, which takes advantage of the higher equilibrium polarization of the electron and increases the sensitivity of low- γ nuclei such as ^{13}C , ^{29}Si , and ^{17}O under microwave irradiation. The theoretical enhancement for ^1H is about a factor of 660 at 100 K (Figure 2.12a).

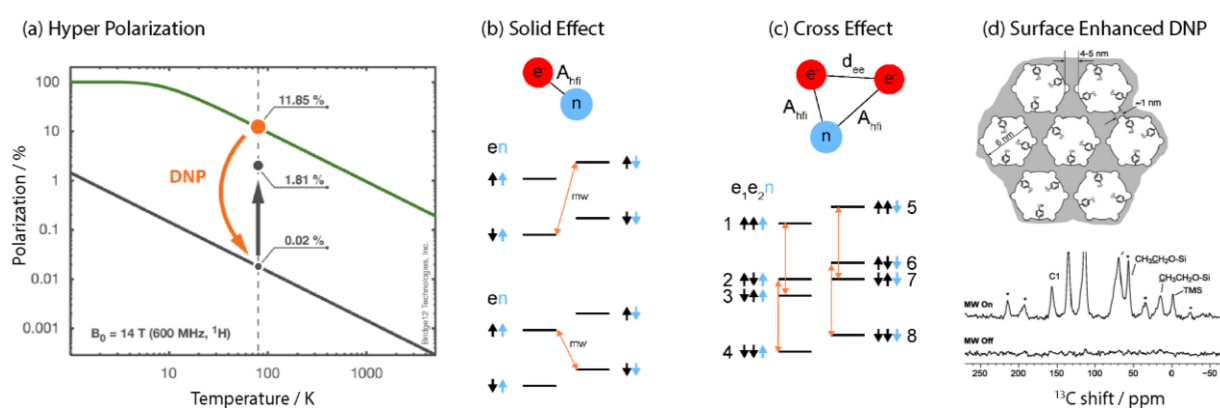


Figure 2.12 Principles and applications of DNP NMR. (a) The polarization difference between electrons (green) and ^1H (black) as a function of temperature at a field strength of 14 T. DNP transfer mechanisms: (b) the solid effect, induced by zero-quantum (middle) or double quantum (bottom) microwave irradiation; these transitions rely on hyperfine interactions (A_{hfi}) between the nucleus and the electron; (c) the cross effect, which involves two electrons and one nucleus, and its corresponding energy diagram when irradiating with microwaves at one frequency. The strong electron-dipolar coupling (d_{ee}) allows mixing of states 2, 3, 6 and 7 which are important for polarization transfer from electrons to nuclei. (d) Example of the use of DNP NMR to obtain surface information on a nanoporous silica-derived material. Figure adapted from ref^{85,86}.

Contemporary MAS DNP experiments are usually based on either the solid effect (SE), which exploits the coupling of an electron-nuclear spin pair, or the cross effect (CE), utilizing a pair of electrons in the form of a biradical and a nuclear spin. CE is currently the most commonly used polarization transfer mechanism for measurements at ~ 100 K, while SE is the mechanism of choice for 25 K or lower.⁸⁵

In SE, microwave irradiation excites the nominally forbidden zero and double quantum transitions for electron and nuclear spin pairs. The microwave amplitude, $\omega_{\mu W}$, must meet the matching condition given by:

$$\omega_{\mu W} = \omega_{OS} \mp \omega_{OI} \quad (2.12)$$

where ω_{OS} and ω_{OI} are the Larmor frequencies for the electron and nucleus, respectively. The difference between these frequencies corresponds to the energy of the DQ transitions, whereas their sum is equivalent to that of the ZQ transitions (Figure 2.12b). The hyperfine interaction (A_{hfi}) between the nucleus and the electron causes a small degree of electron-nuclear spin state mixing, and excited DQ/ZQ transitions result in a greater nuclear polarization. The SE enhancement factor scales as B_0^{-2} .

In contrast to the SE, the CE makes use of allowed single quantum (SQ) transitions. Continuous microwave irradiation at the Larmor frequency of one of the electrons leads to a build-up of non-equilibrium polarization, the condition is described as $\omega_{\mu W} = \omega_{OS,1} \vee \omega_{OS,2}$. If the difference between the Larmor frequencies of the two electrons is equal to the nuclear Larmor frequency (that is $\Delta\omega_{OS} = |\omega_{OS,1} - \omega_{OS,2}| = \omega_{OI}$), the built-up polarization can be transferred to the nucleus by a concerted $e-e-n$ triple spin flip (states 2 to 7 and states 3 to 6 in Figure 2.12c). The relevant matching condition can be summarized below:

$$(\Delta\omega_{OS} = |\omega_{OS,1} - \omega_{OS,2}| = \omega_{OI}) \wedge (\omega_{\mu W} = \omega_{OS,1} \vee \omega_{OS,2}) \quad (2.13)$$

Organic biradicals, which are two radicals tethered via an organic linker with controlled spacing and geometry orientations, have been synthesized to meet the conditions required for the CE. It is worth noting that the CE is less affected by high magnetic field and has a much greater probability in transferring polarization than does SE.

With recent advancements in both hardware and theory, DNP NMR has been used to study biomaterials as well as inorganic and hybrid materials. For example, surface-enhanced ^{13}C DNP NMR reveals the organic species on the surface of nanoporous silica (Figure 2.12d).⁸⁷ Without DNP, such experiments would require expensive isotope labelling and long experimental times. In addition, the signal enhancement provided by DNP enables 2D

correlation experiments to be performed, and thus more detailed structural information can be obtained.

In this work, DNP NMR is performed using the CE, with a schematic of the relevant DNP experiments illustrated in Figure 2.13. Since the SEI sample is water sensitive, non-aqueous-based DNP radical-solvent system (so-called “DNP matrix”) is chosen, which consists of a nitroxide-based biradical (TEKPol)⁸⁸ dissolved in dichlorobenzene (DCB)^{88,89} or tetrachloroethane (TCE). The powder sample is impregnated by the DNP juice to wet the surface of the SEI with biradicals. Microwave irradiation induces polarization transfer from electrons to protons, or the nucleus of interest, via the cross effect.

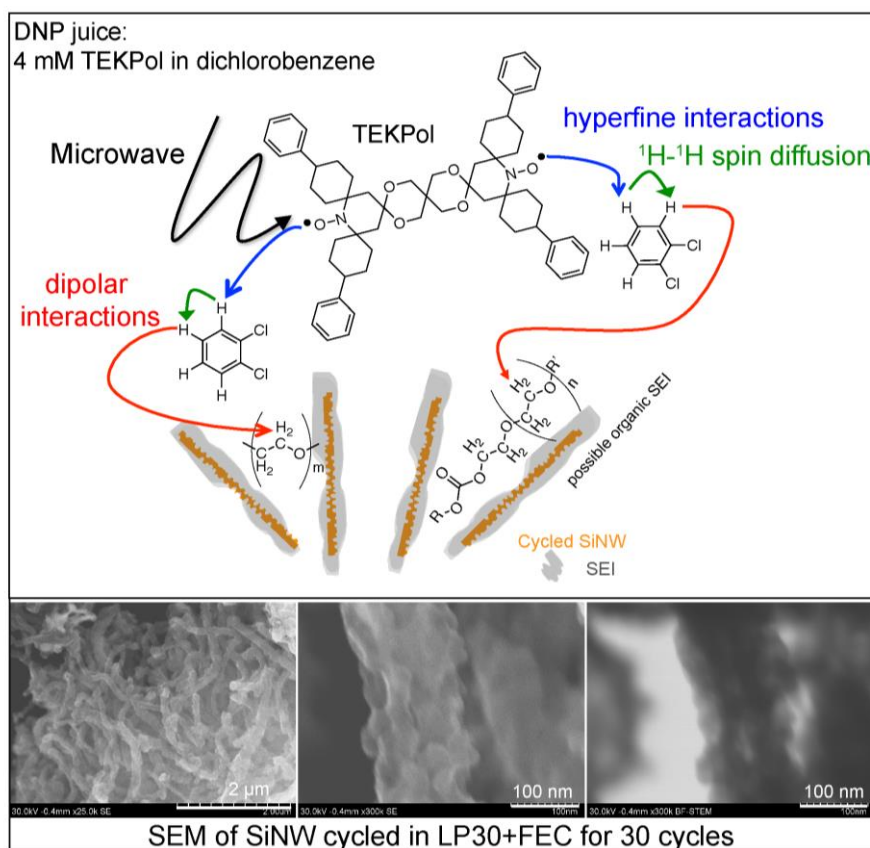
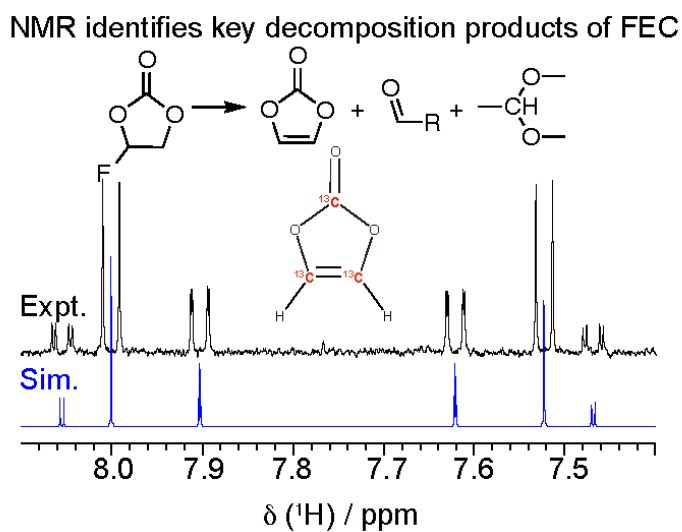


Figure 2.13 Schematic of the DNP NMR experiments performed in this work.

In a direct DNP experiment, the magnetization is transferred from electrons to nuclei and directly acquired from the latter. By contrast, in an indirect DNP experiment, the

hyperpolarized ^1H magnetization is first distributed throughout the sample via ^1H spin diffusion, then the magnetization on ^1H is transferred to the nuclei of interest via dipolar coupling techniques (i.e. cross polarization). Typically, indirect DNP NMR experiments provide better sensitivity for surface species in the SEI as the surface components are more protonated than the bulk, and ^1H spin diffusion is more effective than for other nuclei. Both direct and indirect DNP techniques are used in this thesis to study the SEI structure with favorable signal enhancement.

Chapter 3 Identifying key degradation products of fluoroethylene carbonate

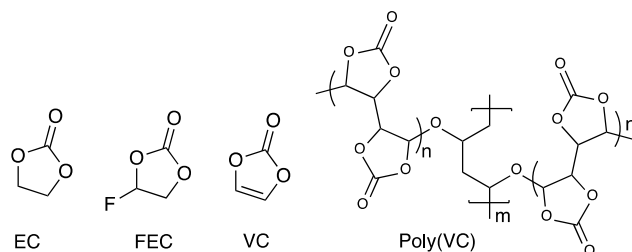


3.1 Introduction

Fluoroethylene carbonate (FEC) is one of the most important electrolyte additives and its degradation products are believed to be the key for achieving performance enhancement, however, the detailed structural information about its reduction products is still unclear. Here, a combination of solution and solid-state NMR techniques was used to characterize both the soluble and insoluble decomposition products of FEC. In order to overcome the inherently low sensitivity issue of NMR, uniformly labelled $^{13}\text{C}_3$ -FEC was synthesized by Nis-Julian H. Kneusels (University of Cambridge). The samples were then prepared by cycling binder-free silicon nanowires (SiNWs) in conventional ethylene carbonate (EC)-based electrolyte with and without 10 vol% FEC. The cycled SiNWs were then used for ssNMR experiments with dynamic nuclear polarization (DNP) enhancement to provide a more comprehensive understanding of the organic SEI. The results clearly show that chemically distinct products

such as vinylene carbonate (VC) and poly(VC) shown in scheme 3.1 are formed in the presence of FEC, which may be responsible for the increased cycle life.

Scheme 3.1. Structures of ethylene carbonate (EC), fluoroethylene carbonate (FEC), vinylene carbonate (VC), and a possible structure of the polymer “poly(VC)” as reported in reference ⁴⁹.



3.2 Experimental

3.2.1 Materials

Sulfuryl chloride (Sigma-Aldrich, 97%) was purified by distillation under reduced pressure. Acetonitrile (Sigma-Aldrich) was dried over anhydrous CaH₂ and distilled prior to use, all other materials were used as received: ¹³C₃-ethylene carbonate (Sigma-Aldrich, 97%, ¹³C-labelled 99 atom-%), ethylene carbonate (EC) (Sigma-Aldrich, anhydrous, ≥99%, ≤0.005% H₂O), dimethyl carbonate (DMC) (Sigma-Aldrich, anhydrous, ≥99%, ≤0.002% H₂O), LP30 electrolyte solution (1M LiPF₆ in EC/DMC, Sigma-Aldrich, battery grade, ≥99.99%), azobisisobutyronitrile (Sigma-Aldrich, 98%), carbon tetrachloride (Sigma-Aldrich, 99.9%), and potassium fluoride (Acros Organics, 99%, anhydrous).

3.2.2 Synthesis of ¹³C₃-fluoroethylene carbonate

¹³C₃ FEC was synthesized from ¹³C₃-EC via chlorination of EC and subsequent fluorination using standard Schlenk techniques under N₂ atmosphere. ¹³C₃-EC (200 mg, 2.27 mmol, 1.00 equiv) was suspended in 5 mL of carbon tetrachloride. Sulfuryl chloride (0.19 mL, 2.38 mmol, 1.05 equiv) and azobisisobutyronitrile (AIBN) (15 mg, 0.91 mmol, 0.04 equiv) were added, and further AIBN was added twice every 30 min. The reaction mixture was left stirring at 65 °C for 16 h before the solvent was removed *in vacuo*, and the liquid residue was purified by column purification (silica 100:1, dichloromethane, R_f = 0.50). ¹³C₃-Chloroethylene carbonate (180 mg, 1.47 mmol, 65%) was received as a clear colourless liquid.

Anhydrous potassium fluoride (2.50 g, 43.0 mmol, 29.3 equiv.) was suspended in 7 mL of acetonitrile *abs.* and $^{13}\text{C}_3$ -chloroethylene carbonate (180 mg, 1.47 mmol, 1.00 equiv), dissolved in 3 mL acetonitrile *abs.*, was added. The mixture was stirred at 75 °C for 16 h, and then filtered, and the solid residue was washed with 10 mL of acetonitrile. The filtrates were combined, and the solvent was removed *in vacuo*. The dark liquid was purified by column purification (silica 100:1, dichloromethane, $R_f = 0.45$). $^{13}\text{C}_3$ -FEC (40 mg, 0.38 mmol, 26 %) was separated as a clear colourless liquid.

3.2.3 Synthesis of silicon nanowires

Silicon nanowires were synthesized by chemical vapor deposition (CVD) as previously described.⁹⁰ Briefly, 50 nm gold was thermal-sputtered onto 20 μm -thick stainless steel (SUS304, Agar Scientific) foil. The gold-coated stainless-steel foil was cut into $1 \times 1 \text{ cm}^2$ substrates, which were transferred into the CVD chamber. The substrates were heated in 1 mbar of argon atmosphere at 510–530 °C for 10 min to anneal the gold catalyst. After annealing, a mixture of argon and silane gases ($\text{Ar}/\text{SiH}_4 = 100 \text{ sccm} / 20 \text{ sccm}$) was introduced. The growth was carried out in 15 mbar at 510–530 °C for 15 min. The substrates were weighed before and after CVD growth to determine the mass of SiNWs. The average mass loading of SiNWs was around 0.5–0.8 mg / cm^2 .

3.2.4 Electrolyte preparation and coin cell assembly

The five different electrolyte formulations used here are listed in Table 3.1. The LP30 + $^{13}\text{C}_3$ -EC enrichment of electrolytes was prepared by mixing $^{13}\text{C}_3$ -EC with a non-labelled EC/DMC in a 1:1:2 v/v/v ratio, then dissolving the LiPF_6 salt into the solvent to achieve a final concentration of 1 M. The LP30 + FEC and LP30 + $^{13}\text{C}_3$ -FEC electrolytes were prepared by either adding 0.5 mL of FEC or $^{13}\text{C}_3$ -FEC into 5 ml of commercial LP30 electrolyte.

Table 3.1 Electrolyte formulation with 1M LiPF_6 in different solvent mixtures

electrolyte solvents	abbreviation
EC/DMC = 50/50 (v/v)	LP30
$^{13}\text{C}_3$ EC/EC/DMC = 25/25/50 (v/v/v)	LP30 + $^{13}\text{C}_3$ -EC
EC/DMC/FEC = 50/50/10 (v/v/v)	LP30 + FEC
EC/DMC/ $^{13}\text{C}_3$ FEC = 50/50/10 (v/v/v)	LP30 + $^{13}\text{C}_3$ -FEC
$^{13}\text{C}_3$ EC/EC/DMC/FEC=25/25/50/10 (v/v/v/v)	LP30 + $^{13}\text{C}_3$ -EC + FEC

SiNWs electrodes were then assembled into Li-half 2032 coin cells using the five electrolytes. Porous glass fibre mats (Whatman GF/B, 1 mm thick) were used as separators and around 10 drops (~0.15 mL) of electrolyte were used for each cell. All the assembling procedures were carried out in an Ar filled glovebox ($H_2O < 0.1\text{ppm}$, $O_2 < 0.1\text{ppm}$). The coin cells were discharged/charged at a constant current (C/30, 120 mA/g) between 0.001 V and 2 V for 30 cycles using a Biologic VSP or MPG-2. Approximately 50 days were needed to complete 30 cycles. The slow cycling protocol ensures that the electrolyte solvents are held at a low voltage for sufficiently long time for extensive SEI formation. The electrochemical results obtained for the enriched electrolyte were similar to those of the non-enriched electrolyte: the cycling performance is mainly influenced by the presence of FEC.

3.2.5 Solution NMR

After the SiNW coin cells finished the first and 30th cycles, the cells were disassembled in an Ar filled glovebox. The glass fibre separators were extracted and soaked in 0.75 mL DMSO- d_6 for 2–3 min. The solution was then transferred to an airtight J-Young tube. Spectra were recorded on a 500 MHz Bruker Avance III HD, with a DCH (carbon observe) cryoprobe or Bruker AVANCE 400 equipped with a BBO probe. ^1H and ^{13}C NMR spectra were internally referenced to DMSO- d_6 at 2.50 ppm and 39.51 ppm, respectively. Details information about the pulse programs can be found below:

- 1D ^1H NMR spectra were recorded using a 30° pulse.
- 1D $^{13}\text{C}\{^1\text{H}\}$ NMR spectra were recorded using either the standard 30° observe pulse, using ‘waltz16’ pulse-gated decoupling or with the $u\text{def}t^{91}$ sequence. In cases where ^1H decoupling artifacts were too intrusive; they were minimized by changing the decoupling sequence to ‘bi_waltz65_256’.⁹²
- HQSC spectra were recorded using the ‘hsqcedetgsp.3’ pulse program: 2D H-1/X correlation via double inept transfer. Acquisition was phase sensitive using ‘Echo/Antiecho-TPPI’ gradient selection with decoupling during acquisition, and trim pulses in inept transfer with multiplicity editing during selection step. Shaped pulses were used for inversion on f2-channel for matched sweep adiabatic pulses. The pulses are calibrated to achieve ‘dept135’ editing of the spectra acquired. F2 (^1H) was acquired using a time domain of 1816 points, F1 (^{13}C) 256 increments, over 13 ppm and 190 ppm. The relaxation delay was 0.8 s and 4 scans per slice were used.

- HMBC spectra were recorded using the ‘hmbcetgpl3nd’ pulse program: 2D H-1/X correlation via heteronuclear zero and double quantum coherence. Acquisition was phase sensitive using Echo/Antiecho gradient selection, with three-fold low-pass J-filter to suppress one-bond correlations; no decoupling during acquisition. The long-range coupling parameter was set to 10 Hz. F2 (^1H) was acquired using a time domain of 4096 points, F1 (^{13}C) 768 increments, over 12 ppm and 250 ppm. The relaxation delay was 2 s and 16 scans per slice were used. Processed into magnitude data with the ‘xf2m’ command.
- ^{13}C – ^{13}C COSY spectrum was recorded using pulse program ‘cosydcqf’: 2D homonuclear X-nucleus shift correlation. Acquired in ‘QF’ mode. F2 (^{13}C) was acquired using a time domain of 4096 points, F1 (^{13}C) 1024 increments, over 236 ppm. The relaxation delay was 3 s and 40 scans per slice was used.
- 1D ^{19}F NMR spectra were recorded using a 90° pulse with inverse-gated waltz16 ^1H decoupling and a recycle delay of 30 s.

3.2.6 Solid-state NMR

After cell disassembly, the SiNW electrodes were dried under vacuum overnight (~16–20 h) to remove the DMC and FEC; this procedure also removes most of the EC.⁴⁸ Note that the electrodes were not rinsed. After drying, the SiNW electrodes were scratched from the substrate and packed into rotors for multinuclear ssNMR measurements.

^1H – ^{13}C cross polarization (CP) of LP30 + $^{13}\text{C}_3$ -EC sample was performed on a Bruker Avance III 700 (16.4 T) spectrometer using a 3.2 mm HXY probe at MAS frequency of 20 kHz, with a CP contact time of 1 ms. RF nutation frequency were (^1H) 92.5 kHz (50 – 100 % linearly ramped during CP⁹³), (^{13}C) 82.5 kHz, and SPINAL-64⁸³ ^1H decoupling at 80 kHz. A total of 3482 scans separated by a 3 s recycle interval were acquired over 3 h. The LP30 + $^{13}\text{C}_3$ -FEC sample was measured on a Bruker Avance III HD 500 (11.7 T) spectrometer using a 2.5 mm HX probe at MAS frequency of 10 kHz, with a CP contact time of 2 ms and SPINAL-64 ^1H decoupling at 80 kHz. A total of 24576 scans separated by a 3 s recycle delay were acquired over 20.5 h. ^1H and ^{13}C , shifts were externally referenced to adamantane at 1.87 and 38.6 ppm (of CH_2 group), respectively. The experimental parameters are summarized in Appendix A, table A.2.

3.2.7 DNP NMR

The cycled SiNW samples were sealed under Ar and transferred to the Nottingham DNP MAS NMR Facility in three layers of sealed plastic bags. The samples were then quickly pumped into the N₂-filled glovebox. Since the SiNWs were in the delithiated state, we assumed that there was no reaction between N₂ and the electrode material. The sample was diluted with predried KBr powder by mixing homogeneously in a mortar. A minimum amount of radical solution (4 mM TEKPol in 1,2-dichlorobenzene, DCB)^{88,89} was added to wet the powder. The resulting paste-like samples were packed into the center of 3.2 mm sapphire MAS rotors and sealed with PTFE film. The rotor was capped with a Vespel drive cap and quickly inserted into the precooled DNP NMR probehead for measurement.

All DNP NMR experiments were performed on a 14.09 T AVANCE III HD spectrometer, corresponding to ¹H Larmor frequency of 600 MHz, with a 395 GHz gyrotron microwave (MW) source and using a 3.2 mm triple resonance wide-bore probe. All experiments were performed at 12.5 kHz MAS frequency. A microwave source power of 11 W (at the source, equivalent to 110 mA collector current) was used for ¹H-¹³C DNP experiments. All MW on/off experiments were performed with a train of saturation pulses prior to a longitudinal relaxation delay followed by signal excitation. The characteristic build-up time of the enhanced ¹H polarization was measured via a saturation recovery experiment. The ¹H enhancement ratios with the microwave on versus off are listed in Appendix A, table A.1. ¹H-¹³C CP experiments were performed with 90 – 100 % ramp on the ¹H channel and 100 kHz ¹H decoupling using a swept-frequency two-pulse phase modulation (SW_f-TPPM) sequence⁹⁴. The relaxation delay in the CP experiments varied between 4 and 7 s, with a CP contact time of 2 ms. Note for the LP30 +¹³C₃-FEC sample, only 1 mg was used for measurement. The small sample amount is due to the small quantity of ¹³C₃-FEC that was obtained in the synthesis.

3.3 Results

3.3.1 Electrochemistry

The electrochemical performance of SiNWs cycled in LP30 and LP30 + FEC electrolytes is shown in Figure 3.1. In in Figure 3.1a, the discharge/charge (lithiaton/delithiation) capacities on the order of the theoretical capacity of Si (3579 mAh/g) were obtained for both LP30 and

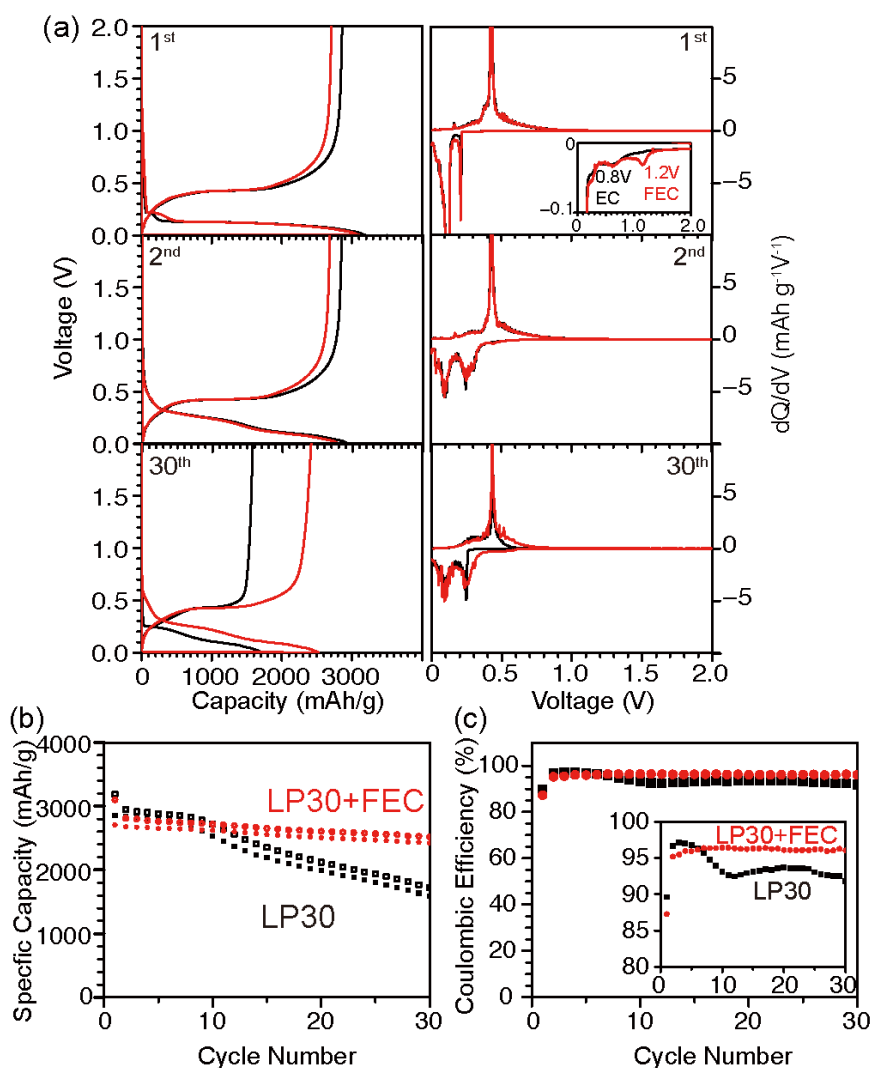


Figure 3.1. Electrochemical performance of SiNWs half-cells cycled with LP30 electrolyte (1 M LiPF₆ in EC/DMC=50/50, v/v, black), and LP30 with 10 vol % FEC (LP30 + FEC, red) electrolytes at a rate of C/30 (120 mA g⁻¹) between 0.001–2 V at room temperature. (a) Galvanostatic charge-discharge profiles and the corresponding dQ/dV plots of SiNWs cycled in LP30 and LP30 + FEC in the 1st, 2nd, and 30th cycles, (b) the cycling stability and (c) the coulombic efficiency for LP30 (black squares) and LP30 + FEC (red dots). The open dots/squares denote the discharge/lithiation capacity and the filled denote the charge/delithiation capacity.

LP30 + FEC electrolytes during the first two cycles. However, over long-term cycling, obvious deviations are observed between LP30 and LP30 + FEC samples. At the 30th cycle, the LP30 sample exhibits only 55% capacity retention whereas the LP30 + FEC sample retains 89% of the initial charge capacity (Figure 3.1b).

The voltage profile of SiNWs cycled in LP30 and LP30 + FEC during the first two cycles are similar (Figure 3.1a, left), indicating that both systems undergo similar structural transformations during the initial discharge/charge cycles. During the first discharge, the

voltage quickly drops from the open circuit voltage (OCV) to 0.2 V with a small lithiation capacity, suggesting little SEI formation on the SiNWs from OCV to 0.2 V. The dQ/dV plot (Figure 3.1a, right) reveals the reduction process of FEC at 1.2 V and the reduction of EC at 0.8V during the first cycle. A flat discharge profile is then observed at approximately 0.1 V, which corresponds to the conversion of crystalline Si to amorphous lithium silicide (a-Li_xSi).⁹⁵ Further lithiation results in the formation of crystalline Li₁₅Si₄ (c-Li₁₅Si₄), which is manifested as a characteristic process at approximately 0.4 V in the charge voltage curve. The 0.4 V process corresponds to the delithiation of c-Li₁₅Si₄ and the formation of amorphous silicon (a-Si).⁹⁶ The c-Li₁₅Si₄ phase is highly reactive and induces severe electrolyte decomposition.⁹⁷ For the second discharge, the SiNWs show a voltage profile characteristic of a-Si. The two sloping processes at about 0.25 V and 0.10 V correspond to the lithiation stages (a-Si + x Li⁺ → a-Li_xSi, where x is approximately 2.5 and 3.5 for the processes at 0.25 V and 0.1 V, respectively).⁹⁰ On the 30th cycle, the voltage profiles of the SiNWs cycled in LP30 or LP30 + FEC diverge (Figure 3.1a). Here, the SiNWs cycled in the presence of FEC maintain a voltage profile that is similar to that of the second cycle. In contrast, the onset of lithiation in the 30th cycle of the SiNWs is lower in LP30 than in the LP30+FEC sample as seen more clearly in the dQ/dV plot (Figure 3.1a, 30th cycle), suggesting a larger internal resistance inside the cell. This can be attributed to the formation of a more resistive SEI and increased electrode tortuosity, which limits Li ion diffusion through the bulk of the electrode and ultimately decreases lithiation capacity unless extremely low currents are used.^{48,98}

The Coulombic efficiency (CE, defined as the delithiation capacity divided by the lithiation capacity) of SiNWs in LP30 and LP30 + FEC is compared in Figure 3.1c. During the first five cycles, the FEC sample shows a slightly lower CE than the LP30 sample, which may be due to the preferential decomposition of FEC over EC. From cycles 5 to 30, the average CE of LP30 + FEC is 96.2%, which is an improvement over LP30 alone (average CE 94.0%) but is still much lower than required for a practical cell, emphasizing the need for further understanding of the chemistries that influence CE.

3.3.2 Soluble degradation products as measured by solution NMR.

Electrolytes from cells after the first and 30th cycles were compared with pristine electrolytes using ¹H solution NMR spectroscopy (Figure 3.2) and a series of two-dimensional (2D) correlation experiments. Several new ¹H NMR signals were detected in the cycled LP30 electrolyte between 3 and 5 ppm (Figure 3.2a) that are not present in the FEC-containing

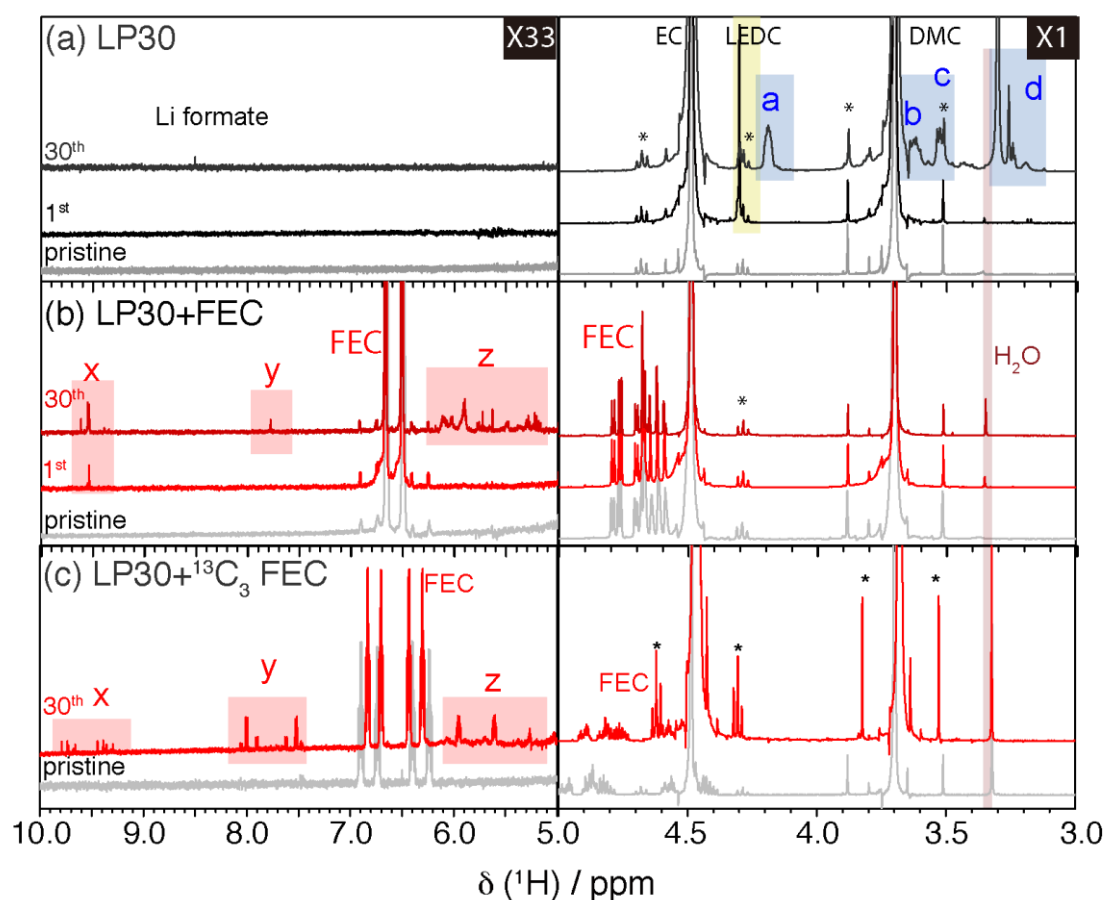


Figure 3.2. ^1H solution NMR of (a) LP30 and (b) LP30 + FEC (c) LP30+ $^{13}\text{C}_3$ FEC (LP30 + 10 vol% $^{13}\text{C}_3$ FEC) before cycling (pristine), and after the 1st and 30th cycles. The y scale of the 5–10 ppm region is enlarged by 33 times compared to the 3–5 ppm region. ^{13}C satellites are marked with an asterisk. All spectra were measured with a magnetic field strength of 9.4 T, except for the 30th cycle LP30+ $^{13}\text{C}_3$ FEC sample was measured at 11.7 T.

samples (Figure 3.2b and c) indicating that very different soluble breakdown products are formed. In the LP30 samples, these include an intense singlet at 4.30 ppm that appears after the first cycle (yellow shading) and several multiplets (blue shading, labelled from a–d) at 4.19, 3.62, 3.52 and 3.4–3.1 ppm.

The singlet at 4.30 ppm is assigned to lithium ethylene dicarbonate (LEDC),⁹⁹ which is supported by 2D ^1H – ^{13}C heteronuclear single quantum correlation (HSQC) and ^1H – ^{13}C heteronuclear multiple bond correlation (HMBC) experiments performed on cycled LP30 electrolytes extracted from Li symmetric cells (Figure A.1 in Appendix A) as well as previously reported DFT shift calculations.⁴⁷ LEDC is a decomposition product of EC, which is formed via a ring-opening reduction of EC, followed by a dimerization and the elimination of ethylene gas (see schemes presented in the discussion).⁴² Interestingly, LEDC disappears by the 30th cycle, suggesting that LEDC is a metastable species that decomposes upon further cycling.

Decomposition of LEDC is consistent with theoretical predictions that indicate that LEDC is thermodynamically unstable on contact with the lithiated silicides.^{51,100} The multiplets labelled a–d are assigned to oligomers comprising different linear polyethylene oxide (PEO) species, i.e., R-OCH₂CH₂O- /R'-OCH₃ groups and is fully characterized in Chapter 5. Similar PEO species or oligomers have also been previously detected by mass spectroscopy.^{101–103}

The ¹H NMR spectra of the LP30 + FEC electrolyte after 30 cycles exhibits three distinct new sets of resonances in the 9.5–9.7 ppm region (three singlets), a singlet at 7.77 ppm, and a cluster of multiplets at approximately 5.0–6.2 ppm (Figure 3.2b, shaded red and labelled x, y, and z, respectively), which are all absent in the LP30 sample. These three sets of resonances are also observed in the cycled LP30 + ¹³C₃-FEC with further splitting of the peaks resulting from the ¹³C labelling. Assignment of the species present in the FEC-containing samples was facilitated by a combination of 2D correlation NMR spectroscopy and J-coupling pattern analysis of the ¹³C-labelled sample (vide infra). By contrast, the 1D ¹H NMR spectra of the LP30 sample only shows a small singlet at 8.42 ppm in this spectral region after 30 cycles, which can be assigned to lithium formate on the basis of its unique chemical shift.¹⁰⁴ Lithium formate can form via reduction of CO₂ and proton abstraction from other organic molecules in solution (see discussion).⁴⁷ The resonances seen in the 5–10 ppm region of the ¹H NMR spectra indicate that distinct chemical species are formed in the presence of the FEC additive that are not formed in LP30 alone.

In addition to chemical composition, the ¹H NMR data also provides information on the relative populations of electrolyte breakdown products. In Figure 3.2, the ¹H NMR resonances in the 5–10 ppm region are magnified by a factor of 33, over the 3–5 ppm region. The intense peaks of the degradation product seen in the LP30 sample (peaks a–d in Figure 3.2a) in the latter region suggest that more soluble oligomers are present in the electrolyte. In contrast, the ¹H NMR peak intensities associated with the decomposition products found in the LP30 + FEC sample are significantly weaker than those in the LP30 sample, suggesting less soluble SEIs are formed in the presence of FEC.

Two-dimensional (2D) correlation NMR spectroscopy experiments were then performed with ¹³C₃-FEC sample, in order to carry out a more in-depth characterization of the structure of the decomposition products, ¹³C₃-FEC being synthesized as described in the experimental section using a modification of a published route.¹⁰⁵ The HSQC spectrum of the LP30 + ¹³C₃ FEC

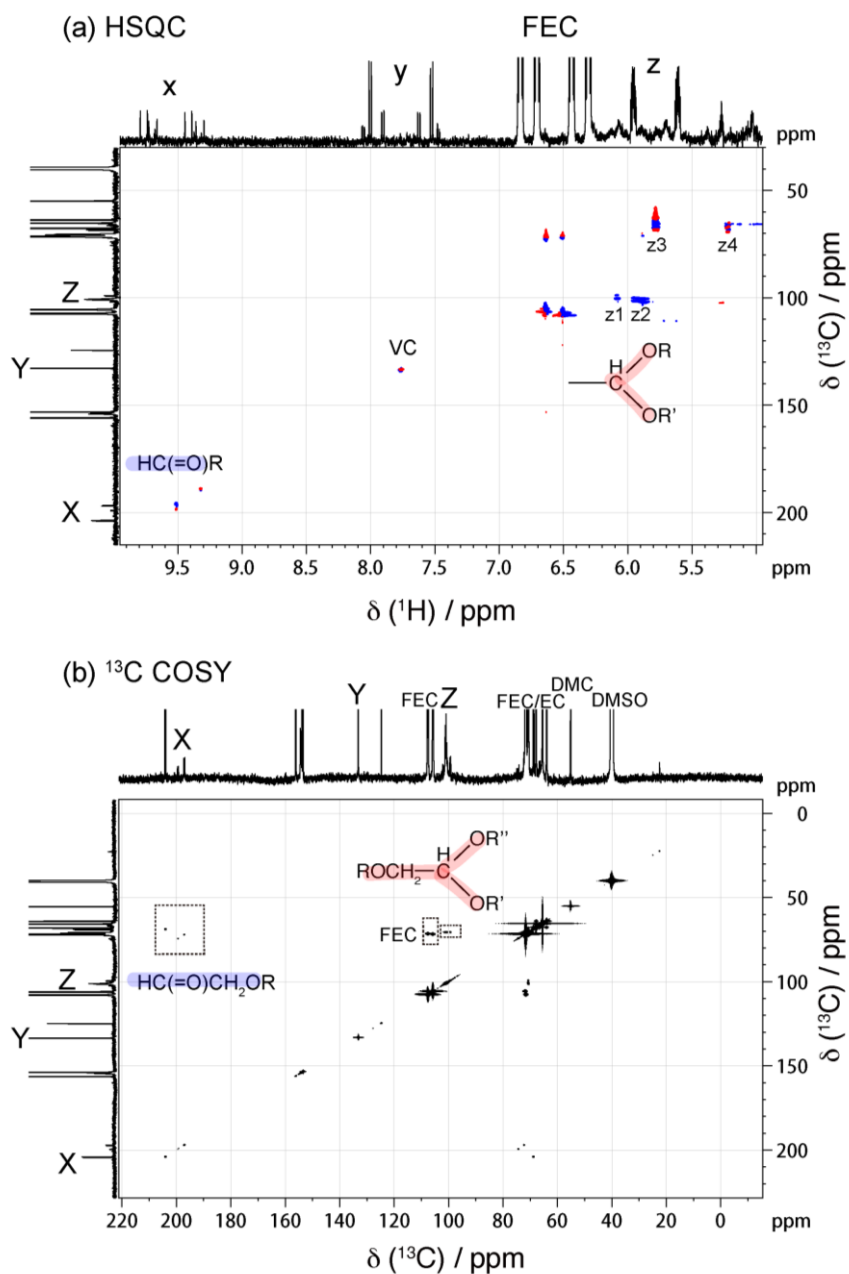


Figure 3.3. 2D solution NMR spectra of the LP30 + $^{13}\text{C}_3$ FEC electrolyte after 30th cycles. (a) ^1H - ^{13}C HSQC with ^{13}C decoupling, blue and red represent positive and negative peaks, respectively. (b) ^{13}C - ^{13}C COSY spectra. The off-diagonal peaks are marked with dashed squares. Possible structures are given next to the corresponding peaks; species containing aldehyde terminal groups are shaded in blue and the cross-linking units are shaded in red.

samples (Figure 3.3a) shows two cross peaks between the ^1H NMR signals at 9.53–9.34 ppm with the ^{13}C NMR signals at 188.5 and 195.7 ppm, respectively, which are consistent with a

Table 3.2 Summary of the assignments from HSQC, HMBC and ^{13}C COSY experiments for cycled LP30 + $^{13}\text{C}_3$ FEC electrolyte.

Samples	Index	Shift / ppm					Possible assignments
		HSQC		HMBC	^{13}C COSY		
		^1H	^{13}C	^{13}C	^{13}C	^{13}C	
LP30 + $^{13}\text{C}_3$ FEC	x	9.50	196	68.3/71.9	197.1	72.3	HC(=O)-CH ₂ OR
	y	7.76	134.1	153.6			RCH=CHOCOOR'/ VC
	z1	6.07	99.1		98.8	70.2	ROCH ₂ CH(OR') ₂
	z2	5.88	100.6		100.3	70.2	
	z3	5.78	65.8	66.4/153.2			ROCOOCH(CH ₂ OR) ₂
	z4	5.23	66.7	68.2 / 203.3	204.0	68.8	HC(=O)-CH ₂ OCH ₂ R

terminal aldehyde/vinoxyl species, HC(=O)-R. The HMBC spectrum (Figure A.5 in Appendix A) shows that there are multiple vinoxyl oligomers, with the HC(=O) groups being bound to ethylene oxide (-CH₂O-) carbons with ^{13}C chemical shifts of either 68.3, 71.9 or 73.8 ppm (all these ^{13}C shifts are consistent with a formula such as HC(=O)CH₂OR). The carbon connectivity of this structure is further supported by ^{13}C - ^{13}C correlation spectroscopy (COSY, Figure 3.3b), which shows a cross peak between the vinoxyl carbons at 204.0 ppm and the ethylene oxide carbons (-CH₂O-) around 68–73 ppm (see Table 3.2 for a summary of all 2D correlation peaks).

In addition to the vinoxyl species, other soluble components are also observed in the 2D NMR spectra. According to the HSQC spectrum in Figure 3.3a, the ^1H NMR peak at 7.77 ppm (y) belongs to a proton directly bound to a sp² hybridized carbon (as indicated by the ^{13}C chemical shift of 132.9 ppm). In addition, the corresponding ^1H - ^{13}C HMBC spectrum (Figure A.5) shows that the proton giving rise to y is also 2–3 bonds away from a carbonate group, since a ^{13}C cross peak is observed at 153.8 ppm. Thus, y likely originates from a highly symmetric decomposition product of FEC, e.g., either vinylene carbonate (VC) or lithium vinyl dicarbonate (LVDC), both of which contain the chemical fragment OCH=CHR. Note that in the non-labelled sample (or under ^{13}C decoupling), a singlet at 7.77 ppm is observed, whereas in the $^{13}\text{C}_3$ FEC sample, a distinct pattern of multiplets is observed (Figure 3.2b and c, region y). Of note, the splitting pattern observed in the ^{13}C labelled sample contains further information that allows us to unravel the environments that give rise to the peaks in region y.

3.3.3 Assignment of VC from analysis of the J-coupling

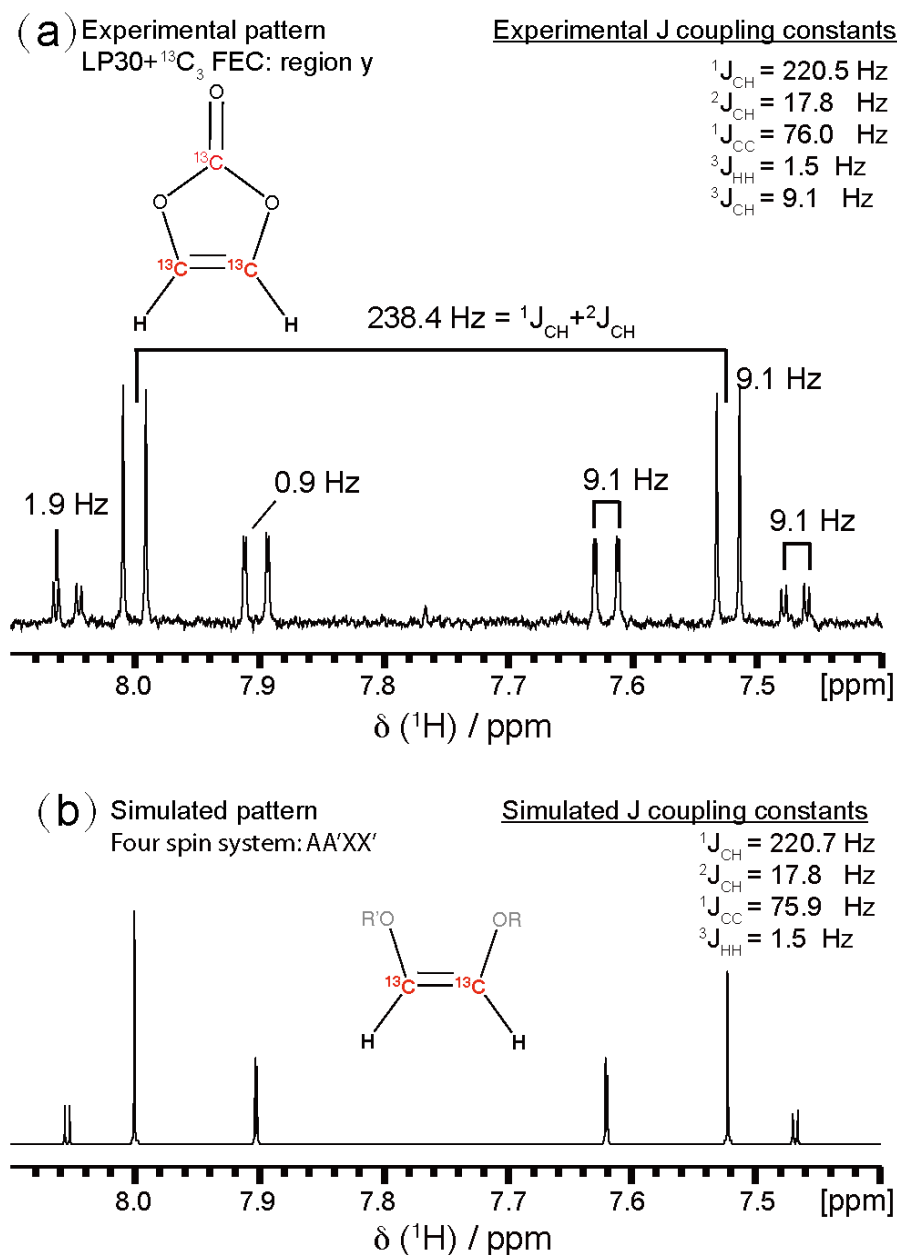


Figure 3.4. Multiplet pattern of cycled LP30 +¹³C₃ FEC in region y, (a) experimental pattern (the inset on the upper right-hand corner is the J-coupling constants of VC obtained from the ¹H NMR spectrum of VC as illustrated in Figure A.6); (b) simulated pattern of a four-spin system AA'XX' (cis-H-CR=CR-H) with the J-coupling constants used in the simulation listed on the upper right corner.

The experimental ¹H NMR spectrum in region y of the cycled LP30 +¹³C₃ FEC sample is compared with the simulated ¹³C₂ VC spectrum as shown in Figure 3.4. In order to simulate the proton-splitting pattern of ¹³C₂ VC, various J coupling constants ($^1J_{CH}$, $^2J_{CH}$, $^1J_{CC}$, $^3J_{HH}$, $^3J_{CH}$) were extracted from the ¹H NMR spectrum of natural abundance VC, which is also associated

with a ^1H shift of 7.77 ppm (Figure A.6 in Appendix A). The experimental J coupling constants are listed on the inset of Figure 3.4a. These J coupling constants were then used to simulate the ^1H NMR spectrum of $^{13}\text{C}_2$ VC, by considering the four-spin system, AA'XX' (Figure 3.4b). Here, we simplified the simulation by omitting $^3\text{J}_{\text{CH}}$ and, as a result, neglected the coupling to the carbonate group even though this sample originated from $^{13}\text{C}_3$ -labelled FEC. (We note that in an AA'XX' system, each proton (A) is coupled to a different carbon (X), which gives second-order multiplets because $^1\text{J}_{\text{CH}}$ is different from $^2\text{J}_{\text{CH}}$). The appearance of the spectrum is defined by the four coupling constants ($^1\text{J}_{\text{CH}}$, $^2\text{J}_{\text{CH}}$, $^1\text{J}_{\text{CC}}$ and $^3\text{J}_{\text{HH}}$).

The peak position and its intensity can be calculated as described by Pople.¹⁰⁶⁻¹⁰⁸ A least squares minimization was carried out to adjust the J coupling constants in order to match the experimental pattern. Figure 3.4b shows the simulated $^{13}\text{C}_2$ VC pattern with the corresponding J coupling constants. The simulation provides an excellent match to the experimental spectrum with the exception that the $^3\text{J}_{\text{CH}}$ coupling (9.1 Hz) is omitted since we only considered a four-spin system; including this would lead to the observed 9.1 Hz splitting of all of the peaks. In contrast, LVDC, which contains carbonate groups on both ends of the molecule, will have a more complex J_{CH} multiplet pattern: $^4\text{J}_{\text{CH}}$ (<10 Hz),¹⁰⁹ in addition to $^3\text{J}_{\text{CH}}$ couplings, will exist, leading to additional splitting of the ^1H signals (a doublet of doublets). Therefore, region y can be assigned to VC, not LVDC. LVDC is also excluded on the basis of the measured $^3\text{J}_{\text{HH}}$ value (1.5 Hz), this coupling constant likely arising from a cis-conformation (as in VC) rather than a trans one, which would be associated with a larger $^3\text{J}_{\text{HH}}$ value.¹¹⁰

3.3.4 Assignment of branched oligomers and vinoxyl species

The third region, labelled z, in the ^1H NMR of the cycled LP30 + $^{13}\text{C}_3$ FEC sample shows multiplets at 6.07, 5.88, 5.78, and 5.20 ppm (which are labelled as z1, z2, z3 and z4 in Figure 3.3a). From the peaks observed in the HSQC spectrum, the ^1H resonances z1 and z2 are connected to carbon resonances at 99.1 and 100.6 ppm, respectively. These resonances can be assigned to protonated carbons with two oxygen groups attached ($-\underline{\text{CH}}(\text{OR})_2$) on the basis of their chemical shifts (and their similarity to the shifts found in polysaccharides with similar local environments¹¹¹). In the ^{13}C - ^{13}C COSY spectrum (Figure 3.3b) the branched carbons at 100.3 and 98.8 ppm are directly bound to the ethylene oxide carbon at 70.2 ppm, suggesting a motif structure: $\text{RO}\underline{\text{C}}\text{H}_2\underline{\text{C}}\text{H}(\text{OR})_2$. This key observation is indicative of the formation of branched oligomers in the FEC-containing electrolyte, which appear after prolonged cycling.

Similarly, structural assignments for the ^1H NMR z3 and z4 resonances can be made. The ^1H resonance z3 is connected to a ^{13}C resonance at 65.8 ppm in the HSQC spectrum and the protons are 2–3 bonds away from carbons with ^{13}C resonances at 66.4 and 153.2 ppm in the HMBC spectrum. These resonances can be assigned to a branched carbon near a carbonate group and two ethylene oxide groups ($\text{ROCOO}\underline{\text{CH}}(\text{CH}_2\text{OR}')_2$) based on their chemical shifts. The z4 proton is bound to a carbon at 66.7 ppm. The HMBC spectrum shows that z4 is further bonded to carbon atoms with ^{13}C resonance at 68.2 and 203.3 ppm. The chemical structure of z4 can therefore be assigned to the methylene units in the vinoxyl species ($\text{HC}(=\text{O})\underline{\text{CH}}_2\text{OCH}_2\text{R}$), which confirms our identification of the vinoxyl species in region x.

3.3.5 ^{13}C ssNMR and DNP NMR detection of the SEI

Characterization of the insoluble species in the SEI was carried out with $^{13}\text{C}_3$ -labelled EC, $^{13}\text{C}_3$ -labelled FEC electrolyte, and electrolyte/additive formulations (see Table 3.1 for electrolyte formulation) using a combination of ssNMR and DNP NMR spectroscopies. Cycled SiNWs were extracted from cells without rinsing and were dried under vacuum overnight to remove EC/DMC/FEC before measurement. Figure 3.5 shows a comparison of the ^1H – ^{13}C cross polarization (CP) NMR spectra measured at room temperature (RT) using conventional ssNMR and the spectra acquired with DNP NMR at 100 K. All DNP spectra show intense DCB solvent peaks at 120 and 140 ppm with the corresponding spinning sidebands at 40–55 ppm (Figure 3.5) due to the addition of the DNP biradical solution (4 mM TEKPol in DCB). Apart from these solvent peaks, there is no obvious difference in the species detected via ssNMR and DNP NMR, suggesting that the biradical solution has not altered the chemical structure of the SEI. Moreover, the sensitivity provided by low temperature DNP is obvious: the room temperature (RT) spectrum of the LP30 + $^{13}\text{C}_3$ FEC sample took approximately 20 h, whereas, under DNP conditions (100 K), a similar signal-to-noise ratio spectrum was achieved within 1.3 h and allowed characterization of the SEI via ^1H – ^{13}C heteronuclear correlation (HETCOR) experiments (Figure 3.6).

LP30: The ^{13}C NMR spectrum of LP30 containing 25 vol % enriched EC (LP30 + $^{13}\text{C}_3$ EC, Figure 3.5a) is dominated by a broad peak at 68 ppm with a shoulder at 61 ppm. In addition, a semicarbonate resonance at 160 ppm is observed. The shoulder at 61 ppm becomes sharper in the spectrum acquired with DNP at 100 K, likely due to reduced dynamics of the organic SEI species at lower temperatures, as observed in the previous reported DNP experiments performed on graphene electrodes.¹¹² The broad ^{13}C resonance at 68 ppm (labelled C₁) is

correlated to a proton at 4.5 ppm in the HETCOR (Figure 3.6a), allowing C₁ to be assigned to either the carbon in ethylene oxide ($-\underline{\text{C}}\text{H}_2\underline{\text{C}}\text{H}_2\text{O}-$) or to residual EC. The shoulder at 61 ppm in the ¹³C ssNMR spectrum (labelled C₂) shows a one-bond correlation to a proton resonance at approximately 3.75 ppm, and is assigned to an ethylene oxide carbon with a terminal alcohol ($\text{R}\underline{\text{C}}\text{H}_2\text{OH}$).⁴⁷ Three other local maxima are observed in the HETCOR spectra between C₁ and C₂ (numbered 3, 4 and 5 in Figure A.9), the different shifts possibly being a result of different PEO chain lengths and/or a variation in terminal groups of polyethylene oxide. The intensity of aliphatic carbons in both the conventional and DNP ¹³C NMR spectra is low, which suggests that the SEI formed here primarily consists of polyethylene oxide that contains few aliphatic units.

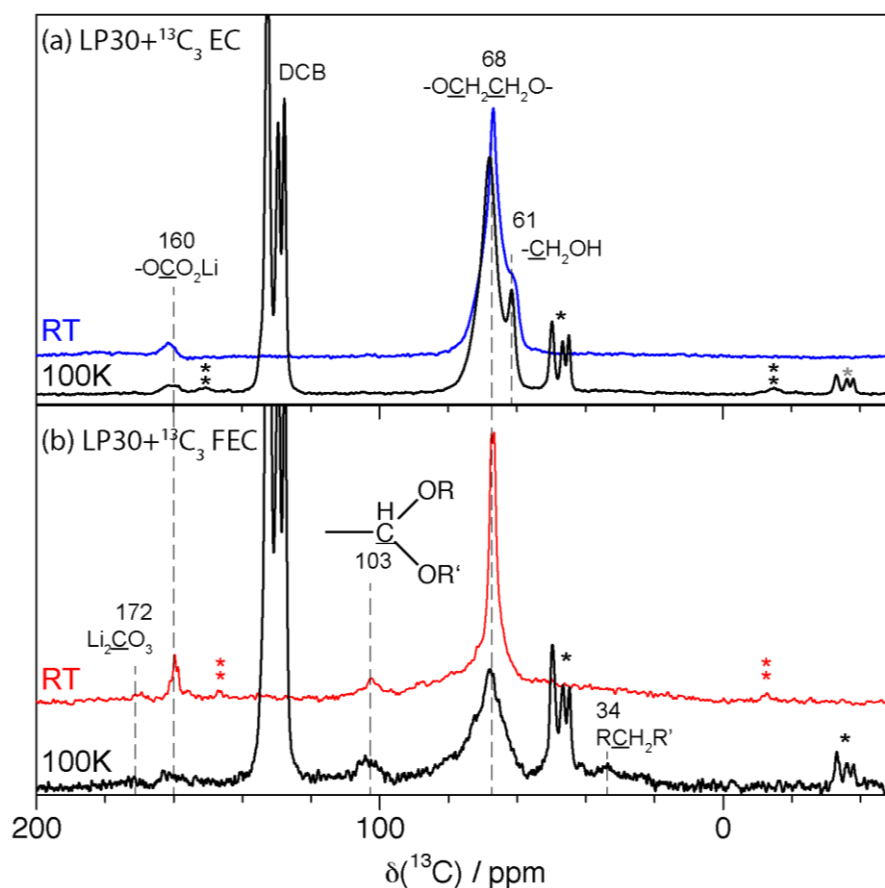


Figure 3.5 ¹H-¹³C CP NMR spectra of SiNWs cycled in LP30 with 25 vol % ¹³C₃ EC (LP30 + ¹³C₃ EC). (a) and LP30 with 10 vol% ¹³C₃ FEC (LP30 + ¹³C₃ FEC) (b) electrolytes, for 30 cycles. The RT spectra were measured at room temperature by conventional ssNMR, while the 100 K spectra were measured using DNP NMR with the microwaves turned on. Ortho-dichlorobenzene (DCB) was used as a radical solvent in the DNP experiments and its isotropic resonances are labelled “DCB”; the spinning sidebands of all the resonances are marked with asterisks. Possible structures are given next to the various isotropic resonances where R represents CH/CH₂/CH₃ groups.

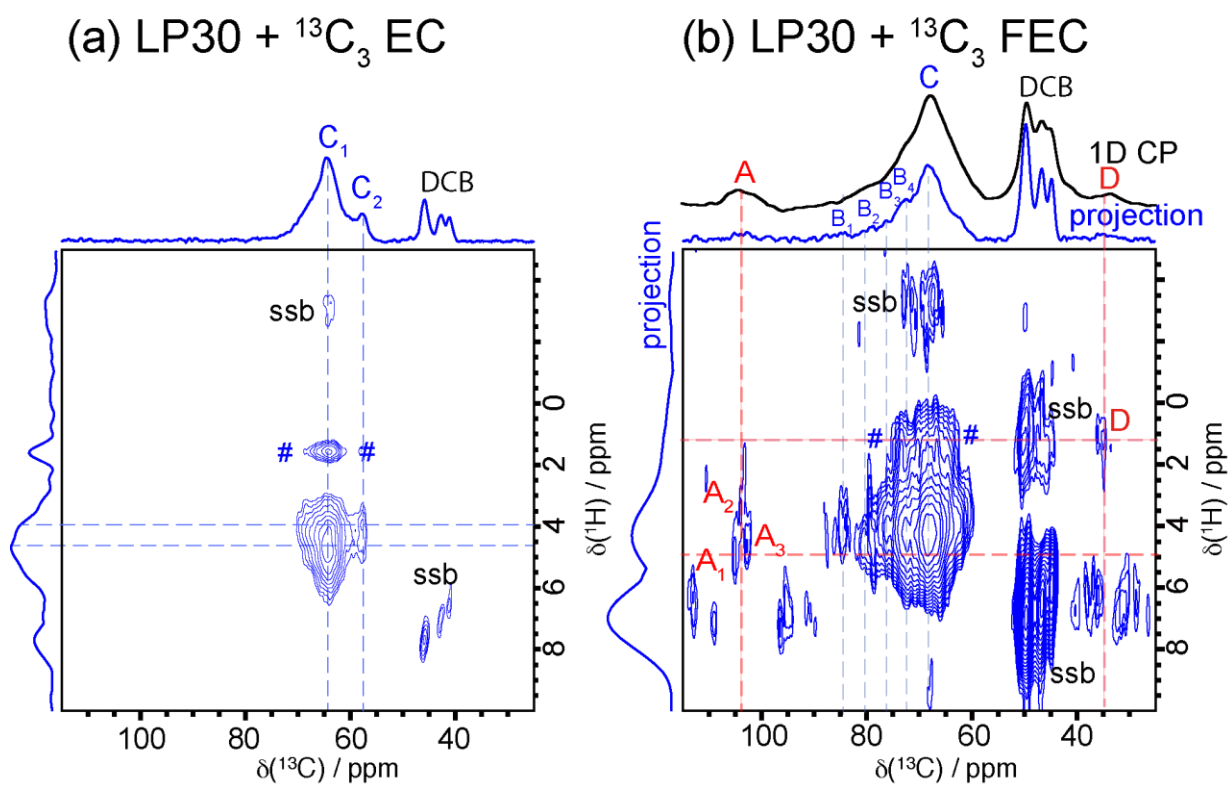


Figure 3.6 2D ^1H - ^{13}C heteronuclear correlation (HETCOR) DNP-NMR of SiNWs cycled in LP30+ $^{13}\text{C}_3$ EC electrolyte (a) and LP30 + $^{13}\text{C}_3$ FEC electrolyte (b) for 30 cycles. Spinning sidebands arising from the DCB solvent are marked “ssb”; artefact peaks marked with # are due to spin locking along the effective field arising from the proton decoupling and they appear at the ^1H carrier frequency.¹¹³ Full spectra and additional experimental details can be found in the Appendix A.

LP30 + FEC: Similar carbon environments at 68 ppm and 160 ppm are observed in the spectrum of LP30 with 10 vol % of ^{13}C -enriched FEC (LP30 + $^{13}\text{C}_3$ FEC, Figure 3.5b), along with two new peaks: a ^{13}C resonance at 103 ppm that is present in both the ssNMR and DNP spectra, as well as a weak resonance at approximately 34 ppm that is much more clearly resolved in the DNP spectrum. The main peak at 68 ppm has a different peak shape compared to that observed in the LP30 + $^{13}\text{C}_3$ EC spectrum, and no shoulder at 61 ppm is observed. The signal at 68 ppm in the RT spectrum is broadened near the baseline, possibly indicating that two peaks are superimposed in this region. It is hypothesized that the sharp peak at 68 ppm is due to residual EC. The broader component of the peak as well as the ^{13}C resonance at 68 ppm is consistent with a distribution of different ethylene oxide environments ($-\text{CH}_2\text{CH}_2\text{O}-$).⁴⁷ In contrast to the LP30 + $^{13}\text{C}_3$ EC sample, the SEI signal at 68 ppm becomes broader when

measured at 100 K (Figure 3.5b). Here, spectral broadening may be a result of sample heterogeneity, leading to a wider distribution of chemical shifts at low temperature.

The HETCOR spectrum of the FEC-containing sample (Figure 3.6b) has three extra peaks at 103, 75–85, and 34 ppm, labelled A, B, and D, respectively, which are absent in the LP30 + $^{13}\text{C}_3$ EC sample. The broad peak, B, is correlated to a ^1H peak at around 4.5–5.0 ppm. At least four components (B_1 – B_4) can be resolved, which are assigned to branched ethylene oxide units ($-\underline{\text{C}}\text{HRO}$) with different substituting groups or chain lengths. The ^{13}C resonance at 34 ppm (peak D) is correlated a ^1H resonance at 1.3 ppm and is assigned to $\text{R}\underline{\text{C}}\text{H}_2\text{R}'$ units. Both the aliphatic units (peak D) and the series of resonances round 80 ppm (peak B) are only present in the FEC-containing sample and imply that the structure that originates from FEC is more complex than a simple linear ethylene oxide polymer.

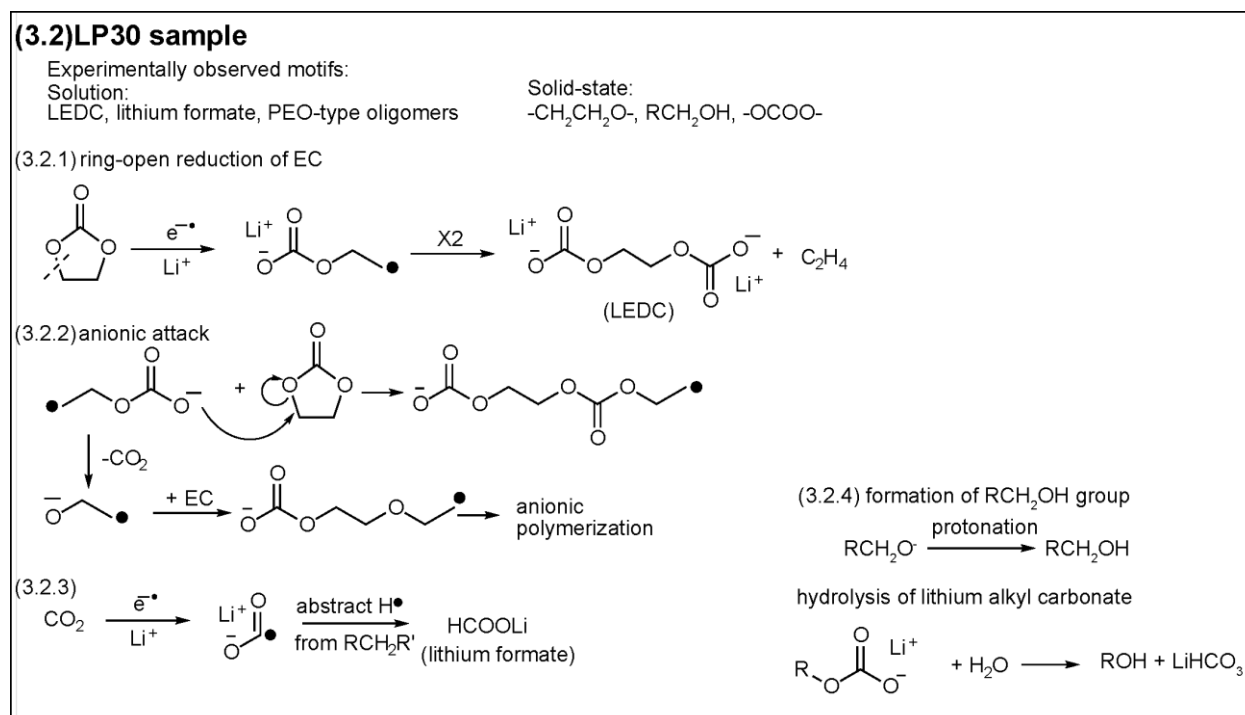
In the HETCOR spectrum, the peak at 103 ppm (peak A) is bound to protons that resonate between 4.2–5.2 ppm, and can be assigned to a protonated carbonate bound to two oxygens based on prior DFT shift calculations of proposed cross-linked VC polymers (see Scheme 3.1 and discussion).⁴⁹ This unique chemical shift is consistent with branched structures and was observed in the spectrum of chemically reduced FEC.⁴⁹ The peak at 103 ppm is not due to residual FEC as no FEC was detected by ^{19}F ssNMR (Figure A.7). Interestingly, similar resonances were also detected in solution NMR of cycled LP30 + FEC electrolyte (resonance z1 and z2: the proton at 5.78 ppm is bonded to a carbon at 100 ppm in HSQC, Figure 3.3a), suggesting that these might be the precursors that eventually form the insoluble, higher molecular weight SEI polymers as will be discussed later. Similar cross-linking units are present as glycosidic linkages in natural polysaccharides and also exhibit ^{13}C resonances close to 100 ppm.¹¹¹

3.4 Discussion

Different electrolytes with $^{13}\text{C}_3$ enriched EC and/or $^{13}\text{C}_3$ enriched FEC were cycled in SiNW half-cells to study the organic electrolyte degradation products. FEC-containing electrolytes display an obvious improvement on the cycle life of Si anodes compared to electrolytes that do not contain FEC. The SiNWs cells were stopped at the delithiated state after the first and 30th cycle for ex-situ NMR analysis. The cycled electrolytes were examined by solution NMR and the electrodes by solid-state and DNP NMR spectroscopies. Both soluble and insoluble

chemical structures detected in LP30 samples with and without FEC are listed in Schemes 3.2 and 3.3 along with possible formation reactions.

Scheme 3.2. Possible Reaction Schemes Consistent with the Chemical Signatures Detected by Solution and Solid-State NMR for the LP30 Sample: (2.1) Reduction of Ethylene Carbonate,^{114,119} (2.2) Anionic Polymerization of EC, (2.3) Formation of Lithium Formate, and (2.4) Two Possible Reactions for the Formation of ROH^{116,120}



For the LP30 sample, soluble products such as LEDC, lithium formate and PEO-type oligomers are detected in the cycled electrolyte and their respective formation pathways are shown in Scheme 3.2. The insoluble SEI that forms from LP30 mainly consists of ethylene oxides (-CH₂CH₂O-), ethylene oxides with hydroxide terminal units (RCH₂OH) and carbonate (-OCOO-) units. The presence of these ethylene oxide species is consistent with the PEO-type and lithium alkyl carbonate polymers formed from EC that were reported by Shkrob.¹¹⁴

Previous studies on EC decomposition^{115–117} suggest that EC can undergo one-electron ring-opening reduction to form a lithium alkyl carbonate anion radical (Scheme 3.2.1). The radical can then dimerize and form LEDC with concurrent loss of ethylene gas, which has been previously detected by GC-MS (Scheme 3.2.1).¹¹⁸ To form oligomers or polymers, the alkyl carbonate radical anion can elongate the chain via a nucleophilic attack on the EC. Alternatively, it can lose CO₂, forming an ethylene oxide radical anion (•CH₂CH₂O⁻).¹¹⁹ This radical anion can also attack EC to initiate anionic polymerization (Scheme 3.2.2).¹¹⁹ In either

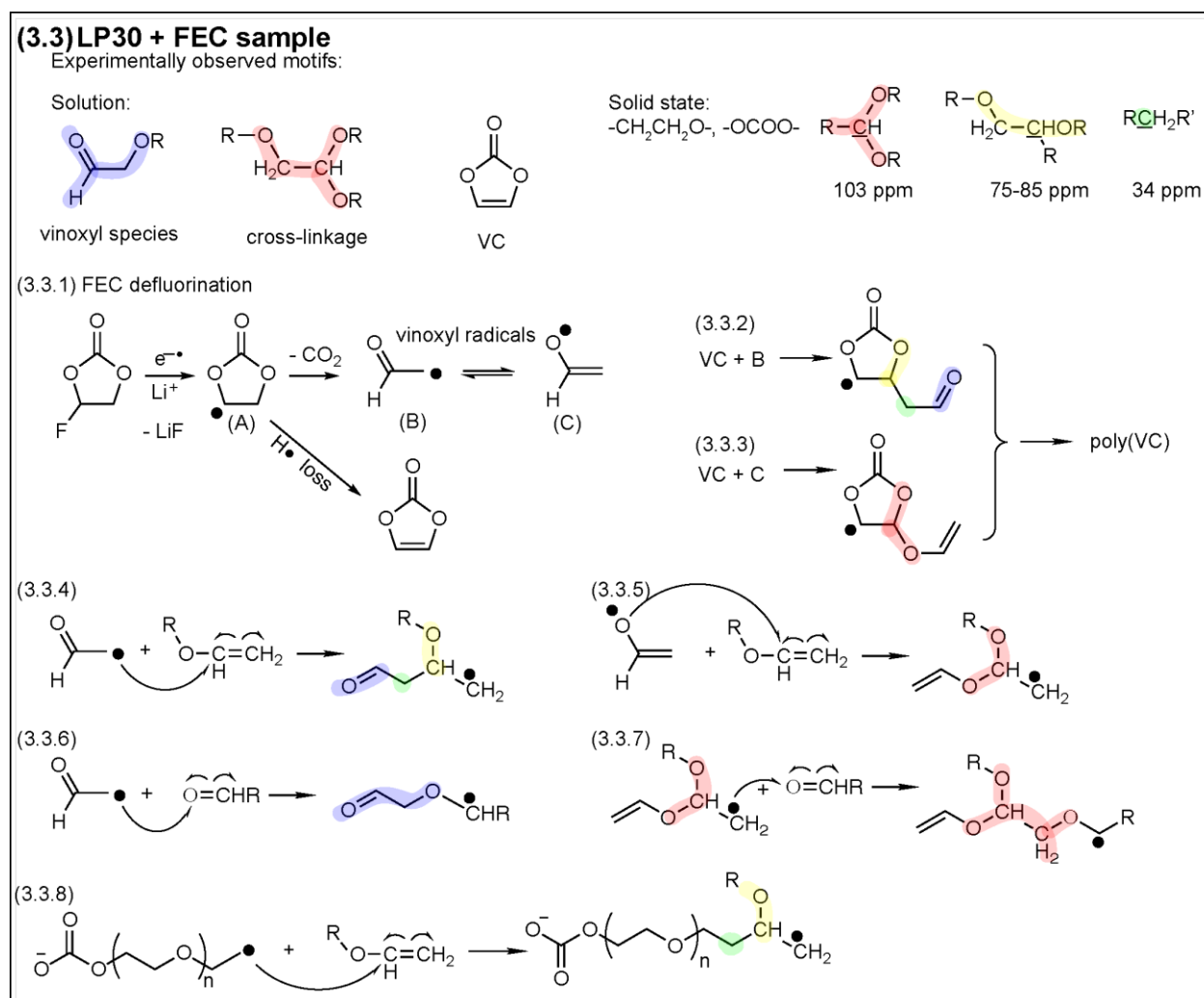
case, the resulting polymer will primarily consist of linear carbonates and ethylene oxide units which are consistent with the ssNMR data in this study as well as those published in previous report.⁴⁸ During these processes, lithium formate can be formed by the reduction of CO₂, resulting in a lithium carbon dioxide radical with subsequent hydrogen abstraction from other species in the solution (Scheme 3.2.3).⁴⁹

Short-chain lithium alkyl carbonates such as LEDC are highly soluble and thus are unable to protect the Si anode, as they are easily detected in the cycled electrolyte. LEDC is only transiently detected in the first cycle electrolyte and not in the electrolyte extracted after multiple cycles, confirming its instability.⁵¹ Significant amounts of PEO-type oligomers are present in the electrolyte after prolonged cycling, which suggests that the degradation products derived from LP30 are highly soluble. Since they are not part of the SEI, they will not help preventing further electrolyte decomposition. Their formation contributes to the irreversible consumption of lithium and it agrees well with the capacity fading observed in the electrochemistry of the LP30 sample (Figure 3.1b).

The insoluble polymeric SEI formed from LP30 contains similar chemical units to those detected in the solution NMR. Note that significant amounts of hydroxide-terminated groups (RCH₂OH) are detected in the ssNMR of the LP30 sample, which is consistent with previous study.⁴⁸ Hydroxide terminal units can be formed via protonation of the alkoxide (RCH₂O⁻) or by the hydrolysis of lithium alkyl carbonate (Scheme 3.2.4).^{116,120} Although the ¹³C CP NMR is not quantitative, the long contact time used in the experiments here (1–2 ms) ensures a homogenized ¹H polarization transfer throughout the molecule, allowing a semi-quantitative comparison. The higher percentage of hydroxide-terminated carbon versus ethylene oxide carbon in the LP30 sample suggests a higher population of polymers with shorter chain lengths compared to highly polymerized PEO species. Such short-chain polymers/oligomers are likely to be chemically similar to the oligomers detected in the cycled electrolyte (peak a–d in Figure 1a). These short-chain polymers derived from EC do not appear to be able to form a stable SEI on the Si anode and thus, cannot prevent further electrolyte breakdown.

Very different chemical motifs were detected in the solution and solid-state NMR of the FEC-containing sample (Scheme 3.3, top). Specifically, minor amounts of vinoxyl species, VC, and a possible cross-linking site are present as the soluble products in the cycled electrolyte. Note that PEO-type oligomers were not detected by solution NMR in the FEC

Scheme 3.3. Possible Reaction Schemes Consistent with the Chemical Signatures Detected by Solution and Solid-State NMR for the LP30 + FEC Sample: (3.3.1) Reduction of Fluoroethylene Carbonate, (3.3.2 and 3.3.3) Examples of Reactions between VC and Vinoxyl Radicals as the Initial Steps for Radical Polymerization To Form Poly(VC), (3.3.4 and 3.3.5) Reactions between Alkene Termination and Vinoxyl Radicals, (3.3.6) Possible Reactions between Vinoxyl Radical B and Aldehyde Species, Forming the Vinoxyl Units of the Type Detected by Solution NMR, (3.3.7) Reaction between Secondary Radical Formed in (3.3.5) and Aldehyde Species, Forming Branched Structure Found in Solution NMR, and (3.3.8) Possible Reaction between Alkene Termination with Reduced EC Intermediate.



a

^a The aldehyde terminal units and vinoxyl species are all shaded in blue. R/R' groups are organic fragments. The cross-linking units, branched ethylene oxide, and aliphatic carbon are shaded in red, yellow, and green, respectively, and their corresponding ¹³C chemical shifts are marked.

sample. The absence of soluble PEO-type species suggests that FEC can effectively suppress the formation of soluble oligomers formed in the LP30 sample.

Vinoxyl species are present in both the first and 30th cycle, indicating that they form during the initial stage of FEC decomposition. In contrast, VC and branched oligomers are only found in the 30th cycle of the FEC-containing sample. We speculate that VC may be highly reactive and thus, rapidly being consumed to form other species in the initial formation cycles. However, after long-term cycling, a stable SEI forms and VC begins to accumulate in the electrolyte. The observed conversion of FEC to VC is also consistent with the mechanistic studies performed by Balbuena and co-workers using density functional theory and ab initio molecular dynamics simulations methods.¹²¹ The branched soluble oligomers detected in the cycled electrolyte appear to be similar to the species present in the insoluble portion of the SEI, but with shorter chain lengths (i.e. lower molecular weight species and higher solubility; they therefore saturate in the electrolyte and likely prevent further SEI dissolution). The soluble components may also serve as precursor for the insoluble SEI polymers. Another possibility is that the chemical structures of the soluble oligomers are different from the insoluble polymer as they are formed by different reactions. Certain pathways lead to short-chain oligomers, while other reactions form insoluble polymers.

The insoluble SEI products formed from the FEC-containing sample are consistent with ethylene oxides and carbonate species along with the minor structural features as follows: acetal carbons (with ¹³C chemical shift at 103 ppm), branched ethylene oxides (with ¹³C chemical shift at 75–85 ppm), and aliphatic carbons (with ¹³C chemical shift at 34 ppm), which are shaded in red, yellow and green, respectively (Scheme 3.3, top). The observation of ethylene oxides and carbonate species is consistent with prior NMR,⁴⁹ XPS^{41,122} and FTIR studies¹²³.

Scheme 3.3 summarizes the possible reduction reactions of FEC, which are based on the species detected in this study and prior experimental and theoretical work. First, FEC is defluorinated, forming an EC• radical (denoted as radical A) and LiF (Scheme 3.3.1), as proposed by Nie.⁴² As fluorinated carbon species are not detected by solution or solid-state NMR (Figure A.7), we suggest that FEC defluorinates prior to further reaction. At this stage, the formed EC radical can abstract hydrogen from other species in solution and convert back

to EC. Alternatively, the EC radicals can disproportionate to form VC and EC. Experiments using mass spectrometry in conjunction with additional NMR to compare decomposition products using unlabelled and ^{13}C -labelled EC and FEC are currently underway in our laboratory to determine which reaction pathway is occurring and will be reported in a future study. If the EC radicals disproportionate to form VC and EC in the LP30 + $^{13}\text{C}_3$ FEC sample, the $^{13}\text{C}_3$ -labelled EC that is generated can be reduced as suggested in Scheme 3.2 and subsequently contribute to the PEO-type signal that is detected in ^{13}C ssNMR (Figure 3.5a).

Radical A is identical to the radical that results from EC via H abstraction. However, although its existence has been proposed, such cyclic EC radicals have not been experimentally observed in the absence of FEC or VC, even under cryogenic conditions (77 K) during the irradiation of EC.¹¹⁴ The inability of EC to form such an EC radical may be one explanation for the difference in the decomposition products seen with EC and FEC. Once formed, radical A can lose hydrogen to form VC, otherwise, radical A can lose CO_2 , forming the vinoxyl radicals as shown in Scheme 3.3.1. Due to resonance, there are two forms of the vinoxyl radicals: one with the radical centre on the carbon ($\text{CH}(\text{=O})\text{CH}_2\bullet$, radical B) and the other with the radical centre on the oxygen ($\bullet\text{OCH}=\text{CH}_2$, radical C). While the vinoxyl radicals have not been directly detected in this work, such radicals have been observed in a radiolysis experiment on FEC and were proposed to initiate the formation of highly cross-linked polymers.¹²⁴ Because our NMR results only revealed stable vinoxyl species instead of unstable vinoxyl radicals, we now propose possible reaction schemes that result in the formation of vinoxyl species as well as some branched units with predicted chemical shifts similar to those observed experimentally (Scheme 3.3.2–Scheme 3.3.8). Vinoxyl species can, for example, be formed by the vinoxyl radicals (either B or C) attacking the sp^2 hybridized carbon in VC. When radical B reacts with VC (Scheme 3.3.2), it can form a structure that contains an aldehyde terminal group, an aliphatic carbon, and a branched ethylene oxide (shaded in blue, green and yellow, respectively, with corresponding NMR parameters given). If VC reacts with radical C (Scheme 3.3.3), the radical will be transformed into a stabilized carbon radical, which has a branched acetal carbon (shaded in red) and an alkene termination. These newly formed radicals (in the form of $\text{RCH}\bullet\text{R}'$) can abstract H from other species in solution to stabilize themselves (forming $\text{RCH}_2\text{R}'$). Alternatively, these secondary radicals can then further react with the vinyl group in VC to form poly(VC).^{49,100,118}

Note that neither alkene units (^{13}C shifts at 120–140 ppm) nor aldehyde carbon (^{13}C shift at 200 ppm) are observed by ssNMR. We hypothesize that such terminations can be consumed by further reacting with the vinoxyl radical and resulting in chain elongation.¹²⁵ Such terminal groups would be present in very low quantities and therefore, below the detection limit of ssNMR. Furthermore, decomposition products that contain alkene terminal units can undergo reactions similar to those of VC (Scheme 3.3.4 and 3.3.5), forming a mixture of polymer products that is consistent with the cross-linked species detected in this study.

Interestingly, the chemical structures observed in solution can be rationalized by considering the radical attack of the aldehyde terminal group. When radical B reacts with a molecular species with an aldehyde group (Scheme 3.3.6), a new radical containing the vinoxyl units ($\text{CH}(\text{=O})\text{CH}_2\text{OR}$, shaded in blue) is formed. When the secondary radical formed in Scheme 3.3.5 attacks an aldehyde group (Scheme 3.3.7), a cross-link containing the acetal carbon forms ($\text{ROCH}_2\text{CH}(\text{OR})_2$, shaded in red). These two chemical units are consistent with the soluble products identified by solution NMR (Figure 3.3). It is speculated that the radical attack on the aldehyde group will lead to oligomers that have short-chain lengths and remain solubilized. In contrast, radical attack on the alkene terminal group is more likely to form higher molecular-weight polymers that are incorporated into the insoluble portion of the SEI.

The reduced EC intermediate (alkyl carbonate anion radical) can also react with the alkene carbon as illustrated in Scheme 3.3.8. The anion radical ($\text{RCH}_2\bullet$) that forms from reduced EC can attack the alkene group and graft the PEO chain to the decomposition products of FEC. If it occurs, this reaction also consumes the anion radicals and reduces the possibility of anionic polymerization of EC. In Scheme 3.3.8, $\text{R}\underline{\text{C}}\text{H}_2\text{R}'$ (shaded in green) could, in principle, originate from the decomposition of EC. To determine whether this reaction takes place, ^{13}C CP NMR of the SiNWs cycled in LP30 + $^{13}\text{C}_3$ EC + FEC (see Table 1 for electrolyte formulation) was performed. The resulting ^{13}C CP NMR spectrum shows an extra set of resonances that span the range of 15–40 ppm (Figure A.8). The presence of additional ^{13}C NMR peaks in the region of 15–40 ppm strongly suggests that FEC contributes to the formation of the aliphatic carbon signal and the result is consistent with the mechanism proposed in Scheme 3.3.8.

Although alkene termination is not directly observed in solid-state NMR, we speculate that sp^2 carbon/alkene termination is necessary to create the cross-linked polymer and may play an

important role in capacity retention in general. Recent reports indicate that novel additives, such as methylene ethylene carbonate that contain sp^2 hybridized carbons show promise for increasing capacity retention in LIBs.^{126,127} The SEI formed in the presence of FEC clearly shows cross-linked species, whereas the SEI formed in the standard EC/DMC electrolyte mainly contains linear PEO-type polymers, providing a molecular rationale for the observed increase in capacity retention in LIBs when FEC additive is used. Similar cross-linking units are also present as glycosidic linkages in natural polysaccharides, (which exhibit similar ^{13}C resonances at approximately 100 ppm¹¹¹) many of which have been successfully demonstrated as a binder for Si that improves capacity retention, further suggesting that this structural motif may impart stability to the SEI.^{128–130}

The mechanical properties of the branched polymer derived from FEC may be more elastic, which can accommodate the volume expansion that occurs in Si during cycling. Additional experiments are required to determine whether the polymers formed from FEC differ in their Li ion conductivity from the linear PEO-like species formed from EC and whether the reduced overpotentials seen on cycling in the presence of FEC are due to a thinner SEI or to improved Li transport.

3.5 Conclusions

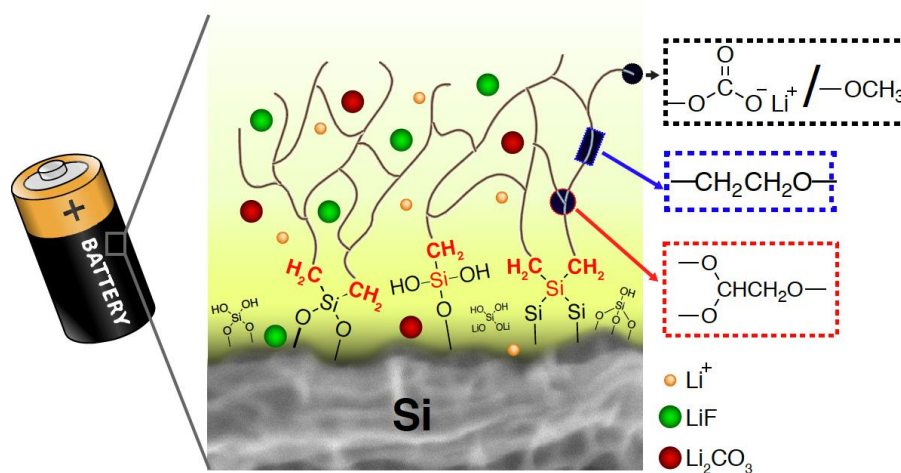
Organic species in the SEI on SiNWs were characterized by solution and solid-state NMR to understand the role of FEC as an electrolyte additive in performance enhancement in LIBs. After long-term cycling, the standard EC/DMC electrolyte decomposes and forms a variety of soluble oligomers in addition to the transient formation of LEDC. The addition of FEC into the electrolyte allows the formation of a stable SEI and suppresses the decomposition of EC/DMC, resulting in increased coulombic efficiency after the first few cycles. The ^1H and ^{13}C NMR spectra provide compelling evidence for the defluorination of FEC to form soluble vinoxyl species (HCOCH_2OR) and VC. Importantly, we emphasize that we have conclusively shown that FEC converts to VC instead of LVDC by ^1H NMR using ^{13}C -labeled FEC. Oligomers with characteristic peaks that can be assigned to protonated carbons bonded to two adjacent oxygen groups due to cross-linking units were also identified. These oligomeric precursors presumably

react further to form insoluble polymeric species in the SEI, with similar cross-linking groups. Neither these cross-linking units nor the vinoxyl species are observed in the absence of the FEC additive.

The vinoxyl species are signatures for the formation of the vinoxyl radicals that are believed to initiate the polymerization that eventually results in a highly cross-linked network.¹²⁴ While the study of Shkrob et al. focused on the reduction products of FEC alone,¹²⁴ we too, detect similar vinoxyl species and cross-linking motifs when FEC is used as an additive in EC-containing electrolytes. Based on our NMR results, we find that the stepwise elimination of CO₂ results in a polymeric species that contains a mixture of aliphatic units (¹³C shifts at 34 ppm) and cross-linking motifs (¹³C shifts at 103 ppm) similar to poly(VC), with several regions of PEO-type structures (¹³C shifts 72–65 ppm). Overall, FEC breakdown products (e.g. increased population of cross-linking moieties) lead to a suppression of soluble, linear PEO-type polymeric products that occur in the standard cycled LP30 electrolyte.

It is speculated that the formation of cross-linked polymer is key to the higher stability of SEI formed on Si anodes in the presence of FEC, motivating studies with additives that may promote cross-linking. Further insight into the molecular nature of the SEI and the parameters that impart stability offer the opportunity to tailor the SEI chemistry to maximize performance in LIBs.

Chapter 4 Probing the interfacial structure between the SEI and the Si anode



4.1 Introduction

In this chapter, 1 M LiPF₆ in either pure FEC or VC electrolytes without EC are prepared for studying their decomposition mechanisms. Solid electrolyte interphase (SEI) formed in these pure FEC and VC electrolytes are characterized by conventional and DNP-enhanced solid-state NMR. The structure-performances relationship is found for the organic SEI and Si anodes: heterogeneous cross-linked polymers are formed during the reduction of FEC and VC, which consist of cross-linked PEO-type polymers and aliphatic chains, and the presence of the highly cross-linked polymers correlates with good capacity retention. The interfacial region between the SEI and Si surface is also revealed for the first time by NMR spectroscopy.

4.2 Experimental

Coin cells: SiNWs were grown by chemical vapor deposition (CVD) as described previously.⁹⁰ ¹³C₃-labelled FEC was synthesized by using a previously reported procedure.¹³¹ Li half-cells were then assembled with the SiNWs electrodes in 2032-type coin cells, using the freshly prepared electrolytes listed in Table 1. Borosilicate glass fiber was used as the separator and around 10 drops (~0.15 mL) of electrolyte were used for each cell. Coin cell assembly was carried out in an Ar filled glovebox (H₂O < 0.1 ppm, O₂ < 0.1 ppm). The coin cells were discharged/charged at room temperature at a constant current (C/30, 120 mA/g) between 0.001 V – 2 V vs Li/Li⁺ for the first cycle using a Biologic VSP, MPG-2 or Lanhe (Wuhan, China) battery test systems. After the first cycle, the coin cells were then cycled at C/10 (360 mA/g). Approximately 30 days were needed to complete 50 cycles. After cycling, the cells were disassembled in the glovebox and the SiNW electrodes were dried under vacuum overnight (~16-20 h) to remove excess electrolyte solvents without rinsing.

Table 4.1 Electrolyte formulations with 1 M LiPF₆ in different solvent mixtures

Electrolyte solvents	Abbreviation
EC/DMC = 50/50 (v/v)	LP30
EC/DMC/FEC = 45/45/10 (v/v/v)	LP30 + FEC
FEC (fluoroethylene carbonate)	FEC
VC (vinylene carbonate)	VC
FEC/ ¹³ C ₃ FEC = 95/5 (v/v)	¹³ C ₃ FEC

Solid-state NMR measurements (¹H, ¹³C) were performed at 11.7 T with a Bruker Avance III spectrometer equipped with a 2.5 mm probe-head at a MAS speed of 30 kHz for ¹H NMR spectra and 10 kHz for ¹H–¹³C CP NMR spectra. The $\pi/2$ pulse lengths were 2.7 μ s for ¹H. The chemical shifts of ¹H, ¹³C were referenced with adamantane (¹H at 1.87 and ¹³C at 38.6 ppm). Between 64–256 transients were collected using recycle delays of 15 s for ¹H experiments. ¹H–¹³C CP NMR spectra were acquired with a CP contact time of 2 ms, a recycle delay of 3 s and 21k – 28k scans. RF nutation frequencies were (¹H) 92.5 kHz (50-100% linearly ramped during CP), (¹³C) 82.5 kHz, and SPINAL64⁸³ (¹H) decoupling at 80 kHz. ¹³C direct excitation of ¹³C₃

FEC 100 sample was measured with recycle delay of 60 s and 5648 scans over the duration of 102.5 hours.

DNP NMR experiments were performed on a 14.1 T Bruker Avance III HD spectrometer with a 395 GHz gyrotron microwave source and using a 3.2 mm triple resonance wide-bore probe at the Nottingham DNP MAS NMR Facility. The sample transfer and preparation procedure have been described before,¹³¹ with the exception that a radical solution of 16mM TEKPol dissolved in 1,1,2,2-tetrachloroethane (TCE) instead of dichlorobenzene was used to achieve better signal enhancement. The sample mass, dilution ratio of KBr and the volume of radical solutions are listed in Table 4.2.

Table 4.2 Summary of the DNP NMR samples

Sample No.	Sample description	Sample mass (mg)	KBr (mg)	Radical solution	Radical volume (μL)	^1H $\epsilon_{\text{on/off}}$
1	FEC30	5.7	13.0	16 mM TEKPol in TCE/d-	4.0	5
2	FEC50	6.2	18.0	16 mM TEKPol in TCE/d-TCE	4.0	16
3	$^{13}\text{C}_3\text{FEC10}$	4.0	15.0	16 mM TEKPol in TCE/d-TCE	4.0	3
4	VC50	5.0	15.0	16 mM TEKPol in TCE/d-TCE	4.0	13
5	LP30, 50	9.5	24.0	16 mM TEKPol in TCE	6.0	16
6	LP30, 1 st	5.4	14.7	16 mM TEKPol in TCE	3.5	16
7	FEC, 1 st	8.1	21.0	16 mM TEKPol in TCE	5.0	6
8	VC, 1 st	6.6	17.0	16 mM TEKPol in TCE	4.0	10

^1H - ^{13}C CP and ^1H - ^{29}Si CP DNP NMR spectra were acquired with a 90–100% ramped contact pulse⁹³ on the ^1H channel and 100 kHz ^1H decoupling using swept frequency two pulse phase modulation (SW_f -TPPM)⁹⁴ sequence with MAS frequency of 12.5 kHz. The relaxation delay was 3-4 s, and the CP contact time 2 ms for ^{13}C and 5 ms for ^{29}Si . ^{29}Si DNP direct excitation spectrum was acquired using high powder proton decoupling with a recycle delay of 10 s and 3072 scans at a spinning speed of 12.5 kHz.

Double quantum (DQ)–single quantum (SQ) ^{13}C – ^{13}C dipolar correlation spectra were acquired using POST-C7⁸⁴ for DQ excitation and reconversion at a MAS rate of 8 kHz. The mixing time is 2 ms. Proton decoupling was achieved by a SW_f-TPPM sequence with 100 kHz RF amplitude on the ^1H channel. 256 transients were recorded for each of 128 complex points interleaved, by using a 2 s of recycle delay for the recovery of ^1H magnetization.

^1H – ^{29}Si HETCOR spectra were measured using 5 ms contact time, continuous wave Lee Goldberg (CWLG) proton decoupling, 2048 scans per slice with 32 increments and a recycle delay of 3 s with MAS frequency of 12.5 kHz.

4.3 Results

4.3.1 Electrochemistry

The electrochemical performance of SiNWs cycled in Li half-cells using the electrolytes listed in Table 4.1 are shown in Figure 4.1. The features in the first discharge/charge curves of the SiNWs in Figure 4.1a are similar to one another, indicating that pure FEC and pure VC based electrolytes do not affect the Si lithiation and delithiation mechanisms. However, the corresponding dQ/dV plot in Figure 4.1b reveals that FEC and VC are preferentially decomposed as early as 1.3 V vs. Li/Li^+ , whereas LP30 electrolyte decomposition starts around 0.8 V. The process at around 0.2 V is due to the lithiation of gold, which is used as a catalyst for SiNWs growth. In the 50th cycle (Figure 4.1c), both the pure FEC and VC samples maintain similar voltage curves with the characteristic Si de/lithiation plateaus. However, the voltage profile of the LP30 sample shows a lower lithiation voltage (0.24 V vs. Li/Li^+) than the SiNWs cycled in pure FEC and VC electrolytes (~0.35 V), with the lower lithiation voltage reflecting an increase in resistance, which may come from the reduced porosity of the electrodes and a thicker SEI.⁴⁸ The delithiation voltage curves are similar for all three samples in the 0–0.42 V range, but after this point they begin to diverge, as manifested in a change in the peak intensity around 0.42–0.70 V in the dQ/dV plots (Figure 4.1d). A lower delithiation capacity is obtained

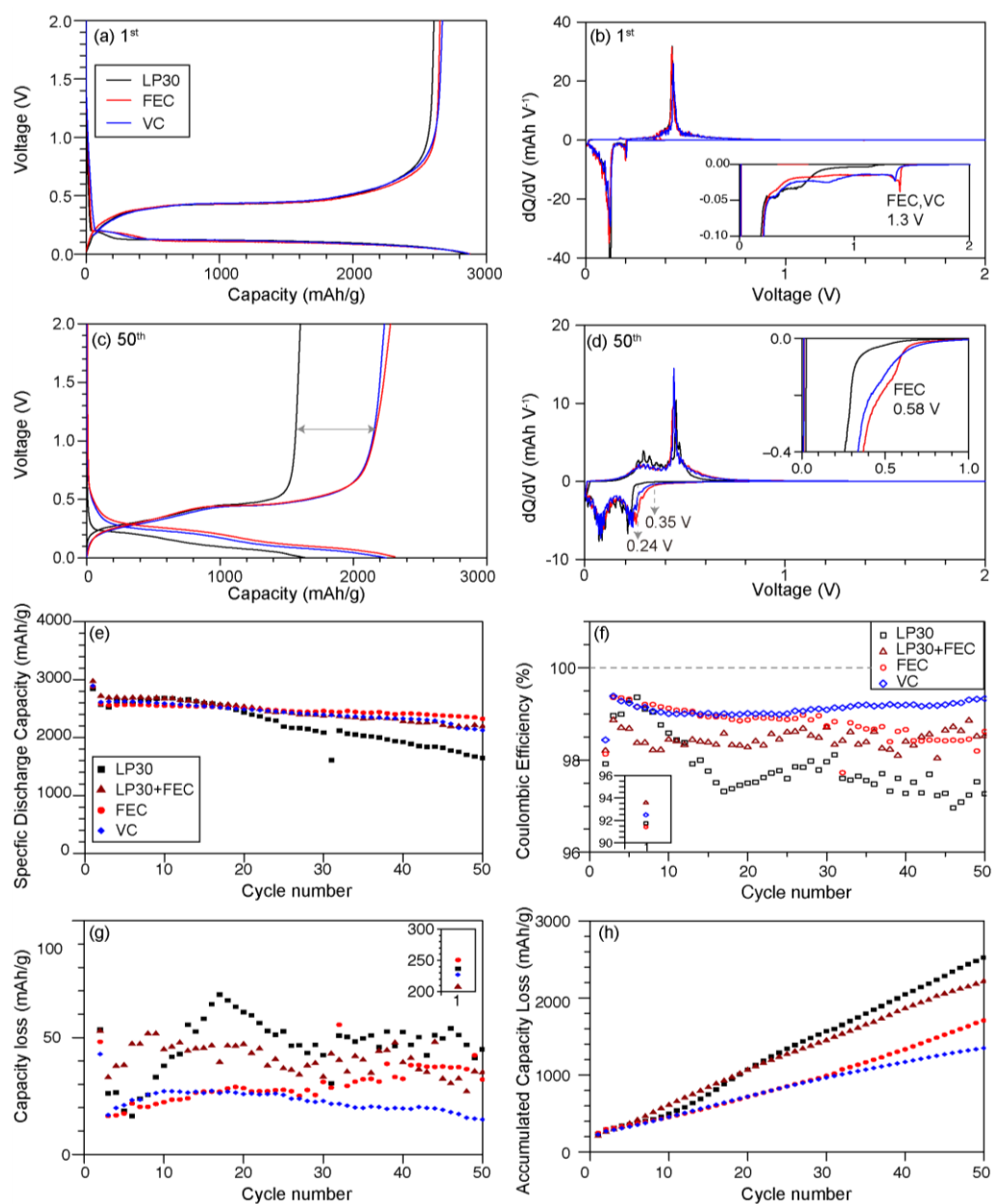


Figure 4.1. Electrochemistry of SiNWs cycled in standard LP30, LP30 + 10 vol % FEC, and 1 M LiPF₆ in FEC or VC, electrolytes (colored in black, dark red, red and blue, respectively). The voltage profiles and the dQ/dV curves of the SiNWs at the 1st cycle (a-b) and the 50th cycle (c-d) for LP30, FEC and VC. Discharge/lithiation capacity versus cycle number (e) and the corresponding Coulombic efficiency (CE) during cycling (f) for all four electrolytes. The initial CE is shown in the insert in (f). Capacity loss (defined as the lithiation capacity minus the delithiation capacity) during each cycle (g) and accumulated capacity loss versus cycle number (h). The capacity loss of the 1st cycle is shown in the insert in (g). The legend in (g-h) is the same as in (e). Cells were cycled at C/30 for the 1st cycle, then at C/10 for later cycles between 0.001 V – 2 V.

in the LP30 sample after 50 cycles than with pure FEC and VC electrolytes in this voltage range, as seen in Figure 4.1c; this may again be related to the transport properties and resistance of the SEI as suggested by the work of Michan et al.⁴⁸, which showed that most of the capacity could be regained when the cells containing LP30 only were cycled at extremely low rates.

In general, SiNWs cycled with FEC or VC-containing electrolytes show improved capacity retention when compared to standard LP30 electrolytes without any additives (Figure 4.1e). After 50 cycles, the LP30 sample retains only 58% of the initial capacity; whereas, cells cycled with FEC or VC based electrolytes retain 73–81% of their initial capacities (see Table B.1 in Appendix B for details). The Coulombic efficiencies (CE) (defined as the delithiation capacity versus lithiation capacity) of SiNWs cycled in FEC- and VC- containing electrolytes show marked differences (Figure 4.1f). SiNWs cycled with pure VC show the highest average CE of 99.1% from the 2nd to the 50th cycle. FEC-containing samples exhibit a slightly lower average CE of 98.8% with pure FEC and 98.4% for LP30 + FEC sample. Yet, both FEC-containing samples are higher than the standard LP30 sample (97.8%). The CE provides a measure of the irreversible reactions that occur during each cycle (e.g. Li⁺ and/or solvent consumption), the higher the CE, the more reversible the reaction is. The CEs of FEC and VC samples, while noticeably improved over those in LP30 electrolytes, are still less than 99.5%. Pure FEC and VC electrolytes outperform the LP30 based electrolyte, as their capacity loss during each cycle (i.e. the lithiation capacity minus the delithiation capacity) and the accumulated capacity losses across multiple cycles are all smaller than LP30 samples (Figure 4.1g and h).

¹³C₃ labelled FEC is synthesized and prepared as an electrolyte (1M LiPF₆ in FEC/¹³C₃ FEC) for cycling with SiNWs and for further NMR studies. The electrochemical performance of ¹³C₃ FEC sample is shown in Figure B.1 and it exhibits similar capacity retention to the ¹³C natural abundance FEC and LP30+FEC samples. The electrochemical results suggest that the cells containing the ¹³C₃ FEC synthesized as part of this study are representative of cells cycled in pure (non-enriched) FEC electrolytes.

Additional electrochemical impedance spectroscopy data (Figure B.2) and rate performance data (Figure B.3) also suggest that the SEI formed in FEC has a higher Li⁺ conductivity than those formed in LP30 electrolyte. Further chemical analysis was then carried out to understand the observed electrochemical differences.

4.3.2 Organic SEI components revealed by ^1H and ^{13}C ssNMR

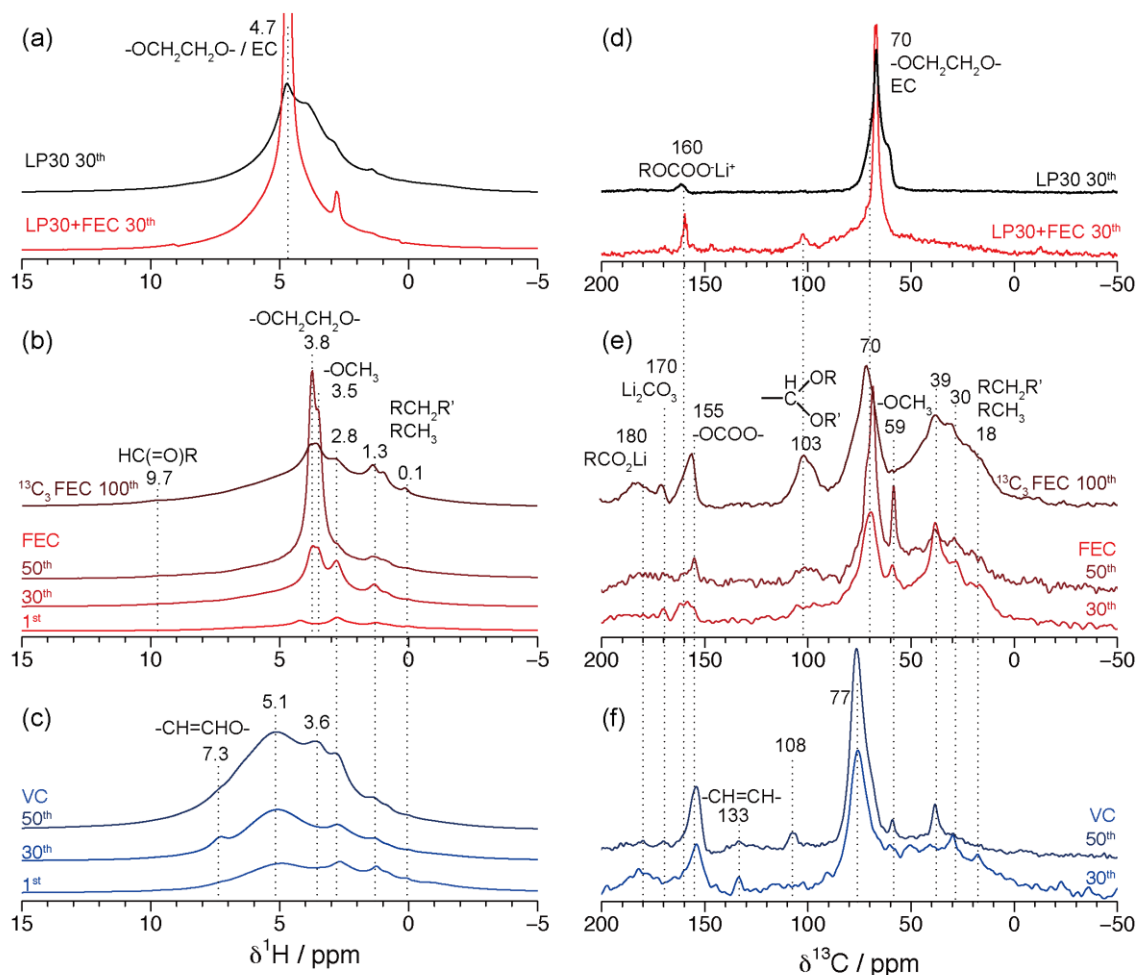


Figure 4.2. ^1H MAS NMR spectra (a-c) and ^1H - ^{13}C CP MAS NMR spectra (d-f) of SiNWs cycled in LP30, LP30 + 10 vol% FEC, pure FEC and VC electrolytes for the 1st, 30th and 50th cycle. Spectra of SiNWs cycled in 95% natural abundance FEC+5 vol% $^{13}\text{C}_3$ FEC for 100 cycles are included in (b, e). All spectra were measured at room temperature using conventional ssNMR.

Figure 4.2 shows the ^1H and ^1H - ^{13}C CP NMR spectra of SiNWs cycled in all the electrolyte formulations after the first, 30 and 50 cycles in the delithiated state. The results and assignments for the LP30 and LP30 + FEC system have been discussed in detail previously¹³¹, but are included here to facilitate comparison with the pure FEC and VC systems. For SiNWs cycled in the standard LP30 electrolyte with and without 10 vol% FEC (Figure 4.2a and d), the organic SEI mainly consists of PEO-type polymeric species ($-\text{CH}_2\text{CH}_2\text{O}-$) as indicated by both the

prominent ^1H and ^{13}C resonances at 4.7 ppm and 70 ppm, respectively.^{47,48} On adding 10 vol% FEC, an extra ^{13}C resonance at approximately 103 ppm is seen (Figure 4.2d), which is assigned to a cross-linking acetal carbon ($\text{R}\underline{\text{C}}\text{H}(\text{OR}')_2$) moiety.¹³¹

Similar to the LP30 + FEC sample, ^{13}C NMR spectra of SiNWs cycled in pure FEC and VC (Figure 4.2e and f) also contain acetal carbons (100–108 ppm) and ethylene oxide carbons (70–77 ppm), consistent with the presence of cross-linked PEO-type polymers and the formation of poly(VC)-like polymers. However, although both FEC and VC induced SEIs show a beneficial effect in terms of the capacity retention of the Si electrode, the chemical compositions of FEC- and VC-derived polymers are not identical.

The acetal carbons in VC and FEC samples have ^{13}C chemical shifts at 108 and 103 ppm, respectively. Based on the prior study by Leifer and coworkers⁵⁶, the chemical shift is influenced by the R group in the acetal carbon, the 108 ppm in the VC sample being tentatively attributed to an acetal carbon connected to a cyclic R group, potentially in a poly(VC) type cross-linking species⁴⁹; the 103 ppm component of the broader peak in the FEC sample is likely an acetal carbon bound to linear R groups, with the FEC samples also containing the higher frequency peak but in smaller proportions. Note that small differences in chemical shifts will also likely result from differences in the nearby chemical species and from different polymer conformations. The assignments of these shifts to acetal carbons is validated by DFT NMR shift calculations described in the Appendix B.7, which were performed to explore the effect of different functional groups on the carbon shifts.

The presence of poly(VC) in the VC samples is supported by the ^1H and ^{13}C NMR of the ethylene oxide region: the most intense ^{13}C peak of the pure VC sample (77 ppm) is 7 ppm higher in frequency than that of the FEC sample (Figure 4.2e and 2f) indicating a more strained polymer (e.g. poly(VC)^{36,49}) is present. The ^1H NMR shows a similar trend: the main broad peak is at around 5.1 ppm for pure VC samples (Figure 4.2c), yet the primary ^1H resonance is observed at approximately 3.8 ppm for FEC samples (Figure 4.2b). The broad 5.1 ppm peak is assigned to a proton on branched ethylene oxide ($-\text{C}\underline{\text{H}}\text{O}-$) in poly(VC), consistent with the solution NMR result reported by Ota et al.⁴⁶ Note that the broad peak in ^1H NMR at around 5.1 ppm in the VC sample can also arise from vinylic protons ($\underline{\text{H}}\text{C}=\text{CR}_2$), but such an alkene carbon is only present in small amounts in the ^{13}C NMR spectra.

In contrast to the LP30-containing systems, SEIs produced from pure FEC or VC contain a higher concentration of aliphatic species, as indicated by the ^{13}C resonances between 0–40 ppm (Figure 4.2e and 2f). Aliphatic carbons can be formed by reducing FEC and VC, with the release of CO_2 gas (see discussion for more details) and involve reactions of more than one FEC/VC molecule. Methoxide groups ($\text{RO}\underline{\text{C}}\text{H}_3$) are also seen for all the FEC and VC samples, which are manifested as a ^1H peak at 3.5 ppm and a sharp ^{13}C peak at 59 ppm and are correlated to one another in the ^1H – ^{13}C heteronuclear correlation (HETCOR) spectrum (Figure B.8). The assignment is further supported by the narrow peak width of the 59 ppm ^{13}C NMR resonance, where the relatively sharp peak can be explained by motional averaging due to fast rotation of the methoxide group.

In order to improve the signal to noise ratio in the ^{13}C NMR spectra of ^{13}C natural abundance samples, DNP NMR was used to compare the SEIs formed in LP30, FEC, and VC electrolytes after 50 cycles (Figure 4.3a). With a signal enhancement of around 15 for each sample, ^1H – ^{13}C CP DNP NMR reveals the finer details concerning the polymeric species in the 100–200 ppm region. Figure 4.3a shows that sp^2 -hybridized carbon species ($-\text{CH}=\text{CH}-$) with ^{13}C resonances in the range of 120–140 ppm are present in both FEC and VC samples (shaded in grey), but not in the LP30 sample. SiNWs cycled in FEC contain additional aldehyde carbons ($\text{H}\underline{\text{C}}(=\text{O})\text{R}$) with a ^{13}C resonance at 210 ppm. Lithium carboxylate species ($\text{R}\underline{\text{C}}\text{OO}^-\text{Li}^+$) with a ^{13}C resonance around 180 ppm are also more pronounced in the FEC sample. Both FEC and VC samples contain an intense ^{13}C NMR peak at 155 ppm and a weak signal at 170 ppm that can be assigned to alkyl carbonate ($\text{RO}\underline{\text{C}}\text{OOR}'$) and Li_2CO_3 , respectively.¹¹² For the LP30 sample, the intense ^{13}C peak at 160 ppm is assigned to lithium alkyl carbonate ($\text{RO}\underline{\text{C}}\text{OO}^-\text{Li}^+$), likely from the terminal carbonate species found in linear oligomers or polymer chains.⁴⁷ In short, ^{13}C DNP NMR shows that, apart from the cross-linked PEO polymer, the organic SEIs derived from FEC and VC also contain lithium/alkyl carbonates and additional small amounts of unsaturated carbons.

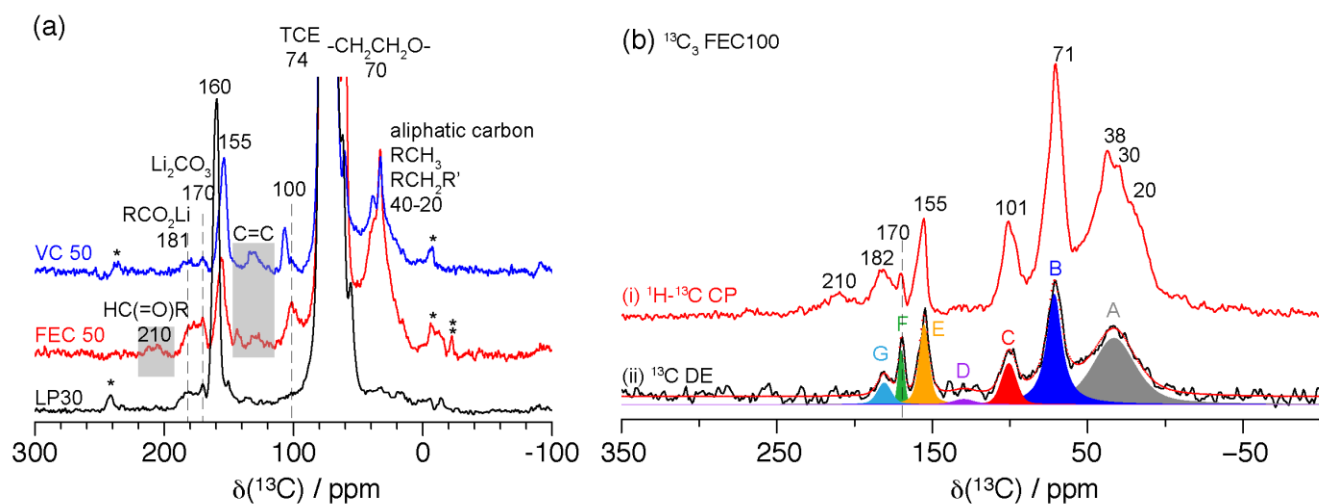


Figure 4.3. (a) ^1H - ^{13}C CP DNP NMR (105 K) spectra of SiNW cycled in LP30 (black), FEC (red) and VC (blue) for 50 cycles, where the intense (truncated) peak at 74 ppm is due to the DNP solvent tetrachloroethane (TCE); * = spinning sidebands. (b) Conventional, room temperature ^{13}C CP NMR of SiNW cycled in FEC + 5% $^{13}\text{C}_3$ FEC for 100 cycles (i) measured by ^1H - ^{13}C CP, (ii) measured by ^{13}C direct excitation (DE) with a recycle delay of 60 s to extract quantitative information.

^{13}C NMR spectra were also recorded for SiNWs cycled with ^{13}C -enriched electrolyte (FEC + 5 % $^{13}\text{C}_3$ FEC after 100 cycles, abbreviated as $^{13}\text{C}_3$ FEC100) using room-temperature NMR techniques (Figure 4.3b). The ^1H - ^{13}C CP NMR spectrum (Figure 4.3b, i) of $^{13}\text{C}_3$ FEC100 is comparable to the spectrum of SiNWs cycled in FEC for 50 cycles (FEC50) obtained using DNP NMR (Figure 4.3a). The striking resemblance between the spectra of FEC50 and $^{13}\text{C}_3$ FEC100 suggests that the chemical units of the organic SEI formed in FEC from the 50th to the 100th cycle are chemically similar, indicating that the chemical units of the polymeric SEI are stable during cycling at this point, though the SEI thickness may vary. Although no quantitative comparisons of these spectra were performed, we did not see any significant alteration in the chemical species found in the SEI, following the preparation of the sample for the DNP experiment, though it is possible that some of the organic components may dissolve in the TCE solvent used for DNP experiments.

Quantitative information about the organic SEI in the $^{13}\text{C}_3$ FEC100 sample is obtained from direct excitation (DE) room-temperature ^{13}C NMR spectra (Figure 4.3b, ii). The integrated intensities of the deconvoluted peaks are summarized in Table 4.3. The organic species in the $^{13}\text{C}_3$ FEC100 sample primarily consist of aliphatic moieties (41% of the total peak area) and

PEO-type oligomers (30%). Relatively small concentrations of alkyl carbonate (11%), carboxylate (4%) and lithium carbonate (4%) species are also present in the SEI. The quantitative ^{13}C NMR spectrum suggests that the branching units (acetal carbons, **C** in Table 4.3) account for 8% of the total integral of the spectrum, indicating that the polymers are highly cross-linked. Peak **D** at 128 ppm (Figure 4.3b, ii), which is attributed to alkene carbons, is also present in the deconvoluted spectrum and it is consistent with the DNP NMR spectra of FEC and VC samples (Figure 4.3a). Note that such alkene species are also observed as soluble products in the cycled FEC and VC electrolyte (Figure B.5). The unsaturated carbon units are likely the base units for polymerization.^{100,131}

Table 4.3. Summary of the intensity and assignments of the peaks obtained by deconvolution of the ^{13}C direct excitation ssNMR spectrum of the $^{13}\text{C}_3$ FEC sample

Label	Peak centre / ppm	Peak width/ppm	Relative Intensity (%)	Assignment
A	33.1	32.2	41	$\text{R}\underline{\text{C}}\text{H}_2\text{R}'$
B	71.5	11.6	30	$-\text{CH}_2\underline{\text{C}}\text{H}_2\text{O}-$
C	100.7	11.4	8	$\text{R}\underline{\text{C}}\text{H}(\text{OR}')_2$
D	129.7	15.9	2	$\text{R}\underline{\text{C}}\text{H}=\underline{\text{C}}\text{HR}'$
E	155.3	7.3	11	$\text{RO}\underline{\text{C}}\text{O}_2\text{R}'$
F	169.9	4.4	4	$\text{Li}_2\underline{\text{C}}\text{O}_3$
G	180.9	10.4	4	$\text{R}\underline{\text{C}}\text{O}_2\text{Li}$

4.3.3 Molecular fragments in the organic SEI

To establish the connectivity between distinct chemical motifs observed in the organic SEI, we performed a 2D double-quantum single-quantum (DQ–SQ) ^{13}C homonuclear dipolar correlation experiment using POST-C7 with DNP enhancement on the $^{13}\text{C}_3$ FEC100 sample (Figure 4.4). In this spectrum, two spins with resonance frequencies ν_1 and ν_2 result in a correlation at $\nu_1 + \nu_2$ in the indirect dimension of the 2D spectrum if they are coupled through space. Here, the spectrum mainly shows one-bond carbon-carbon correlations. Three broad

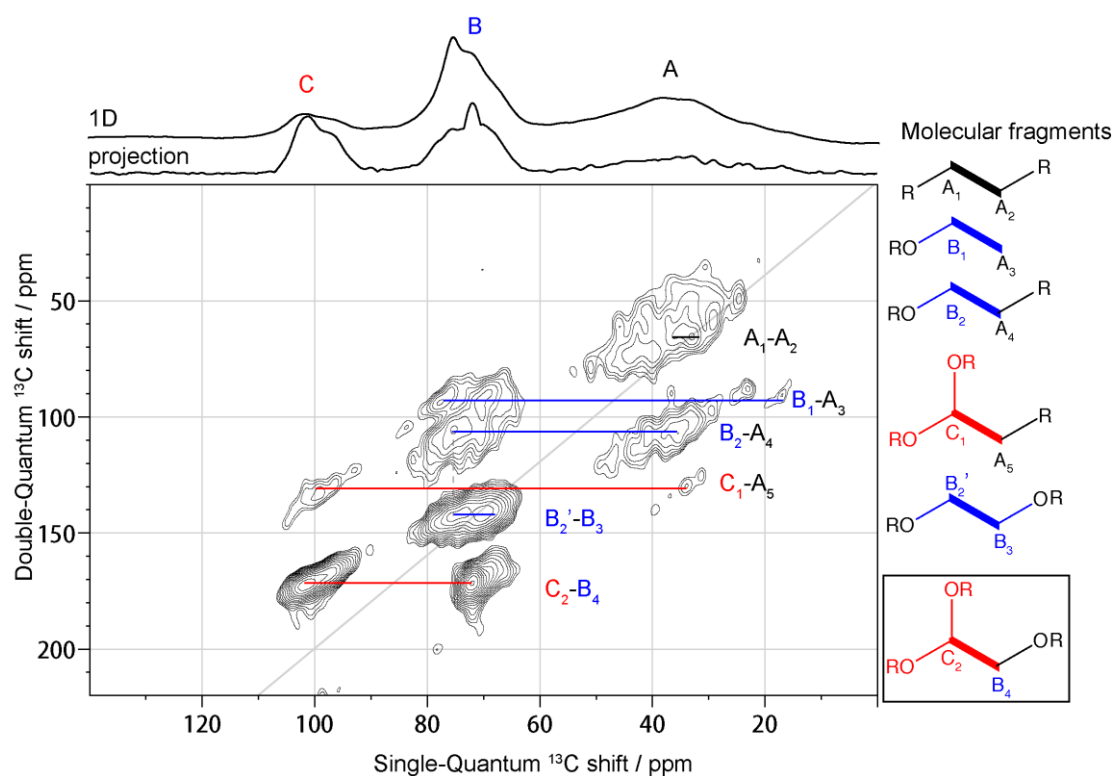
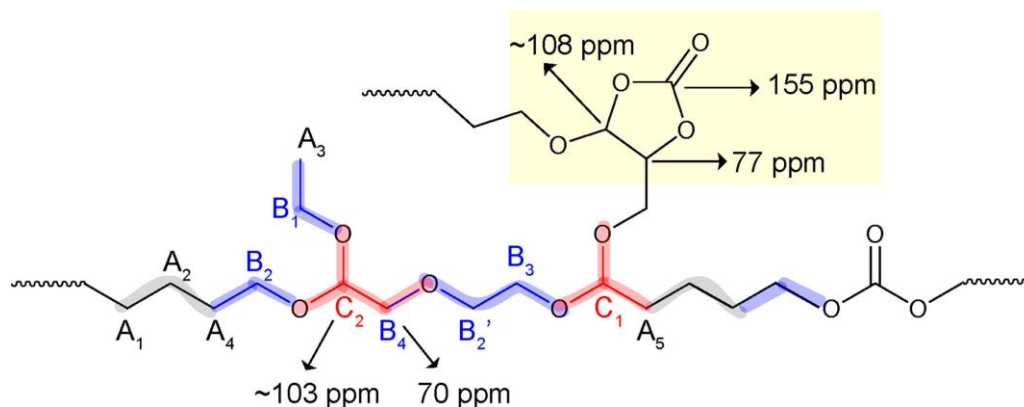


Figure 4.4. DNP enhanced 2D DQ – SQ ^{13}C – ^{13}C POST-C7 dipolar correlation spectrum of SiNW cycled in FEC+ 5% $^{13}\text{C}_3$ FEC for 100 cycles. 1D ^1H - ^{13}C CP NMR and the total projection in the SQ dimension are overlaid on top. The corresponding molecular fragments are listed on the right panel. The branching fragments are colored in red; the fragments containing ethylene oxide carbons are colored in blue and the alkyl chains in black.

peaks are observed in the ^{13}C spectrum with spectral ranges of 10 – 40 ppm, 60 – 85 ppm and 90 – 110 ppm, which are labelled **A**, **B** and **C**, respectively, consistent with the labelling scheme shown in Table 4.3. **A** is assigned to alkyl groups, **B** is attributed to PEO-type ethylene oxide carbons⁴⁷ ($-\text{CH}_2-\underline{\text{C}}\text{H}_2\text{O}-$) in linear and branched moieties, and **C** mainly arises from an acetal carbon with two oxygen bound to it ($-\underline{\text{C}}\text{H}(\text{OR})_2$)^{48,56,131}. Possible molecular fragments based on the one-bond correlations are depicted on the right panel in Figure 4.4. The strongest correlation observed is between **B**₄ and **C**₂, followed by **B**₂' and **B**₃. The **B**₂' – **B**₃ correlation is assigned to connections between ethylene oxide fragments ($-\text{O}\underline{\text{C}}\text{H}_2\underline{\text{C}}\text{H}_2\text{O}-$) that are found in PEO-type polymers.⁴⁹ The strongest **B**₄ – **C**₂ correlation indicates that acetal carbon **C** is directly bound to a PEO-type ethylene oxide carbon **B**, which provides strong evidence that the acetal carbon **C** is, indeed, a branching unit in the PEO-type polymer. Note that **B**₄ has a ^{13}C shift of 72 ppm (see Table B.3 for all the correlation peaks in Figure 4.4), which can be assigned to a linear ethylene oxide (EO) carbon instead of a branched EO unit ($-\text{CH}_2\underline{\text{C}}\text{HRO}-$,

Scheme 4.1. Possible molecular fragments observed in the FEC/VC decomposition products. The cyclic region is highlighted in yellow, the branching units are colored in red, ethylene oxide units in blue and alkyl chains in grey. Carbons labelled with A- C are consistent with the results from the 2D carbon correlation NMR experiment shown in Figure 4. The ^{13}C NMR shifts are derived from Figures 2e and f. The relative concentrations of the different species vary between the SEIs formed with different electrolytes.



with ^{13}C shift around 77 ppm)¹³². Moreover, the **B₄ – C₂** fragment ((RO)₂CH-CH₂OR') has the same connectivity as that of a soluble decomposition product we previously identified in the cycled LP30 + FEC electrolyte¹³¹ (the structure is highlighted in the box in Figure 4.4). In the presence of FEC, the **B₄ – C₂** branched molecular fragment is found in both the soluble degradation products and in the insoluble component; it appears to be a unique decomposition product from FEC that is absent in standard LP30 electrolyte.

Weaker **A – B**, **A – A** and **A – C** correlations are also observed, the latter being assigned to acetal carbons connected to aliphatic groups. Within the broad peak **A**, the **A₃** environment with ^{13}C resonance at 18 ppm is assigned to a terminal methyl group (CH₃)⁴⁷, while other **A** sites with ^{13}C shifts spanning from 30–40 ppm arise from other alkyl groups (CH₂R, CHR₂, CR₃). The **A₁ – A₂** correlations correspond to the connections within aliphatic carbon chains, while the **A₃ – B₁** and **A₄ – B₂** peaks correspond to PEO-type carbons being bound to aliphatic carbons.

Aliphatic carbons (**A**) are the major species in the organic SEI (Table 4.3), but its correlations to other peaks are weaker than the correlations for **B – C** and **B – B** in Figure 4.4. The aliphatic carbon chain with **A – A** correlation is less pronounced probably due to its formation pathway that involves more than one molecular fragment. Since only 5 vol % $^{13}\text{C}_3$ FEC is used in the

electrolyte, the probability of finding two ^{13}C labelled spin pairs in aliphatic chains is largely decreased.

A possible molecular fragment containing the correlations observed in Figure 4.4 is depicted in Scheme 4.1. The branching units are shaded in red, ethylene oxide chains in blue and alkyl carbons in grey. Characteristic ^{13}C NMR shifts observed in the cycled FEC/VC sample (Figure 2e and f) are also tentatively assigned in this structure. The structure also contains a cyclic acetal unit highlighted in yellow, but the poly(VC) found to a larger extent in the VC samples is not shown. In part due to the low enrichment level (5% $^{13}\text{C}_3$ FEC in the electrolyte) and dipolar truncation, multiple-bond correlations were not obtained. Nevertheless, various one-bond correlations detected in the system reflect the heterogeneous polymeric structure that is formed.

4.3.4 Lithiated and fluorinated components in the SEI

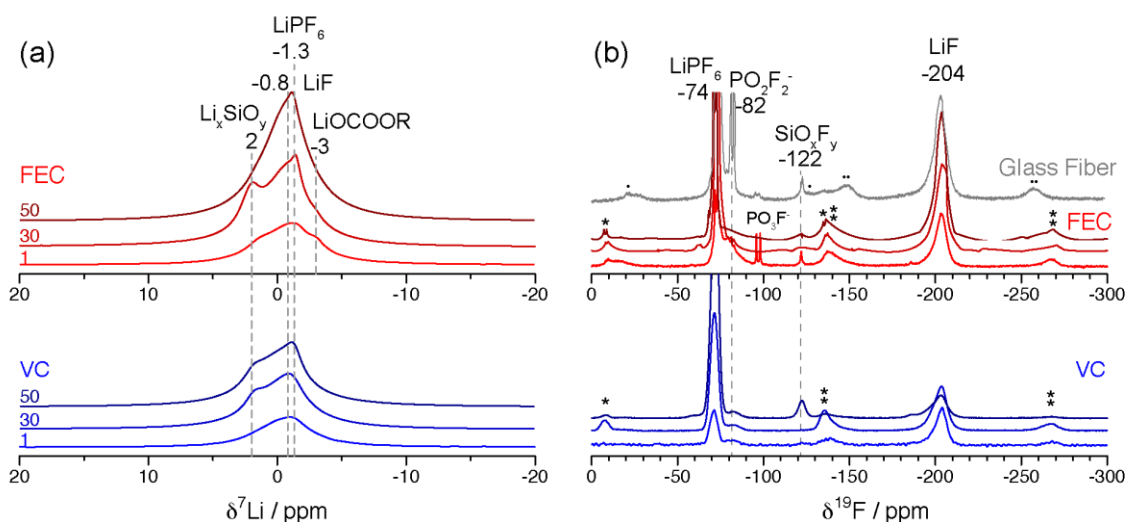


Figure 4.5. ^7Li and ^{19}F ssNMR spectra of SiNWs cycled 1M LiPF_6 in pure FEC or VC electrolytes after 1st, 30th and 50th cycles measured at MAS speed of 30 kHz. The grey line in (b) is ^{19}F NMR spectra of glass fiber separator after 50 cycles in FEC electrolytes measured at MAS of 25 kHz. Spinning sideband are marked with asterisks and dots.

Inorganic Li salts are also observed by ^7Li and ^{19}F ssNMR (Figure 4.5). For all FEC and VC samples, LiF is observed as a distinct peak at -204 ppm in the ^{19}F NMR (Figure 4.5b), with

FEC samples containing more LiF than VC samples. Apart from LiF, residual LiPF₆ salt (¹⁹F NMR shift at -74 ppm) is the dominant inorganic species in the SEI, as the samples were not rinsed. The PF₆⁻ anion also hydrolyses, forming PO₂F₂⁻ (¹⁹F chemical shift = -82 ppm) and PO₃F⁻ anions (¹⁹F doublet = -97 ppm) probably due to presence of trace amount of water impurity in the electrolyte or physisorbed on the surface of the SiNWs. In the ¹⁹F ssNMR spectra of cycled SiNWs (Figure 4.5), a small peak at -122 ppm was observed, which can be assigned to SiO_xF_y species.⁴⁸ However, this peak is not consistently observed, and it is attributed to the contamination from glass fibre.

No evidence of a fluorinated polymer is found in the ¹⁹F and ¹³C ssNMR spectra (fluorinated polymers resonating between -100 to -130 ppm and 100 to 130 ppm in ¹⁹F and ¹³C ssNMR, respectively). The absence of a fluorinated polymer suggests that FEC defluorinates prior to further reduction/reaction. The result is consistent with our previous study¹³¹ and theoretical work from Balbuena's group.¹²¹

4.3.5 The SiO_x-SEI interface

Figure 4.6a shows the ¹H-²⁹Si CP NMR spectra of pristine Si nanoparticles (SiNPs) measured with conventional ssNMR compare to SiNWs after the first, 50 and 100 cycles in different electrolytes with DNP enhancement. The spectrum of pristine SiNPs is shown here for comparison since the SiNPs are expected to show similar surface species to the SiNWs. Moreover, SiNPs are available in larger quantities allowing us to collect a spectrum with improved signal-to-noise ratio. The spectrum of the pristine SiNPs mainly consists of sharp resonances from bulk crystalline Si (-82 ppm)¹³³ and Q-site hydroxyl-terminated silicates (²⁹Si resonances at -102 ppm for Q³ and -112 ppm for Q⁴, where Qⁿ represents (SiO)_nSi(OH)_{4-n} environments).¹³⁴ The weak peak at -50 ppm is tentatively assigned to the amorphous Si component in the nanoparticles.¹³⁵

After cycling, the Si surface changes dramatically and di- (D), tri- (T), substituted siloxanes are observed (Figure 4.6a). We excluded the formation of hydrogen terminated Si species because no dramatic intensity decrease was observed in the ¹H-²⁹Si dipolar dephasing experiment for all the resonances observed in the ²⁹Si NMR spectra (Figure B.11), indicating that there are no Si-H bonds.

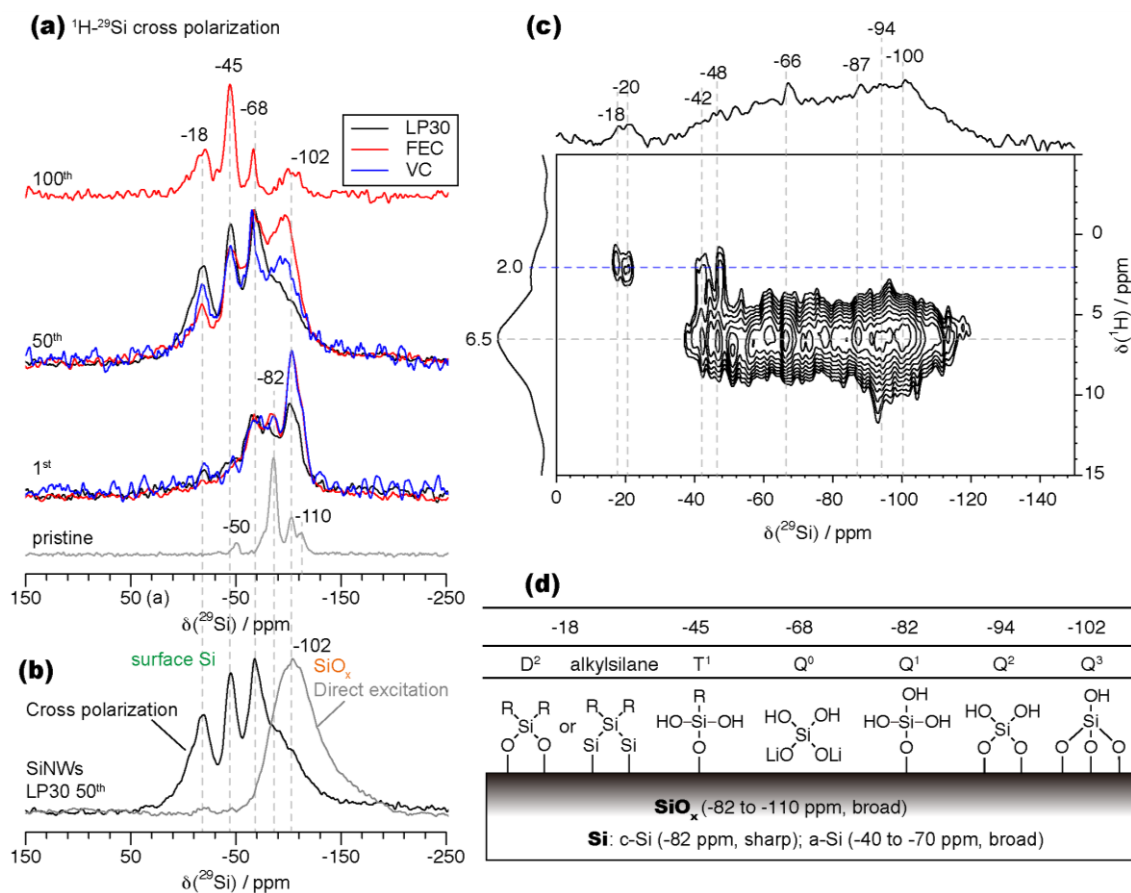


Figure 4.6 ^{29}Si NMR spectra of cycled Si using different techniques. (a) ^1H - ^{29}Si CP DNP NMR of SiNWs after the first, 50 and 100 cycles; pristine silicon nanoparticles were measured by ^1H - ^{29}Si CP NMR without DNP and its spectrum is included for comparison. (b) ^{29}Si DNP NMR using cross polarization (CP) and direct excitation (DE) on SiNWs cycled in LP30 for 50 cycles, with recycle delay of 3.5 s and 10 s, respectively. The CP spectrum mainly shows proton-containing surface species, whereas the DE spectrum (grey in b) mainly contains signals from the outer SiO_x shell on the SiNWs. (c) ^1H - ^{29}Si HETCOR of SiNWs cycled in FEC for 50 cycles with a 5 ms contact time and recycle delay of 3 s. (d) Cartoon showing possible Si surface structures and their corresponding chemical shifts; R denotes an alkyl group. The proposed structures are mainly based on the ^1H - ^{29}Si HETCOR result. ^{29}Si shifts of SiO_x and Si species are summarized: crystalline silicon (c-Si) -81 ppm; amorphous silicon (a-Si) -40 to -70 ppm¹³⁵.

After the first cycle, a new resonance at approximately -68 ppm arises, which can be tentatively assigned either to T³ organosiloxane ($(\text{SiO})_3\text{SiR}$, where R is aliphatic carbons)⁸⁷ or to Q⁰ single (non-bridging) tetrahedral silicate (possibly with some charge-balancing Li^+ ions, $\text{Li}_n\text{H}_{4-n}\text{SiO}_4$, where $n = 1$ to 3). The ^1H - ^{29}Si HETCOR of the SiNWs cycled in FEC for 50 cycles (Figure

4.6c) shows that the ^{29}Si resonance around -66 ppm is connected to hydroxyl group(s) with ^1H shift at 6.5 ppm, but shows no cross peaks with protons on alkyl carbons (with ^1H shift around 2.0 ppm), indicating that Si-C(H) groups are not present. Therefore, the HETCOR data support the assignment of the -68 ppm ^{29}Si resonance to a Q^0 silicate rather than T^3 organosiloxane. By using various CP contact times, we find that the -68 ppm component has a fast CP build-up curve (Figure B.10), confirming that this species is in close proximity to protons, suggesting that it is associated with a silanol group ($\text{Li}_n\text{H}_{4-n}\text{SiO}_4$) instead of a proton-free lithium orthosilicate (Li_4SiO_4). Moreover, the intensity of the -68 ppm peak increased dramatically after air exposure and a second resonance at -60 ppm is observed (Figure B.12). This may be due to the further hydrolysis of the $\text{Li}_n\text{H}_{4-n}\text{SiO}_4$ and the other Q site species leading to the formation of a species that contains more abundant protons.

The -82 ppm peak in the SiNWs after the first cycle is attributed to Q^1 sites ($(\text{SiO})_2\text{Si}(\text{OH})_3$) instead of crystalline Si (^{29}Si shift at -81 to -85 ppm)¹³⁶, as crystalline Si is completely amorphised during the first cycle based on the electrochemistry (amorphous Si has a very broad ^{29}Si shift around -40 to -70 ppm¹³⁵). The HETCOR spectrum (Figure 4.6c) confirms that the -82 ppm species is associated with a silanol proton (6.5 ppm)⁸⁷. Of note, the HETCOR spectrum reveals that although the Q^1 (-82 ppm) resonance is more distinct, the broad silanol resonance spreads from -40 to -120 ppm, the region around -94 ppm corresponding to a Q^2 environment (i.e., $\text{Si}(\text{OSi})_2(\text{OH})_2$). The broad resonance reflects the distribution of local environments in the amorphous $\text{Si}(\text{OR})_n(\text{R}')_{(4-n)}$ ($n = 0, 1$) network, (including Si-OH vs. Si-O Li^+ termination and Si-O vs. SiR connectivity).

Two new ^{29}Si peaks at -18 ppm and -45 ppm become more pronounced in the SiNWs after 50 cycles. Based on its distinct chemical shift, the -18 ppm peak can be assigned to D^2 $(\text{SiO})_2\text{SiR}_2$ ¹³⁷ or an alkylsilane $(\text{Si})_2\text{SiR}_2$ ¹³³ (Figure 4.6d). This assignment is confirmed by ^1H - ^{29}Si HETCOR (Figure 4.6c), where the ^{29}Si peak at -18 ppm is only correlated to the protons on alkyl species (2.0 ppm). For the -45 ppm Si peak, correlations to both the protons on alkyl carbons (2.0 ppm) and hydroxide protons (6.5 ppm) are observed in the ^1H - ^{29}Si HETCOR spectrum, thus the -45 ppm resonance can be ascribed to a T^1 site $(\text{SiO})_2\text{SiR}(\text{OH})_2$.¹³⁸ Such organosiloxane species can be formed via the reduction of the hydroxyl groups on the surface forming a Si-C bond (possible reactions will be discussed later). A similar trend is observed

in SiNWs after 100 cycles in $^{13}\text{C}_3$ FEC electrolyte: the intensity of organosiloxane species with a ^{29}Si shift at -45 ppm increases further, while the relative intensity of the Q^3 sites at -102 ppm significantly decreases. In general, we find that the hydroxyl terminated species on the Si surface are gradually converted to organosiloxanes as a function of cycling.

Figure 4.6b compares the ^{29}Si NMR spectra obtained by cross polarization (CP) vs. direct excitation (DE) of SiNWs cycled in LP30 for 50 cycles. In the $^1\text{H} \rightarrow ^{29}\text{Si}$ CP experiment, polarization of ^{29}Si nuclei located near the surface is enhanced as there are few protons inside the bulk Si and CP transfers are only effective up to a few angstroms. In the DE experiment, any Si species (both protonated and non-protonated) close to DNP biradicals are enhanced with a penetration depth of 1-5 nm.¹³⁹ The broad peak around -102 ppm in the DE spectrum indicates that a wide range of environments are present, including Q^3 site hydroxide terminated silicates and SiO_x non-protonated species. Both the -18 and -45 ppm peaks are also observed but are much weaker. These results suggest that the organosiloxane species observed in the ^1H - ^{29}Si CP DNP NMR spectra are at the extreme surface of the SiO_x layer and only account for a small fraction of the oxide layer (1-5 nm) in the cycled Si anode.

Apart from the cycle number, the electrolyte solvents also affect the relative intensities of each Si component. Though CP DNP NMR is not absolutely quantitative, the intensity difference allows an estimation of the relative populations of different Si sites. All spectra are normalized by the -68 ppm Q^0 silicate peak (arbitrarily selected) to facilitate the comparison. After the first cycle, the relative intensity of Q^3 site (-102 ppm) in the LP30 sample is much smaller than those in the FEC and VC samples. This indicates that native hydroxyl groups are converted to the silicate/organosiloxane sites, but that this conversion is more pronounced (or rapid) in LP30 than in pure FEC and VC electrolytes (i.e. more organosiloxanes and Q^0 species are formed in LP30). In the 50th cycle, the same trend is observed: the Q^3 sites in LP30 are weaker compared to VC and FEC, with FEC still having the most intense Q^3 peak. The peak intensities of organosiloxanes (-18 ppm and -45 ppm) are also slightly larger in the LP30 sample than in the FEC and VC samples. In short, the SiO_x surface reduction is more pronounced in the LP30 than in FEC and VC electrolytes.

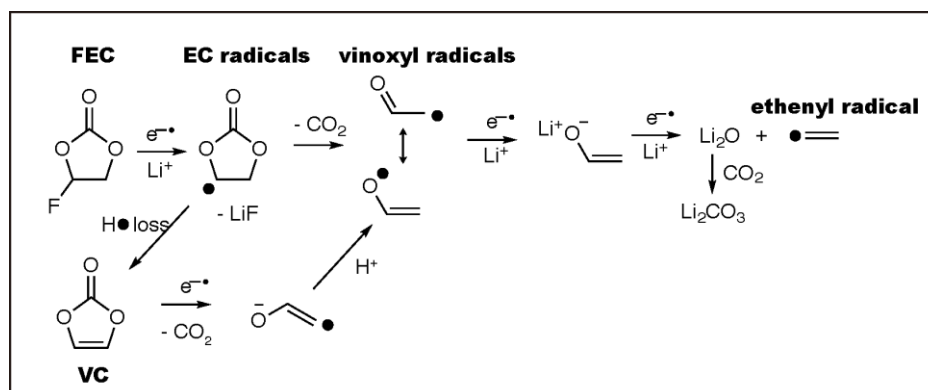
4.4 Discussion

The SEI derived from pure FEC and VC electrolytes contains a large amount of branched or cross-linked PEO, which is similar to LP30 + 10 vol% FEC, but different from the linear PEO-type polymer observed in the additive-free LP30 sample.^{47,48,131} In this study, the cross-linking units were found to be acetal carbons connected to PEO-type carbons, as confirmed by a ^{13}C - ^{13}C homonuclear correlation NMR experiment (Figure 4.4). Across all samples, we find that the presence of the acetal carbon is consistently associated with improved capacity retention. Methoxide groups are also observed, which likely represent end (terminal) groups of the organic polymer. Of note, the hydroxyl groups in PEO-type solid polymer electrolytes have been chemically modified to form methoxide groups, which are expected to reduce the polymers' reactivity towards Li metal¹⁴⁰ and potentially increase the chemical stability of the SEIs.

Cross-linked PEO can be formed following the reaction pathway described in our previous work.¹³¹ Briefly, FEC defluorinates forming an EC radical, which transforms to VC via hydrogen loss. Alternatively, the EC radical forms vinoxyl radical ($\text{O}=\text{CHCH}_2\bullet$ or $\bullet\text{OCH}=\text{CH}_2$) with concurrent loss of CO_2 (Scheme 4.2). VC can also be reduced to a radical anion ($\text{OCH}=\text{CH}\bullet$), which is stabilized by π conjugation. The vinoxyl radical can react with a sp^2 -hybridized carbon, forming branched species containing acetal carbons, aldehyde and alkene terminations (see Chapter 3, Scheme 3.2), all of which are observed in our ^{13}C NMR experiments. In EC based electrolyte, no such branched species were observed. One possible explanation is that for EC ring-opening reduction dominates, and the reduced species (e.g. $\bullet\text{CH}_2\text{CH}_2\text{OCOO}^-$) cannot easily lose protons to form the vinoxyl radicals. Due to the lack of vinoxyl radicals and unsaturated carbons, no significant concentrations of branched polymers are formed in standard LP30 electrolyte.

Apart from the cross-linked PEO, the SEIs formed from pure FEC and VC also contain a large amount of aliphatic carbons, which are absent in EC based sample. The large quantities of alkyl carbons in the FEC and VC samples are consistent with the oxygen-deficient species identified by Nakai et al. in the SEI formed on Si thin films in a FEC/DMC solvent.⁴¹ Based on XPS and

Scheme 4.2. Possible reduction reactions for FEC and VC based on Ref ^{52,131}.

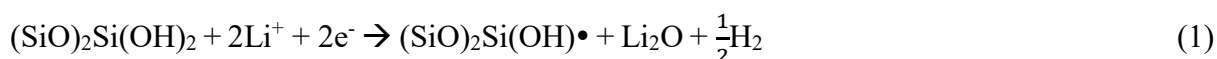


ToF-SIMS results, the authors concluded that the oxygen-deficient species is a polyene type polymer. Here, we observed that such oxygen-deficient polymers primarily contain alkyl chains instead of unsaturated carbons (with ^{13}C resonances around 120–140 ppm), although a small amount of alkenes are observed in pure FEC/VC electrolytes (Figure B.5 in the Appendix B). Oxygen deficient species can be formed by further reduction of vinoxyl radicals with the formation of Li_2O (Scheme 4.2). The reduced species, such as ethenyl radicals⁵², can form dimers that subsequently polymerize, resulting in cross-linked aliphatic chains. Reactions with other radicals, including those formed on reductive ring-opening of the cyclic carbonate can also generate aliphatic groups; this mechanism is thought to be responsible for LEDC and LBDC formation.⁴⁷ Though we have not observed the radicals, reduction reactions of this nature must occur as the aliphatic carbons account for ~41% of the total carbon signal (Table 4.3). Fewer aliphatic carbons were observed in the EC/DMC system, presumably because the major reduction reactions do not involve the formation of ethylene radicals and/or require reactions involving radical (re)combination.⁴⁹

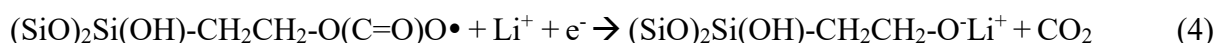
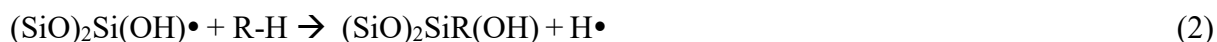
²⁹Si DNP NMR reveals the bonding nature between the organic SEIs and Si surface. Organosiloxane species grow on the Si surface as a function of cycling. The formation of Si–C bonds has previously been predicted by Balbuena and coworkers using DFT and *ab initio* molecular dynamic simulations.¹²¹ Prior experimental evidence of a Si–C species comes from XPS Si 2p spectra, where the SiO₂ peak shifts to lower binding energy after cycling (from 103 eV to 101 eV), indicating that the SiO₂ surface undergoes a reduction process during cycling.^{60–62} Our XPS Si 2p peaks of cycled SiNWs sample are broad: the 101 eV peak is not well resolved

from the 103 eV peak (see Figure B.6 for details). Nevertheless, the XPS data seems to suggest that the SEI in the VC sample is thicker than the FEC and LP30 samples after the same number of cycles.

Here, we utilized DNP and revealed detailed molecular structure concerning the Si surface. The formation of the organosiloxane is correlated with the reduction of the native oxide layer (SiO_x) on SiNWs. Reduction of the hydroxyl groups on SiO_x surface likely leads to the formation of thermodynamically stable species (e.g. LiOH , Li_2O and H_2) as well as an under-coordinated silica radical $(\text{SiO})_2\text{Si}(\text{OH})\bullet$ (one possible reaction is illustrated in reaction 1). Note that the evolution of H_2 gas from the reduction of FEC-based electrolyte has been reported by Jung et al. using on-line electrochemical mass spectrometry.⁵²



The under-coordinated silica species can react further with the solvent, forming Si-C bonds as outlined by reactions 2, 3 and 4. Reactions with radicals formed via direct transfer of electron from the Li-Si-O surface may also occur.¹²¹



The D^2 site (-18 ppm) observed in ^{29}Si NMR (Figure 4.6) can be formed via the reduction reactions proposed above, by substitution of two -OH groups in $(\text{SiO})_2\text{Si}(\text{OH})_2$ with two R groups. The growth of the D_n and T_n species as a function of cycle number indicates a dynamic change of Si surface species and a sequential reduction process of the SiO_x surface.

SiNWs cycled in LP30 electrolyte show more severe reduction of SiO_x compared to those cycled in pure FEC or VC electrolytes. One possible origin for this difference may lie in the variation of the polymeric SEI structures. For example, the cross-linked polymer formed from FEC and VC may inhibit solvent permeation through the SEI and thus slow down the reaction between the solvents and the SiO_x surface. Since the EC reduction mechanism occur at lower voltages, i.e., EC is more stable, it may be that coupled reactions involving EC reduction and

Si–C bond formation play an important role in reducing the SiO_x surface. Finally, the differences may also be related to the different changes in silicon morphologies on cycling EC vs. FEC/VC electrolytes, leading to variations in the nature and quantities of exposed surfaces.

Calculations have shown that the lithiated silicon reacts with EC (and related molecules) by attack of the carbonate carbon, which does not result in the formation of a long-lived Si–C bond.¹⁰⁰ Instead breakdown products such as ethylene and Li₂CO₃, are formed.¹⁰⁰ Thus, although the exposure of fresh (lithiated) silicon surfaces presumably promotes further electrolyte reactions, the fully lithiated silicides may not generate the stable Si–C species seen in this study, consistent with our suggestion that they arise from reactions of the silanol groups. Perez-Beltran et al. have shown by calculations that reduction of Si–OH groups can lead to the formation of Si–H,¹⁴¹ but we see no evidence for them in our NMR studies.

Since these organosiloxanes are formed on Si surfaces during electrochemical cycling, this suggests some stability of the Si–C bonds in the reducing environment. SiNP uniformly coated with PEO-VC type polymer that contain such Si–C bonds via click chemistry have been demonstrated to improve the cycle life of Si anodes,⁶⁷ and the formation of such Si–C species may also be relevant for strategies involving conformal coating Si with carbon and, in part, explain why carbon coatings help increase the CE and capacity retention.^{23,25} Additional information concerning the spatial arrangement of the organosiloxane layer on Si will be helpful to understand its passivating ability (e.g. is it a monolayer, or a core-shell structure, or simply formed in discrete regions on the surface).¹⁴² It is possible that such an interfacial layer maybe further tailored to achieve certain binding modes on the Si surface that might help to decrease the side reactions between Si and the electrolyte.

The previous XPS study of the SEI by Schroder et al. suggest that the Si surface can be passivated by forming Si–F species.⁴⁰ In this work, no strong evidence to support the formation of Si–F species was found in the ²⁹Si NMR and Si 2p XPS spectra of cycled electrodes: these species have ²⁹Si NMR signals at around -105 to -130 ppm¹⁴³ (Figure B.9) and Si 2p XPS peaks around 106 eV¹⁴⁴ (Figure B.6), but no obvious peaks were observed in either the XPS or NMR spectra. The ¹⁹F ssNMR spectra of cycled SiNWs (Figure 4.5), do contain a small peak at -122 ppm, which is assigned to SiO_xF_y species. This peak is not consistently observed, however, and is attributed to the contamination of the sample by glass fiber (Figure 4.5) from the borosilicate

separator. The results imply that while small amounts of Si–F species may be present on the electrode surface, they are not the dominant species, as they are below the detection limit of ^{19}F NMR and XPS.

According to the well-known mosaic model¹⁴⁵ and experimental evidences from XPS and TOF-SIMS⁴⁰, the SEI consists of two layers: the inner SEI close to the electrode surface that mainly consists of inorganic Li salts (such as Li_2O , LiF and Li_2CO_3) and the outer layer of the SEI which primarily contains the polymeric components. Our ^7Li and ^{19}F ssNMR spectra (Figure 4.5) shows that LiF , residual LiPF_6 salt and PF_6^- breakdown products are clearly present in the cycled electrodes, with decomposition of both the PF_6^- anion and FEC contributes to the formation of LiF . The presence of Li_2CO_3 is also confirmed by ^{13}C NMR as evidenced by the ^{13}C NMR resonance at 170 ppm. The role of inorganic species in the SEI is still unclear as they are observed in all the electrolyte formulations studied here and yet the LiF concentration for example, does not correlate with improved electrochemistry. The role of the inorganic Li salts may depend on both the chemical structure as well as other factors including particle size, spatial distribution in the SEI, and interaction with the organic SEI. However, the important conclusion we draw from the ^{29}Si DNP NMR and the multinuclear NMR studies is that the Si surface is not entirely covered by inorganic species but is partially bonded to the organic SEI.

Based on our initial chemical analysis, the difference in the electrochemical performance of LP30, FEC and VC can be explained at least in part by the differences in their polymeric SEIs. In EC-based electrolyte, linear PEO-type polymers form and some of the degradation products are more soluble than those derived from electrolyte containing FEC additives.¹³¹ The linear PEO-type polymer may not be able to accommodate the volume expansion of Si anode or have poorer Li ion conductivity than the branched PEO.¹⁴⁶ Furthermore, continuous solvent decomposition on the Si surface leads to pore clogging of the electrode, which ultimately restricts the Li ion diffusion through the SEI.⁴⁸

With the addition of FEC or VC, a heterogeneous polymer forms with specific functionalities: the cross-linked PEO/poly(VC) part can conduct Li ions and the aliphatic region may be electronic insulating and/or help prevent permeation of polar solvents. However, the cross-linked polymers formed in pure FEC and VC electrolytes do not form perfect barrier coatings

as we still observe the continuous formation of organosiloxanes and Coulombic efficiencies of less than 99.5% in these systems.

The mechanical properties of cross-linked polymers formed in FEC and VC systems may also be different from their linear counterpart as they can be more elastic, thus helping to sustain the volume expansion of the Si anode and better protect the active material during cycling.¹⁴⁷ In addition to the composition, the microstructure of the polymer (chain length, molecular weight, arrangement of repeating units in the backbone, etc.) can also influence the mechanical and ionic properties of the SEI, which is outside the scope of this current study.

To understand the heterogeneous organic SEI detected in the FEC and VC electrolyte better, knowledge from the field of solid polymer electrolytes (SPE) is of relevance, where new hybrid- and block-co-polymers show promising results for increasing ionic conductivity.¹⁴⁸ For example, Khurana et al. reported a cross-linked SPE consisting of polyethylene and PEO with short chain polyethylene glycol plasticizer, which is chemically similar to the organic SEI we detected in the FEC/VC sample. Such SPE was found to exhibit high lithium conductivity ($> 1.0 \times 10^{-4}$ S/cm at 25 °C) and was able to suppress the growth of Li dendrites.⁶⁶ The relationship between the degree of cross-linking and Li ion conductivity was also explored by Thiam et al.,¹⁴⁹ who showed that the higher Li ion conductivity of PEO polymers (1.0×10^{-4} S/cm at 30°C) can be obtained by controlling the cross-link density. Correlating the structure of the polymeric SEI with the electrochemical performance is key to fully understanding the SEI on alloy type anodes.

It is clear that solvent still penetrates through the SEI and approaches the SiO_x surface sufficiently closely to allow electron tunnelling and solvent reduction. Strategies that reduce solvent penetration are required to improve the SEI and it is speculate that the success of cellulose binders¹⁵⁰ lies in part due to the strong bonds to the SiO_x surface and the fact that it does not swell in carbonate electrolytes.

4.5 Conclusions

This work has identified key chemical signatures on the surface and interphase of Si electrodes cycled in pure FEC and VC and a standard LP30 carbonate electrolyte with 1 M LiPF₆. The SiNW electrodes cycled in FEC and VC electrolytes show better electrochemical performance than those cycled in standard LP30 based electrolytes. ¹³C NMR experiments of both ¹³C enriched and natural abundance electrolytes reveal that the organic electrochemical decomposition products of FEC and VC mainly consist of cross-linked PEO and alkyl chains with carbonate and carboxylate units forming 15% of the carbon content of the FEC-derived polymer.

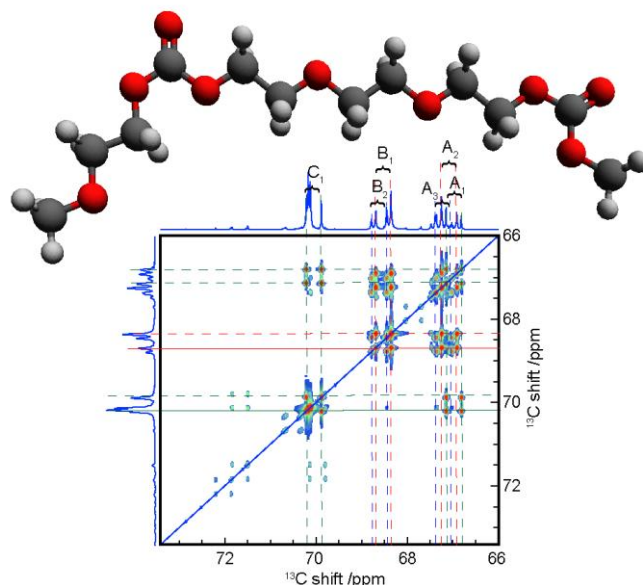
For the FEC system, ¹³C-labelled electrolyte was used to perform the 2D ¹³C–¹³C correlation experiment, which reveals key molecular fragments containing branched acetal carbons. The branched polymers formed in VC electrolyte show noticeable difference from FEC sample: the cross-linked acetal units and the ethylene oxide regions exhibit higher ¹H and ¹³C ssNMR chemical shift in the VC samples than the FEC samples. The chemical shift difference may be due to polymer conformations or the nearby chemical species. Since ¹³C-labelled VC is not available, 2D ¹³C–¹³C correlation experiment on the VC samples was not performed to confirm the formation of poly (VC).

The highly cross-linked PEO has three potentially positive implications for the stability of Si anodes. It may (i) reduce solvent penetration and swelling of the SEI helping to reduce further solvent reduction, (ii) accommodate the expansion and contraction of the silicon and (iii) may possibly have improved Li ion conductivities than linear PEO found in EC-based electrolytes¹⁴⁹. Studies are currently underway to test these hypotheses.

The evolution of the Si surface structure is revealed by ²⁹Si DNP NMR. The hydroxyl terminated SiO_x is gradually reduced to form organosiloxane species containing Si–C bonds, indicating that the Si surface is not entirely covered by inorganic Li salts but some SiO_x groups are also bonded to organic SEI components. We believe that the Si–C bonds formed on cycling have intrinsic stability in the reducing environment. However, the presence of the Si–C bond alone does not necessarily correlate to improved electrochemical performance. Likely it is both the chemical structures of the organic SEI and the uniformity of the SEI coverage on the active

material that influence the cycle life of Si. Overall, this work has provided fundamental insight into the chemical species that form on cycling and result in increased Coulombic efficiencies and capacity retention in Si anodes for Li-ion batteries.

Chapter 5 Electrochemical reduction products of ethylene carbonate



5.1 Introduction

Ethylene carbonate (EC) is one of the most critical components in commercial electrolytes, as its decomposition products form a stable passivation layer on the graphite anode, preventing further electrolyte degradation. Moving from graphite to high-capacity Si anodes, EC-based electrolyte, however, cannot form such a stable interphase: large amounts of soluble degradation species has been identified in the cycled electrolytes and continuous capacity fading is observed.

Lithium ethylene decarbonate (LEDC) has been reported as the major degradation product of EC.¹¹⁶ However, LEDC is highly soluble and cannot passivate the electrodes. Insoluble organic SEI components derived from ¹³C₃-labelled-EC electrolytes mainly consist of PEO-type polymers^{47,48}. Similar PEO-carbonate copolymers are observed in EC based system by ssNMR

in Chapter 3. Covalent bonds between the polymeric SEI and Si surface are also identified. Nonetheless, it is still unclear why these degradation products passivate graphite, but not the Si anode. Detailed information about the chemical structures of these polymers remains unclear. Further understanding about the connectivity between the ethylene oxide (EO) and the carbonate units as well as the conformation of these oligomers are relevant to fully understand the SEI's properties. Solution NMR is a powerful tool for solving the puzzle. Techniques such as diffusion ordered spectroscopy (DOSY), and 2D correlation experiments can be used to clearly identify these chemical structures.

As a continuation from Chapter 3, the electrochemical reduction products from both $^{13}\text{C}_3$ -labelled EC and non-labelled EC have been analysed by various solution NMR techniques. Additional calculation was performed to find the trend of the ^1H and ^{13}C solution NMR shifts in these oligomers. Empirical rules summarized from the calculation are then used to aid experimental assignment. Unique linear ethylene oxide (EO)-carbonate oligomers with methoxide end groups are identified as the major degradation products from EC. Electrospray ionization high resolution mass spectrometry (ESI-HRMS) is then used to confirm the chemical formulas of these oligomers.

5.2 Experimental

Coin cells: silicon nanowires (SiNWs)-Li half cells were prepared using LP30 or LP30+ $^{13}\text{C}_3$ EC (1M LiPF₆ in EC/ $^{13}\text{C}_3$ EC/DMC=1/1/2, v/v/v) electrolyte. Cells were cycled at C/30 (120 mA/g) between 0–2 V for 30–50 cycles. Details about the materials, synthesis of SiNWs and coin cell preparation can be found in Chapter 3.

Solution NMR: after cycling, cells were disassembled, and the separator was soaked in ~0.6ml d_6 -DMSO, then the solution was transferred into an air-tight J-Y NMR tube for solution NMR measurement. Spectra were recorded on a 500 MHz Bruker Avance III HD, with a DCH (carbon observe) cryoprobe or Bruker AVANCE 400 equipped with a BBO probe. Spectra are internal referenced to d_5 -DMSO (^1H at 2.50 ppm and ^{13}C at 39.53 ppm). ^{13}C - ^{13}C COSY spectrum was recorded using a Bruker COSY-DQF pulse program: F2 (^{13}C) was acquired using

a time domain of 4096 points, F1 (^{13}C) 1024 increments, over 236 ppm. The relaxation delay was 3 s and 40 scans per slice was used.

^1H Diffusion Spectroscopy (DOSY) experiment was performed using a Bruker pulse program 'ledbpgp2s' with bipolar gradient pulse for diffusion.¹⁵¹ 32 spectra with varying gradient strengths have been recorded with a diffusion delay of 10 ms and the gradient pulse width of 2 ms. Linear fitting of the intensity decay versus the gradient using Dynamic Center (Bruker) software provides the diffusion coefficients for each species.

ESI-HRMS: Cycled SiNWs were soaked in acetonitrile for 48 h to dissolve the organic SEI. SiNWs were removed by centrifuge and the supernatant was diluted by a factor of 3 for three times using CH_3CN before the measurements. All procedures were performed in air. ESI-HRMS experiments were performed in the positive ion mode on a Q-TOF instrument (Waters Xevo G2-S) equipped with a pneumatically assisted electrospray ion source (Z-spray) and an additional sprayer for the reference compound (LockSpray). The prepared solutions were directly introduced via an integrated syringe pump ($5\text{--}10\text{ L min}^{-1}$) in the electrospray source. The source and desolvation temperatures were kept at 80 and 150 $^\circ\text{C}$, respectively. Nitrogen was used as a drying and nebulizing gas at flow rates of 350 and 50 L h^{-1} , respectively. The capillary voltage was 2.5 kV, the cone voltage 100 V, and the rf lens 1 energy 60 V. Calibration of the instrument was performed using the ions produced by a phosphoric acid solution (0.2% in $\text{H}_2\text{O}/\text{CH}_3\text{CN}$, 50/50 v/v). The mass range was 50–1000 Da and spectra were recorded at 1 s scan^{-1} in the profile mode at a resolution of 10,000 full width at half-maximum (FWHM). Data acquisition and processing were performed using MassLynx v 4.0 software.

Calculations of ^1H and ^{13}C chemical shift were obtained from ChemDraw Software via empirical method.

5.3 Results

5.3.1 Electrochemistry

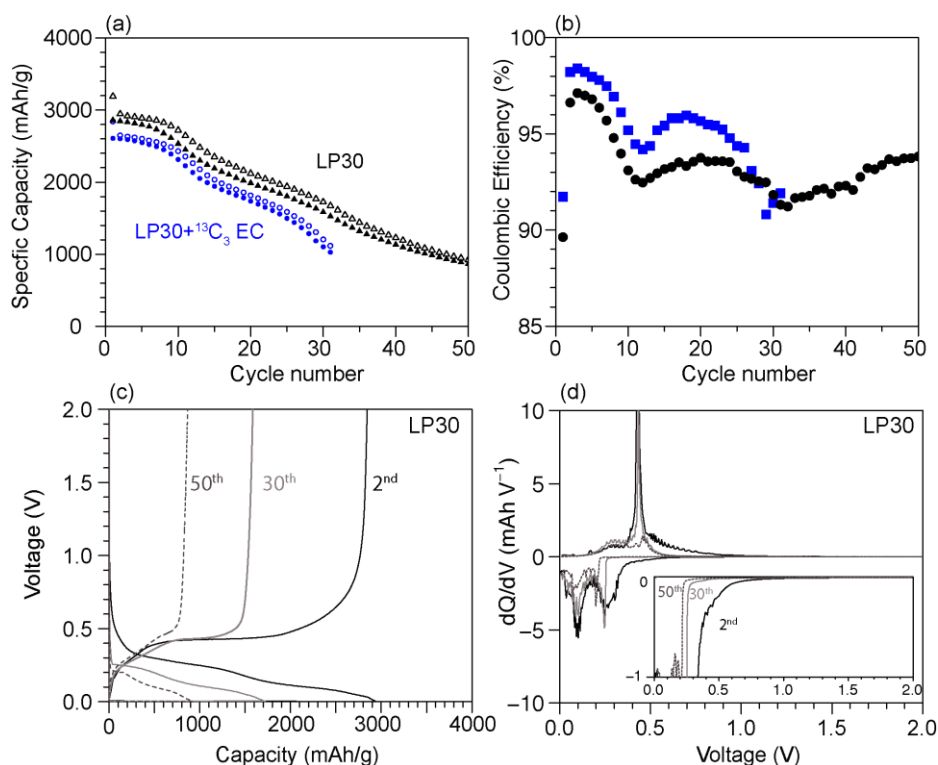


Figure 5.1 Electrochemical performance of SiNWs cycled in LP30 (black) and LP30+ $^{13}\text{C}_3$ EC (blue) electrolytes. (a) Capacity retention, (b) Coulombic efficiency versus cycle number. (c) The voltage curves at the 2nd, 30th and 50th cycle and (d) the their corresponding dQ/dV plot of cells cycled in LP30 electrolyte.

The electrochemical performance of SiNWs cycled in EC-based electrolytes is shown in Figure 5.1. Though the capacities are slightly different (probably due to the measurement error associated with the SiNWs mass), similar capacity fading trends are observed for both LP30 electrolytes with and without $^{13}\text{C}_3$ labelled EC. Note that the Coulombic efficiency of these cells are around 92–97 %, far below the requirement for commercial batteries. The origin of the capacity fade can be partially revealed by their voltage curves and dQ/dV plots. Figure 5.1c–d show that the first lithiation process around 0.2–0.5 V diminishes between 30 and 50 cycles. This is probably due to the formation of a thick, blocking SEI, which impedes Li-ion diffusion and increases the barrier for further lithiation.⁴⁸ The chemical structure of this blocking layer is analysed by solution NMR.

5.3.2 ^1H solution NMR of cycled electrolyte

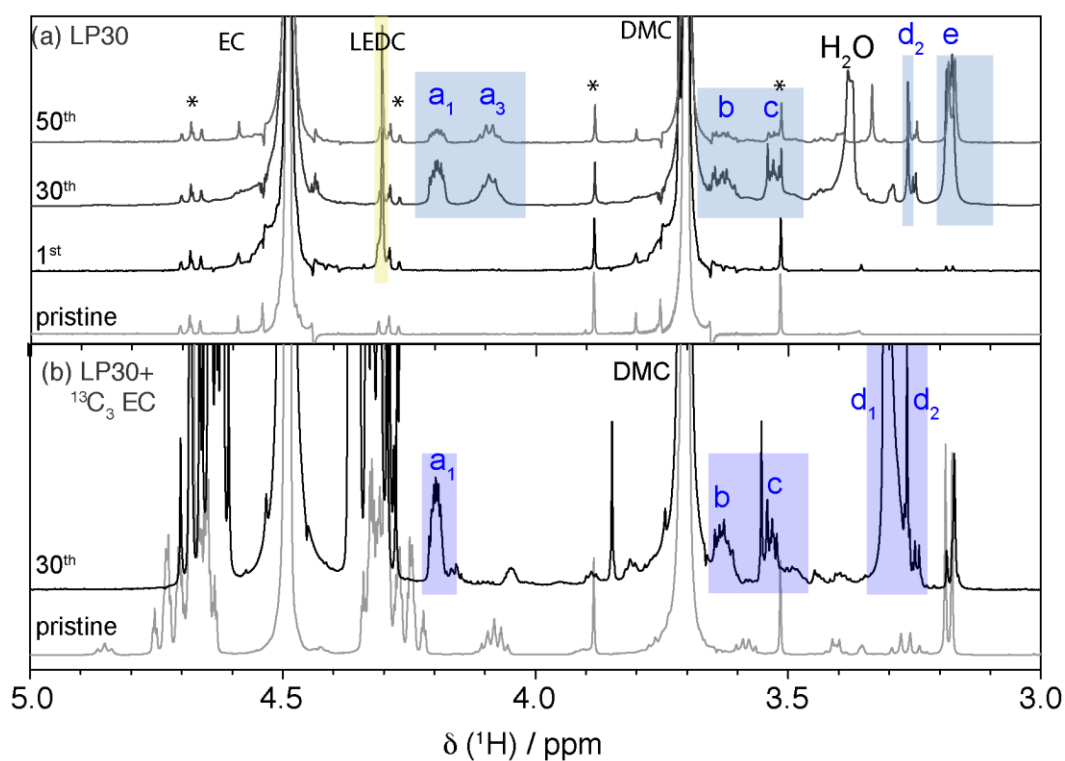


Figure 5.2 ^1H solution NMR of the pristine and cycled electrolytes. The intensity is normalized by the most intense peak. The ^{13}C satellites are marked with asterisks.

The ^1H NMR spectra of pristine LP30, LP30+ $^{13}\text{C}_3$ EC, and those electrolytes after the first, 30 and 50 cycles are shown in Figure 5.2. Strong ^1H NMR signals arising from EC, DMC, and deuterated DMSO solvent are at 4.48, 3.70 and 2.50 ppm, respectively. After the first cycle, one singlet at 4.30 ppm was observed in LP30 electrolyte (coloured in yellow), which is assigned to LEDC and the assignment is discussed in detail in Chapter 3. In electrolytes after 30 and 50 cycles, multiple peaks are observed at around 4.2, 3.6, and 3.5 ppm and in the region of 3.0–3.3 ppm (coloured in blue and labelled from **a** to **d**). The presence of multiplets in the ^1H NMR spectra indicates the existence of small soluble molecules or oligomers in the cycled electrolytes. To understand these new peaks, additional 2D ^1H – ^{13}C NMR correlation experiments were performed.

5.3.3 Oligomers identified by ^1H - ^{13}C correlation NMR

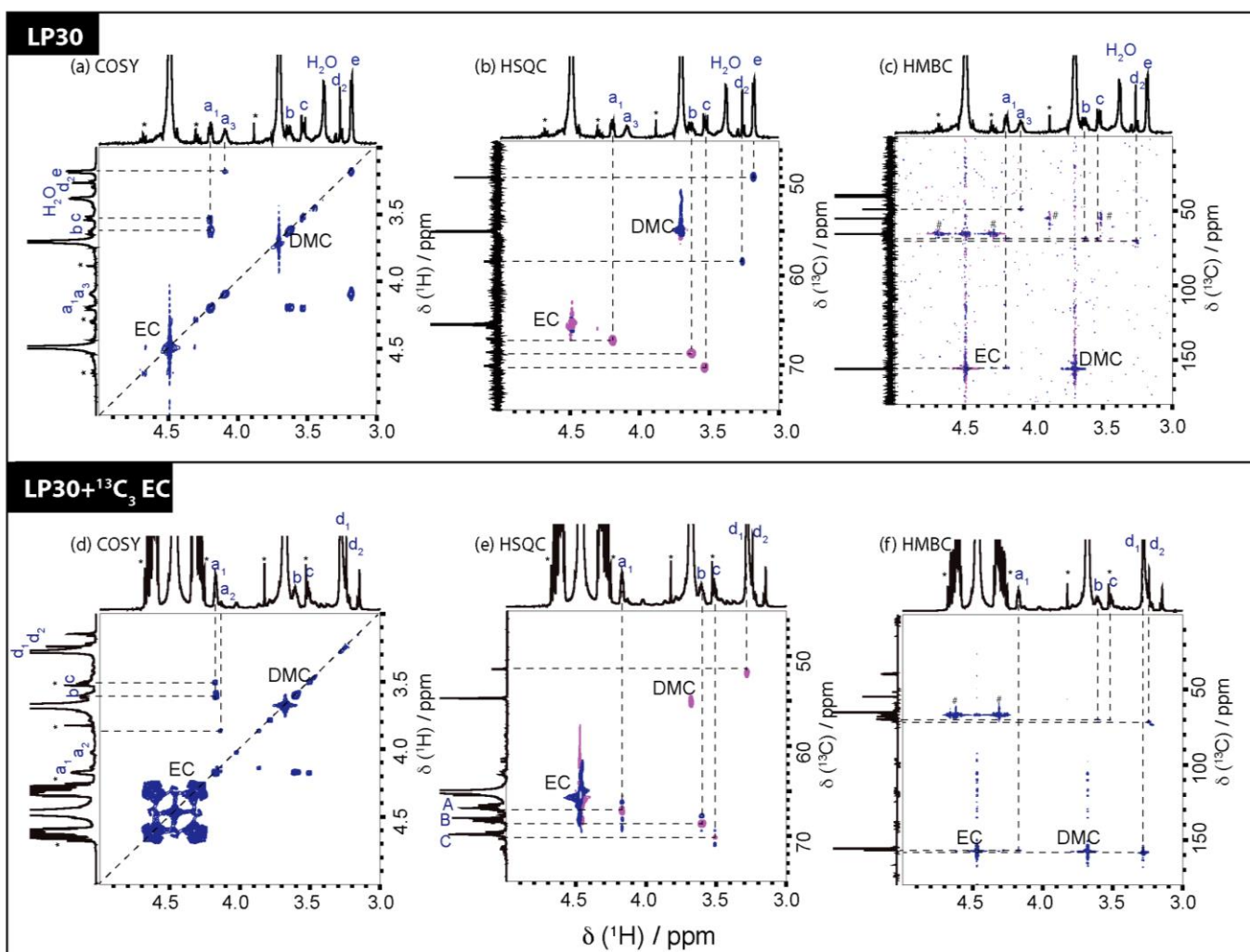


Figure 5.3 2D correlation NMR spectra of electrolytes after 30 cycles: LP30 sample in the upper panel and LP30+ $^{13}\text{C}_3$ EC sample in the lower panel. (a, d) ^1H - ^1H COSY, showing the proton-proton correlation; (b, e) ^1H - ^{13}C HSQC showing the one bond proton-carbon correlation; (c, f) ^1H - ^{13}C HMBC showing proton-carbon correlation through 2 to 4 bonds, one bond correlation artefact in HMBC is marked with "#".

Figure 5.3 show the ^1H - ^{13}C one-bond (HSQC) and multi-bonds correlation (HMBC) spectra as well as ^1H - ^1H correlation spectra (COSY) of the cycled electrolytes. These 2D spectra provide clear assignment of these emerging peaks labelled from **a–e** in the ^1H NMR. For example, the protons giving rise to **a**₁ (4.20 ppm) are bound to a carbon with a ^{13}C resonance at 67.4 ppm in the HSQC spectra in Figure 5.3b and e, the chemical shift indicating an ethylene oxide (EO, $-\text{OCH}_2\text{CH}_2$) unit. Longer correlations between protons and carbons over two to

four chemical bonds can be identified by the HMBC spectra: the proton with resonance **a**₁ is further bonded to a carbonate carbon at 155 ppm (Figure 5.3c and f). Based on these correlations, a chemical fragment can be deduced for **a**₁: ROCOO-CH₂CH₂OR' (R and R' denote alkyl groups). This structure is verified by the ¹H–¹H COSY spectrum (Figure 5.3a), which shows that **a**₁ is correlated to both **b** (3.63 ppm) and **c** (3.52 ppm), confirming the structure of ROCOO-CH₂CH₂OR', probably with different R' groups leading to slightly different ¹H chemical shifts for **b** and **c**. Note that ¹H peaks at **a**₁, **b**, **c** are all multiplets with unidentified J-coupling patterns. This is likely due to the overlapping of ¹H peaks with similar chemical environments.

While the same one-bond and multi-bonds correlations are identified for protons at **a**₁, **b** and **c** in the ¹H NMR for both ¹³C-labelled and non-labelled samples, differences are observed for the protons in the **d** region (3.24–3.28 ppm). For the non-labelled LP30 sample, the proton at **d**₂ (3.26 ppm) is connected to a carbon with a ¹³C shift at 58.5 ppm in the HSQC spectrum (Figure 5.3b). Based on the one-bond correlation, **d**₂ is assigned to a methoxide group (ROCH₃). Such correlation is, however, not visible in the ¹³C-labelled sample (Figure 5.3e) as its intensity is below the contour level shown here. The fact that the correlation intensity for **d**₂ protons in the ¹³C₃ EC sample is weak indicates that the methoxide group may not come from ¹³C₃ EC but DMC, which contains mainly ¹²C isotope (i.e. RO¹²CH₃). Interestingly, multi-bonds correlation is observed for protons at **d**₂ and an ethylene oxide carbon with ¹³C resonance at 70 ppm for the LP30+¹³C₃ EC sample (Figure 5.3f). This correlation peak has similar intensity as those peaks contain protons at **a**₁, **b** and **c**. Normally, correlations peak intensities are weaker in HMBC spectrum than those observed in the HSQC spectrum. The appearance of correlation for **d**₂ in the HMBC but not in HSQC spectrum suggests that the proton at **d**₂ is further bound to a ¹³C isotope, probably formed from ¹³C₃ EC. We now assign the **d**₂ peak to a motif with the structure of R¹³CH₂O¹²CH₃, and it may be the product formed due to a reaction between DMC and ³C₃ EC.

A standard workflow is followed to analyse all the features in the 2D correlation NMR spectra. First, chemical motifs are identified in the ¹H–¹³C one-bond correlation experiment (HSQC). Second, these motifs are linked together by HMQC experiment. Finally, the ¹H–¹H COSY

Table 5.1 Assignments in 2D correlation NMR in Figure 5.3. Correlations value marked with * are not shown in the figure but are present in a lower contour level.

Electrolyte	Index	Shift/ ppm					Possible assignments
		HSQC		HMBC	¹ H- ¹ H COSY		
		¹ H	¹³ C	¹³ C	¹ H	¹ H index	
LP30	a ₁	4.20	67.4	155.5/68.6	3.6/3.5	b/c	a₁-b/c ROCOO- CH₂CH₂OR '
	a ₃	4.10	-	49.1	3.18	e	CH₃OH
	b	3.63	68.6	68.6/70.1	4.20	a ₁	ROCOO-CH ₂ CH₂OCH₂R '
	c	3.52	70.0	68.6/70.1	4.20	a ₁	ROCOO-CH ₂ CH₂OCH₂R '
	d ₂	3.26	58.5	70.0			RCH ₂ OCH₃
	e	3.18	49.1		4.10	a ₃	CH₃OH
LP30+ ¹³ C ₃ EC	a ₁	4.17	67.1	156.9	3.6/3.5	b/c	ROCOO CH₂CH₂OR '
	b	3.60	68.6	68.6/70.1	4.17	a ₁	ROCOOCH ₂ CH₂OR '
	c	3.51	70.1	68.6	4.17	a ₁	ROCOOCH ₂ CH₂OR '
	d ₁	3.28	51.8	158.7	1.15		CH₃OCOOLi/R (lithium/alkyl methyl carbonate)
	d ₂	3.24	58.4*	70.1			RCH ₂ OCH₃

spectra are used to verify these connections. All the 2D correlation data is tabulated in Table 5.1. Here, at least three compounds can be identified in the cycled electrolyte: one is noted as **a₁-b-c** that consists of a linear chain with carbonate group and ethylene oxide unit (ROCOO-CH₂CH₂OCH₂R'). The second compound is **a₃-e**, and its formation will be explained later. The third is lithium methyl carbonate (LMC, CH₃OCOO-Li⁺) detected as **d₁** in the ¹H NMR spectra.

We note that the **a₃-e** and LMC molecules are correlated to each other. Figure 5.4 shows that **d₁** proton disappears with the concurrent appearance of the **a₃-e** species after water contamination. For the ¹³C₃ EC sample, the **a₃** peak at 4.07 ppm is clearly a quartet with J = 5.2 Hz, and the proton peak **e** at 3.16 ppm is a doublet with J = 5.2 Hz. The peak integral ratio between **a₃** and **e** is 1:3. Moreover, protons **a₃** and **e** are linked to each other in the ¹H-¹H COSY spectrum (Figure 5.3a). Combining all the information, **a₃-e** is unambiguously assigned to methanol. It worth noting that methanol shows two singlets in CDCl₃ solvent, but it shows a well-defined J-coupling pattern when measured in DMSO solvent, probably due to the

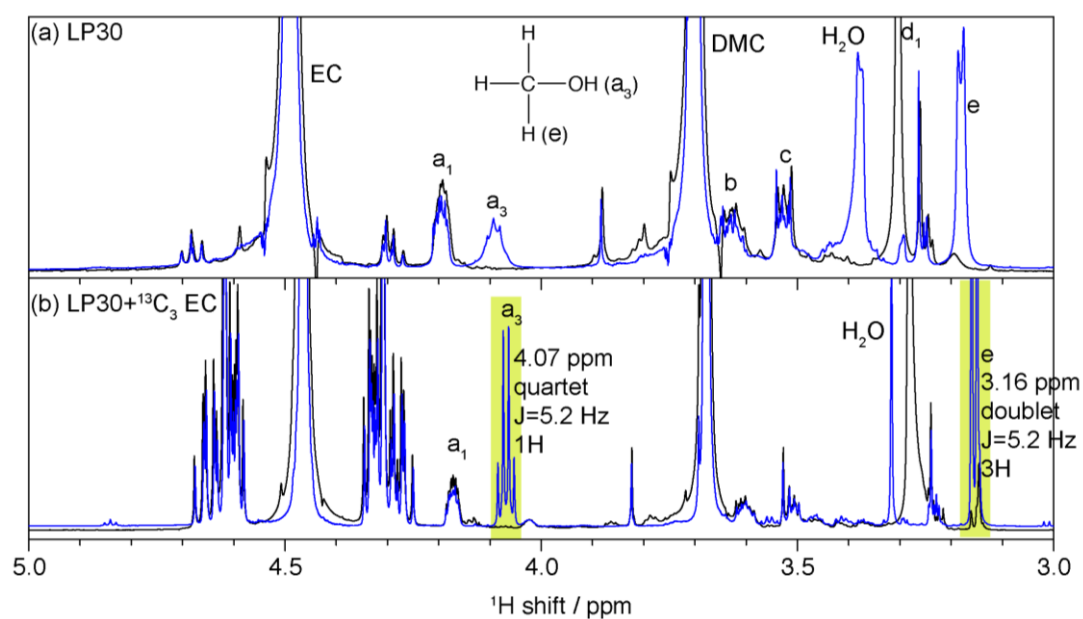


Figure 5.4 ^1H solution NMR of cycled LP30 and LP30+ $^{13}\text{C}_3$ EC electrolytes. The black spectrum is the electrolyte measured immediately after cell disassembly, while the blue spectrum is acquired on the same sample but after water contamination. After moisture permeates into the NMR tube, the d_1 peak at 3.30 ppm corresponding to lithium methyl carbonate (LMC, LiOCOOCH_3) decreases with the concomitant emergence of new peaks labelled as a_3 and e that corresponds to methanol.

viscosity of the solvent used. The complete conversion from LMC to methanol also indicates that LMC is highly water-sensitive.

To separate the mixture, ^1H DOSY experiment was performed on the cycled LP30 electrolyte. Figure 5.5 shows the that least two compounds (a_1 - b - c and a_3 - e) are present in the electrolyte besides EC, DMC, d_5 -DMSO and water impurities. The a_1 - b - c molecule has a lowest diffusion coefficient of $4.3\text{E}-10 \text{ m}^2/\text{s}$, smaller than EC and DMC molecules (6.5 and $7.0\text{E}-10 \text{ m}^2/\text{s}$), whereas the methanol (a_3 - e) has a much higher diffusion rate of $7.5\text{E}-10$ to $8\text{E}-10 \text{ m}^2/\text{s}$. The diffusion rate can be correlated to the radius of hydrodynamic molecule, further confirming that a_1 - b - c should be an oligomer.

Solving the structure of the a_1 - b - c oligomer is not easy. First, we note that the ^1H peaks at a_1 , b and c between (3.8 to 4.2 ppm) are all protons bound to carbons with ^{13}C shifts around 68–70 ppm in the HSQC spectra (Figure 5.3b and e), these chemical shifts corresponding to an EO

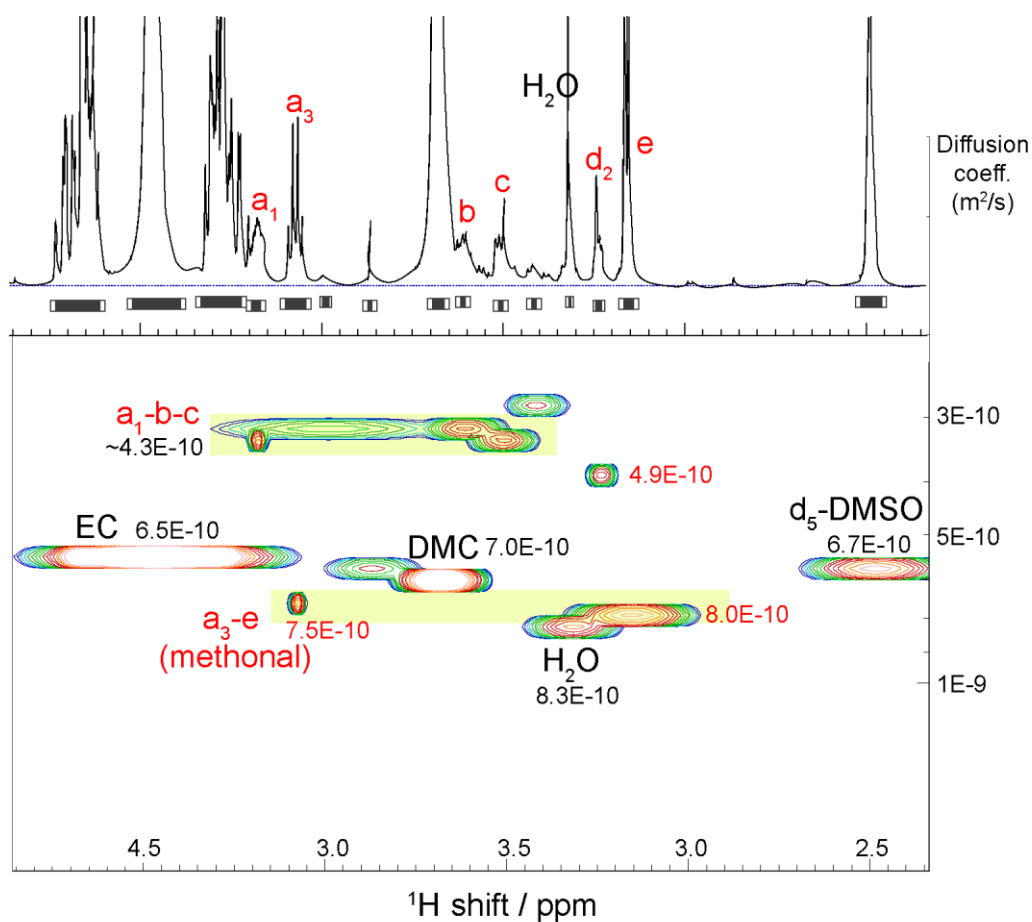


Figure 5.5 ^1H DOSY of the LP30+ $^{13}\text{C}_3$ EC electrolyte after 30 cycles. The centre of the peak corresponds to the diffusion coefficient and the peak width is associated with fitting error.

environment. For the $^{13}\text{C}_3$ EC sample (Figure 5.3e), new intense ^{13}C peaks are observed in the carbon dimension at 67.1 (marked as **A**), 68.6 (**B**) and 70.1 (**C**) ppm, which are clearly correlated to proton peaks at **a**₁, **b** and **c**, respectively. The improved ^{13}C signal in the $^{13}\text{C}_3$ EC sample confirms that the **a**₁-**b**-**c** oligomer arises from the decomposition of EC instead of DMC.

5.3.4 ^{13}C - ^{13}C correlation NMR

With enhanced ^{13}C signal intensity in the ^{13}C -labeled sample, the ^{13}C COSY experiment was successfully performed to find long-range correlations in the **a**₁-**b**-**c** oligomer. A full spectrum of the ^{13}C COSY experiment is shown Figure 5.6. An off-diagonal peak indicates a direct bonding between the two carbons. Strong correlation peaks between **A**-**B**-**C** in the region of

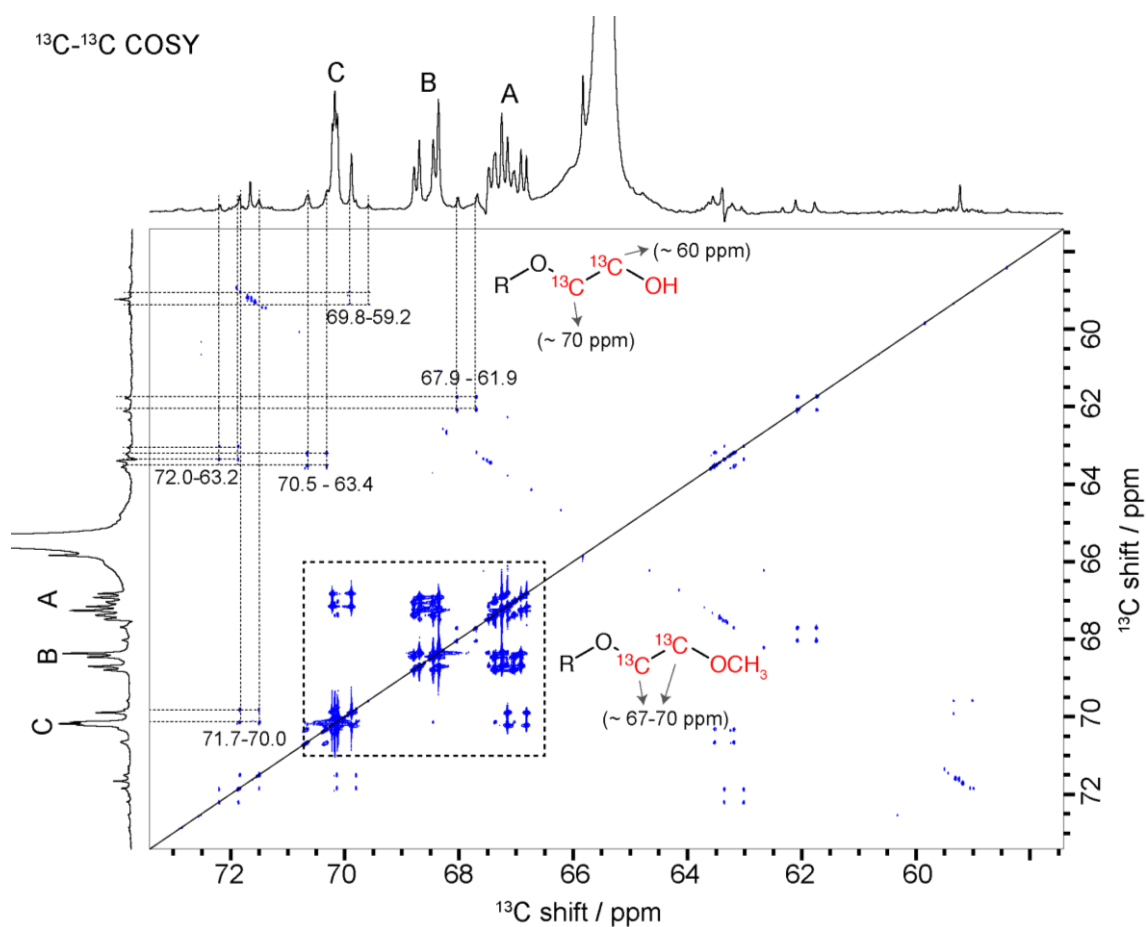


Figure 5.6 Full ^{13}C - ^{13}C COSY spectrum of cyclized LP30+ $^{13}\text{C}_3$ EC. The central diagonal peak of $^{13}\text{C}_3$ EC is removed for spectrum clarity.

67–70 ppm are observed and these peaks can be assigned to long-chain PEO, or EO with methoxide terminal. Weak cross-peaks for carbons at ~ 70 ppm and ~ 60 ppm regions are also present and are assigned to EO units with hydroxyl terminals based on their chemical shifts. Epoxy carbon bound to a methoxide ($\text{R}\underline{\text{C}}\text{H}_2\text{OCH}_3$) has the ^{13}C shift around 70 ppm, while the carbon bound to a hydroxyl end group ($\text{R}\underline{\text{C}}\text{H}_2\text{OH}$) should have a lower ^{13}C shift at about 60 ppm based on empirical calculations.

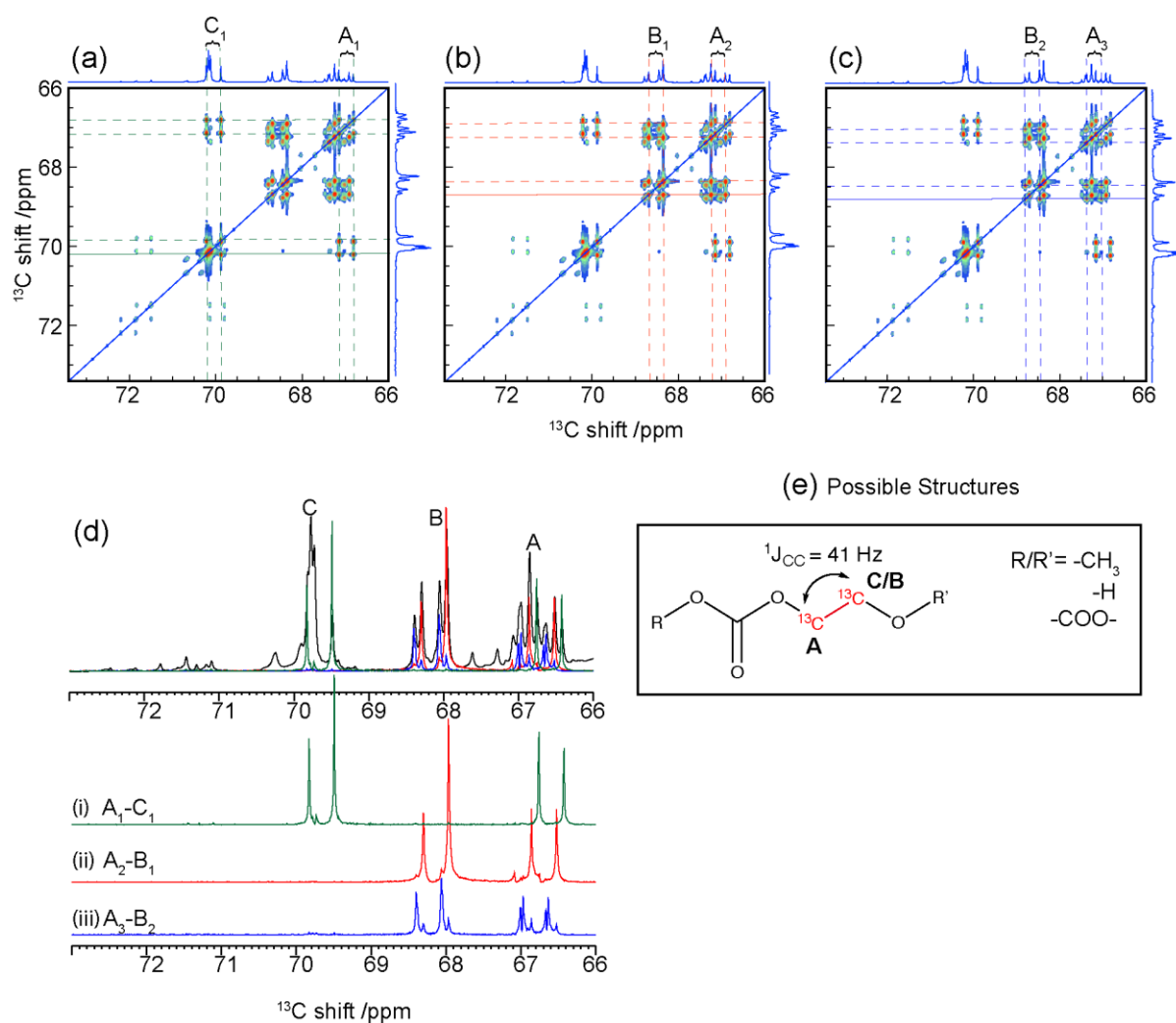


Figure 5.7 ^{13}C - ^{13}C COSY spectra of cycled LP30+ $^{13}\text{C}_3$ EC electrolyte after 30 cycles (a-c). The 1D ^{13}C NMR spectrum and the extracted 1D slices from the COSY spectra (d). Proposed chemical structures derived from the correlation experiments (e).

An enlarged ^{13}C COSY spectrum in the A-B-C region is shown in Figure 5.7. A cross peak can be found between the doublet A_1 and doublet C_1 , confirming the formation of a $-\text{O}^{13}\text{CH}_2^{13}\text{CH}_2\text{O}-$ unit (the doublet arises from $^1J_{\text{CC}} = 41 \text{ Hz}$). Similarly, carbon pairs A_2 - B_1 and A_3 - B_2 should also be both ^{13}C labelled. The 1D slices extracted from the 2D spectra are overlaid in Figure 5.7 d. The carbon correlation matches well with the ^1H - ^1H COSY data: proton a_1 is connected to proton b and c , but b and c are not connected to each other. Questions remain as what molecular structure leads to such correlation patterns and what leads to the different ^1H and ^{13}C shifts in the ethylene oxide region?

5.3.5 ^1H and ^{13}C chemical shifts of oligomers.

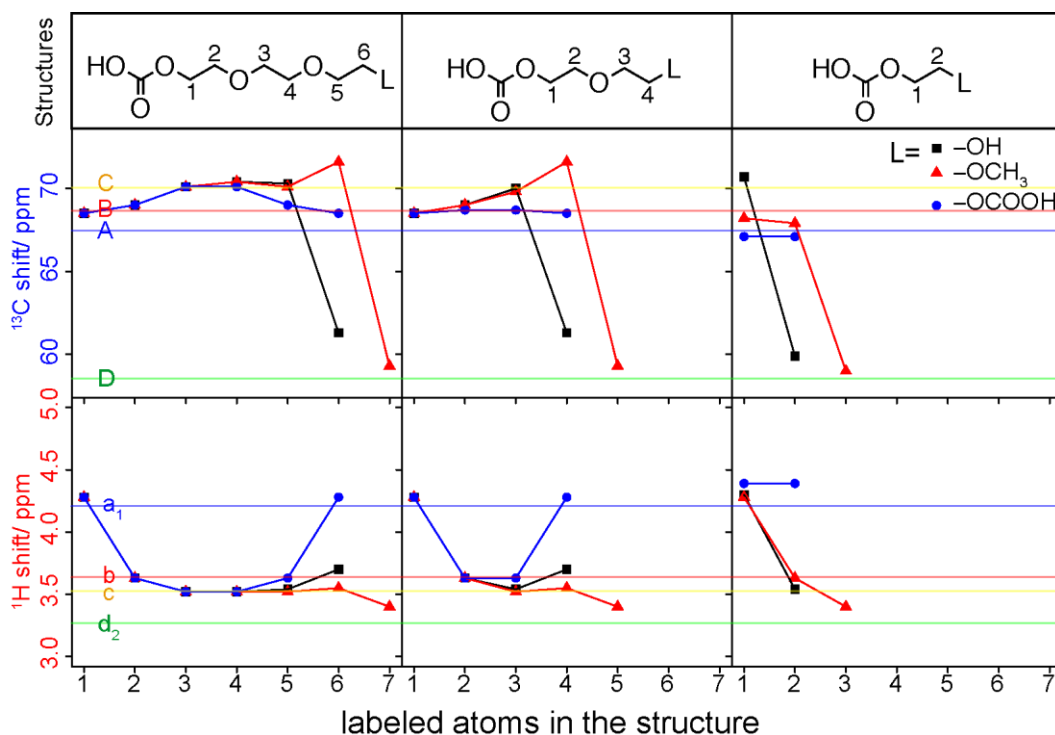


Figure 5.8 ^{13}C and ^1H NMR shift predicted by ChemDraw Software for alkyl carbonate oligomers with different ending groups (hydroxide in black square, methoxide in red triangle, carbonate in blue dot) and different chain lengths (increasing ethylene oxide units from left to right). The atoms connected to the carbonate are labelled from 1 and onwards. The experimental ^{13}C and ^1H NMR shifts values are drawn as solid lines with labels corresponding to the peaks observed in ^{13}C and ^1H NMR spectra. For oligomers containing methoxide ending group, the ^1H and ^{13}C NMR is also predicted for the methoxide, and they are labelled as the last number.

A systematic investigation was made of oligomers with different end groups and varying chain lengths ($\text{HOCO}-(\text{OCH}_2\text{CH}_2)_n\text{-R}$, $\text{R}=\text{-OH, -OCH}_3, \text{-OCOOH}$, $n = 1 - 3$) in order to better understand the trend of the ^1H and ^{13}C shifts for these species. Figure 5.8 summarizes the chemical shifts within these oligomers. A general trend is that the ethoxy carbon near a carbonate group has a lower ^{13}C shift (~ 67 ppm) than carbons in the PEO chains (~ 70 ppm). The ethoxy carbon near a carbonate is labelled as site 1 (the middle panel in Figure 5.8), the chemical shift of which is always smaller than the ^{13}C shifts at sites 2 and 3. The lower ^{13}C shift is due to the electron withdrawing nature of the carbonate group. On the other hand, the

ethoxy carbon bound to the electron donating methoxide group ($R\text{CH}_2\text{-OCH}_3$) has a higher ^{13}C shift (~ 72 ppm) than PEO carbon.

Experimental ^1H and ^{13}C shifts observed in the cycled electrolyte are shown as coloured lines in Figure 5.8, and the same labelling scheme is used here as it is in Figure 5.3. Comparing the calculation values and the experimental results, proton **d**₂ can be safely assigned to a terminal methoxide group. The decrease of ^1H shift values from **a**₁ to **b** and **c** can be explained by their distance to the next carbonate group. The structure derived from the calculation trend is consistent with the 2D NMR experimental data, further confirming that **a**₁ is part of a $\text{ROCOOCH}_2\text{CH}_2\text{R}$ fragment.

5.3.6 Confirmation of oligomers by mass spectrometry

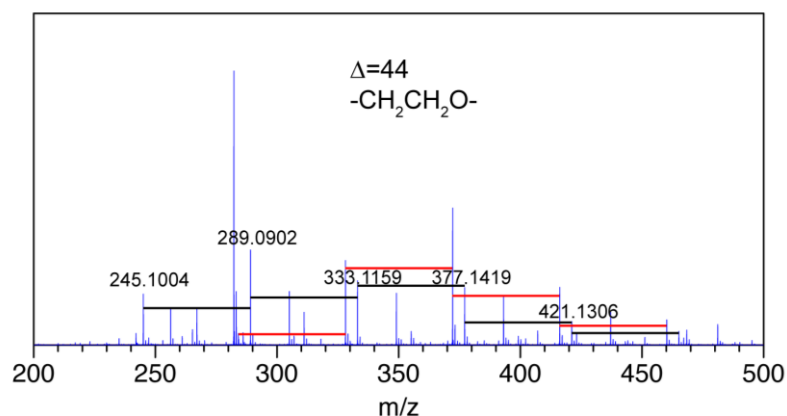
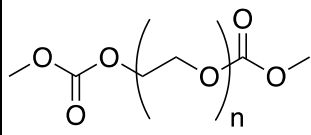


Figure 5.9 ESI-HRMS spectrum of SiNWs cycled in LP30 electrolyte for 30 cycles. The cycled SiNWs were soaked in CH_3CN , then the solution is diluted before MS measurement.

The molecular weights of the soluble SEI oligomers are analysed by ESI-HRMS. The result of the cycled LP30 sample is presented in Figure 5.9 with experimental values marked on the peaks. First, a regular spacing of 44.026 between these peaks is observed and this value matches the mass of an ethylene oxide unit with ^{12}C isotope. Second, the experimental molecular mass can be assigned to the oligomers shown in Table 5.2 with high confidence. The proposed oligomers consist of ethylene oxides units, two carbonates, and methoxide end groups. The comparison between the experimental data and the calculation values are summarized in Table 5.2.

The presence of Na⁺ and the absence of Li⁺ in the HRMS data is attributed to the sample preparation procedures. The cycled SiNWs were soaked in CH₃CN solvent to dissolve the polymeric SEI, then the solid SiNWs were removed by centrifuge. Since the concentration of the polymer solution is unknown, the supernatant was diluted with 1:3 ratio for three times with by CH₃CN before HRMS measurement to avoid possible damage on the chromatography. The Li⁺ may be diluted below the detection limit during this procedure and Na⁺ may be introduced during sample handling. Nevertheless, the presence of the dicarbonate oligomers is reproducible and the result is consistent with a comprehensive study by Gachot *et al.*,¹⁰² who reported the same series of degradation products in the EC-based electrolyte after electrochemical cycling.

Table 5.2 Mass spectroscopy data and the proposed structures with their corresponding mass.

Structure	n	Mass	Experimental mass	Calculated mass	Formula	error / ppm
	3	245	245.0638	245.0637	C ₈ H ₁₄ O ₇ Na ⁺	0.4
	4	289	289.0901	289.0899	C ₁₀ H ₁₈ O ₈ Na ⁺	0.7
	5	333	333.1159	333.1161	C ₁₂ H ₂₂ O ₉ Na ⁺	0.6
	6	377	377.1419	377.1424	C ₁₄ H ₂₆ O ₁₀ Na ⁺	1.3
	7	421	421.1666	421.1686	C ₁₆ H ₃₀ O ₁₁ Na ⁺	4.7

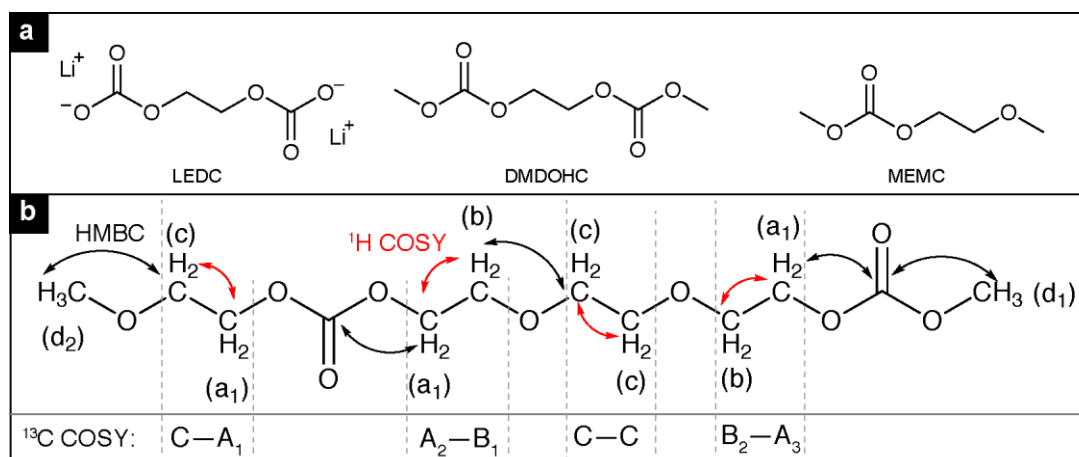
5.4 Discussion

Oligomers containing ethylene oxide and carbonate units are identified as the major electrochemical reduction products from EC. Smaller oligomers have been reported before. For example, lithium ethylenedicarbonate (LEDC), dimethyl-2,5-dioxahexane dicarboxylate (DMDOHC) and 2-methoxyethyl methyl carbonate (MEMC) as shown in in Scheme 5.1a have been observed as singlets in ¹H NMR spectroscopy,¹⁵² but the structure of the major oligomers with more complex ¹H patterns remain unsolved.

Here, we identified one major degradation oligomer of EC, called **a1-b-c**, based on the 2D correlation NMR experiments and mass spectroscopy data. A possible chemical structure of **a1-b-c** is shown in Scheme 5.1b. It contains two carbonate groups separated by three ethylene oxide units with methoxide end groups. The assignment of carbon **A**, **B**, **C** and their

corresponding proton **a**, **b**, **c** are labelled besides the structure. The correlation peaks observed in the 2D HSQC and HMBC NMR spectra are also illustrated on the structure. The proton integral ratios obtained from ^1H NMR spectra of different samples consistently show that $\mathbf{a}_1:\mathbf{b}:\mathbf{c}:\mathbf{d}_2 = 1:1:1:0.5$ (Figure 5.4). This value is similar to the proton ratio in the proposed structure ($\mathbf{a}_1:\mathbf{b}:\mathbf{c}:\mathbf{d}_2 = 1:\frac{2}{3}:1:0.5$).

Scheme 5.1 Possible reduction products of EC. (a) Small molecules reported in literatures.^{116,152} (b) oligomers identified in this work. Protons labelled from (a-d) are consistent with the labelling in Figure 5.3. Carbon correlation observed in Figure 5.7 are marked on the structures. Correlation observed in the ^1H - ^1H COSY are denoted as red arrows and the ^1H - ^{13}C HMBC in black arrows.



The trend of the ^{13}C shifts for carbon **A**, **B** and **C** in the proposed structure is also consistent with the calculation results: the ethoxy carbon bound to a methoxide group (carbon **C**, 70.0 ppm) has a higher ^{13}C shift than the ethoxy carbon bound to another EO unit (carbon **B**₁ and **B**₂, 68.6 ppm) due to the electron donating nature of the methoxide terminal group. As a result, the carbon **C**-**A**₁ unit should show different chemical shifts from the carbon **A**₂-**B**₁ pairs, and these assignments are consistent with the observation shown in the ^{13}C COSY spectrum.

The carbon unit in the middle of the PEO chain is also assigned to carbon **C** as it should also have a carbon shift at 70 ppm. Thus, the proposed structure explains the observation of **A**-**B** and **A**-**C** correlations, but not **B**-**C** correlations in both ^1H and ^{13}C COSY experiment. (Note that ^{13}C COSY spectrum only shows direct bonded carbon pairs, but not carbons bridged by an oxygen) Only three EO units should be in between the two carbonate groups. If more than three EO units are present, it should give rise to more PEO-type carbons (~ 70 ppm, carbon **C**) and

PEO protons (~ 3.5 ppm, proton **c**). Then the proton integral ratio for **a₁:b:c** would not be 1:1:1 as observed in the experimental data. If only two EO units are in between the carbonate groups, the structure is similar to LEDC and we should only observe proton **a** and **b** without proton **c**. And the correlation peaks for proton **b** and **c** with carbon **B** and **C** in HMBC spectra would not be detectable.

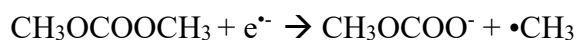
The terminal methoxide group is identified by a clear correlation between the proton **d₂** and a carbon with resonance at 70 ppm, which is carbon **C** in the labelling scheme in the HMBC spectra (Figure 5.3c and f). This confirms that proton **d₂** is connected to the **a₁-b-c** oligomer. However, the diffusion coefficient for proton **d₂** is slightly higher than proton **c** as shown in the DOSY NMR spectrum ($4.94\text{E-}10$ m/s² for **d₂** and $4.41\text{E-}10$ m/s² for **c**). This small difference may arise from the systematic error in the DOSY experiment. Because proton **a₃** and **e** exhibits different diffusion coefficients at $7.46\text{E-}10$ and $8.04\text{E-}10$ m/s², respectively, while they have been clearly identified to be protons in the methanol molecule. Therefore, it is believed that proton **d₂** is most likely to be the end group for the **a₁-b-c** oligomer instead of being a part of another oligomer.

Based on the ESI-HRMS data, two methoxide end groups instead of hydroxyl groups are proposed for the **a₁-b-c** oligomer. Apart from the methoxide containing **d₂** proton, the other terminal group is tentatively assigned to a methoxide bound to a carbonate containing protons resonating at **d₁**. The proton **d₁** in the proposed **a₁-b-c** oligomer may overlap with the proton peaks in LMC ($\text{C}\underline{\text{H}}_3\text{OCOO}^-\text{Li}^+$), thus, its integral is not considered here.

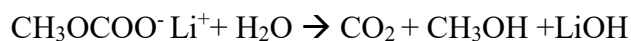
The proposed structure in Scheme 5.1b corresponds to the structure with $n = 4$ in Table 5.2. Though a series of oligomers are detected by HRMS, these oligomers may form due to the decomposition of insoluble SEI (because HRMS was performed on the acetonitrile solution that is mixed with SiNW to dissolve the insoluble SEI). Note that the HRMS measurement was performed in air with water contamination as water is an inevitable component in the carrier phase for HRMS measurement. Therefore, the detected species listed in Table 5.2 only indirectly aided our interpretation of the observed NMR data but does not directly contain the structural information nor the relative abundance of the degradation product.

The proposed **a₁-b-c** oligomers with methoxide terminals should be chemically more stable than those terminated by -OH or -OCOOH groups on highly lithiated silicide. However, the **a₁-b-c** oligomer potentially have a lower affinity to the Si surface than molecules with -O⁻Li⁺ or -OCOO⁻Li⁺ end groups. This may be part of the reason why it is observed as the major soluble degradation species in the cycled electrolyte. Future modelling on the conformation of this oligomer would be helpful to better understand its properties.

The other major degradation species comes from DMC. A strong singlet at 3.28 ppm (**d₁**) in the ¹H NMR spectrum is identified as lithium methyl carbonate (**CH₃OCOO⁻Li⁺**, LMC). LMC forms from the one electron reduction of DMC together with the formation of a methyl radical.



Here, LMC is found to be highly water sensitive. When water is present in the sample, the ¹H resonance at **d₁** decreases, and new peaks at **a₃** and **e** appear. This confirms a hydrolysis reaction of LMC to form CO₂ and methanol, and the reaction is given below:



It is worth noting that DMC is not ¹³C labelled and the fact that we are able to clearly identify the formation of LMC via 2D correlation NMR experiments indicates that the concentration of LMC formed in the electrolyte must be higher than the detection limit of these NMR experiments.

5.5 Conclusion

EC is chemically unstable in low voltages window (<1.2 V vs. Li⁺/Li) and its major electrochemical reduction products are identified to be linear ethylene oxide carbonate type oligomers by a combination of solution NMR and ESI–HRMS experiments. The major oligomer has three EO units in between two carbonate groups and contains methoxide as end groups (Scheme 5.1). The major degradation product from DMC, lithium methyl carbonate (LMC), is also observed. LMC is unstable in the presence of trace amount of water and decomposes to form methanol.

All the observed degradation products are of a linear structure and are highly soluble in the electrolyte. Oligomers with methoxide terminal groups may have low affinity to the Si surface, therefore, they detach from the Si surface and cannot form a stable SEI. Methods to reduce the solubility of these oligomers by electrolyte saturation would be helpful for suppressing further EC degradation. Lastly, it may be useful to probe the state of health of a battery by monitoring the formation of these oligomers quantitatively using either NMR or mass spectrometry. With the chemical shift database implemented and all characterization techniques available, solution NMR combined with ESI–HRMS can be routinely used to analyse the degradation of other electrolyte formulations.

Chapter 6 Conclusions and Future Work

This study investigated the chemical composition of the interfacial species formed on high-capacity Si anodes in lithium ion batteries and identified key polymeric species implicated in battery performance enhancement. A variety of NMR techniques including dynamic nuclear polarization were used to understand the reduction mechanisms of conventional ethylene carbonate (EC)-based electrolytes as well as the two most-widely used electrolyte additives in lithium ion batteries: fluoroethylene carbonate (FEC) and vinylene carbonate (VC). As such, there are many insights derived from this work that have important implications for future research on electrolyte additives, surface engineering and solid polymer electrolytes.

First, a combination of model system and enriched electrolyte is used to analyze the amorphous interphase. Silicon nanowires (SiNW) have been employed, for the first time, for the studies on the solid electrolyte interphase (SEI) by NMR spectroscopy, because SiNW electrodes provide a large specific surface area, ensure electronic wiring and avoid interference from the polymeric binders commonly present in conventional composite electrodes. $^{13}\text{C}_3$ enriched FEC was successfully synthesized to overcome the sensitivity issue of ^{13}C NMR experiments, enabling the detection of organic SEI species. The ^{13}C -labelled FEC leads to unique ^1H NMR J-coupling patterns after electrochemical cycling, which provide unambiguous assignment of the spectra. FEC is found to defluorinate and convert to VC and vinoxyl species in the electrolyte, which subsequently react to form an insoluble polymer on the Si anode. Clear differences in the organic decomposition products formed with and without $^{13}\text{C}_3$ -FEC additive are observed by ^{13}C NMR: a crosslinking polymer containing acetal carbon forms in the presence of FEC, whereas a linear poly(ethylene oxide)-type polymer forms in the additive-free electrolyte.

The advantageous effects of these additives were explored by cycling SiNW with pure FEC and VC electrolytes containing 1M LiPF_6 . An improved electrochemical performance is observed for pure FEC and VC electrolytes and the improvements are again linked to the presence of a cross-linked polymer formed from the reduction of FEC/VC. Quantitative

information about the cross-linked polymer is obtained by ^{13}C NMR, showing that it consists of ~40 % alkyl chains, 30 % poly(ethylene oxide), and 10 % crosslinking acetal carbons and other carbonate and carboxylate functional groups. With the improved sensitivity obtained by DNP NMR, connectivity between these polymeric species is further confirmed by ^{13}C - ^{13}C correlation NMR, and atomic information about the interphase between the SEI and the Si anode is revealed by ^{29}Si DNP NMR. Organosiloxanes are found to form as a function of cycling in all electrolyte formulations, suggesting that the Si-C bond is intrinsically stable in the reducing environment. This study demonstrated that surface-enhanced DNP NMR methods can be successfully applied to study the air- and water-sensitive interphase on battery materials; DNP also enables us to probe the buried interphase (e.g. SiO_x -SEI) previously considered invisible by conventional NMR techniques.

Finally, an intriguing problem about a soluble degradation product is solved by a combination of solution NMR and mass spectrometry. The reduction product of EC has unique ^{13}C and ^1H shifts in solution NMR, and its chemical structure is determined by 2D correlation and diffusion NMR experiments. The degradation product is revealed to be a highly soluble oligomer which forms continuously in the EC-based electrolyte; its formation irreversibly consumes Li sources and leads to the capacity fading observed in the Si anode.

These findings shed light on future research on new electrolyte additives and the design of passivation layers on alloy-type anodes. First, FEC and VC preferentially undergo reduction prior to the more abundant EC molecules. Secondly, in the proposed decomposition mechanisms for FEC and VC, species containing unsaturated double bonds or aldehyde groups are the precursors for forming cross-linked polymers. Combining this information together, it is expected that novel additives containing vinyl or aldehyde groups with high reduction potential should also form similar cross-linked polymers that likely exhibit improved cycle life for alloy-type anodes. Further experimental screening is needed, however, to optimize the electrolyte formulation for Si anodes.

A second research question relates to the role of inorganic Li salts such as LiF in the SEI. Since FEC converts to VC, the functional difference between these two additives can be attributed to the formation of LiF or the concentration difference of VC present in the electrolyte. LiF is found to be electronically insulating and exhibits low Li ionic conductivity at room temperature,

thus its role may depend on other factors such as its morphology, crystallinity, particle size and its spatial distribution within the SEI. Further studies are needed to investigate the nature of LiF and its interaction with organic SEI components. Properties of the SEI such as electronic and Li-ionic conductivity, elasticity and solvent permeability should be measured to fully understand SEI's influence on battery performance.

Using electrolyte additives at high concentration does not adequately solve the problem of capacity retention. Novel artificial coating layers or solid polymer electrolytes are safer alternatives to the flammable liquid electrolyte.¹⁴⁸ Based on the characterization results reported in this thesis, it is hoped that the cross-linked poly(ethylene oxide) material can be synthesized with controlled porosity and elasticity to test its compatibility with alloy-type anodes. The use of a composite solid polymer electrolyte based on this material together with inorganic fillers such as nano SiO₂ and LiF may lead to promising results in the future. Apart from the bulk properties of the solid polymer electrolyte, the interfacial region between the polymer and the active material should also be carefully engineered to achieve certain bonding modes (e.g. hydrogen or covalent bonding), so as to reduce the interfacial resistance and to maintain strong mechanical integrity of the electrode.

The studies undertaken in this thesis show that a combination of solution and solid-state NMR techniques provides important structural information about the degradation products in the liquid electrolyte system. Only by understanding the structure-property relationship in these passivation products that are present in conventional batteries will it be possible to find a rational way forward to develop artificial SEI coatings or solid polymer electrolytes for next-generation lithium ion batteries.

References

- (1) Goodenough, J. B.; Park, K. *J. Am. Chem. Soc.* **2013**, *135*, 1167–1176.
- (2) Dunn, B.; Kamath, H.; Tarascon, J.-M. *Science*. **2011**, *334*, 928–935.
- (3) Kwade, A.; Haselrieder, W.; Leithoff, R.; Modlinger, A.; Dietrich, F.; Droeder, K. *Nat. Energy* **2018**, *3*, 290–300.
- (4) Cano, Z. P.; Banham, D.; Ye, S.; Hintennach, A.; Lu, J.; Fowler, M.; Chen, Z. *Nat. Energy* **2018**, *3*, 279–289.
- (5) Goodenough, J. B.; Kim, Y. *Chem. Mater.* **2010**, *22*, 587–603.
- (6) Sun, Y.-K.; Myung, S.-T.; Kim, M.-H.; Prakash, J.; Amine, K. *J. Am. Chem. Soc.* **2005**, *127*, 13411–13418.
- (7) Rozier, P.; Tarascon, J. M. *J. Electrochem. Soc.* **2015**, *162*, A2490–A2499.
- (8) Xu, K. *Chem. Rev.* **2004**, *104*, 4303–4417.
- (9) Xu, K. *Chem. Rev.* **2014**, *114*, 11503–11618.
- (10) Obrovac, M. N.; Chevrier, V. L. *Chem. Rev.* **2014**, *114*, 1144–1502.
- (11) He, Y. B.; Liu, M.; Huang, Z. D.; Zhang, B.; Yu, Y.; Li, B.; Kang, F.; Kim, J. K. *J. Power Sources* **2013**, *239*, 269–276.
- (12) Zhang, H.; Eshetu, G. G.; Judez, X.; Li, C.; Rodriguez-Martínez, L. M.; Armand, M. *Angew. Chemie Int. Ed.* **2018**. DOI: 10.1002/anie.201712702
- (13) Kato, Y.; Hori, S.; Saito, T.; Suzuki, K.; Hirayama, M.; Mitsui, A.; Yonemura, M.; Iba, H.; Kanno, R. *Nat. Energy* **2016**, *1*, 16030.
- (14) Haregewoin, A. M.; Wotango, A. S.; Hwang, B.-J. *Energy Environ. Sci.* **2016**, *9*, 1955–1988.
- (15) Xia, J.; Petibon, R.; Xiao, A.; Lamanna, W. M.; Dahn, J. R. *J. Electrochem. Soc.* **2016**, *163*, A1637–A1645.
- (16) Chen, G.; Zhuang, G. V.; Richardson, T. J.; Liu, G.; Ross, P. N. *Electrochem. Solid-State Lett.* **2005**, *8*, A344.
- (17) Han, G. B.; Ryou, M. H.; Cho, K. Y.; Lee, Y. M.; Park, J. K. *J. Power Sources* **2010**, *195*, 3709–3714.
- (18) Ryu, Y.-G.; Lee, S.; Mah, S.; Lee, D. J.; Kwon, K.; Hwang, S.; Doo, S. *J. Electrochem. Soc.* **2008**, *155*, 583–589.

- (19) Sun, X.; Lee, H. S.; Yang, X.-Q.; McBreen, J. *Electrochem. Solid-State Lett.* **2002**, *5*, 248-251.
- (20) Jerliu, B.; Hüger, E.; Dörrer, L.; Seidlhofer, B. K.; Steitz, R.; Oberst, V.; Geckle, U.; Bruns, M.; Schmidt, H. *J. Phys. Chem. C* **2014**, *118*, 9395–9399.
- (21) Choi, J. W.; Aurbach, D. *Nat. Rev. Mater.* **2016**, *1*, 16013.
- (22) Kwon, T. W.; Choi, J. W.; Coskun, A. *Chem. Soc. Rev.* **2018**, *47*, 2145–2164.
- (23) Ng, S. H.; Wang, J.; Wexler, D.; Konstantinov, K.; Guo, Z. P.; Liu, H. K. *Angew. Chemie - Int. Ed.* **2006**, *45*, 6896–6899.
- (24) Hu, Y. S.; Demir-Cakan, R.; Titirici, M. M.; Müller, J. O.; Schlögl, R.; Antonietti, M.; Maier, J. *Angew. Chemie - Int. Ed.* **2008**, *47*, 1645–1649.
- (25) Liu, N.; Lu, Z.; Zhao, J.; McDowell, M. T.; Lee, H. W.; Zhao, W.; Cui, Y. *Nat. Nanotechnol.* **2014**, *9*, 187–192.
- (26) Han, X.; Chen, H.; Liu, J.; Liu, H.; Wang, P.; Huang, K.; Li, C.; Chen, S.; Yang, Y. *Electrochim. Acta* **2015**, *156*, 11–19.
- (27) Han, X.; Chen, H.; Zhang, Z.; Huang, D.; Xu, J.; Li, C.; Chen, S.; Yang, Y. *J. Mater. Chem. A* **2016**, *4*, 17757–17763.
- (28) Li, Y.; Yan, K.; Lee, H.-W.; Lu, Z.; Liu, N.; Cui, Y. *Nat. Energy* **2016**, *1*, 16017.
- (29) Miyachi, M.; Yamamoto, H.; Kawai, H.; Ohta, T.; Shirakata, M. *J. Electrochem. Soc.* **2005**, *152*, 2089–2091.
- (30) Komaba, S.; Shimomura, K.; Yabuuchi, N.; Ozeki, T.; Yui, H.; Konno, K. *J. Phys. Chem. C* **2011**, *115*, 13487–13495.
- (31) Magasinski, A.; Zdyrko, B.; Kovalenko, I.; Hertzberg, B.; Burtovyy, R.; Huebner, C. F.; Fuller, T. F.; Luzinov, I.; Yushin, G. *ACS Appl. Mater. Interfaces* **2010**, *2*, 3004–3010.
- (32) Bridel, J. S.; Azais, T.; Morcrette, M.; Tarascon, J. M.; Larcher, D. *Chem. Mater.* **2010**, *22*, 1229–1241.
- (33) Han, Z.-J.; Yamagiwa, K.; Yabuuchi, N.; Son, J.-Y.; Cui, Y.-T.; Oji, H.; Kogure, A.; Harada, T.; Ishikawa, S.; Aoki, Y.; Komaba, S. *Phys. Chem. Chem. Phys.* **2015**, *17*, 3783–3795.
- (34) Choi, S.; Kwon, T.; Coskun, A.; Choi, J. W. *Science* **2017**, *283*, 279–283.
- (35) Dalavi, S.; Guduru, P.; Lucht, B. L. *J. Electrochem. Soc.* **2012**, *159*, A642.
- (36) Etacheri, V.; Haik, O.; Goffer, Y.; Roberts, G. a.; Stefan, I. C.; Fasching, R.; Aurbach, D. *Langmuir* **2012**, *28*, 965–976.
- (37) Etacheri, V.; Geiger, U.; Gofor, Y.; Roberts, G. a.; Stefan, I. C.; Fasching, R.; Aurbach, D. *Langmuir* **2012**, *28*, 6175–6184.
- (38) Schroder, K. W.; Celio, H.; Webb, L. J.; Stevenson, K. J. *J. Phys. Chem. C* **2012**, *116*, 19737–19747.
- (39) Schroder, K. W.; Dylla, A. G.; Harris, S. J.; Webb, L. J. *Appl. Mater. interfaces* **2014**, *6*, 21510–21524.
- (40) Schroder, K.; Alvarado, J.; Yersak, T. a.; Li, J.; Dudney, N.; Webb, L. J.; Meng, Y. S.;

- Stevenson, K. J. *Chem. Mater.* **2015**, *27*, 5531–5542.
- (41) Nakai, H.; Kubota, T.; Kita, A.; Kawashima, A. *J. Electrochem. Soc.* **2011**, *158*, 798–801.
- (42) Nie, M.; Abraham, D. P.; Chen, Y.; Bose, A.; Lucht, B. L. *J. Phys. Chem. C* **2013**, *117*, 13403–13412.
- (43) Nie, M.; Demeaux, J.; Young, B. T.; Heskett, D. R.; Chen, Y.; Bose, A.; Woicik, J. C.; Lucht, B. L. *J. Electrochem. Soc.* **2015**, *162*, 7008–7014.
- (44) Xu, K.; Cresce, A. Von; Lee, U. *Langmuir* **2010**, *26*, 11538–11543.
- (45) Cabo-Fernandez, L.; Mueller, F.; Passerini, S.; Hardwick, L. J. *Chem. Commun.* **2016**, *52*, 3970–3973.
- (46) Ota, H.; Sakata, Y.; Inoue, A.; Yamaguchi, S. *J. Electrochem. Soc.* **2004**, *151*, A1659.
- (47) Michan, A. L.; Leskes, M.; Grey, C. P. *Chem. Mater.* **2015**, *28*, 385–398.
- (48) Michan, A. L.; Divitini, G.; Pell, A. J.; Leskes, M.; Ducati, C.; Grey, C. P. *J. Am. Chem. Soc.* **2016**, *138*, 7918–7931.
- (49) Michan, A. L.; Parimalam, B. S.; Leskes, M.; Kerber, R. N.; Yoon, T.; Grey, C. P.; Lucht, B. L. *Chem. Mater.* **2016**, *28*, 8149–8159.
- (50) Nie, M.; Chalasani, D.; Abraham, D. P.; Chen, Y.; Bose, A.; Lucht, B. L. *J. Phys. Chem. C* **2013**, *117*, 1257–1267.
- (51) Leung, K.; Soto, F.; Hankins, K.; Balbuena, P. B.; Harrison, K. L. *J. Phys. Chem. C* **2016**, *120*, 6302–6313.
- (52) Jung, R.; Metzger, M.; Haering, D.; Solchenbach, S.; Marino, C.; Tsiouvaras, N.; Stinner, C.; Gasteiger, H. A. *J. Electrochem. Soc.* **2016**, *163*, 1705–1716.
- (53) Ma, L.; Glazier, S. L.; Petibon, R.; Xia, J.; Peters, J. M.; Liu, Q.; Allen, J.; Doig, R. N. C.; Dahn, J. R. *J. Electrochem. Soc.* **2017**, *164*, A5008–A5018.
- (54) El Ouatani, L.; Dedryvère, R.; Siret, C.; Biensan, P.; Reynaud, S.; Iratçabal, P.; Gonbeau, D. *J. Electrochem. Soc.* **2009**, *156*, A103–A113.
- (55) Chen, L.; Wang, K.; Xie, X.; Xie, J. *Electrochem. Solid-State Lett.* **2006**, *9*, A512.
- (56) Leifer, N.; Smart, M. C.; Prakash, G. K. S.; Gonzalez, L.; Sanchez, L.; Smith, K. A.; Bhalla, P.; Grey, C. P.; Greenbaum, S. G. *J. Electrochem. Soc.* **2011**, *158*, A471–A480.
- (57) Markevich, E.; Salitra, G.; Aurbach, D. *ACS Energy Lett.* **2017**, *2*, 1337–1345.
- (58) Metzger, M.; Strehle, B.; Solchenbach, S.; Gasteiger, H. A. *J. Electrochem. Soc.* **2016**, *163*, A798–A809.
- (59) Philippe, B.; Dedryveire, R.; Gorgoi, M.; Rensmo, H.; Gonbeau, D.; Edström, K. *J. Am. Chem. Soc.* **2013**, *135*, 9829–9842.
- (60) Chan, C. K.; Ruffo, R.; Hong, S. S.; Huggins, R. a.; Cui, Y. *J. Power Sources* **2009**, *189*, 34–39.
- (61) Lindgren, F.; Xu, C.; Niedzicki, L.; Marcinek, M.; Gustafsson, T.; Björefors, F.; Edström, K.; Younesi, R. *ACS Appl. Mater. Interfaces* **2016**, *8*, 15758–15766.

- (62) Xu, C.; Lindgren, F.; Philippe, B.; Gorgoi, M.; Björefors, F.; Edström, K.; Gustafsson, T. *Chem. Mater.* **2015**, *27*, 2591–2599.
- (63) Siqi, S. Direct Calculation of Li-Ion Transport in the Solid Electrolyte Interphase, 2012.
- (64) Tang, M.; Newman, J. *J. Electrochem. Soc.* **2012**, *159*, A281–A289.
- (65) Han, X.; Chen, H.; Li, X.; Wang, J.; Li, C.; Chen, S.; Yang, Y. *J. Mater. Chem. A* **2016**, *4*, 434–442.
- (66) Khurana, R.; Schaefer, J. L.; Archer, L. A.; Coates, G. W. *J. Am. Chem. Soc.* **2014**, *136*, 7395–7402.
- (67) Gao, Y.; Yi, R.; Li, Y. C.; Song, J.; Chen, S.; Huang, Q.; Mallouk, T. E.; Wang, D. *J. Am. Chem. Soc.* **2017**, *139*, 17359–17367.
- (68) Piper, D. M.; Yersak, T. A.; Son, S. B.; Kim, S. C.; Kang, C. S.; Oh, K. H.; Ban, C.; Dillon, A. C.; Lee, S. H. *Adv. Energy Mater.* **2013**, *3*, 697–702.
- (69) Piper, D. M.; Woo, J. H.; Son, S. B.; Kim, S. C.; Oh, K. H.; Lee, S. H. *Adv. Mater.* **2014**, *26*, 3520–3525.
- (70) Khurana, R.; Schaefer, J.; Archer, L. A.; Coates, G. W.; Schaefer, J. L.; Coates, G. W. *J. Am. Chem. Soc.* **2014**, *136*, 7395–7402.
- (71) Gao, Y.; Zhao, Y.; Li, Y. C.; Huang, Q.; Mallouk, T. E.; Wang, D. *J. Am. Chem. Soc.* **2017**, *139*, 15288–15291.
- (72) Wagner, R. S.; Ellis, W. C. *Appl. Phys. Lett.* **1964**, *4*, 89–90.
- (73) Schmidt, V.; Wittemann, J. V.; Senz, S.; Gösele, U. *Adv. Mater.* **2009**, *21*, 2681–2702.
- (74) Cui, Y.; Duan, X.; Hu, J.; Lieber, C. M. *J. Phys. Chem. B* **2000**, *104*, 5213–5216.
- (75) Chen, L.; Lu, W.; Lieber, C. M. In *Semiconductor Nanowires: From Next-Generation Electronics to Sustainable Energy*; The Royal Society of Chemistry, 2015; pp 1–53.
- (76) Cui, L. F.; Ruffo, R.; Chan, C. K.; Peng, H.; Cui, Y. *Nano Lett.* **2009**, *9*, 3370–3374.
- (77) Ni, Q. Z.; Daviso, E.; Can, T. V.; Markhasin, E.; Jawla, S. K.; Swager, T. M.; Temkin, R. J.; Herzfeld, J.; Griffin, R. G. *Acc. Chem. Res.* **2013**, *46*, 1933–1941.
- (78) Chaudhari, S. R.; Griffin, J. M.; Broch, K.; Lesage, A.; Lemaur, V.; Dudenko, D.; Olivier, Y.; Siringhaus, H.; Emsley, L.; Grey, C. P. *Chem. Sci.* **2017**, *8*, 3126–3136.
- (79) Duer, M. J. *Introduction to Solid-State NMR Spectroscopy*; Wiley, 2005.
- (80) Keeler, J. *Understanding NMR Spectroscopy*; Wiley, 2011.
- (81) Levitt, M. H. *Spin Dynamics: Basics of Nuclear Magnetic Resonance*; Wiley, 2013.
- (82) Johnson Jr., C. S. *Prog. Nucl. Magn. Reson. Spectrosc.* **1999**, *34*, 203–256.
- (83) Fung, B. M.; Khitrin, A. K.; Ermolaev, K. *J. Magn. Reson.* **2000**, *101*, 97–101.
- (84) Hohwy, M.; Jakobsen, H. J.; Edén, M.; Levitt, M. H.; Nielsen, N. C. *J. Chem. Phys.* **1998**, *108*, 2686–2694.
- (85) Lilly Thankamony, A. S.; Wittmann, J. J.; Kaushik, M.; Corzilius, B. *Prog. Nucl. Magn. Reson. Spectrosc.* **2017**, *102–103*, 120–195.
- (86) Lesage, A.; Lelli, M.; Gajan, D.; Caporini, M. A.; Vitzthum, V.; Miéville, P.; Alauzun,

- J.; Roussey, A.; Thieuleux, C.; Mehdi, A.; Bodenhausen, G.; Copéret, C.; Emsley, L. *J. Am. Chem. Soc.* **2010**, *132*, 15459–15461.
- (87) Lelli, M.; Gajan, D.; Lesage, A.; Caporini, M. A.; Vitzthum, V.; Miéville, P.; Héroguel, F.; Rascón, F.; Roussey, A.; Thieuleux, C.; Boualleg, M.; Veyre, L.; Bodenhausen, G.; Copéret, C.; Emsley, L. *J. Am. Chem. Soc.* **2011**, *133*, 2104–2107.
- (88) Zagdoun, A.; Casano, G.; Ouari, O.; Schwarzwälder, M.; Rossini, A. J.; Aussenac, F.; Yulikov, M.; Jeschke, G.; Coperet, C.; Lesage, A.; Tordo, P.; Emsley, L. *J. Am. Chem. Soc.* **2013**, *135*, 12790–12797.
- (89) Sangodkar, R. P.; Smith, B. J.; Gajan, D.; Rossini, A. J.; Roberts, L. R.; Funkhouser, G. P.; Lesage, A.; Emsley, L.; Chmelka, B. F. *J. Am. Chem. Soc.* **2015**, *137*, 8096–8112.
- (90) Ogata, K.; Salager, E.; Kerr, C. J.; Fraser, a E.; Ducati, C.; Morris, a J.; Hofmann, S.; Grey, C. P. *Nat. Commun.* **2014**, *5*, 3217.
- (91) Piotto, M.; Bourdonneau, M.; Elbayed, K.; Wieruszkeski, J.-M.; Lippens, G. *Magn. Reson. Chem.* **2006**, *44*, 943–947.
- (92) Zhou, Z.; Kümmerle, R.; Qiu, X.; Redwine, D.; Cong, R.; Taha, A.; Baugh, D.; Winniford, B. *J. Magn. Reson.* **2007**, *187*, 225–233.
- (93) Metz, G.; Wu, X. L.; Smith, S. O. *Journal of Magnetic Resonance.* **1994**, *110*, 219–227..
- (94) Thakur, R. S.; Kurur, N. D.; Madhu, P. K. *Chem. Phys. Lett.* **2006**, *426*, 459–463.
- (95) Limthongkul, P.; Jang, Y. Il; Dudley, N. J.; Chiang, Y. M. *Acta Mater.* **2003**, *51*, 1103–1113.
- (96) Obrovac, M. N.; Christensen, L. *Electrochem. Solid-State Lett.* **2004**, *7*, A93–A96.
- (97) Key, B.; Bhattacharyya, R.; Morcrette, M.; Seznec, V.; Tarascon, J.-M.; Grey, C. P. *J. Am. Chem. Soc.* **2009**, *131*, 9239–9249.
- (98) Oumellal, Y.; Delpuech, N.; Mazouzi, D.; Dupré, N.; Gaubicher, J.; Moreau, P.; Soudan, P.; Lestriez, B.; Guyomard, D. *J. Mater. Chem.* **2011**, *21*, 6201.
- (99) Zhuang, G. V; Xu, K.; Yang, H.; Jow, T. R.; Ross, P. N. *J. Phys. Chem. B* **2005**, *109*, 17567–17573.
- (100) Soto, F. A.; Ma, Y.; Martinez De La Hoz, J. M.; Seminario, J. M.; Balbuena, P. B. *Chem. Mater.* **2015**, *27*, 7990–8000.
- (101) Gireaud, L.; Grugeon, S.; Pilard, S.; Guenot, P.; Tarascon, J. M.; Laruelle, S. *Anal. Chem.* **2006**, *78*, 3688–3698.
- (102) Gachot, G.; Grugeon, S.; Armand, M.; Pilard, S.; Guenot, P.; Tarascon, J. M.; Laruelle, S. *J. Power Sources* **2008**, *178*, 409–421.
- (103) Tavassol, H.; Buthker, J. W.; Ferguson, G. a.; Curtiss, L. a.; Gewirth, A. a. *J. Electrochem. Soc.* **2012**, *159*, A730–A738.
- (104) Liu, T.; Kim, G.; Casford, M. T. L.; Grey, C. P. *J. Phys. Chem. Lett.* **2016**, 4841–4846.
- (105) Zhu, Y.; Xianfeng; Huang; Guoqiang; Song. *Guangzhou Chem. Ind.* **2012**, *40*, 97–98.
- (106) Bernstein, H. J.; Pople, J, A.; Schneider, W. G. *Can. J. Chem.* **1957**, *35*, 65–81.
- (107) Pople, J, A.; Schneider, W. G.; Bernstein, H. J. *Can. J. Chem.* **1957**, *35*, 1060–1072.

- (108) Schneider, W. G.; Bernstein, H. J.; Pople, J. A. *Can. J. Chem.* **1957**, *35*, 1487–1495.
- (109) Findeisen, M.; Berger, S. *Magn. Reson. Chem.* **2003**, *41*, 431–434.
- (110) Williams, D. H.; Fleming, I. *Spectroscopic Methods in Organic Chemistry*; McGraw-Hill, 1995.
- (111) Heinze, T.; Koschella, A. *Macromol. Symp.* **2005**, *223*, 13–39.
- (112) Leskes, M.; Kim, G.; Liu, T.; Michan, A. L.; Aussenac, F.; Dorffer, P.; Paul, S.; Grey, C. P. *J. Phys. Chem. Lett.* **2017**, *8*, 1078–1085.
- (113) Cho, H. *J. Magn. Reson.* **1999**, *141*, 164–179.
- (114) Shkrob, I. a.; Zhu, Y.; Marin, T. W.; Abraham, D. *J. Phys. Chem. C* **2013**, *117*, 19270–19279.
- (115) Aurbach, D.; Daroux, M. L.; Faguy, P. W.; Yeager, E. *J. Electrochem. Soc.* **1987**, *134*, 1611–1620.
- (116) Xu, K.; Zhuang, G. R. V; Allen, J. L.; Lee, U.; Zhang, S. S.; Ross, P. N.; Jow, T. R. *J. Phys. Chem. B* **2006**, *110*, 7708–7719.
- (117) Aurbach, D.; Markovsky, B.; Weissman, I.; Levi, E.; Ein-Eli, Y. *Electrochim. Acta* **1999**, *45*, 67–86.
- (118) Zhang, B.; Metzger, M.; Solchenbach, S.; Payne, M.; Meini, S.; Gasteiger, H. A.; Garsuch, A.; Lucht, B. L. *J. Phys. Chem. C* **2015**, *119*, 11337–11348.
- (119) Shkrob, I. a.; Zhu, Y.; Marin, T. W.; Abraham, D. *J. Phys. Chem. C* **2013**, *117*, 19255–19269.
- (120) Seo, D. M.; Chalasani, D.; Parimalam, B. S.; Kadam, R.; Nie, M.; Lucht, B. L. *ECS Electrochem. Lett.* **2014**, *3*, A91–A93.
- (121) Martínez de la Hoz, J. M.; Balbuena, P. B. *Phys. Chem. Chem. Phys.* **2014**, *16*, 17091.
- (122) Markevich, E.; Fridman, K.; Sharabi, R.; Elazari, R.; Salitra, G.; Gottlieb, H. E.; Gershinsky, G.; Garsuch, A.; Semrau, G.; Schmidt, M. a; Aurbach, D. *J. Electrochem. Soc.* **2013**, *160*, A1824–A1833.
- (123) Markevich, E.; Salitra, G.; Chesneau, F.; Schmidt, M.; Aurbach, D. *ACS Energy Lett.* **2017**, *2*, 1321–1326.
- (124) Shkrob, I. a.; Wishart, J. F.; Abraham, D. P. *J. Phys. Chem. C* **2015**, *119*, 14954–14964.
- (125) Wayland, B. B.; Poszmik, G.; Mukerjee, S. L.; Fryd, M. *J. Am. Chem. Soc.* **1994**, *116*, 7943–7944.
- (126) Chalasani, D.; Li, J.; Jackson, N. M.; Payne, M.; Lucht, B. L. *J. Power Sources* **2012**, *208*, 67–73.
- (127) Xu, S. D.; Zhuang, Q. C.; Wang, J.; Xu, Y. Q.; Zhu, Y. B. *Int. J. Electrochem. Sci.* **2013**, *8*, 8058–8076.
- (128) Kovalenko, I.; Zdyrko, B.; Magasinski, A.; Hertzberg, B.; Milicev, Z.; Burtovyy, R.; Luzinov, I.; Yushin, G. *Science*. **2011**, *334*, 75–79.
- (129) Liu, J.; Zhang, Q.; Zhang, T.; Li, J.-T.; Huang, L.; Sun, S.-G. *Adv. Funct. Mater.* **2015**, *25*, 3599–3605.

- (130) Bie, Y.; Yang, J.; Nuli, Y.; Wang, J. *J. Mater. Chem. A* **2017**, *5*, 1919–1924.
- (131) Jin, Y.; Kneusels, N.-J. H.; Magusin, P. C. M. M.; Kim, G.; Castillo-Martinez, E.; Marbella, L. E.; Kerber, R. N.; Howe, D. J.; Paul, S.; Liu, T.; Grey, C. P. *J. Am. Chem. Soc.* **2017**, *139*, 14992–15004.
- (132) Ichikawa, K.; Dickinson, L. C.; MacKnight, W. J.; Watanabe, M. *Polym. J.* **1997**, *29*, 429–433.
- (133) Lee, D.; Kaushik, M.; Coustel, R.; Chenavier, Y.; Chanal, M.; Bardet, M.; Dubois, L.; Okuno, H.; Rochat, N.; Duclairoir, F.; Mouesca, J. M.; De Paëpe, G. *Chem. A Eur. J.* **2015**, *21*, 16047–16058.
- (134) Lippmaa, E.; Magi, M.; Satnoson, A.; Engelhardt, G.; Grimmer, A.-R. *J. Am. Chem. Soc.* **1980**, *5*, 4889–4893.
- (135) Shao, W.-L.; Shinar, J.; Gerstein, B. C.; Li, F.; Lannin, J. S. *Phys. Rev. B* **1990**, *41*, 9491–9494.
- (136) Giuliani, J. R.; Harley, S. J.; Carter, R. S.; Power, P. P.; Augustine, M. P. *Solid State Nucl. Magn. Reson.* **2007**, *32*, 1–10.
- (137) Glaser, R. H.; Wilkes, G. L.; Bronnimann, C. E. *J. Non. Cryst. Solids* **1989**, *113*, 73–87.
- (138) Mabboux, P.-Y.; Gleason, K. K. *J. Electrochem. Soc.* **2005**, *1*, 7–13.
- (139) Lafon, O.; Rosay, M.; Aussenac, F.; Lu, X.; Trébosc, J.; Cristini, O.; Kinowski, C.; Touati, N.; Vezin, H.; Amoureux, J. P. *Angew. Chemie - Int. Ed.* **2011**, *50*, 8367–8370.
- (140) Kelly, I. E.; Owen, J. R.; Steele, B. C. H. *J. Power Sources* **1985**, *14*, 13–21.
- (141) Perez-Beltran, S.; Ramírez-Caballero, G. E.; Balbuena, P. B. *J. Phys. Chem. C* **2015**, *119*, 16424–16431.
- (142) Lee, D.; Monin, G.; Duong, N. T.; Lopez, I. Z.; Bardet, M.; Mareau, V.; Gonon, L.; Gaël De Paëpe. *J. Am. Chem. Soc.* **2014**, *136*, 13781–13788.
- (143) Hoffner, F. M.; Delmotte, L.; Kessler, H. *Zeolites* **1993**, *13*, 60–63.
- (144) Chan, C. K.; Ruffo, R.; Hong, S. S.; Cui, Y. *J. Power Sources* **2009**, *189*, 1132–1140.
- (145) Peled, E.; Menkin, S. *J. Electrochem. Soc.* **2017**, *164*, A1703–A1719.
- (146) Watanabe, M.; Endo, T.; Nishimoto, A.; Miura, K.; Yanagida, M. *J. Power Sources* **1999**, *81–82*, 786–789.
- (147) Dargel, V.; Shpigel, N.; Sigalov, S.; Nayak, P.; Levi, M. D.; Daikhin, L.; Aurbach, D. *Nat. Commun.* **2017**, *8*, 1389.
- (148) Golodnitsky, D.; Strauss, E.; Peled, E.; Greenbaum, S. *J. Electrochem. Soc.* **2015**, *162*, A2551–A2566.
- (149) Thiam, A.; Antonelli, C.; Iojoiu, C.; Alloin, F.; Sanchez, J. Y. *Electrochim. Acta* **2017**, *240*, 307–315.
- (150) Kovalenko, I.; Zdyrko, B.; Magasinski, A.; Hertzberg, B.; Milicev, Z.; Burtovyy, R.; Luzinov, I.; Yushin, G. *Science* **2011**, *334*, 75–79.
- (151) Wu, D. H.; Chen, A.; Johnson, C. S. *Journal of Magnetic Resonance, Series A.* 1995, pp 260–264.

- (152) Wiemers-Meyer, S.; Winter, M.; Nowak, S. *Phys. Chem. Chem. Phys.* **2016**, *18*, 26595–26601.
- (153) McArthur, M. A.; Trussler, S.; Dahn, J. R. *J. Electrochem. Soc.* **2012**, *159*, A198–A207.
- (154) Widgeon, S. J.; Sen, S.; Mera, G.; Ionescu, E.; Riedel, R.; Navrotsky, A. *Chem. Mater.* **2010**, *22*, 6221–6228.
- (155) Neese, F. *Wiley Interdiscip. Rev. Comput. Mol. Sci.* **2018**, *8*, 4–9.
- (156) Perdew, J. P.; Ernzerhof, M.; Burke, K. *J. Chem. Phys.* **1996**, *105*, 9982–9985.
- (157) Weigend, F.; Ahlrichs, R. *Phys. Chem. Chem. Phys.* **2005**, *7*, 3297.
- (158) Jensen, F. *J. Chem. Theory Comput.* **2015**, *11*, 132–138.

Appendix A

Materials

Battery grade LP30 electrolyte, FEC and VC were obtained from Sigma-Aldrich. The LiPF₆ salt was obtained from Aldrich. DNP solvent TCE (Sigma Aldrich) was dried over molecular sieves to remove water. TEKPol radical were kindly provided by the DNP facility in Nottingham. NMR experiments were used to estimate water content using small quantities 30 μ l of NMR-grade ²H-DMSO and 0.7 ml of FEC, VC or LP30. Although the ²H-DMSO contains trace amounts (15 – 35 ppm) of water complicating the analysis, the natural abundance enriched electrolytes all contained < 120 ppm H₂O.

Additional experiment details

Table A.1. Preparation of DNP NMR samples

Sample No.	Sample description	Sample mass (mg)	KBr diluent mass (mg)	TEKPol in DCB radical concentration (mM)	TEKPol in DCB radical volume (μ L)	¹ H enhancement with microwave $\epsilon_{\text{on/off}}$
1	SiNW cycled in LP30+ ¹³ C ₃ EC for 30 cycles	3	11	4	2.5	12
2	SiNW cycled in LP30+ ¹³ C ₃ FEC for 30 cycles	<1	6	4	2	20

Table A.2. Solid-state NMR measurement parameters for the ^1H - ^{13}C CP spectra shown in Figure 3.5

Parameters	Samples			
	LP30+ $^{13}\text{C}_3$ EC		LP30+ $^{13}\text{C}_3$ FEC	
Temperature	295K (RT)	100 K (DNP)	295K (RT)	100 K(DNP)
Magnet	700 MHz	600 MHz	500 MHz	600 MHz
Rotor (mm)	3.2	3.2	2.5	3.2
Sample mass	2 mg	5 mg	~1 mg	<1 mg
MAS	20 kHz	12.5 kHz	10 kHz	12.5 kHz
Contact time	1 ms	2 ms	2 ms	2 ms
Recycle delay (s)	3	6	3	5
Number of scans	3482	688	24576	1025
Measuring time (h)	3	1	20.5	1.3

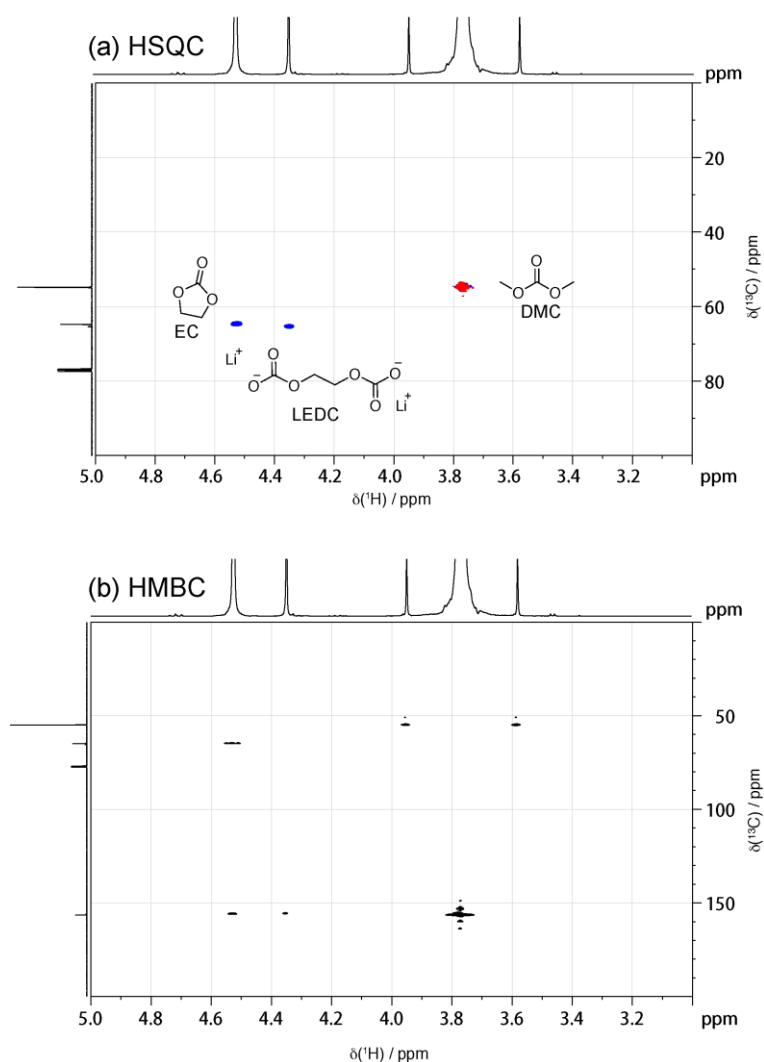


Figure A.1. ^1H – ^{13}C correlation NMR spectra of the cycled LP30 electrolyte extracted from Li symmetric cells 100 cycles (a) HSQC, (b) HMBC.

^1H and ^{13}C solution NMR spectra of the cycled LP30 + $^{13}\text{C}_3$ FEC electrolyte with enlarged spectra are shown in Figure A.2 and A.4, respectively. ^1H NMR in the region of 6–7 ppm region is shown in Figure A.3, which corresponds to the proton in $^{13}\text{C}_3$ FEC. The multiplet analysis is illustrated in Figure A.3 in which six distinct types of J-coupling are observed: two large $^1\text{J}_{\text{CF}}$, $^2\text{J}_{\text{HF}}$ coupling constants of 200 and 64 Hz, respectively, and four relatively smaller ^{13}C – ^1H J-couplings ($^2\text{J}_{\text{CH}} = 7.8$ Hz, $^3\text{J}_{\text{HH, cis}} = 6.9$ Hz, $^3\text{J}_{\text{HH, trans}} = 4.1$ Hz, $^3\text{J}_{\text{CH}} = 1.0$ Hz). Analysis of these patterns confirms the formation of fully labelled $^{13}\text{C}_3$ FEC.

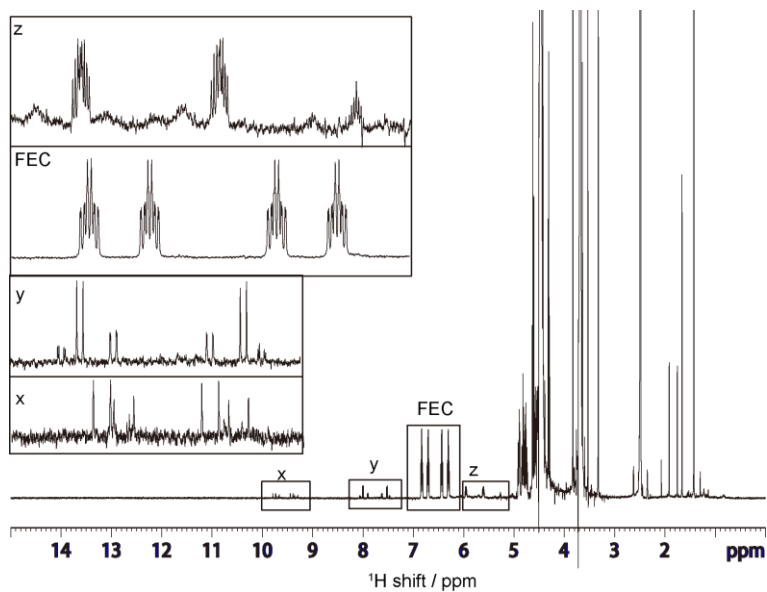


Figure A.2. ^1H solution NMR of LP30 + $^{13}\text{C}_3$ FEC after 30 cycles, the x, y, FEC and z regions are enlarged and are shown in the inserts on the top right.

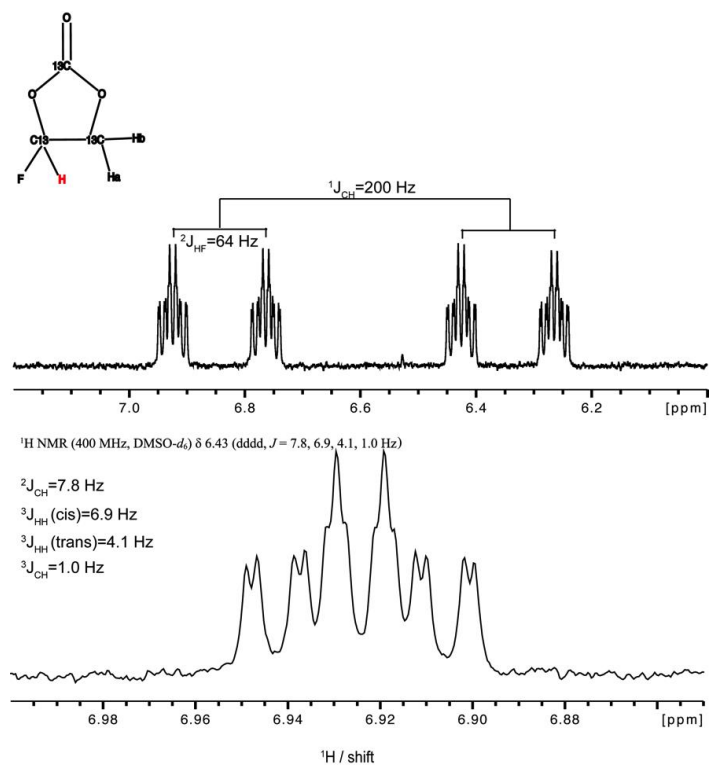


Figure A.3. Multiplet analysis of ^1H NMR of fully enriched $^{13}\text{C}_3$ FEC; the proton region corresponds to the proton bound to the fluorinated carbon (labelled in red in the structure).

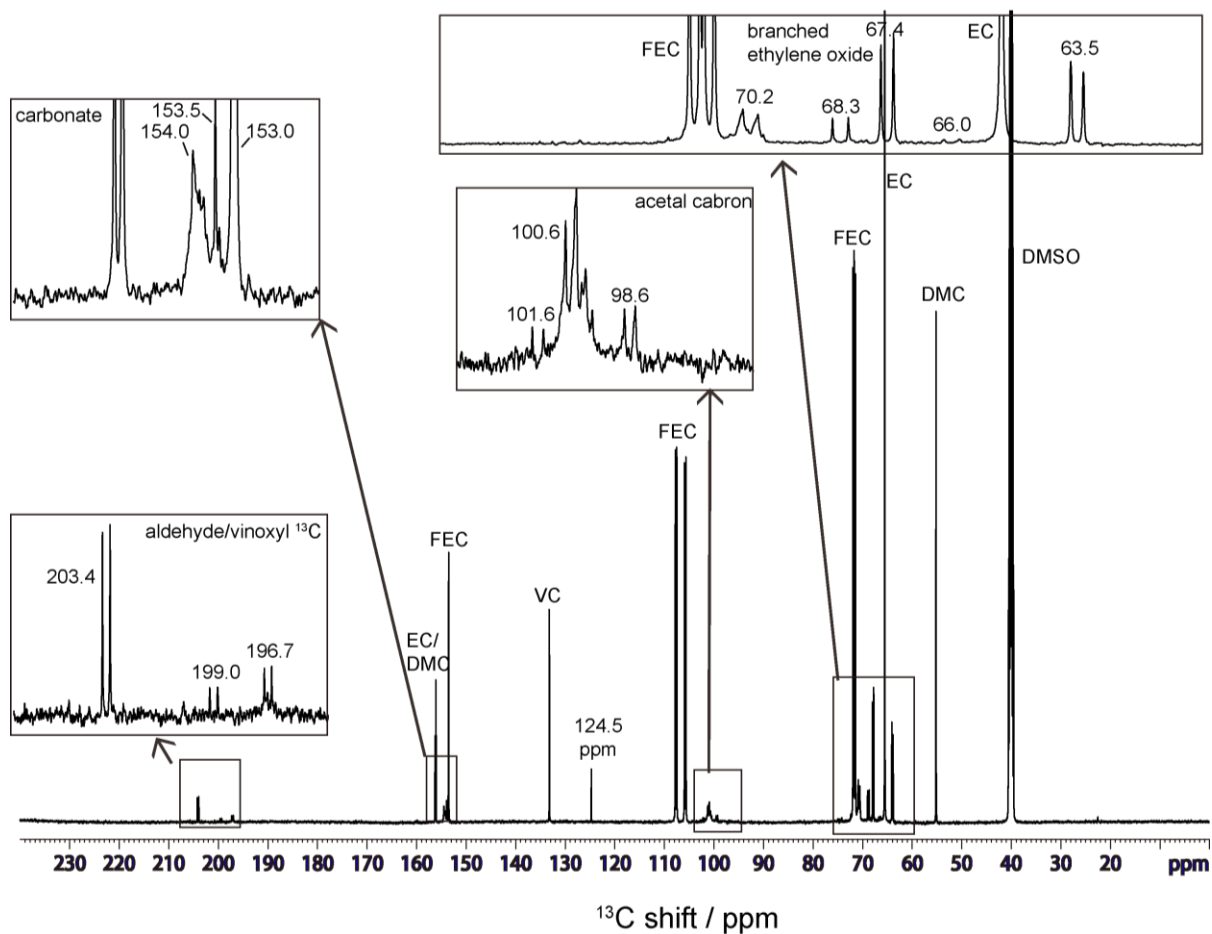


Figure A.4. ^{13}C solution NMR spectra of LP30 + $^{13}\text{C}_3$ FEC after 30 cycles. The insets show enlarged parts of the ^{13}C NMR spectra.

There is an extra peak at 124.5 ppm in ^{13}C NMR of cycled LP30 + $^{13}\text{C}_3$ FEC electrolyte, but it is not correlated to any protons in HSQC in Figure 3.3a, suggesting it is a non-protonated carbon. The 124.5 ppm peak can be assigned to orthocarbonate as previously reported by Leifer et al.⁵⁶

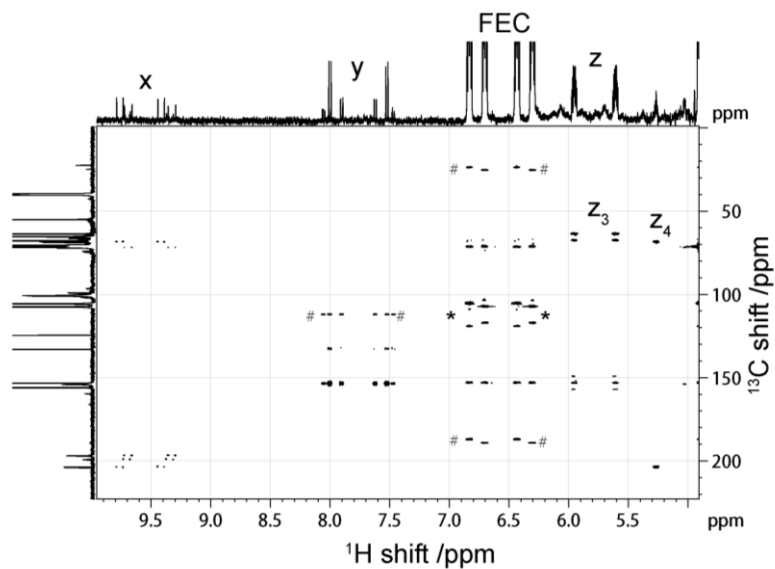


Figure A.5. HMBC of LP30 + $^{13}\text{C}_3$ FEC after 30 cycles. External projections of 1D ^1H and ^{13}C spectra are displayed. No ^{13}C decoupling was applied during acquisition. Artefact peaks are marked with #, one-bond artefacts are marked with *

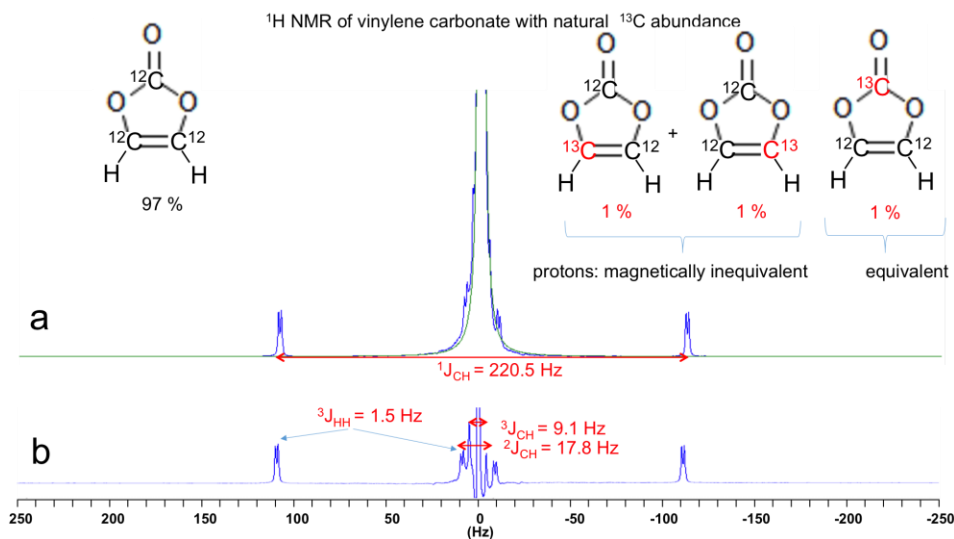


Figure A.6. ^1H solution NMR of ^{13}C natural abundance vinylene carbonate. (a) blue line is the experimental data, green line is the Lorentzian fitting, (b) the difference between the experimental spectrum and the fitting. The inserts show the chemical structures of vinylene carbonate with possible ^{13}C labelling positions. The J-coupling constants derived from the spectrum are displayed in red.

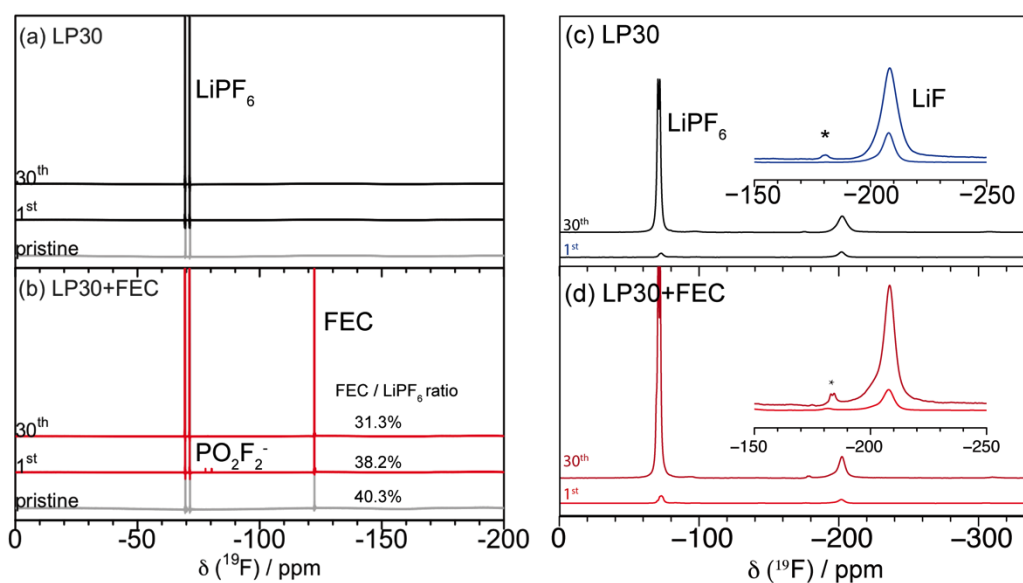


Figure A.7. ^{19}F solution NMR of cycled electrolyte (a–b) and ^{19}F ssNMR of cycled SiNW electrode (c–d). The insets in (c) and (d) show the lithium fluoride region at -204 ppm. The spinning side bands in the ssNMR spectra are marked with asterisks.

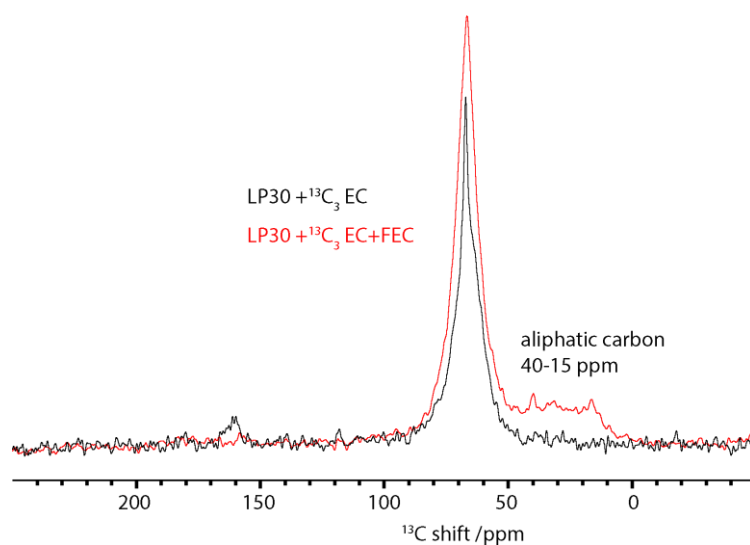


Figure A.8. ^{13}C CP NMR of SiNW cycled in LP30 + $^{13}\text{C}_3$ EC (black) and in LP30 + $^{13}\text{C}_3$ EC + FEC (red) for 30 cycles. Samples were all measured at 700MHz (^1H Larmor frequency) with 500 μs contact time, 3936 scans, and a recycle delay of 7 s.

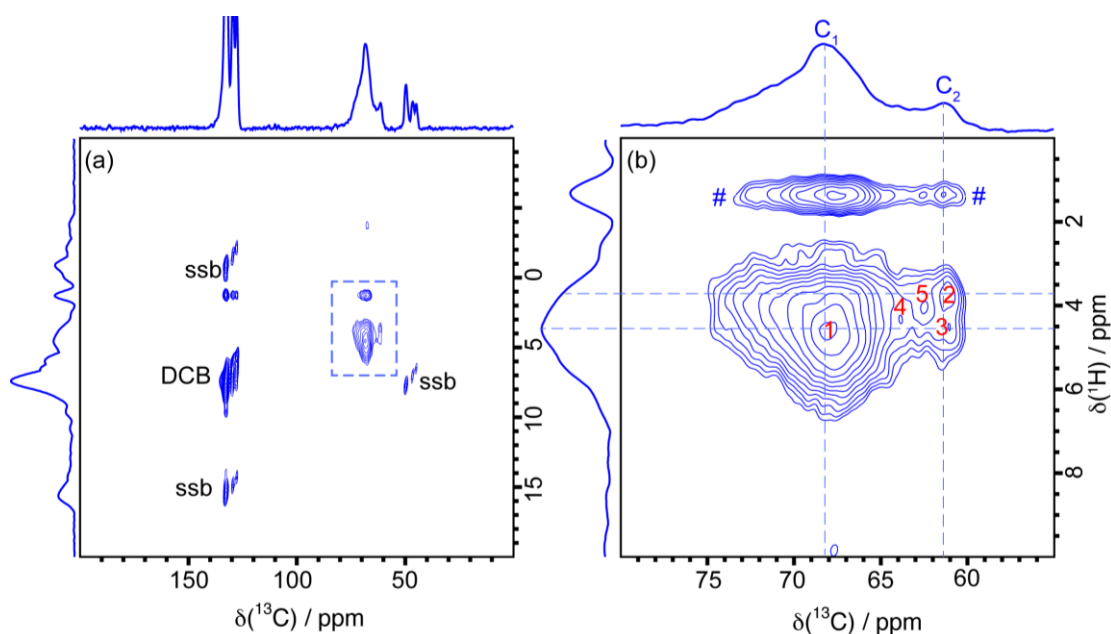


Figure A.9. ^1H - ^{13}C Heteronuclear Correlation NMR spectra of SiNW cycled in LP30 + $^{13}\text{C}_3$ EC electrolyte. Panel (a) shows the full spectrum with large DCB solvent signal and its spinning sidebands (ssb). The sample region with the dashed square is enlarged in Panel (b). Artefact peaks are marked with #, which is due to spin lock at y axis during proton decoupling and it appears at the carrier frequency on proton. The artefact is confirmed by shifting the carrier frequency of the proton. The spectrum was measured at 12.5 kHz spinning speed and a contact time of 50 μs . A total of 128 increments with 8 scans were acquired over 1.7 hours. Five noticeable peaks are marked on the contour plot from 1 – 5.

Table A.3. Summary of peaks in ^1H - ^{13}C HETCOR of SiNW cycled in LP30 + $^{13}\text{C}_3$ EC electrolyte

peak	$^{13}\text{C}/\text{ppm}$	$^1\text{H}/\text{ppm}$
1	68.20 \pm 0.4	4.50 \pm 0.20
2	61.40 \pm 0.4	3.75 \pm 0.30
3	61.27	4.48
4	64.18	4.28
5	62.72	3.97

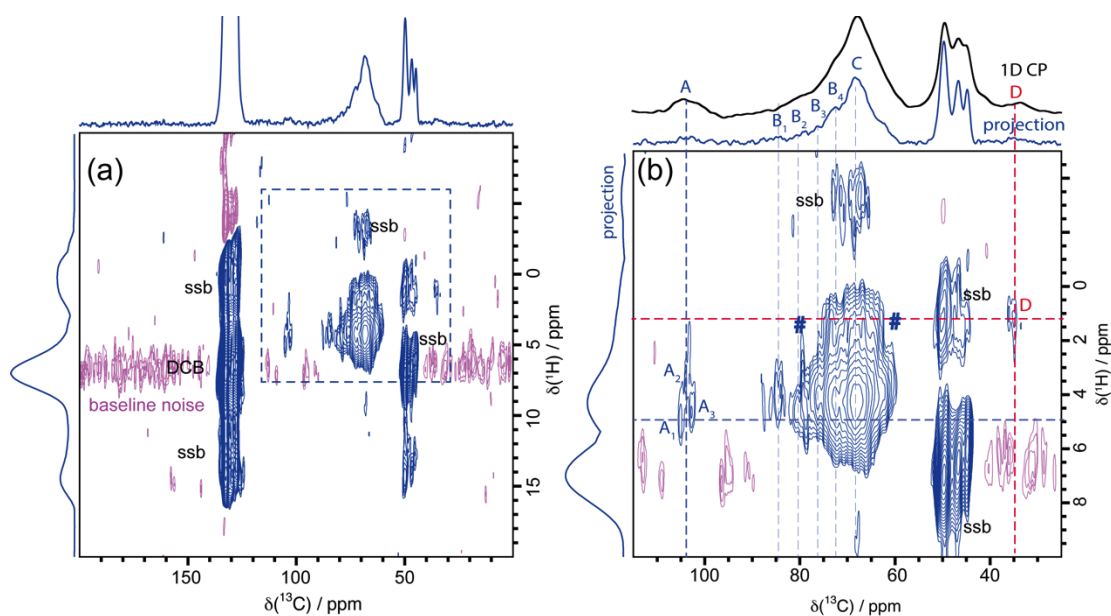


Figure A.10. ^1H - ^{13}C Heteronuclear Correlation NMR spectra of SiNW cycled in LP30 + $^{13}\text{C}_3$ FEC electrolyte. Panel (a) shows the full spectrum, which contains large DCB solvent signal and its spinning sidebands (ssb), since the signal to noise ratio is not ideal, there is some baseline noise. The sample region with dashed square is enlarged in panel (b). Artefact peaks are marked with #. The spectrum was measured at 12.5 kHz spinning speed and a contact time of 500 μs . A total of 64 increments with 256 scans were acquired over 15 hours.

Table A.4. Summary of peaks in ^1H - ^{13}C HETCOR of SiNW cycled in LP30 + $^{13}\text{C}_3$ FEC electrolyte.

peak	$^{13}\text{C}/\text{ppm}$	$^1\text{H}/\text{ppm}$
A ₁	105.1±0.2	5.4±0.6
A ₂	104.0±0.2	4.0±0.4
A ₃	103.0	5.04
B ₁	84.8	4.47
B ₂	80.4	5.05
B ₃	76.0	4.55
B ₄	72.5	4.62
C	68.0±0.2	4.5±0.4
D ₁	35	1.3

Appendix B

B.1 Additional Experimental Details

Electrochemical Impedance Spectroscopy (EIS)

The cells were rested in open circuit voltage for 15 h to reach equilibrium before EIS data was collected. All EIS measurements were made using a Biologic VMP3 electrochemical station at room temperature (18 ± 3 °C) using an excitation signal of 10.0 mV amplitude and a frequency range from 1 MHz to 0.1 Hz.

XPS

XPS spectra were acquired by Steffen Emge and Robert S. Weatherup (University of Cambridge) using the scanning photoemission microscopy (SPEM) instrument at the Escamicroscopy beamline of the Elettra synchrotron facility (Trieste, Italy). Measurements were performed using a 1075 eV X-ray beam that is defocussed to give a ~ 80 μm diameter spot size. Photoelectrons were collected with a SPECS-PHOIBOS 100 hemispherical electron energy analyzer with an in-house customized multichannel plate detector. The binding energy (BE) scale was calibrated on the hydrocarbon C 1s peak at 284.5 eV. All spectra were collected with 30 scans. Samples were transferred using sealed polyethylene glove bags to avoid air exposure.

FTIR

Dried silicon nanowire (SiNWs) electrodes were characterized using a FTIR spectrometer (Agilent, Cary 630) inside an argon-filled glovebox, in attenuated total reflection (ATR) mode on a diamond crystal. Each FTIR spectrum was acquired with a resolution of 4 cm^{-1} with 32 scans with the range from 600 to 4000 cm^{-1} .

B.2 Additional Electrochemistry Data

Table B.1. Summary of the electrochemical performance of SiNWs cycled in various electrolytes

Electrolytes	Capacity Retention (50 th discharge / 1 st discharge, %)	Capacity Retention (50 th charge / 1 st charge, %)	Initial Coulombic Efficiency (%)	Average Coulombic Efficiency (from 2 nd to 50 th , %)
LP30	57.95	61.45	91.73	97.8
LP30 + FEC	73.66	77.57	93.56	98.4
FEC	80.62	86.99	91.40	98.8
VC	73.45	78.89	92.48	99.1

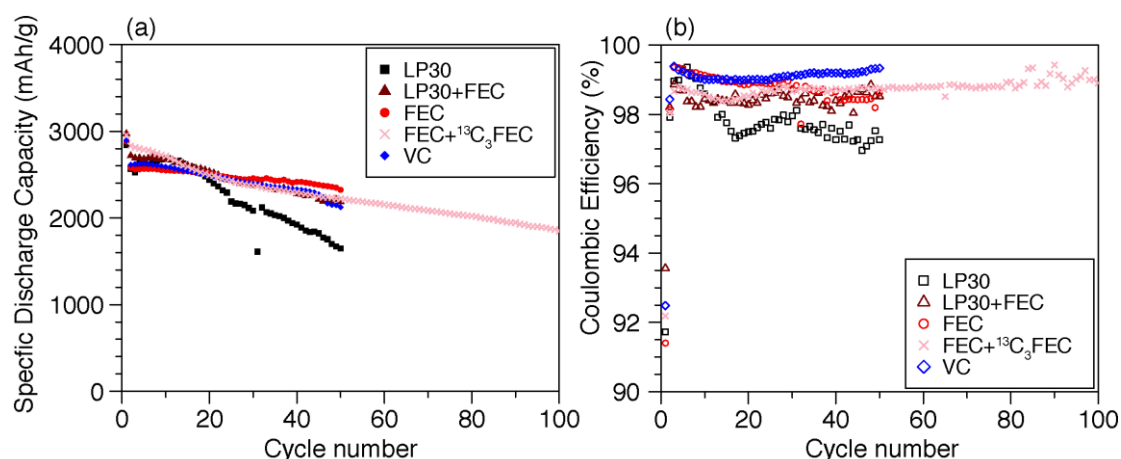


Figure B.1. Electrochemical performances for SiNWs cycled in FEC+¹³C₃ FEC and the results from representative SiNWs cycled using the electrolyte formulations listed in Table 4.1. (a) Specific lithiation capacity and (b) Coulombic efficiency versus cycle number.

To characterize the ionic properties of the SEI formed in LP30, FEC and VC further, electrochemical impedance spectroscopy (EIS) measurements were performed on SiNWs after 30 cycles in the delithiated state. The Nyquist plots are presented in Figure B.2. The depressed semicircle at high frequencies (HF) mainly reflects the charge transfer resistance (R_{ct}) of Li ions between different interphases (from the electrolyte to the SEI and from the SEI to Si), and the tail in the low frequencies region contains information about the mass transfer rate within

the electrode. Note that the EIS is performed in a two-electrode system (i.e., Si vs. Li) and the interphases on the Li metal also contribute to R_{ct} .

A qualitative comparison of the size of the semicircles reveals that the FEC derived SEI has the smallest charge transfer resistance, while the VC sample even has a slightly larger R_{ct} than the LP30 sample. This agrees well with previous studies, which also showed a lower resistance for Si electrodes cycled with the addition of FEC,^{36,40} and an increased resistance in the presence of VC.²⁴ The difference of the resistance developed in the FEC and VC cells is related to the SEI thickness, the chemical structures of the SEI as well as the bonding nature between SEI and SiO_x surface. The results indicate that the FEC-derived SEI may be thinner and/or more Li^+ conductive than the SEI formed in VC and LP30 electrolytes.

Impedance analysis of the SEI:

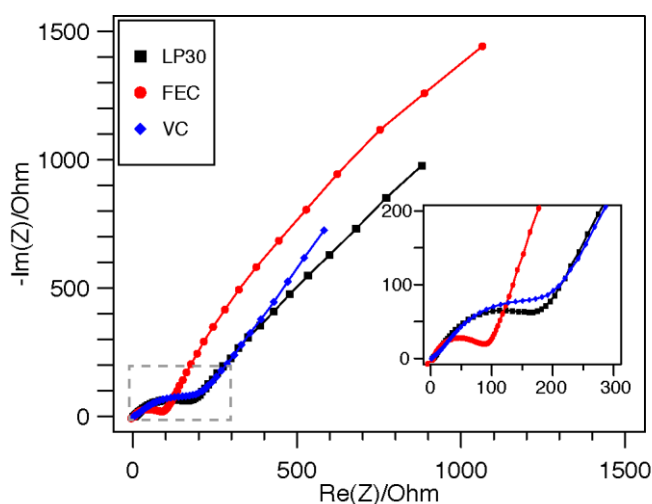


Figure B.2. Electrochemical impedance spectra of SiNW half-cells after 30 cycles in LP30 standard electrolyte (black), FEC (red) and VC (blue) electrolytes in the delithiated state. The insert shows the high frequency region.

Rate performance:

To confirm the observations in the EIS measurements, additional rate performance tests were carried out (Figure B.3). The hypothesis is that FEC samples with lower R_{ct} should have better high rate performance than LP30 and VC samples. The FEC sample indeed exhibits the highest initial capacity compared to LP30 and VC samples when they are all cycled at high rates of $C/5$ and $C/2$ (Figure B.3a). However, the capacity retention trends of these samples are different.

In the LP30 and FEC electrolytes, the capacity drops with each cycle, when cycling at high rates, whereas the VC sample surprisingly shows gradually increasing capacities with cycling, indicating improved Li^+ transport through the electrode structure.

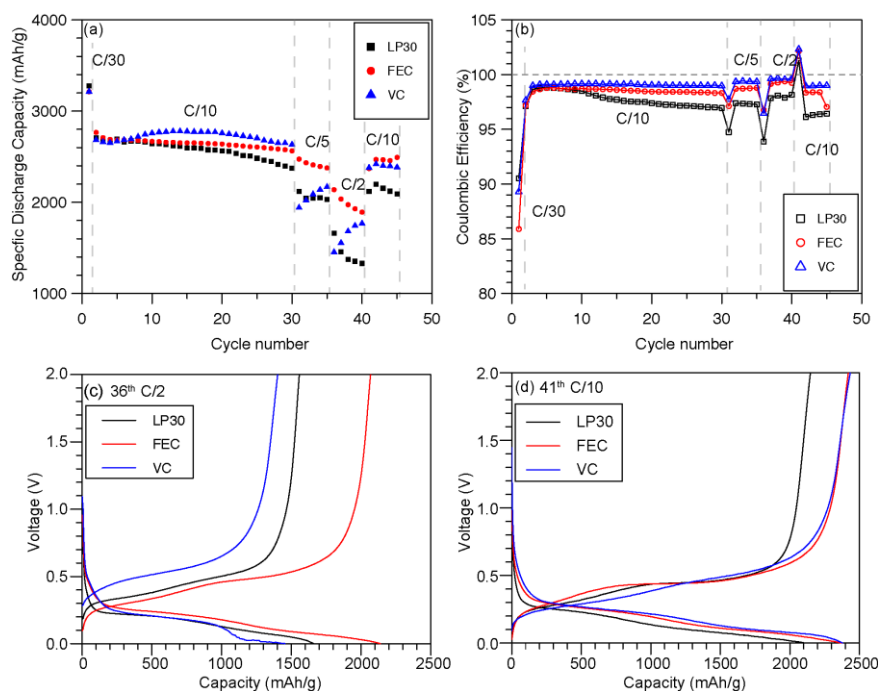


Figure B.3. Rate performance of the SiNWs cycled in LP30, FEC and VC electrolyte (the 1st cycle at C/30, 2nd to 30th cycles at C/10, then cycled at C/5, C/2 and again C/10 for 5 cycles each. (a) discharge capacity and (b) Coulombic efficiency versus cycle number. Voltage curves of (c) 36th cycle at C/2, (d) 41th cycle at C/10. (1 C = 3579 mAh/g, the voltage window is 0.001 – 2 V vs. Li^+/Li)

To examine more closely the behaviour of the VC sample at high currents, the voltage curve of the VC cell is compared to that of FEC and LP30 samples (Figure B.3c and d). When cells are initially cycled at C/2 in the 36th cycle (Figure B.3c), the VC sample has a larger voltage polarization than the FEC sample. During lithiation, the voltage curve of VC almost coincides with that of FEC from 2 V to 0.25 V before it quickly reaches 0.001 V at only ~1400 mAh/g. During the delithiation process, the onset for the VC sample is about 0.15 V higher than the FEC sample, and the delithiation plateau of VC is much higher than the LP30 and FEC cells. The discharge capacity of the VC sample then gradually increases when cycled at C/2 and approaching the capacity of FEC cell in the 40th cycle. The VC sample recovers its lithiation and delithiation capacities when cells are cycled at a slow rate of C/10 after high rate testing (Figure B.3d), which indicates that the capacity loss is due to kinetic effects. Moreover, the VC

sample consistently shows a higher Coulombic efficiency (CE) compared to LP30 and FEC samples at all current densities. The higher CE for VC electrolytes suggests that the VC-derived SEI has a better passivating ability and reduces the irreversible capacity loss during each cycle.

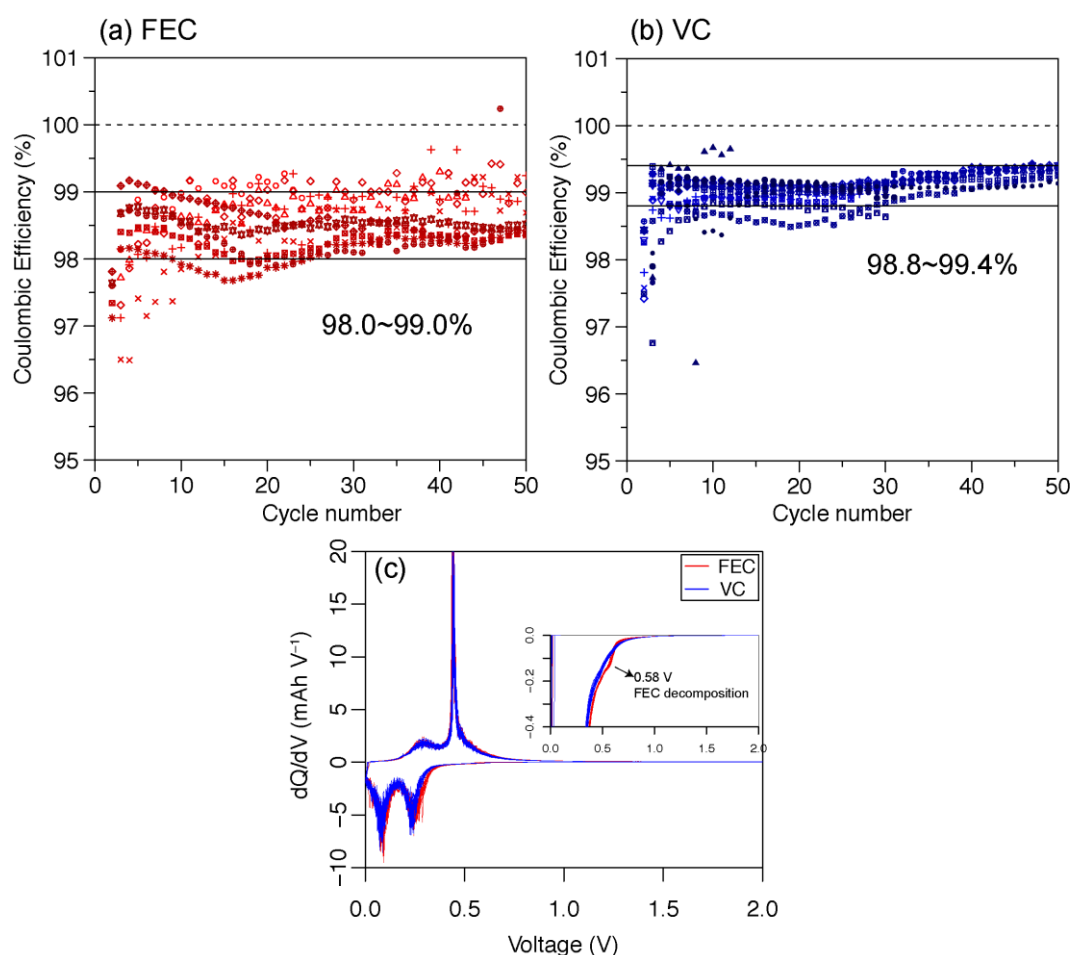


Figure B.4. (a–b) The Coulombic efficiencies of multiple SiNWs cells cycled in 1M LiPF₆ in pure FEC and VC electrolytes. (c) dQ/dV from 30th to 50th cycles of cells cycled in FEC and VC electrolytes (FEC in red, VC in blue).

Experiments were performed to assess the effect of variations between SiNW electrodes on the electrochemistry, since the SiNWs were synthesized individually by CVD methods in different batches. Coulombic efficiencies (CE) of multiple cells used in this study are shown in Figure B.4a and b. SiNWs cells cycled in FEC have CEs in the range of 98.0–99.0%, whereas, cells cycled in VC electrolyte show a higher CEs (98.8%–99.4%). While variations are observed, the VC samples systematically show higher CEs.

Figure B.4c compares the dQ/dV plot of cells cycled in FEC and VC electrolytes. An extra peak at 0.58 V is clearly observed in the FEC sample, indicating FEC is continuously being decomposed as no lithiation of Si occurs in this voltage. The result is consistent with the lower CEs observed in the FEC samples compared to the VC samples, suggesting that VC forms a more stable SEI than FEC.

B.3 Solution NMR Data

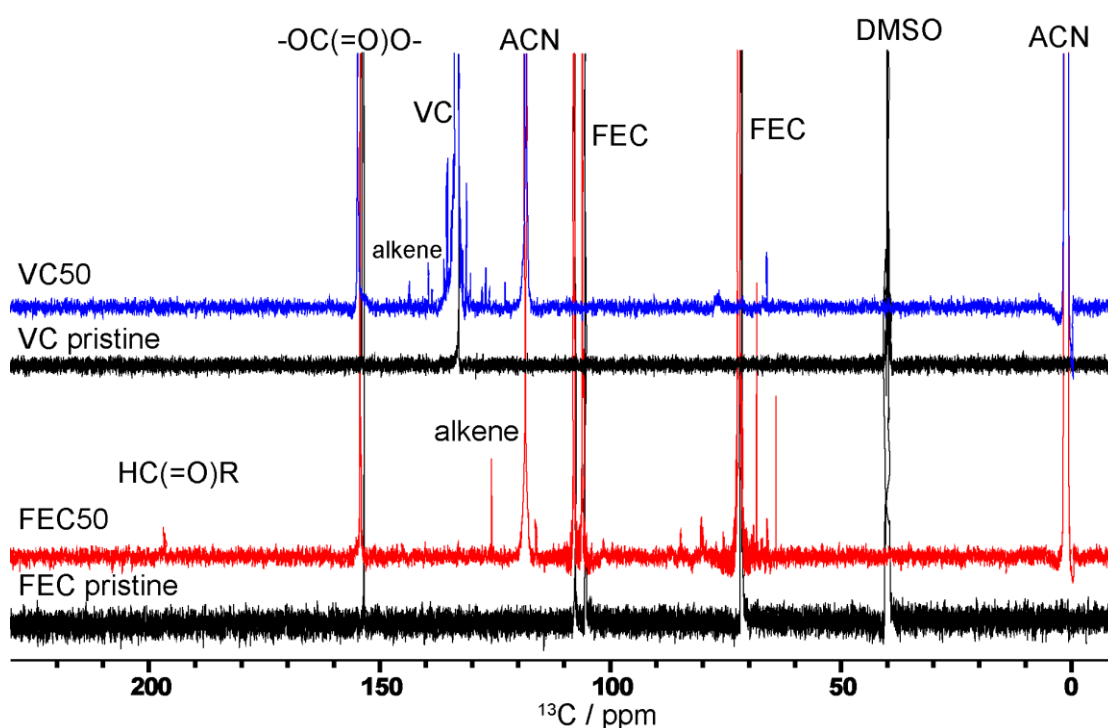


Figure B.5. ^{13}C solution NMR spectra of pristine FEC, VC electrolytes and electrolytes after 50 cycles with ^1H decoupling.

Pristine FEC and VC electrolytes were measured in d_6 -DMSO solvent, whereas the cycled FEC and VC electrolytes were measured in d_3 -ACN solvent. d_3 -ACN solvent was because we observed phase separation in the cycled electrolytes and d_6 -DMSO mixture. In the cycled FEC electrolyte, new ^{13}C NMR peaks around 190 and 125 ppm appear and they are assigned to aldehyde and alkene carbon, respectively. The cycled VC electrolyte also contains additional alkene carbon species with ^{13}C shift spanning from 120-140 ppm.

B.4 XPS and FTIR Data

XPS studies of surface species on the cycled SiNWs

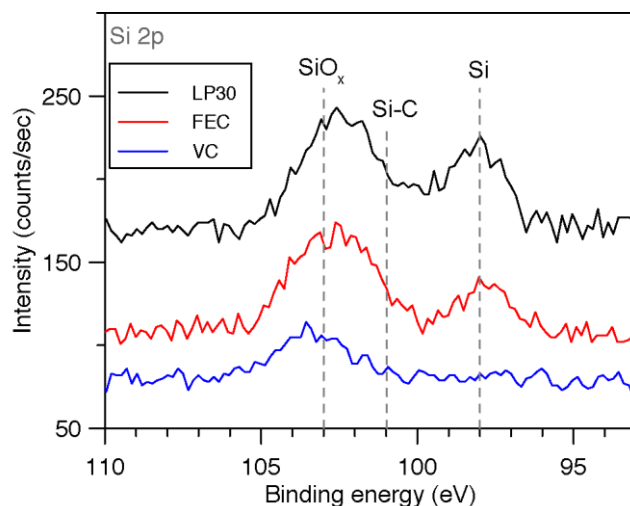


Figure B.6. XPS Si 2p spectra of SiNWs cycled in different electrolyte for 30 cycles in the delithiation state.

Figure B.6 shows the XPS Si 2p core peaks of SiNWs cycled in LP30, FEC and VC electrolytes after 30 cycles in their delithiated states. All spectra contain a broad peak at ~ 103 eV that can be assigned to silicon oxide (SiO_x).⁴¹ The FEC and LP30 samples both show a relatively weak peaks centered at ~ 98 eV that is assigned to elemental Si, whereas, no such Si peak is observed in the VC sample. All samples were measured using the same photon energy (1075 eV), and thus the Si 2p electrons for all three samples have the same inelastic mean free path (~ 2.5 nm). This corresponds to an information depth of ~ 7.5 nm ($\sim 95\%$ of detected photoelectrons originate from within this distance of the surface) and given that the SiO_x is expected to be closer to the surface than the Si, the variations in the intensity of the elemental Si peak provide an indirect measure of the SEI thickness. The Si 2p spectra thus suggest that the VC sample has a thicker SEI than those generated from LP30 and FEC. The conclusion is consistent with McArthur et al., who used in-situ spectroscopic ellipsometry to measure the thickness of the SEI on a-Si film, and concluded that the SEI formed in electrolyte containing 2 wt% VC additive is thicker than those formed in standard electrolyte with and without 2 wt% FEC.¹⁵³ A thicker SEI will extend the Li ion diffusion pathway through the interphase before lithiation of bulk Si takes place. On the other hand, a thicker SEI potentially prevents electronic tunnelling

through the SEI and can better passivate the electrode. Although the thickness of SEI is an important parameter, it does not necessarily determine the electrochemistry performance. Xu et al. previously demonstrated that the desolvation process of Li ions is the rate-determining step in the lithiation of graphite instead of the diffusion rate of Li ions through the SEI.⁴⁴

Organosilane Si-C species with a characteristic Si 2p peak at 101 eV as reported by Chan et al.¹⁴⁴ may also be present beneath the broad peak of SiO_x in Figure B.6. Fluorosilicate that has a Si 2p peak around 106 eV⁵⁹ is not clearly observable in all samples. The XPS Si 2p results are consistent with ²⁹Si NMR, showing the presence of silicate and Si-C species with little fluorosilicate on the Si surface.

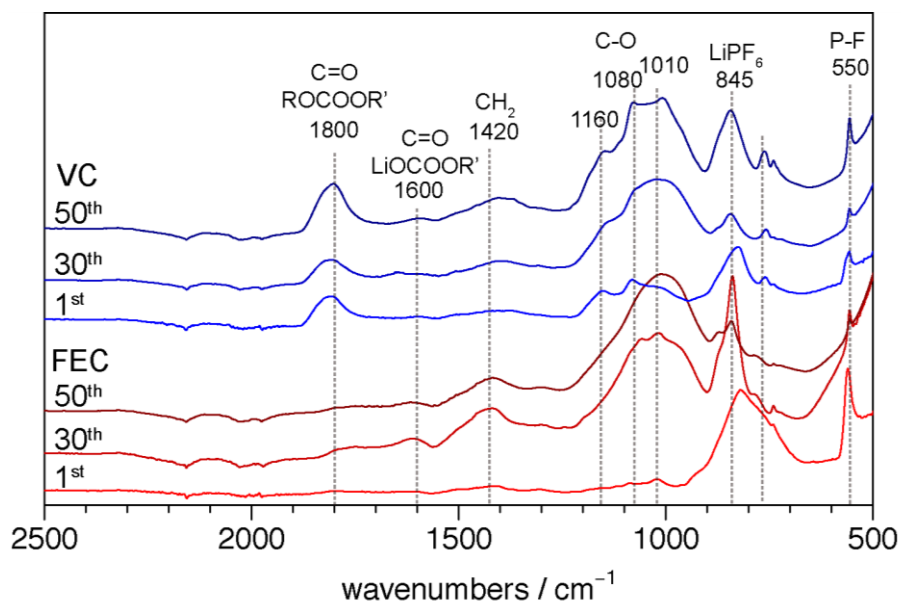


Figure B.7. FTIR spectra of SiNWs cycled in 1M LiPF₆ in pure FEC (red) and pure VC (blue) after 1st, 30th and 50th cycles in the delithiated state without rinsing.

Figure B.7. shows the FTIR spectra of the SiNWs after cycling in different electrolytes. The VC samples contain extra peaks at ~1800 cm⁻¹ that can be assigned to polycarbonate groups (ROCOOR'), whereas the 1800 cm⁻¹ peak is hardly observable for the all FEC samples. It is noteworthy that in Figure 3.2e and 3.2f, the carbonate species with a ¹³C peak at 155 ppm is relatively more intense in the VC samples than the FEC samples. The presence of a polycarbonate suggests that the SEI of the VC samples contains more carbonate groups than

the one formed in the FEC samples. Nie et al⁴² reported similar polycarbonate groups ($\sim 1800\text{ cm}^{-1}$) for Si thin film electrodes cycled in 1.2M LiPF₆ in pure FEC. But it was not reported whether the electrode was rinsed or not. Here the electrodes were not rinsed but dried them under dynamic vacuum overnight to remove excess solvent.

B.5 Additional ¹³C DNP MAS NMR Data

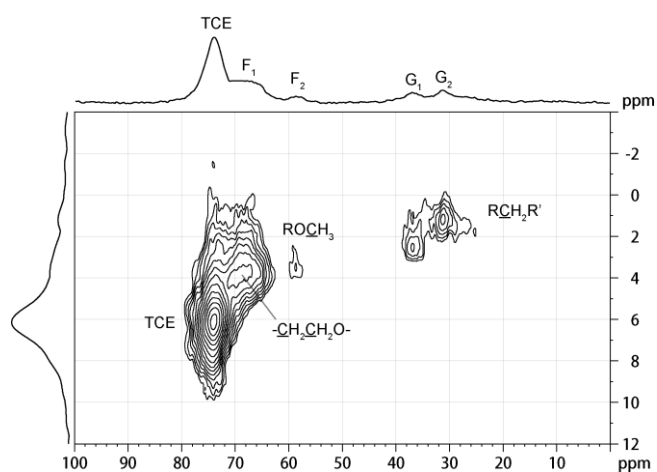


Figure B.8. ¹H-¹³C DNP HETCOR of SiNWs cycled in 1M LiPF₆ in FEC for 30 cycles. Contact time of 200 μ s is used.

Table B.2. Summary of HETCOR peaks in Figure B.8.

Label	¹³ C /ppm	¹ H/ppm	Possible assignment
TCE	74	6.1	TCE
F1	70	4.1	-CH ₂ <u>CH</u> ₂ O-
F2	59	3.5	RO <u>CH</u> ₃
G1	37	2.3	R <u>CH</u> R ₂ '
G2	31	1.3	R <u>CH</u> ₂ R'

Table B.3. Summary of the peaks in ^{13}C - ^{13}C correlation spectrum (Post-C7)

Molecular Fragments	SQ Shift /ppm	SQ Shift /ppm	DQ Shift / ppm	Sum /ppm
A ₁ -A ₂	35.2	31.3	64.9	66.5
B ₂ -A ₄	75.3	35.5	106.4	110.8
B ₂ '-B ₃	75.6	69.9	142.1	145.5
B ₁ -A ₃	76.3	17	91.6	93.3
C ₁ -A ₅	97.8	33.8	130.7	131.6
C ₂ -B ₄	101.8	71.9	172.2	173.7

B.6 Additional ^{29}Si DNP MAS NMR Data

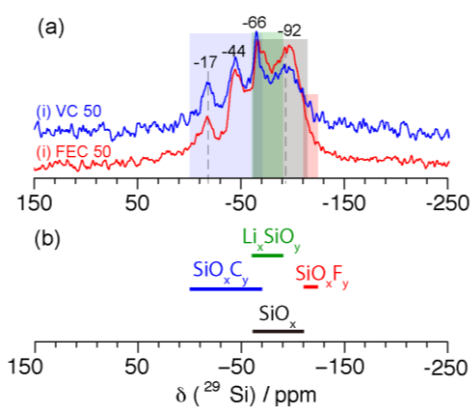


Figure B.9. ^1H - ^{29}Si CP DNP NMR spectra of SiNW cycled in VC, FEC after 50 cycles (a), (b) chemical shift ranges of organosilicate¹⁵⁴, silicate, lithium silicate and fluorosilicate¹⁴³.

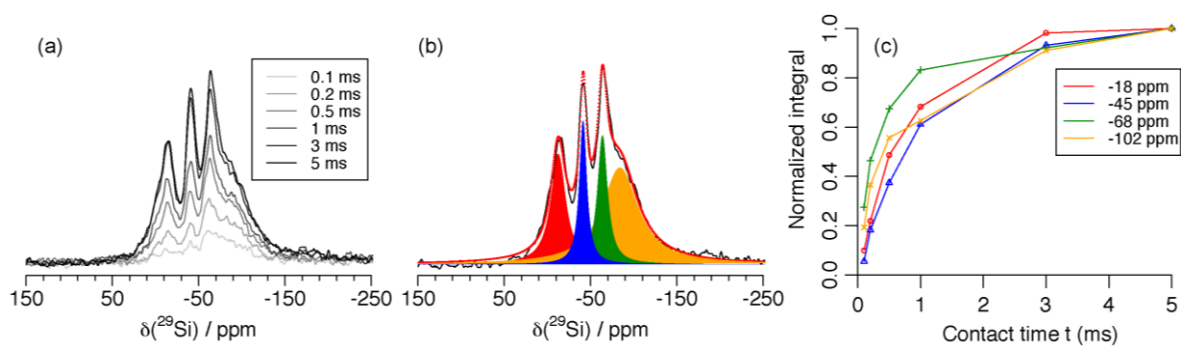


Figure B.10. ^1H - ^{29}Si CP DNP NMR spectra of SiNWs cycled LP30 for 50 cycles with various contact times (a), the deconvoluted spectrum (b), the build-up curve of each deconvoluted peak (c).

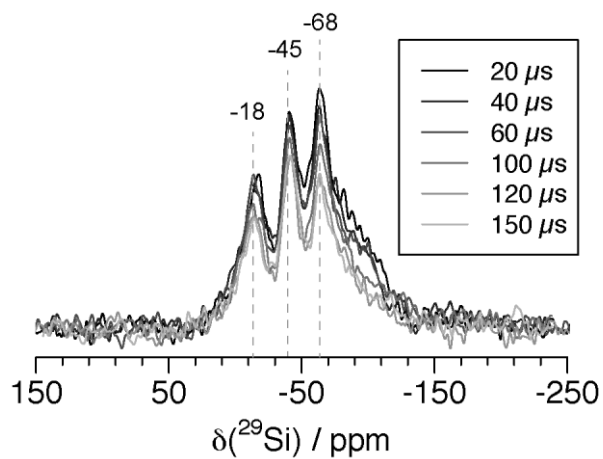


Figure B.11. Spectra of ^1H - ^{29}Si dephasing experiments of SiNWs cycled with LP30 for 50 cycles, spinning at 12.5 kHz.

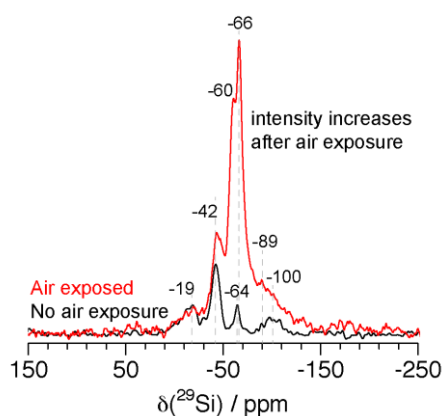


Figure B.12. ^1H - ^{29}Si CP DNP NMR spectra of SiNWs cycled in FEC for 100 cycles before air exposure (black) and after air exposure (red).

B.7 DFT Calculation Results

Computational details

Density Functional Theory (DFT) calculations were performed on a set of molecules that correspond to some of the proposed polymer building blocks of the SEI system by Erlendur Jónssonrun (University of Cambridge). To explore the effect of alkane chain length on the chemical shift, the carbon chains were extended systematically, from R=Me to R=Pr (in essence Et and Pr for the inner linear part). Another set of molecules was also created with a cyclic carbonate functional group. Both of these structures can be seen in Figure B.13, where the main carbon of interest has been made explicit in red.

In each case, the calculations were performed using Orca 4.0.1.2¹⁵⁵. The PBE0 functional¹⁵⁶ with the def2-TZVP¹⁵⁷ basis set was used for the geometry optimization of the molecules. NMR calculations were performed with the same functional and the pcSseg-2¹⁵⁸ basis set. The TightSCF option was also used. The same procedure was used for the calculation of the reference, tetramethylsilane (TMS).

Figure B.13. The branched (left) and cyclic systems (right) used for DFT/NMR calculations. The acetal carbon of interest is emphasized in the structures.

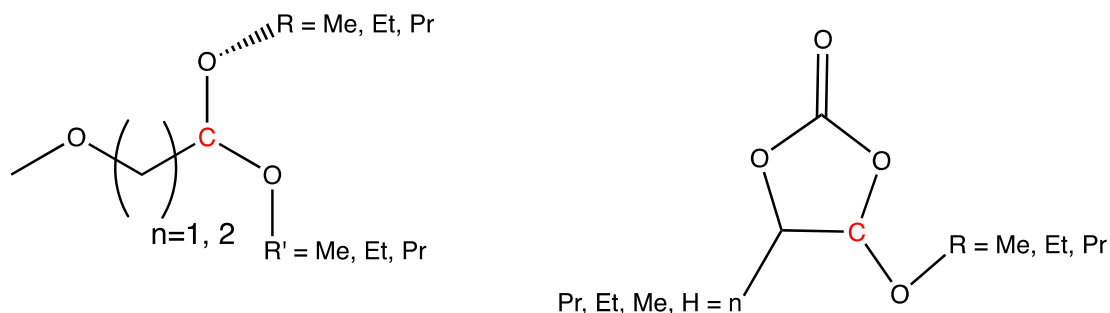


Table B.4. The calculated ^{13}C chemical shifts of the cyclic acetal carbons of Figure S14 (where n and R are defined). In each case, TMS is used as a reference.

n	R	Δ [ppm]	n	R	Δ [ppm]	n	R	Δ [ppm]	n	R	Δ [ppm]
H	Me	106.0	Me	Me	111.2	Et	Me	111.0	Pr	Me	111.1
H	Et	104.8	Me	Et	110.0	Et	Et	109.8	Pr	Et	113.1
H	Pr	105.1	Me	Pr	110.4	Et	Pr	110.3	Pr	Pr	114.0

Table B.5. The calculated ^{13}C chemical shifts of the branched acetal carbons of Figure B.13. (where n, R and R' are defined). In each case TMS is used a reference.

n	R	R'	Δ [ppm]	n	R	R'	Δ [ppm]
1	Me	Me	109.9	2	Me	Me	109.0
1	Me	Et	108.8	2	Me	Et	107.6
1	Me	Pr	109.8	2	Me	Pr	108.4
1	Et	Me	110.3	2	Et	Me	109.4
1	Et	Et	109.0	2	Et	Et	108.2
1	Et	Pr	108.7	2	Et	Pr	107.9
1	Pr	Me	110.0	2	Pr	Me	109.4
1	Pr	Et	109.1	2	Pr	Et	108.1
1	Pr	Pr	113.4	2	Pr	Pr	107.8

The branched systems span a shift range between 107.6 to 113.4 ppm. Comparing the ethyl and propyl cores (n=1 and 2 in Table B.5) there is a small, yet clear trend of a smaller ^{13}C shift

for structure containing propyl cores. Changing the R, R' groups does not result in a clear trend here. These results are in line with the experimental values that are assigned in the paper: acetal carbon in the cyclic structure has higher ^{13}C shift than acetal carbons in the branched structure.

Appendix C

Morphology change of SiNWs after electrochemical cycling in different electrolytes.

SiNW cycled in LP30 for 30 cycles

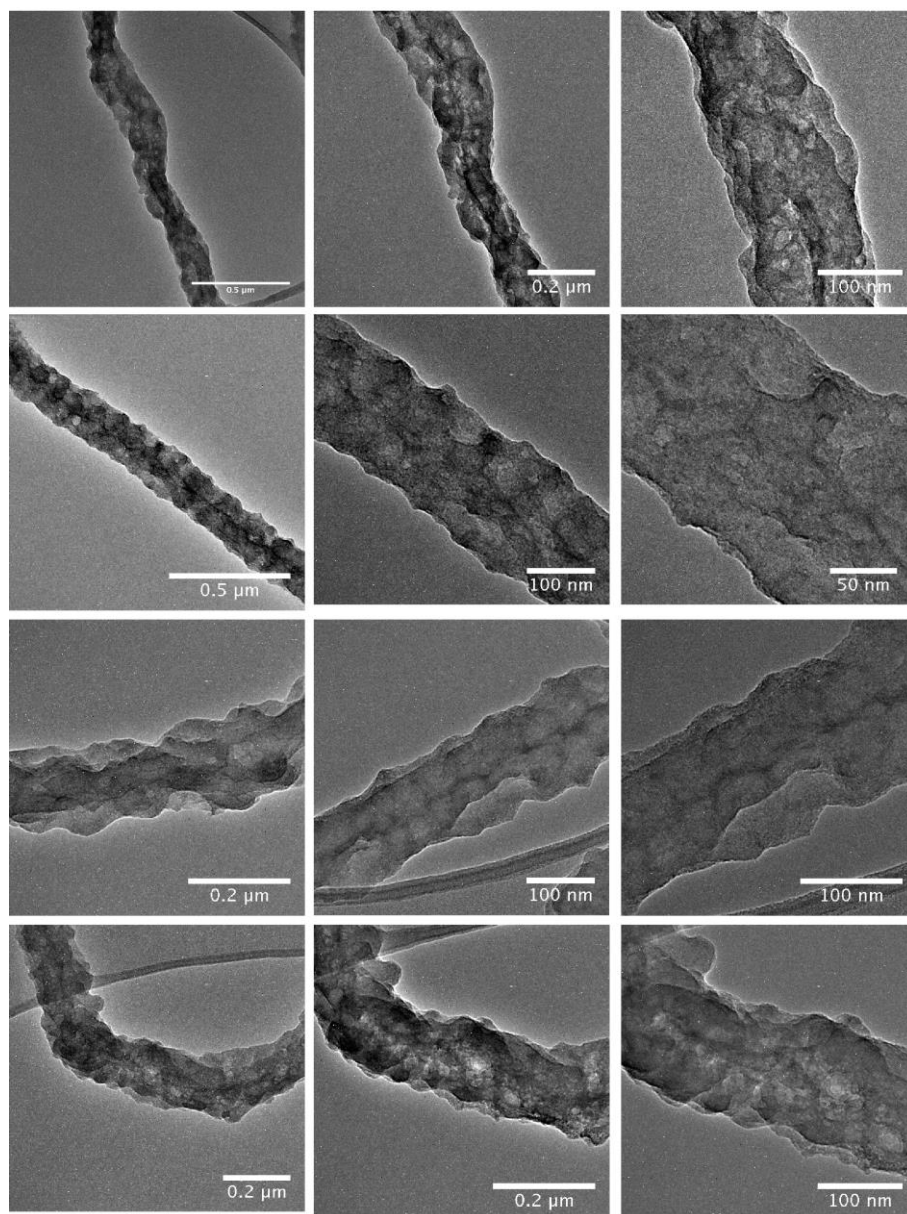


Figure C.1. TEM images of SiNWs cycled in LP30 electrolyte for 30 cycles.

SiNW cycled in pure FEC for 30 cycles

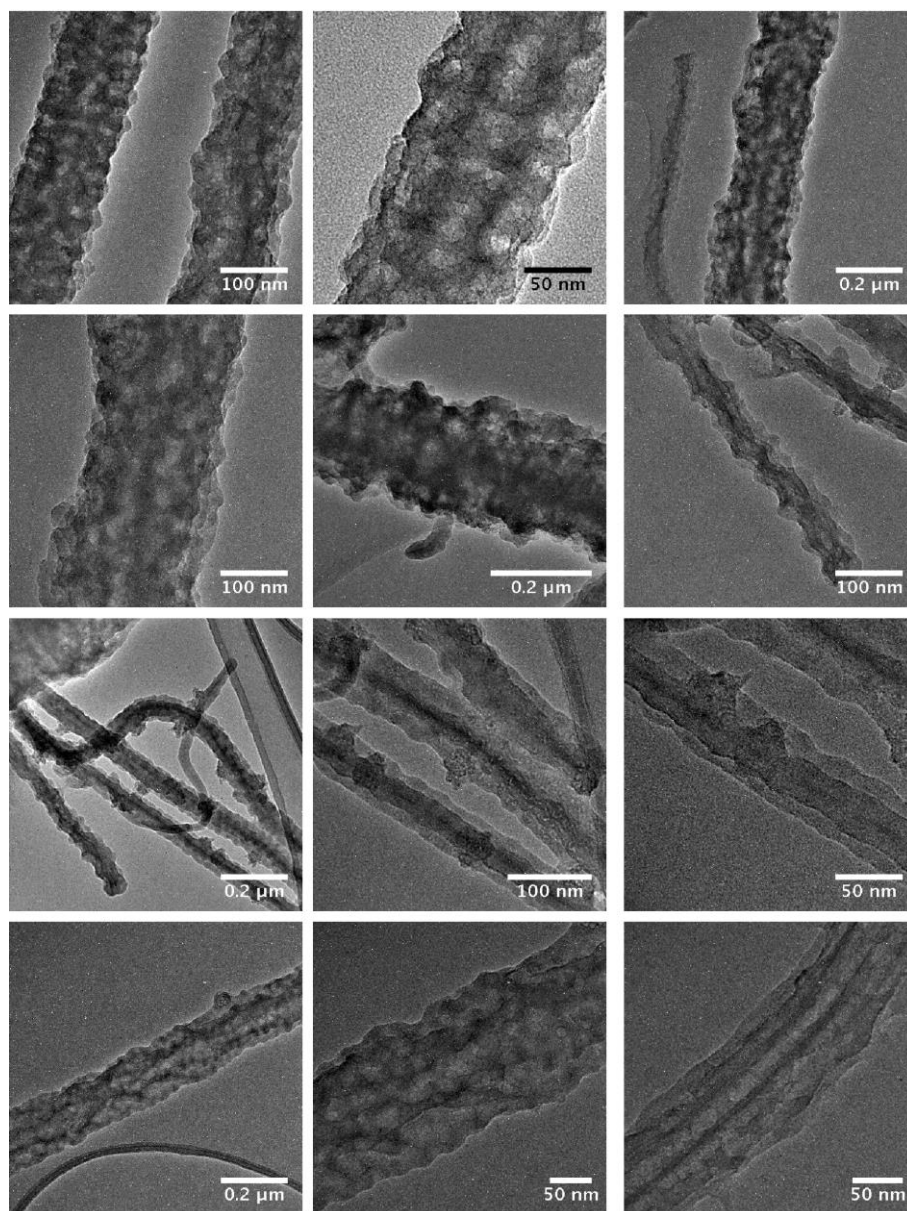


Figure C.2. TEM images of SiNWs cycled in 1M LiFP₆ in FEC electrolyte for 30 cycles.

SiNW cycled in pure VC for 30 cycles

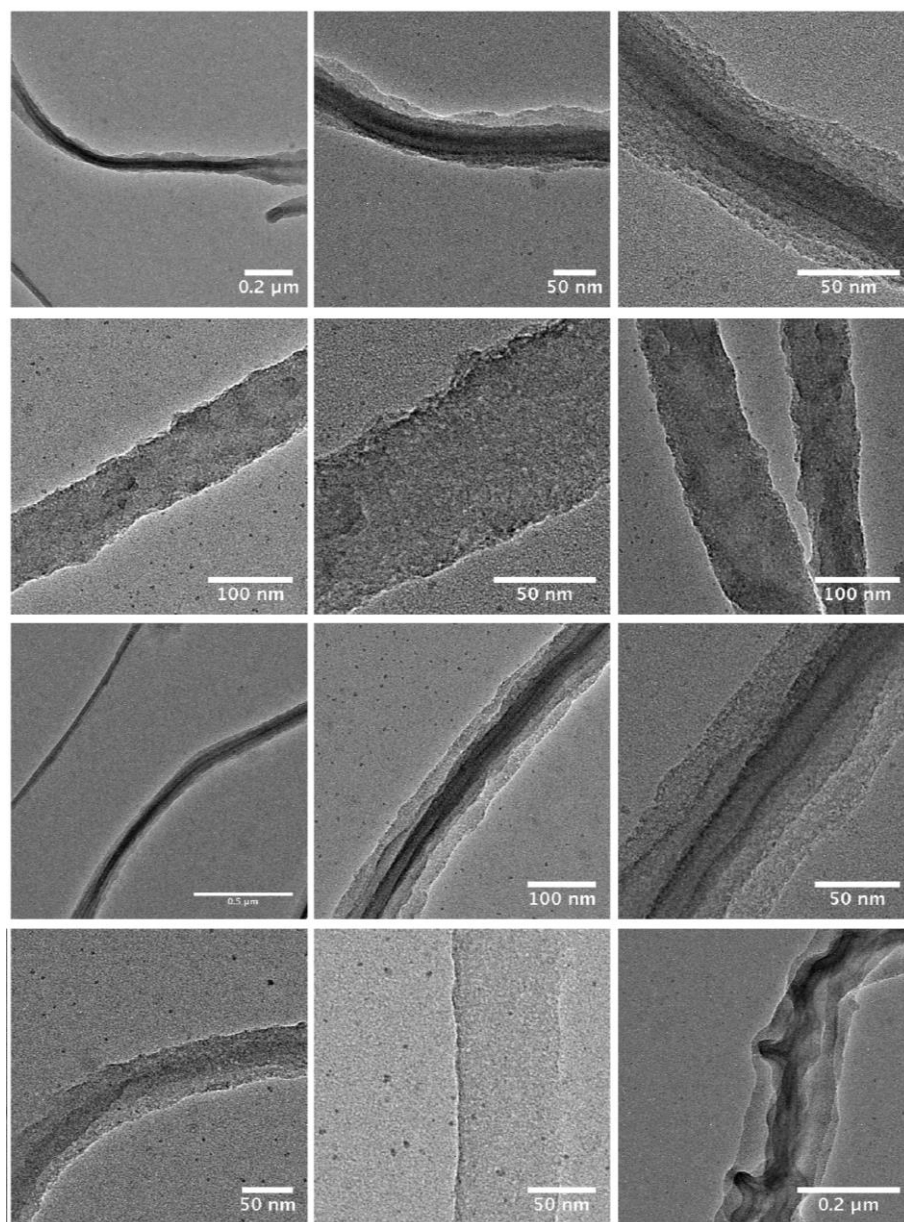


Figure C.3. TEM images of SiNWs cycled in 1M LiPF₆ in VC electrolyte for 30 cycles.

The effect of electrolyte solvent on the structural evolution of SiNWs is explored. The SiNW samples were prepared by rinsing the electrodes with DMC for three times to remove excess Li salts followed by drying it under vacuum overnight to remove DMC. The SiNWs were then scratched off from the stainless-steel substrate and suspended in DMC solutions, and drop cast on the TEM grids. The TEM images were acquired on JEOL JEM-3010 with short time (~5 min) air exposure. After cycling, the SiNWs become porous and it is difficult to discern the

boundaries between SiNW and SEI. Nevertheless, it is clear that the morphology of the SiNWs cycled in VC electrolyte is very different from those cycled in FEC and LP30. The VC samples have a smoother surface and the SiNWs are less porous.

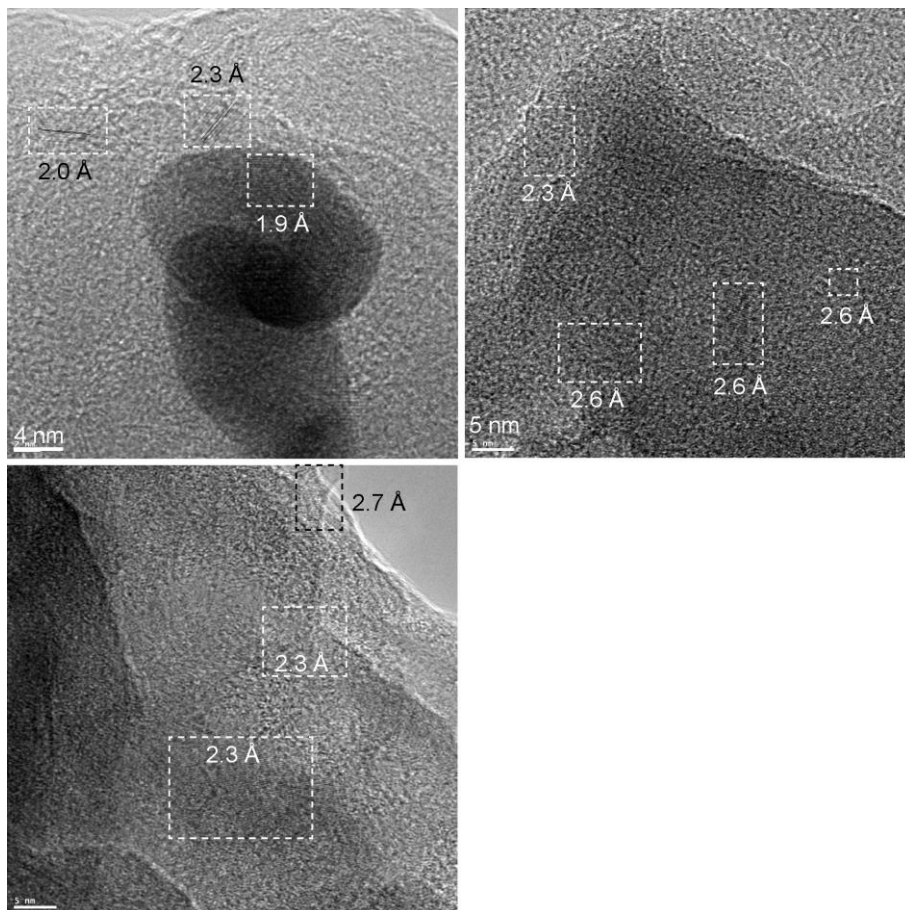


Figure C.4. High resolution TEM images of SiNWs cycled in 1M LiFP₆ in FEC electrolyte for 30 cycles. Crystalline nano-domains with lattice spacings of 1.9 Å, 1.3 Å, 2.6 Å and 2.7 Å are observed at the surface of SiNWs, indicating the presence of inorganic lithium salts such as LiF, Li₂O and Li₂CO₃, LiOH (2.76 and 2.56 Å).

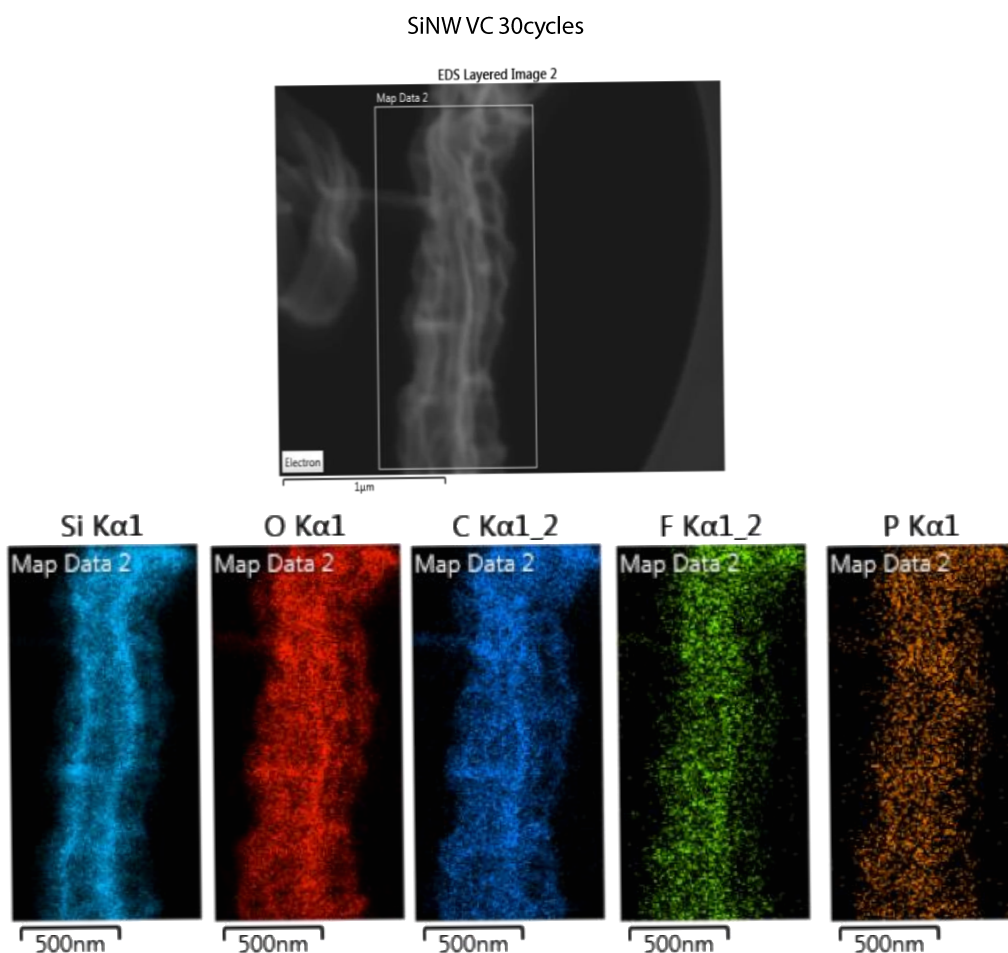


Figure C.5. SEM and EDX mapping of SiNWs cycled in 1M LiFP₆ in VC electrolyte for 30 cycles.

The, the C K_{α1} and O K_{α1} EDX mapping images of the cycled SiNW show a wider width than the Si K_{α1} image, confirm that the NW is coated by an organic layer. The Si surface is also uniformly coated with fluorine-containing species, probably due to LiF instead of fluoro-polymer.

Appendix D

Silicon nanoparticle composite electrodes

The same methodology described in Chapter 3 is applied to study the Si nanoparticle (SiNP) composite electrodes to ascertain the reproducibility of the NMR data. The obtained electrochemical and NMR data is similar to those presented in Chapter 3. Nevertheless, additional data about the mass increase and the morphology change of the SiNP composite electrode is presented here with additional information about the SEI growth.

The SiNP composite electrode is prepared by mixing silicon nanoparticles (Sigma Aldrich, diameter < 100nm), CMC (Sigma Aldrich, average $M_w=700,000$, degree of substitution = 0.90) and carbon super P (Timcal) in 1:1:1 weight ratio and adding certain amount of water and ethonal. After 10 min mixing in the Zr-jar for high energy ball mill for 10 min; the slurry was casted on the Cu foil (15 μ m thickness) using 100 μ m doctor blade. The electrodes were dried at room temperature and were punched into ½ inch diameter coin cell electrodes, followed by further drying in 100°C vacuum oven for 3–4 hours. The dried electrodes were then quickly transferred into glovebox for cell assembly as described in Chapter 3. The mass loading of SiNP is around 0.15–0.20 mg/cm², and the electrode thickness is around 15–20 μ m.

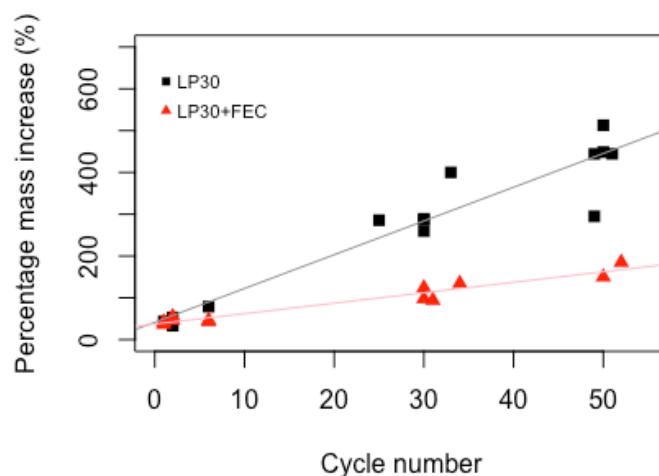


Figure D.1. The gravimetric analysis of the SiNP electrode after cycling in different electrolytes at $C/30$ between 1 mV and 2 V. The percentage of the mass increase is defined as the mass-gain after cycling over the pristine electrode mass. Black square denotes the SiNWs cycled in LP30 electrolyte, red triangle for samples cycled in the LP30+10 vol % FEC. The electrodes were extracted from the coin cell without washing but dried in vacuum for 12–15 hours.

The mass of SiNP composite electrode increases continuously after cycling. In the conventional electrode, the electrode mass increases to 4–5 time after 50 cycles. With the addition of FEC, percentage of the mass gain is smaller (~ 2 time), suggesting that less SEI forms in the presence of FEC.

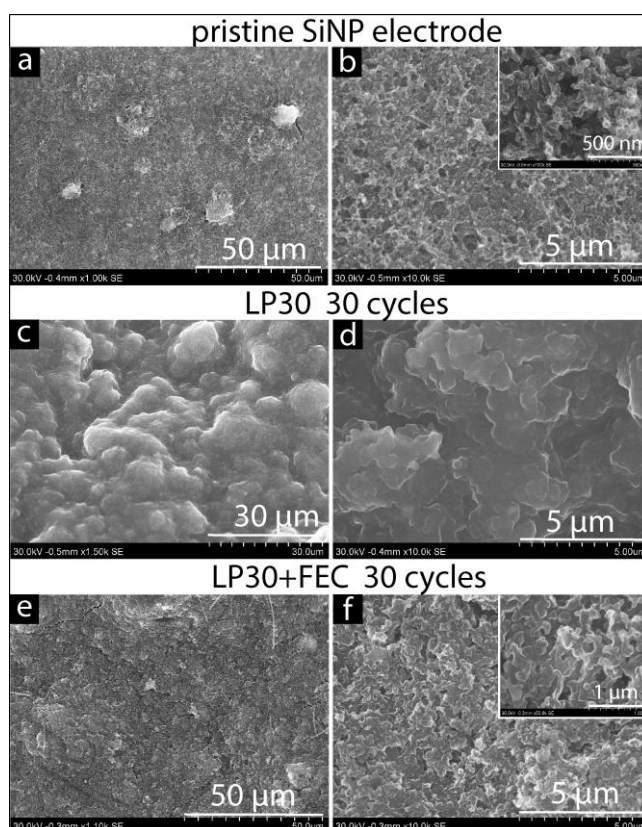


Figure D.2. SEM of SiNP electrodes. (a-b) Pristine electrode, (c-d) electrode after 30 cycles in LP30 electrolyte, (e-f) electrode after 30 cycles in LP30+10 vol% FEC electrolyte.

The pristine SiNP electrodes and those cycled electrodes were characterized by SEM (Figure D.2). The Pristine SiNP electrodes have relatively smooth surface and large porosity (a,b). After cycling in LP30 electrolyte for 30 cycles, the SiNP electrodes contain large secondary particles with size around 10 μm (c, d) and the porosity of the electrode decreases due to the formation of a thick SEI. In contrast, the SiNP electrodes cycled in FEC-containing electrolyte for the same number of cycles has a much thinner SEI and show a similar electrode porosity as these in the pristine sample. The result is consistent with the gravimetric analysis, confirming that a thinner SEI forms with the addition of FEC.